AD NUMBER

AD472298

NEW LIMITATION CHANGE

TO

Approved for public release, distribution unlimited

FROM

Distribution authorized to U.S. Gov't. agencies and their contractors; Administrative/Operational Use; 1965. Other requests shall be referred to Air Force Arnold Engineering Development Center, AEDC/IN STINFO, 251 First Street, Arnold AFS, TN 37389-2305.

AUTHORITY

aedc, usaf ltr, 3 mar 1971

SECURITY MARKING

The classified or limited status of this report applies to each page, unless otherwise marked.
Separate page printouts MUST be marked accordingly.

THIS DOCUMENT CONTAINS INFORMATION AFFECTING THE NATIONAL DEFENSE OF THE UNITED STATES WITHIN THE MEANING OF THE ESPIONAGE LAWS, TITLE 18, U.S.C., SECTIONS 793 AND 794. THE TRANSMISSION OR THE REVELATION OF ITS CONTENTS IN ANY MANNER TO AN UNAUTHORIZED PERSON IS PROHIBITED BY LAW.

NOTICE: When government or other drawings, specifications or other data are used for any purpose other than in connection with a definitely related government procurement operation, the U. S. Government thereby incurs no responsibility, nor any obligation whatsoever; and the fact that the Government may have formulated, furnished, or in any way supplied the said drawings, specifications, or other data is not to be regarded by implication or otherwise as in any manner licensing the holder or any other person or corporation, or conveying any rights or permission to manufacture, use or sell any patented invention that may in any way be related thereto.

TRANSACTIONS OF THE SECOND TECHNICAL WORKSHOP ON DYNAMIC STABILITY TESTING, HELD AT THE ARNOLD ENGINEERING DEVELOPMENT CENTER ARNOLD AIR FORCE STATION, TENNESSEE ON APRIL 20-22, 1965. VOLUME II.

ARNOLD ENGINEERING DEVELOPMENT CENTER ARNOLD AFS TN

1965

TRANSACTIONS OF THE SECOND TECHNICAL WORKSHOP ON DYNAMIC STABILITY TESTING

Volume II

Held at the Arnold Engineering Development Center, Arnold Air Force Station, Tennessee, April 20-22, 1965

Sponsored By

Arnold Engineering Development Center
Air Force Systems Command
United States Air Force

and

ARO, Inc., Subsidiary of Sverdrup and Parcel, Inc.

PREFACE

The Second Technical Workshop on Dynamic Stability Testing was held at the Arnold Engineering and Development Center, Arnold Air Force Station, Tennessee, on April 20-22, 1965. It was sponsored by the Arnold Engineering Development Center, Air Force Systems Command and ARO, Inc., operating contractor for Arnold Center and a subsidiary of Sverdrup and Parcel, Inc.

The transactions are presented in three volumes; Volumes I and II contain unclassified papers, and Volume III contains classified papers. The categories covered in each volume are shown in the Table of Contents.

Requests for copies of the transactions by agencies of the Department of Defense, their contractors, and other government agencies should be directed to Defense Documentation Center, Cameron Station, Alexandria, Virginia, 22314.

The Second Technical Workshop Committee

Major D. K. Calkins
Arnold Engineering Development Center
Symposium Director

C. J. Schueler
ARO, Inc., von Karman Facility
Executive Manager and Program Chairman

J. Arnaiz
General Electric Re-Entry Systems Division

PAPERS PRESENTED AT WORKSHOP

AND

TABLE OF CONTENTS

THEORETICAL METHODS

Chairman: C. H. Murphy
Chief, Free Flight Aerodynamics Branch, Exterior Ballistics Laboratory, Ballistic Research Laboratories, Aberdeen Proving Ground, Maryland

FACILITIES, TECHNIQUES AND TEST RESULTS

Chairman: Bass Redd
Head, Analytical Section, Aerodynamics Branch of the Advanced Space Craft Technical Division, Manned Space Craft Center, NASA, Houston, Texas

PART I

DYNAMIC STABILITY TESTING IN THE 1000-ft HYPERVELOCITY RANGE AT THE ARNOLD ENGINEERING DEVELOPMENT CENTER

by
C. J. Welsh

ABSTRACT

A brief description of the new 1000-ft hypervelocity aeroballistic range* at the Arnold Engineering Development Center is given. The unique procedures involved in obtaining model orientation and trajectory data from this range and the advantages of this length of range for dynamic stability testing are discussed, and preliminary damping data from this test unit are presented.

*Aerophysics Branch, von Karman Gas Dynamics Facility (VKF), Arnold Engineering Development Center (AEDC), Air Force Systems Command (AFSC).

CONTENTS

ILLUSTRATIONS

NOMENCLATURE

A_1, A_2, a_1, a_2	Equation constants (See Eq. 1)
C	Number of cycles of motion over the range length
C_{N_α}	Normal force derivative
$C_{m_{\frac{qd}{2v}}} + C_{m_{\frac{\dot{\alpha}d}{2v}}}$	Damping-in-pitch derivatives
I	Model moment of inertia (relative to a transverse axis)
k_y	Radius of gyration
ℓ	Model length
L	Instrumented length of the range
M	Mach number, free stream
P	Model roll rate
p_∞	Range pressure
R	Ratio of the amplitude of a damped oscillation (at a given distance traveled) to the initial amplitude
Re	Reynolds number based on free-stream conditions and axial length
s	Distance along the flight path
x	Static margin
ξ	Complex yaw angle

INTRODUCTION

The new AEDC-VKF 1000-ft Hypervelocity Aeroballistic Range (G) is currently operational and undergoing extended calibration and evaluation testing. This is a variable-density, aerodynamics range and has an 840-ft instrumented length that includes 43 equally spaced, dual-plane, shadowgraph stations. In consideration of its length and of the number of available shadowgraph stations, the range is expected to be particularly useful for dynamic stability testing.

The purposes of this paper are to briefly discuss the basic capabilities of the range, the unique procedures involved in obtaining model orientation and trajectory data with a fresnel-lens type shadowgraph system, and the use of such a range for dynamic stability testing.

DESCRIPTION OF THE RANGE AND ITS BASIC CAPABILITIES

The range consists of a 10-ft-diam, 1000-ft-long tank that is contained within an underground enclosure, Fig. 1. The current launcher is a two-stage, light-gas gun with a 2.5-in.-diam launch tube. The muzzle end of the launch tube extends 10 ft into a 100-ft-long blast tank which precedes the range tank. In the blast tank the model is separated from the sabot. After a successful launching, the model continues into the main range while the components of the sabot are trapped within the

blast tank section. A bulkhead incorporating a thin mylar diaphragm and a valve separates the blast tank section from the main range.

The first of the 43 fresnel-lens type shadowgraph stations is located approximately 105 ft from the muzzle end of the launch tube. The stations are spaced nominally at 20-ft intervals. The components of a typical shadowgraph station are indicated in Fig. 2. Though only the shadow planes (the front surfaces of the fresnel lens packages) are positioned inside the tank, all of the shadowgraph components are mounted to the range tank. Hence, very small relative changes in the positions of the components can be expected with range pressure changes. This is discussed further in a later section of the paper.

In the present system, a fresnel lens (sandwiched between two 0.75-in.-thick sheets of plexiglas) is used as a light gathering device to provide sufficient lighting to the corresponding camera. As a test model approaches a shadowgraph station, the detector unit (either a shadow or luminosity mode) senses the presence of the model. The output of the detector unit actuates the spark sources. The cameras are focused to the shadowplane, hence shadowgrams of the model as seen in the shadow planes are obtained. A timing system actuated by the output of the x-plane spark sources of each station provides corresponding timing values to within 3×10^{-7} sec.

The current pumping capabilities for the range provide range pressures from one atmosphere down to 15 μ Hg. The 15 μ Hg

pressure level corresponds to an equivalent altitude of approximately 250,000-ft. To date, 0.5-in.-diam aluminum spheres have been launched at velocities above 18,000 fps and 1-in.-base-diam cone models have been launched at velocities above 15,000 fps. Launcher evaluation testing has not been completed, but considering that no effort to achieve maximum velocity has been attempted, these data do not represent the highest performance.

PROCEDURES FOR OBTAINING MODEL ORIENTATION AND TRAJECTORY DATA

The basic purpose of a shadowgraph system in an aerodynamic range is to provide a means of determining the position and attitude of the model at each station. To determine the position and attitude of the model, certain measurements related to the model's shadows in the shadow planes are needed. These measurements, in combination with known geometric parameters of the station, permit computing the model's orientation and position relative to the local axis system of the station. Such information on the model's flight at each of a series of shadowgraph stations permits computing both the yawing motion and the trajectory of the model.

The procedures involved in obtaining model orientation and trajectory data from a fresnel-lens type shadowgraph system in a variable-density range of this length are somewhat unique relative to conventional range practices. These procedures can be discussed better by first examining the more basic system shown in Fig. 3. Here the shadow planes contain the directly exposed film sheets and all of the components can be rigidly supported.

In such a system the two half-stations (each half-station consists of a shadow plane and its corresponding spark source) are orthogonally oriented, and each component is positioned to close tolerances. From the shadow geometry for the view of each half-station indicated in Fig. 3, simple relationships between a point in space, the coordinates of the corresponding shadow, and the spark-to-shadowplane distances can be obtained. Similar shadow geometry exists in the y-z and x-z views of the two half-stations.

As previously stated, in each half-station of the 1000-ft range shadowgraph system the camera provides a shadowgram of the model's shadow on the front surface (shadowplane) of the fresnel-lens sandwich, Fig. 2. The optical distortions caused by the port glass, the lens sandwich, etc., are circumvented by the use of a precision grid of 1-in.-spacing scribed on the front surface of the lens sandwich. All distances on the shadowgrams are measured relative to the grid, and it follows that when any distortions exist in the shadows on a shadowgram, corresponding distortions in the grid will exist. Thus, with use of the precision grid, the required dimensions in the shadow plane can be determined from shadowgram measurements. At this point, an equation defining the relationship between the position of a point in space, the coordinates of its corresponding shadow in the shadow plane, and the geometry defining the spark and shadow plane positions is required. The equation derived for analysis of data from the system, which

must be viewed as a non-orthogonal system in the strict sense, is somewhat complicated. This results from the need to consider possible angular and linear deviations in the relative positions of the sparks and shadow planes compared to their positions in an ideal, orthogonal system. One cause of these deviations is the previously mentioned range tank pressure changes.

The derived equations permit considering the following deviations from an ideal alignment: three linear deviations of each shadow plane (in the x, y, z directions), two angular deviations of the x-plane about axes parallel to the x and z axes, two angular deviations of the y-plane about axes parallel to the y and z axes and three linear deviations of each spark (in the x, y, z directions). Small angular deviations of the spark sources are not critical, and the angular orientation of a shadow plane about an axis normal to the shadow plane is accounted for in the reading of the shadowgrams. In view of the possible deviations already mentioned, eight measurements, referred to in this paper as station geometric parameters, must be determined for each half station in order to define the position of a point in space. It should be noted that the shadow geometry of each half station is independent of the other half station.

Considering that these geometric parameters cannot be measured directly for range pressures less than atmospheric, it is apparent that some type of calibration procedure must be used to determine the relative position of the spark sources and shadow planes at any particular pressure level. With use of such a calibration procedure, equally usable at atmospheric pressure, the initial alignment of the shadowgraph components is somewhat less critical.

The calibration procedure employed for this range incorporates the use of a so-called shadow fixture, Fig. 4. There are 13 holes in the fixture as indicated in Fig. 4 and the relative positions of the holes were precisely measured. In the procedure to determine the geometric parameters of a station, the fixture was supported in the range tank on a double pivot such that the fixture's center hole was nominally positioned at the station origin. The fixture was mass balanced, hence the gravity force oriented the fixture angularly, except about its vertical axis. With use of a theodolite, the fixture was oriented about this axis relative to a reference sight line common to all of the stations. With the fixture positioned, the center hole of the fixture defines the station origin, and it follows that 13 points of known location relative to the station origin, corresponding to the 13 fixture holes, are available for determining the

geometric parameters of the station. Only 6 of the 8 geometric parameters associated with each half station are involved in each view of the half station. Of the 6 geometric parameters involved in each view, 4 are common to both views. Hence, with use of 13 available points the problem becomes the solving of the resulting 13 simultaneous equations (corresponding to the 13 fixture holes) for 6 unknown geometric parameters. The basic equation is nonlinear in terms of the 6 geometric constants, and a differential-correction procedure has been used in obtaining a solution (on a 7074 IBM computer) to the 13 simultaneous equations. With the geometric parameters evaluated for each station, conventional range techniques are used to obtain model orientation and trajectory data.

The measured velocities of a 10-deg half-angle cone are shown in Fig. 5, to indicate that the above procedures for determining the position of a model in the range are quite adequate. The velocity values have been computed for 20-ft station intervals, and the scatter of points about the linear curve is within $\pm$ 0.03 percent. The assumption of a linear variation of the velocity for the cone model follows because the slope of the velocity-distance curve of a model having a constant C_D is proportional to the model's velocity. The 0.03 percent error includes both timing and distance errors; hence, using the previously stated error of 3×10^{-7} sec. in the timing system, errors in determining the position of the model

relative to a shadowgraph station are indicated to be of the order of 0.002 to 0.003 ft. With the velocity values being computed over 20 ft intervals, a missing velocity point for an interval in Fig. 5 indicates that shadowgrams were not obtained from at least one of the two adjacent shadowgraph stations.

DAMPING MEASUREMENTS

Dynamic stability derivatives are obtained from tests in the 1000-ft range by conventional methods. The basic equation,

$$\xi = A_1 \ell^{a_1 s} + A_2 \ell^{a_2 s} + A_3 \ell^{ips} \qquad (1)$$

defining tricyclic model motion is fitted to the measured components (α and β) of the yawing motion of the test model. The first two terms on the right hand side of Eq. (1) define the motion of an axisymmetric model experiencing general rolling-yawing motion. It is of interest to note that, for a symmetrical model, the above equation is of the same form as the equation defining the motion of a model on a one-degree-of-freedom balance system in a wind tunnel. The difference is that the constants in the equation, A_1, A_2, a_1 and a_2 are not complex conjugates, as they necessarily are in the restricted one-degree-of-freedom motion. It is this feature that permits the equation for the restricted model motion to be expressed in the conventional form of sine-cosine terms.

In dynamic stability testing in ranges, the required number of available shadowgraph stations has always been of concern. In an attempt to assess this problem, a brief study was made within the VKF. In the study an arbitrary selection of errors (to simulate experimental errors) was introduced into a set of ideal yaw angle data representative of the angular motion of a model. The corresponding equation of motion was then fitted to these adjusted yaw angles. Using this procedure, errors in determining the damping parameter resulting from the simulated yaw angle errors could be evaluated. Damping computations indicated that when the number of shadowgraph stations per cycle of oscillatory motion is less than about twelve, the accuracy of describing the model's angular motion deteriorates appreciably. In view of this, the number of cycles of model motion in the 1000-ft range is currently being restricted to less than four cycles.

An appreciaton of the usefulness of a range having the number of shadowgraph stations and the length of the 1000-ft range can be obtained by examining the following equations:

$$\ln R \propto L \rho_0 / I \left[k_y^2 C_{N_\alpha} - L^2/2 \left(C_{m_{\dot{\alpha}}} + C_{m_{\dot{w}}} \right) \right] \qquad (2)$$

$$C \propto L\sqrt{(\rho/\rho_0)(p_0/p)} \qquad (3)$$

It should be pointed out that a particular set of range testing conditions can generally be selected such that a given model can be tested satisfactorily in a range having a lesser length and fewer stations than the 1000-ft range. However, the band of range conditions compatible with dynamic stability testing are somewhat restricted, particularly at hypervelocities. Equation (2) indicates that the logarithm of the amplitude ratio of the model motion is directly proportional to the range length and the range pressure, and is inversely proportional to the model's inertia. Because the damping parameter is determined as a function of this amplitude ratio, it follows that the basic requirement in damping measurements is that a measurable amplitude decay exists. Thus, two significant advantages related to an increase in range length are:

1. A model configuration can be tested at a higher velocity and still maintain a feasible amplitude ratio. Here the additional range length can be used to compensate for additional model inertia (and increased radius of gyration) related to the high-

acceleration model structure dictated by high-velocity launchings.

2. A model configuration can be tested (maintaining a feasible amplitude ratio) at a lower Reynolds number by using the additional range length to compensate for the decrease in the range pressure.

In considering the number of available shadowgraph stations it is apparent that there must necessarily be enough stations to adequately define the motion when a minimum number of cycles of motion exists over the range length, (of the order of 1.0 to 2.0 cycles). Additional stations provide a significant increase in the usefulness of a range by providing a cycle band in which data can be adequately obtained. It should be noted that the full advantage cannot be realized from the apparent cycle control afforded by the dimensionless static margin parameter x/ℓ, indicated in Eq. (3), because of model design limitations. Though Eqs. (2) and (3) are for planar motion, the comments referring to the extensions of the test boundaries in a range are equally applicable for general rolling-yawing motion.

The evaluation testing of the 1000-ft range has progressed to a point permitting stability measurements. Three experimental values for the damping parameter

$$\left[-C_{N_\alpha} + 2C_D + \tfrac{1}{2}\left(\frac{d}{\sigma}\right)^2 \left(C_{m_{\frac{qd}{2V}}} + C_{m_{\frac{\dot{\alpha}d}{2V}}}\right)\right]$$

have been obtained for a 10° half-angle cone configuration. These damping values are shown in Fig. 6a, and the limited number of test points indicates that no appreciable effects of Reynolds or Mach number exist for the range of these two parameters covered in the tests. The repeatability of the damping measurements for similar test conditions is very good, cf, the M = 7.9 and M = 9.3 data points. This is particularly true considering that there is a difference in the C_D values pertaining to the two data points. The different C_D values result from the different model amplitudes which are listed in Fig. 6a. The damping in pitch derivatives ($C_{m_{\frac{qd}{2V}}} + C_{m_{\frac{\dot{\alpha}d}{2V}}}$) have been separated from the total damping parameter and are shown in Fig. 6b. Some AEDC wind tunnel data obtained at M = 10, using a one-degree-of-freedom balance system (Ref. 1), are also shown. The tunnel and range data pertain to a similar cone configuration, except for the difference in nose bluntness noted in the figure. Considering the amount of data available at this time, it does not seem justifiable to comment on possible differences between the wind tunnel and free-flight results per se.

REFERENCE

1. Hodapp, A. E., Jr., Uselton, B. L., and Burt, G. E. "Dynamic Stability Characteristics of a 10-deg Cone at Mach Number 10". AEDC-TDR-64-68, May 1964.

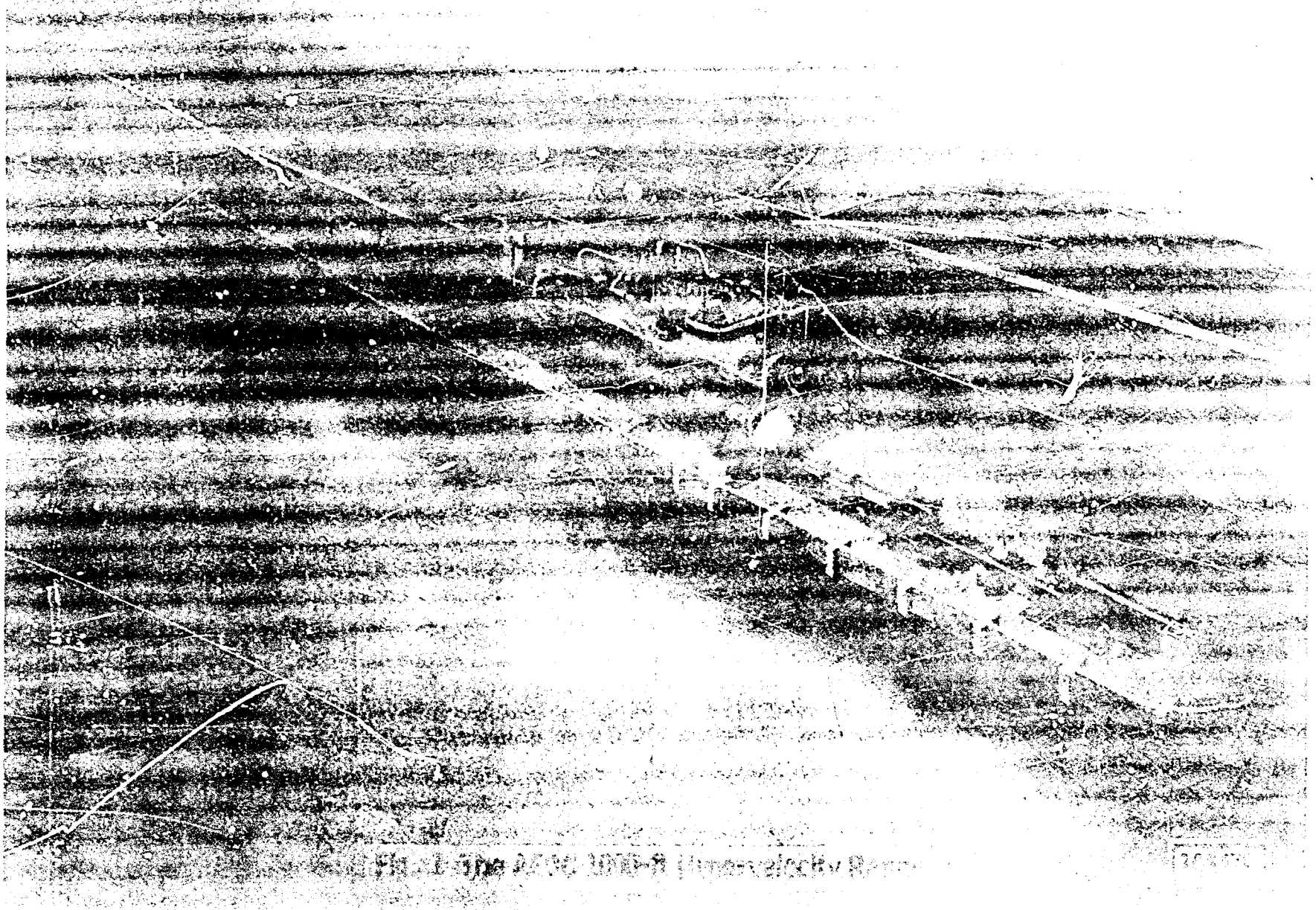

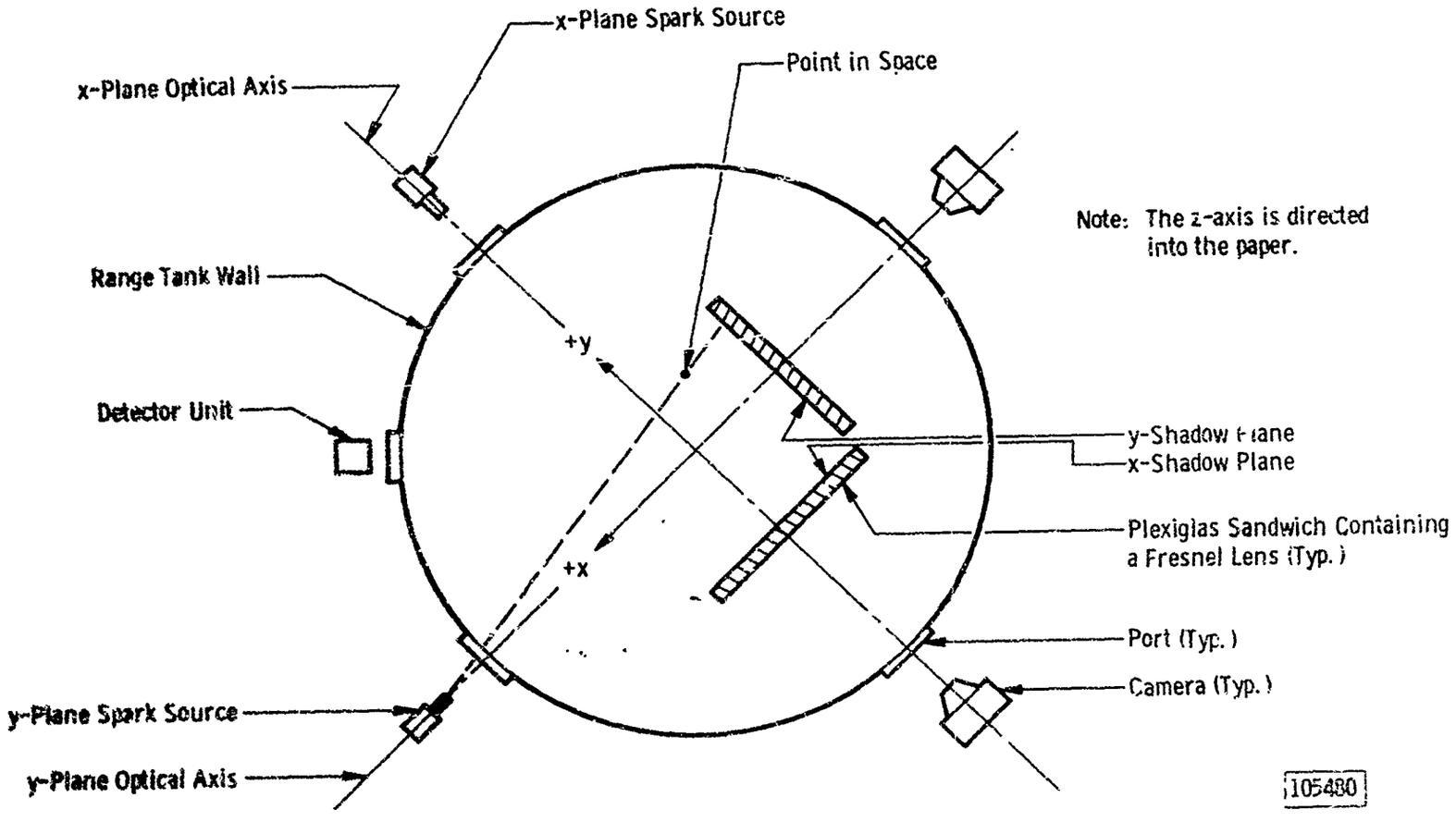

Fig. 2 Cross-Sectional View of a Typical Shadowgraph Station of the 1000-ft Range (as Viewed from the Launcher Position)

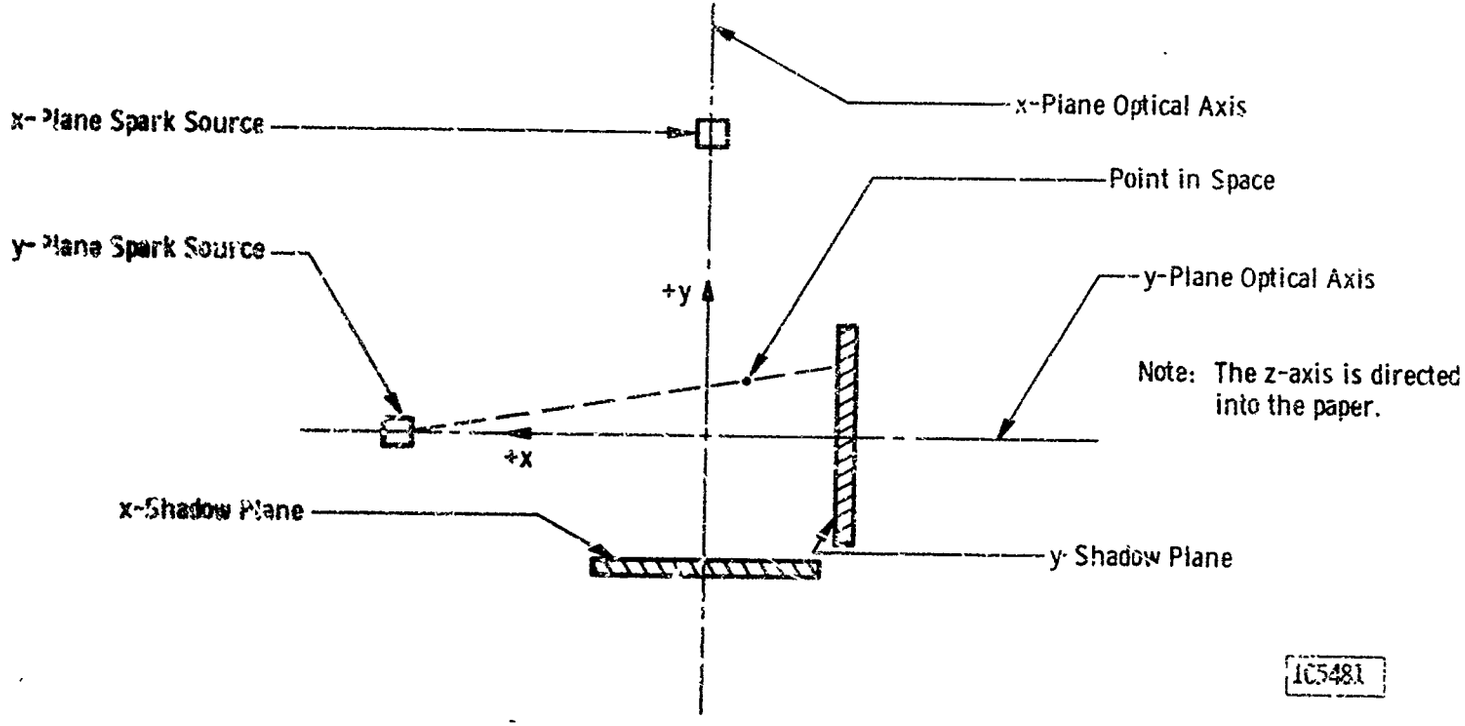

Fig. 3 A Basic Direct-Exposure Shadowgraph Station

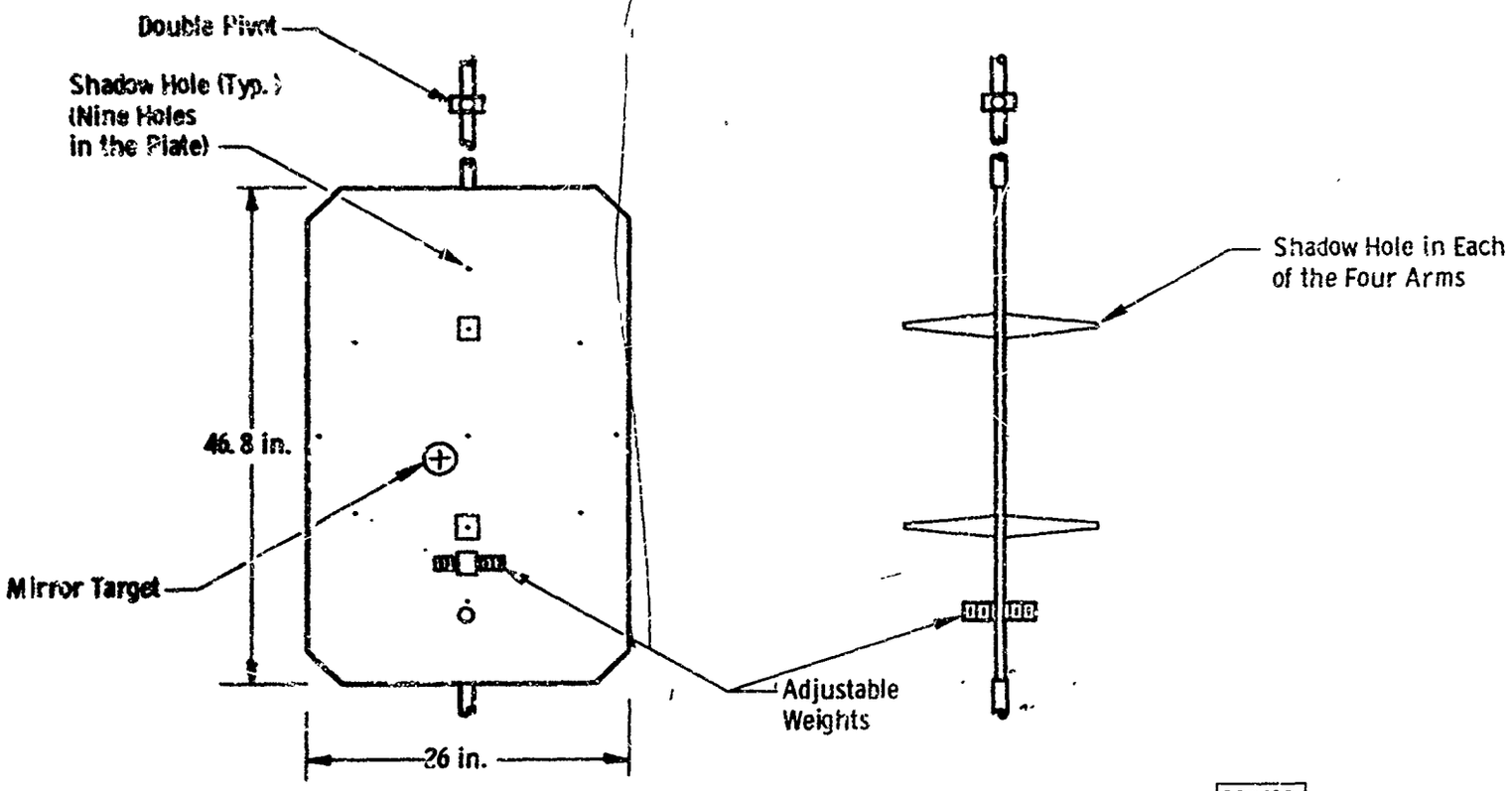

Fig. 4 Shadow Fixture Used in the Calibration of a Shadowgraph Station

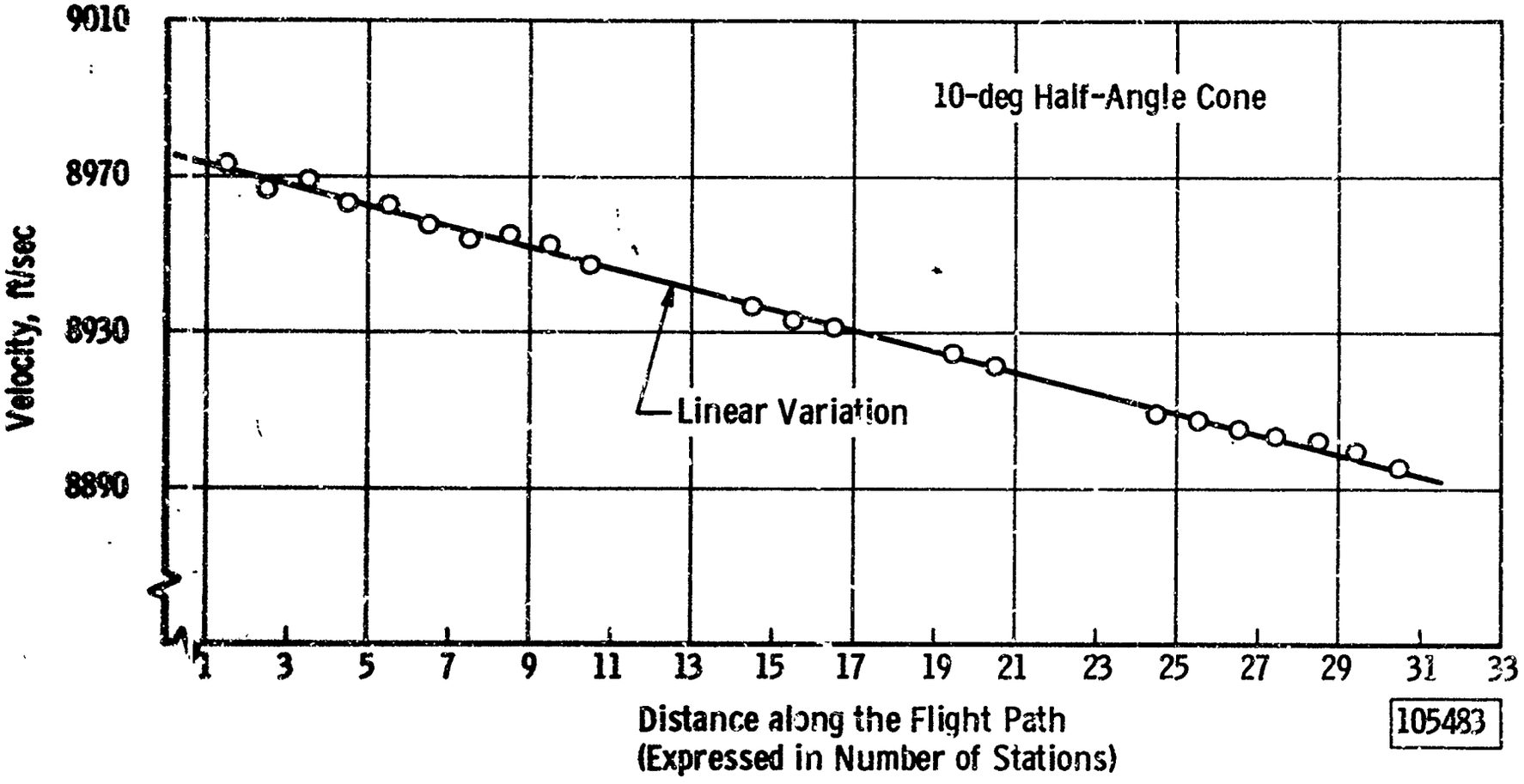

Fig. 5 Measured Velocities of a Cone Flight in the 1000-ft Range

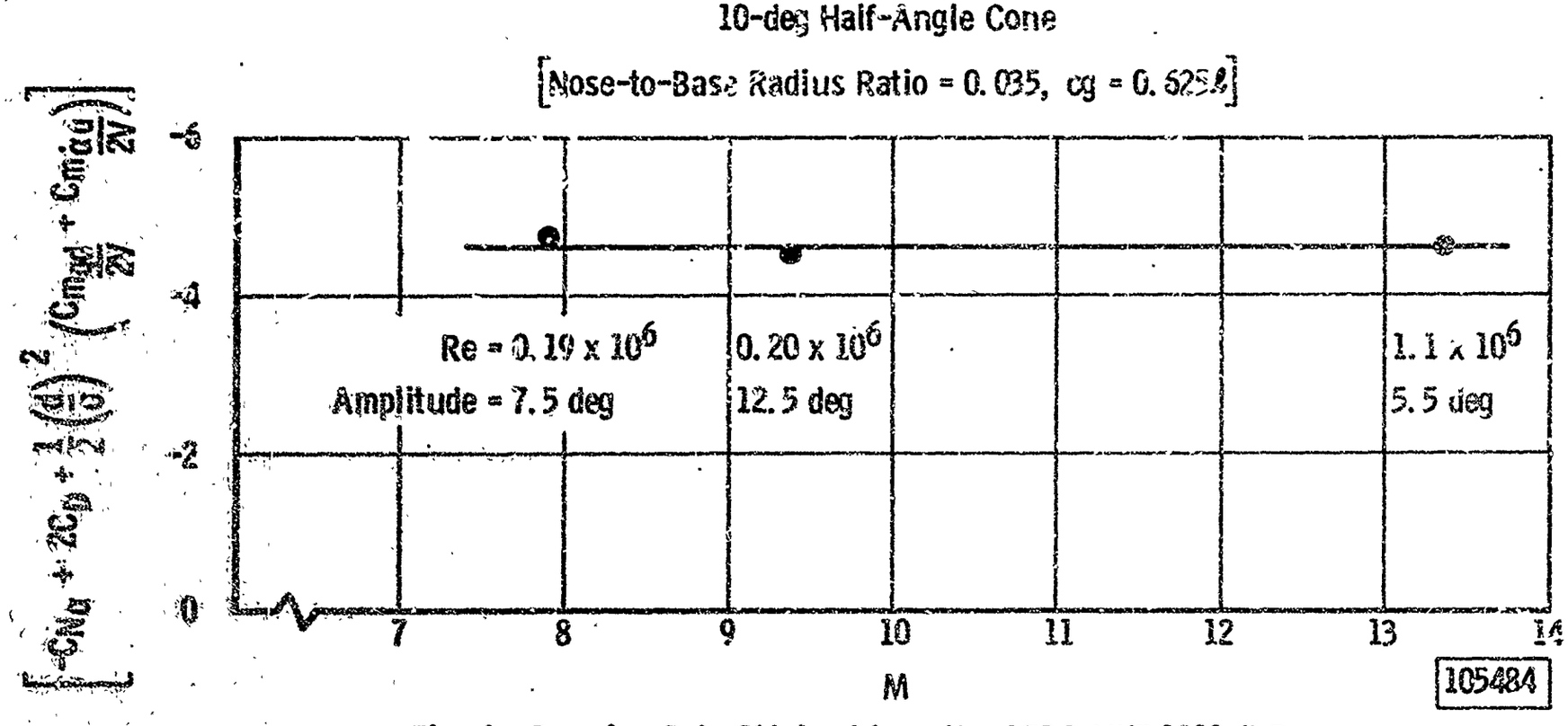

Fig. 6a Damping Data Obtained from the AEDC-VKF 1000-ft Range

10-deg Half-Angle Cone

○ M = 10, AEDC (Tunnel)
Forced Oscillation, ±2 deg
Re = 0.73 x 10^6
Pointed Nose

□ M = 7.9, Amplitude = 7.5 deg, Re = 0.19 x 10^6
◇ M = 9.4, Amplitude = 12.5 deg, Re = 0.20 x 10^6
△ M = 13.35, Amplitude = 5.5 deg, Re = 1.10 x 10^6
Nose-to-Base Radius Ratio = 0.035

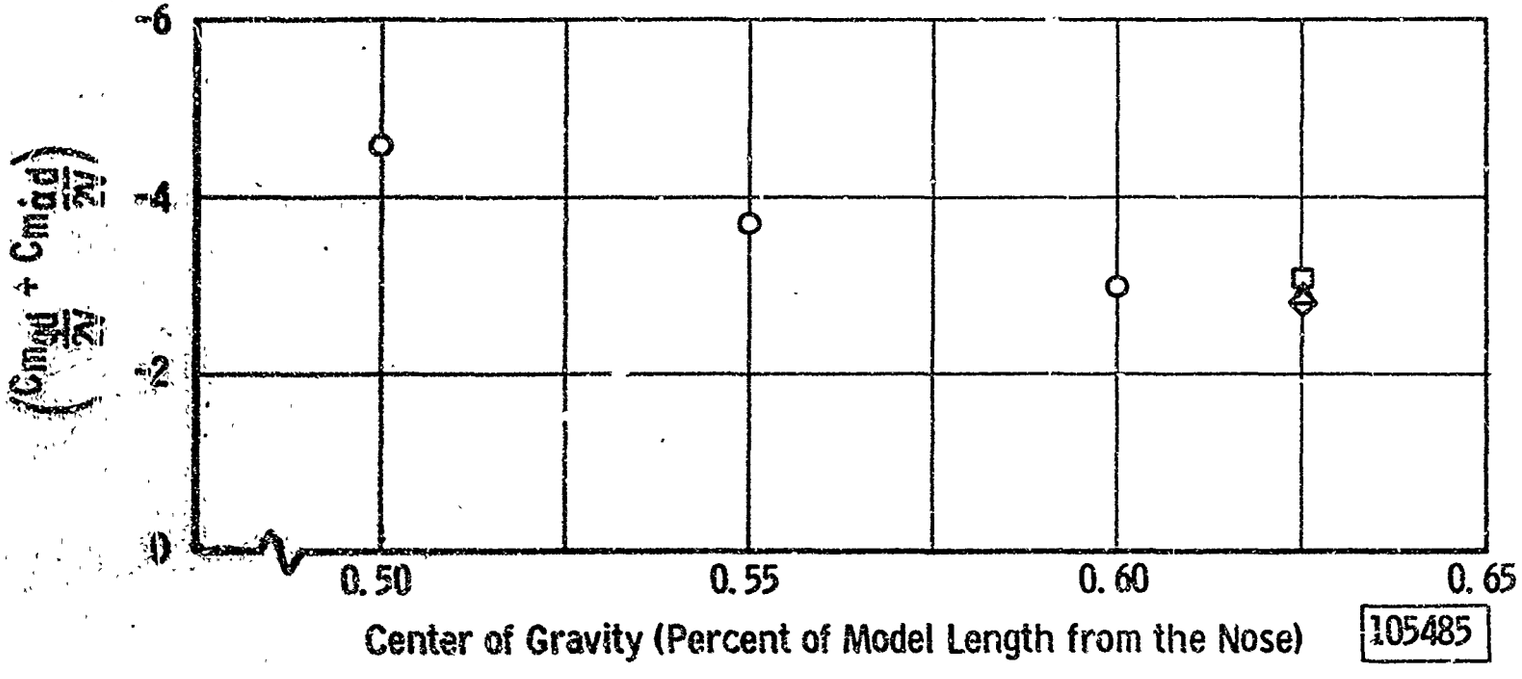

105485

Fig. 6b Damping Data Obtained from the AEDC-VKF 1000-ft Range

DISCUSSION

Bass Redd:

What sort of accuracy do you get in any one given angle of attack in your ballistics range?

C. Welsh:

You refer to measuring the attitude of the model at a particular station?

Bass Redd:

Yes, sir.

C. Welsh:

At this point I couldn't give you a firm answer. We know it will vary someplace say between a tenth and a half of a degree; however, in the fit, if we would indicate residuals from the curve fit of say as high as 4/10 of a degree or 5/10, it is high. Of the data we have so far, the residuals between the curve fit and the measured angular values, that are for given stations are generally a tenth and below.

PROBLEMS ASSOCIATED WITH OBTAINING ACCURATE DYNAMIC STABILITY RESULTS FROM FREE-FLIGHT TESTS*

Gary T. Chapman and Donn B. Kirk

National Aeronautics and Space Administration
Ames Research Center
Moffett Field, Calif.

INTRODUCTION

To obtain dynamic stability results from ballistic range flight tests, angular orientation measurements at discrete points along the trajectory are used to evaluate parameters in the solutions to various equations of motion. A number of factors combine to degrade the derived dynamic stability result. First, the apparent damping of the motion can be significantly influenced by errors that are made in measuring angles from photographs of the model in flight. And second, the equations of motion are influenced by the approximations that are made in both setting up the equations and in solving them.

This paper will cover some phases of each of these problems. We will first review the data reduction procedure presently in use at Ames. Then the effect of experimental errors on dynamic stability results will be considered, first from a simple theoretical standpoint, then from a statistical approach involving perturbations of exact solutions.

Finally we will consider two assumptions involving the equations of motion which can give rise to errors: (1) the assumption that the

*Prepared for the Second Technical Workshop on Dynamic Stability Testing, Arnold Engineering Development Center, April 20-23, 1965.

resultant angle of attack is the square root of the sum of the squares of the two orthogonal projected angles, and (2) the assumption that a linear restoring moment and constant damping coefficient govern the model oscillation. Exact trajectories will be computed and then analyzed by our existing data reduction procedure. Typical examples will be shown to demonstrate the magnitude of errors that can be expected, and ways of eliminating or minimizing these errors will be discussed.

SYMBOLS

A	reference area
$a_1, \ldots, a_8$	constants in equations (1)
C_D	drag coefficient
C_{L_α}	lift-curve slope
C_m	pitching-moment coefficient
C_{m_α}	pitching-moment curve slope
$C_{m_q} + C_{m_{\dot{\alpha}}}$	rate of damping in pitch
d	reference diameter
I_y	moment of inertia about pitch axis
k	constant $\rho A/4m$
M_0, M_2	constants used to define nonlinear restoring moment curves
m	model mass
N	number of observation points per cycle

n	number of cycles of motion
p	roll rate
SD_α	standard deviation in angle of attack due to experimental errors
SD_ξ	standard deviation in ξ
x	distance along flight path
α, β	angles of attack and sideslip
α_r	resultant angle of attack
$\Delta\alpha$	change in pitch amplitude due to damping
Δx	distance between observation stations
$\eta, \eta_2, \omega, \omega_2$	constants in equations (1)
λ	wave length of pitching oscillation
ξ	dynamic stability parameter defined in equation (3)
ρ	air density
σ	radius of gyration of model about pitch axis
φ	angle between observation plane and plane of motion

Subscripts

E	exact value
env	envelope
env_o	envelope at $x = 0$
i	individual readings
RMS	root mean square

DATA REDUCTION PROCEDURE

The current data reduction procedure consists of curve-fitting measured values of α, β, and x (this is where experimental errors enter the problem) with a solution to the equations of motion. This solution is the tricyclic solution of Nicolaides (ref. 1), transformed to distance (x) rather than time (t) dependence. This solution allows for constant roll rate and small asymmetries. The solution is

$$\alpha = e^{\eta_1 x}(a_1 \sin \omega_1 x + a_2 \cos \omega_1 x) + e^{\eta_2 x}(a_3 \sin \omega_2 x + a_4 \cos \omega_2 x) + (a_5 \sin px + a_6 \cos px) \tag{1a}$$

$$\beta = e^{\eta_1 x}(a_1 \cos \omega_1 x - a_2 \sin \omega_1 x) - e^{\eta_2 x}(a_3 \cos \omega_2 x - a_4 \sin \omega_2 x) + (a_5 \cos px - a_6 \sin px) \tag{1b}$$

where the constants $\omega_1, \omega_2, \eta_1, \eta_2, a_1, \ldots, a_8$ are determined by the curve-fitting procedure (p, the roll rate, is related to ω_1 and ω_2); the curve fitting is carried out by a differential correction procedure. The dynamic stability parameter is related to η_1 and η_2 as follows:

$$\xi = \frac{2n}{\rho A}(\eta_1 + \eta_2) \tag{2}$$

where ξ is the constant-altitude power-off dynamic stability parameter related to the aerodynamic coefficients by

$$\xi = C_D - C_{L_\alpha} + \left(C_{m_q} + C_{m_{\dot{\alpha}}}\right)\left(\frac{\rho d^2}{I_y}\right) \tag{3}$$

The static stability parameter C_{m_α} is related to ω_1 and ω_2 as

$$C_{m_\alpha} = \frac{-2\omega_1\omega_2 I_y}{\rho A d} \tag{4}$$

The major assumptions employed in the derivation of equations (1) which give rise to apparent errors, particularly in the dynamic stability parameter, are: (1) the aerodynamic coefficients are assumed to be constants or linear functions of angle of attack; and (2) the resultant angle of attack α_r is assumed to be given as $\alpha_r = \sqrt{\alpha^2 + \beta^2}$ instead of $\tan^{-1}\sqrt{\tan^2 \alpha + \tan^2 \beta}$. The systematic errors generated by these assumptions usually appear as an absolute shift in the results as contrasted to random errors arising in the experimental measurements of α, β, and x. These two sources of error will be treated independently.

ANALYSIS OF RANDOM EXPERIMENTAL ERRORS

A statistical analysis will be presented, which consists of calculating exact trajectories, introducing simulated experimental errors via a Monte Carlo procedure, and analyzing these perturbed trajectories with the data reduction procedure just described. For simplicity we will consider linear aerodynamics and planar motion in calculating the exact trajectories. However, before proceeding further a brief look at a simplified version of the problem will help in interpreting the statistical results and provide some guidelines as to what variables might be important.

Simple Theory

We will consider the error involved in determining the dynamic stability parameter from two data points which represent points on the envelope of the pitching motion (see sketch (a)). The equation for the envelope of the arc is given as

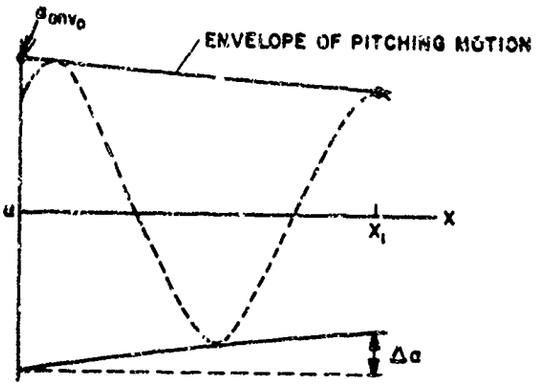

Sketch (a)

$$\alpha_{env} = \alpha_{env_0} e^{k\xi x} \tag{5}$$

where $\alpha_{env_0} = \alpha_{env}$ at $x = 0$, and $k = \rho A/4m$. Equation (5) can be rewritten as

$$\ln\left(\frac{\alpha_{env}}{\alpha_{env_0}}\right) = k\xi x \tag{6}$$

If we now take two data points at $x = 0$ and x_1 and write α_{env_1} as

$$\alpha_{env_1} = \alpha_{env_0} + \Delta\alpha$$

equation (6) becomes

$$\ln\left(1 + \frac{\Delta\alpha}{\alpha_{env_0}}\right) = k\xi x_1 \tag{7}$$

If there is now some error in determining α_{env} at each point (the probable error at each point can be represented as $SD\alpha$),[1] then $\Delta\alpha$ is determined to within $\sqrt{2}\ SD\alpha$ and therefore there will be some probable error in ξ, noted as $SD\xi$. From these ideas we can write equation (7) as

---

[1] SD refers to standard deviation and has its usual statistical definition $SD\alpha = \sqrt{\frac{1}{n}\sum_{i=1}^{n}(\alpha_i - \alpha_E)^2}$ where α_i are individual readings, α_E is the exact value, and n is the number of readings.

$$\ln\left(1 + \frac{\Delta\alpha}{\alpha_{env_o}} + \frac{\sqrt{2}\ SD\alpha}{\alpha_{env_o}}\right) = k(\xi_E + SD\xi)x_1 \tag{8}$$

If

$$\frac{\Delta\alpha}{\alpha_{env_o}} + \frac{\sqrt{2}\ SD\alpha}{\alpha_{env_o}} < 1$$

we can expand the logarithm, and to first order we get

$$\frac{\Delta\alpha}{\alpha_{env_o}} + \frac{\sqrt{2}\ SD\alpha}{\alpha_{env_o}} \simeq k(\xi_E + SD\xi)x_1 \tag{9}$$

We can now associate exact and error terms such that the $SD\xi$ can be expressed as

$$SD\xi \simeq \sqrt{2}\ \frac{SD\alpha}{\alpha_{env_o}}\ \frac{1}{kx_1} \tag{10}$$

If we now consider x_1 to be located at the end of the observed trajectory and replace x_1 by $n\lambda$, where n is the number of cycles and λ is the wave length of the pitching motion, we get

$$SD\xi \simeq 4\sqrt{2}\left(\frac{SD\alpha}{\alpha_{env_o}}\right)\left(\frac{m}{\rho A\lambda}\right)\left(\frac{1}{n}\right) \tag{11}$$

Equation (11) gives an indication of what to expect from a statistical analysis. Note that this equation states that $SD\xi$ does not depend on ξ. This fact will be used to simplify the analysis; however, it will also be checked for validity by comparison with some statistical results.

Note that equation (11) tells nothing about the effect of the number of data points considered. Therefore, in addition to the parameters given in equation (11), we will also consider the number of observation points per cycle (N) defined as $N = \lambda/\Delta x$, where Δx is the distance between observation stations. Note that the total number of observation stations is given as $nN + 1$.

Statistical Analysis

The procedure that was followed was to assume an arbitrary set of linear aerodynamic coefficients $\left(C_{m_\alpha},\ C_{m_q} + C_{m_{\dot\alpha}},\ \text{etc.}\right)$ and generate at discrete points a number of planar trajectories (we will refer to these trajectories as a group). In this group, the only variation was the position of the first station relative to the first maximum in the angle of attack; that is, the phase relationship between observation stations and the motion history was varied. A Monte Carlo technique was then used to introduce errors in both the angle and distance readings, simulating experimental errors. In most cases, a uniform error distribution was used, but several cases were investigated using a normal error distribution as well. This group of trajectories was then analyzed with the existing data reduction procedure and the standard deviations in the parameters of interest were determined (e.g., SDζ and SDλ). This process was repeated for different groups varying the values of SDα, α_{RMS}, $m/\rho A\lambda$, ζ, n (number of cycles), and N (number of data points per cycle).

Before considering the results, however, we must decide how many trajectories will form a meaningful statistical sampling. This question was considered in a reverse manner as follows. It was felt that perhaps 20 independent trajectories would be sufficient to be statistically meaningful. To check this, three different groups of 22 runs each (allowing for the possibility of rejecting several ill-conditioned runs) were statistically analyzed and compared, and it was felt if

each of the three groups showed the same gross results, 22 runs was a big enough sample. This is what happened, as is shown in figure 1. In this figure, the percentage of runs that resulted in an error (in absolute value) in ξ less than some value $\Delta\xi$ is shown as a function of $\Delta\xi$. Note that the standard deviation of ξ in the three different groups (indicated by arrows on the abscissa) agrees within about ±15 percent and that, in general, the three sets of results describe a similar curve. For reference a uniform distribution curve and a normal distribution curve which approximate the results are shown.

Effect of number of cycles and points per cycle on $SD\xi$.- Shown in figure 2 is the standard deviation in ξ, $SD\xi$, versus the number of observed cycles of motion for several values of N (observation points per cycle). These results are for the case where the exact value of ξ is zero. Note that $SD\xi$ increases rapidly below 1-1/2 cycles of motion. Furthermore the effect of N is generally small for values of N greater than about 4. The theoretical curve for the simple two point theory is shown by the upper solid line. It appears to have the proper dependence on n for values of n greater than about 1-1/2; however, the level of the curve is too high in this range. The fact that the shape of the curve is not predicted by the simple theory for values of n less than 1-1/2 is not too surprising since there are fewer than three peaks in the pitching motion and the data reduction procedure has difficulty distinguishing between trim and damping. Also shown in the figure are two curves besides the simple theory curve; one of these is the simple theory adjusted by a constant to

give the best fit to the results. The other curve is an exponential which gives a better fit over the range of variables considered but has no theoretical justification, as is indicated by the fact that it approaches a nonzero asymptote.

Effect of ξ on SD_ξ.- Since the results in figure 2 were obtained for $\xi = 0$, it was of interest to see if the simple theoretical model which indicated that the SD_ξ was independent of ξ did indeed hold. Recall that for large values of ξ the amplitude change can be large and thus the relative error in α, SD_α/α_{env_0} will be different at different points along the trajectory. Therefore in considering the results for large values of ξ it would seem logical that the results should be compared for the same value of SD_α/α_{RMS} where α_{RMS} is the root-mean-square angle of attack over the trajectory. Shown in figure 3 are results for various values of ξ. The solid points are the results as obtained for a constant value of SD_α/α_{env_0}. Note there may be a slight effect of ξ on the SD_ξ. The open points are the same results corrected to the same value of SD_α/α_{RMS} as in the case of $\xi = 0$. The correction was made using the linear approach suggested by the simple theory. This simple correction does appear to reduce the small effect of ξ_E on the SD_ξ. It is therefore felt that for most practical cases SD_ξ is essentially independent of ξ.

Effect of SD_α on SD_ξ.- In figure 4 the SD_ξ is plotted versus SD_α/α_{RMS} for a series of different conditions. Both SD_α and α_{RMS} were varied, as well as the type of error function used to generate

the errors in α. The correlation about a straight line is very good, thus supporting the simple theoretical model. In addition to these considerations a group of runs was treated as though every station had been read twice and both sets of readings analyzed as one run. Theoretically this should be equivalent to reducing SD_α by $1/\sqrt{2}$. This is indeed realized as shown by the triangular data points. The solid point is the result as obtained; the open point has been shifted by $1/\sqrt{2}$, which brings it back to the curve.

Effects of $m/\rho A\lambda$ and SD_x on SD_ξ.- Several different groups of 22 runs were considered with different values of $m/\rho A\lambda$. All of these groups showed excellent agreement with the simple theoretical model.

In addition to the errors in α, errors were also introduced into x. The effect of errors in x was so small as to be hardly detectable. Therefore all of the results that have been presented included errors in x of up to 0.006 inch.

Estimation of SD_ξ.- Combining all of the previous results it is possible to write an equation which expresses SD_ξ in terms of all the variables considered. This equation can be expressed as:

$$SD_\xi = C\left(\frac{m}{\rho A\lambda}\right)\left(\frac{SD_\alpha}{\alpha_{RMS}}\right) f(n) \qquad (12)$$

where C is a constant and $f(n)$ is a function which describes the effect of the number of cycles. If we take the function $f(n)$ as that given by the simple theoretical model, equation (12) can be written as:

$$SD_\xi = 1.70\left(\frac{m}{\rho A\lambda}\right)\left(\frac{SD_\alpha}{\alpha_{RMS}}\right)\left(\frac{1}{n}\right) \qquad (13)$$

On the other hand if we take the best fit to all the data given in figure 2 we get the equation

$$SD\xi = 0.183\left(\frac{m}{\rho A\lambda}\right)\left(\frac{SD\alpha}{\alpha_{RMS}}\right)e^{\frac{2.07}{n}} \qquad (14)$$

Either one of these equations can be used to estimate the standard deviation ξ.

It should be noted that these equations do not include the effect of the number of observation points per cycle (N) as it is generally quite small. Its influence, however, was systematic in that the more points per cycle the better were the results. It would require considerably more statistical results to adequately define the functional effect of this parameter over the range of variables considered; however, it would be a relatively simple matter to apply the procedure outlined to a given test facility.

Implications of equation (13).- At first glance equation (13) would appear to indicate that the best results would be obtained with the most cycles, and this would be true except that usually the term $1/n$ is not truly independent of $m/\rho A\lambda$. If we substitute $n\lambda = x$, where x is the length of the testing range, we get

$$SD\xi = 1.70\left(\frac{m}{\rho Ax}\right)\left(\frac{SD\alpha}{\alpha_{RMS}}\right) \qquad (15)$$

Therefore the longer the facility the smaller $SD\xi$. For a given facility x is fixed; therefore we minimize $SD\xi$ by minimizing $m/\rho A$, being sure that we have more than 1-1/2 cycles. A good optics system yielding a clear image will also minimize errors in angle readings (i.e., reducing $SD\alpha$) thus minimizing $SD\xi$. This may require resorting to

Kerr cells for very high speed tests to reduce blur and to reduce fogging due to model radiation. One can also make multiple readings of each picture to reduce SD_α. However, this will not work unless the errors are truly random. Errors that are not random deserve attention also. Examples of factors which can introduce nonrandom error are the facility reference system, dimensional stability of the film used, extraneous "noise" on the film, and uncorrected optical distortion either in the optics or due to refraction. The use of focussed shadowgraphs can minimize the effect of refraction.

Effect of random experimental errors on the determination of λ.- For all of the cases considered the errors in the determination of λ were less than 1/2 percent. As in the case for damping, the number of cycles of motion had a significant influence on this error. This effect of the number of cycles is shown in figure 5. Note the similar appearance to that shown for SD_ζ in figure 2. Since the errors are so small, this subject was not considered any further.

ANALYSIS OF VARIOUS ASSUMPTIONS

As was stated earlier two assumptions which appear to affect the dynamic stability parameter to a considerable degree are: (1) the resultant angle of attack is the square root of the sum of the squares of the projected angles instead of $\alpha_r = \tan^{-1}\sqrt{\tan^2 \alpha + \tan^2 \beta}$; and (2) the aerodynamics are linear. The method of analysis that follows is similar to that in the previous section except that no random experimental errors are introduced.

Analysis of the Resultant Angle-of-Attack Assumption

This effect was studied by considering a planar trajectory which is observed at different angles of rotation, φ, with respect to the plane of the motion (see sketch (b)).

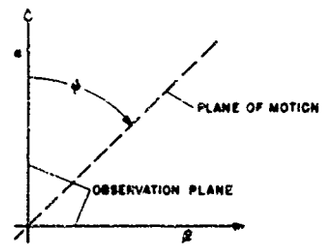

Sketch (b)

Note that for $\varphi = 0^\circ$ or 90° there is no assumption because $\alpha_r = \alpha$ or $\alpha_r = \beta$. To illustrate the magnitude of error that this assumption can introduce at intermediate values φ we will consider a particular example. For our example we will take 11 stations at 4-foot intervals, $\rho A/m = 0.006/ft$ and $\lambda = 25.7$ ft. We consider various values of α_{RMS}, φ, and ξ.

Figure 6 shows the results of this analysis for three values of the dynamic stability parameter, ξ. Plotted here are the apparent values of ξ as a function of φ for various values of α_{RMS}. Note that both α_{RMS} and φ have a strong influence on ξ. Note further that this effect is a strong function of the size of ξ_E. Figure 7 shows the induced errors $(\xi - \xi_E)$ for $\varphi = 45^\circ$ as a function of ξ_E for two values of α_{RMS}. Note the nearly linear dependence of the induced error on ξ_E. Remember that here we are considering exact angle readings and that these errors are introduced by the method of analysis.

These errors can be eliminated completely for planar motion by a simple rotation of coordinates before the data are analyzed. Furthermore for motions which are not planar the influence of this assumption can be minimized by rotating the coordinate system so that most of the angular motion is confined to either the α or the β plane.

Analysis of the Assumption of Linear Aerodynamics

In many cases of practical interest the aerodynamic coefficients are nonlinear functions of angle of attack; the question then arises as to the relationship that exists between the quasi-linear values obtained from the present data reduction procedure and the true values. Nonlinear moments with zero damping have received considerable attention (e.g., refs. 2 and 3). The more complicated cases have received little or no attention.

Here we will consider a slightly more complicated case, that is, $\xi = \text{const} \neq 0$, and $-C_m = M_\alpha \alpha + M_{\alpha^3} \alpha^3$. Again exact planar trajectories, with 11 stations at 4-foot intervals, will be used. Two cases are considered; in both, M_α gave a stabilizing moment. One case had M_{α^3} stabilizing and one had M_{α^3} destabilizing, referred to as stable-stable and stable-unstable, respectively.

Results of Linear Aerodynamic Assumption

Two questions are of interest here. First, does the nonzero damping significantly affect the determination of the nonlinear pitching

moments as outlined by Rasmussen and Kirk (ref. 3)? Second, does the presence of the nonlinear moment significantly affect the measured value of ξ?

For the amounts of damping considered here there was no detectable influence of $\xi \neq 0$ on the nonlinear pitching moment (i.e., the correct pitching-moment curve could be determined using the existing data reduction procedure in conjunction with the method of Rasmussen and Kirk).

This was not usually true for determining the damping. Here the nonlinear moment had a large influence on the damping determined with the present data reduction procedure. These results are shown in figure 8. The circles are the results for a pitching moment which is stable-stable. The scatter is due to the finite number of observation stations. Similar results for a stable-unstable pitching moment are indicated by squares. The sign of the nonlinear term determines whether the observed value of ξ will be larger or smaller than the exact value and that the angle of attack (more precisely the quantity $M_2\alpha^2$) determines the magnitude of the difference between apparent and exact values of ξ. The size of the nonlinearities considered are given in the figure.

Note particularly what this figure demonstrates. A system has been defined where the damping parameter, ξ, is a constant. However, after the analysis ξ appears to be a function of amplitude. Care must be taken that these effects of the nonlinear moment on the damping are interpreted correctly, and some theoretical work toward this end has been done.

Theoretical comparison.- Also shown in figure 8 are some theoretical estimates of the degree of interaction of a nonlinear moment on ξ. This work was done by Maurice Rasmussen and supplied by private communication. His analysis starts by assuming that the nonlinearity is small. A perturbation solution can then be obtained showing the effect of the nonlinearity in the moment. The theory gives the correct trend but not necessarily the correct magnitude. The work of Rasmussen is being expanded and will be published in the near future.

REFERENCES

1. Nicolaides, John D.: On the Free Flight Motion of Missiles Having Slight Configurational Asymmetries. BRL Rep. 858, Aberdeen Proving Ground, 1953. Also IAS Preprint 395, 1953.

2. Kirk, Donn B.: A Method for Obtaining the Nonlinear Aerodynamic Stability Characteristics of Bodies of Revolution From Free-Flight Tests. NASA TN D-780, 1961.

3. Rasmussen, Maurice L.; and Kirk, Donn B.: On the Pitching and Yawing Motion of a Spinning Symmetric Missile Governed by an Arbitrary Nonlinear Restoring Moment. NASA TN D-2135, 1964.

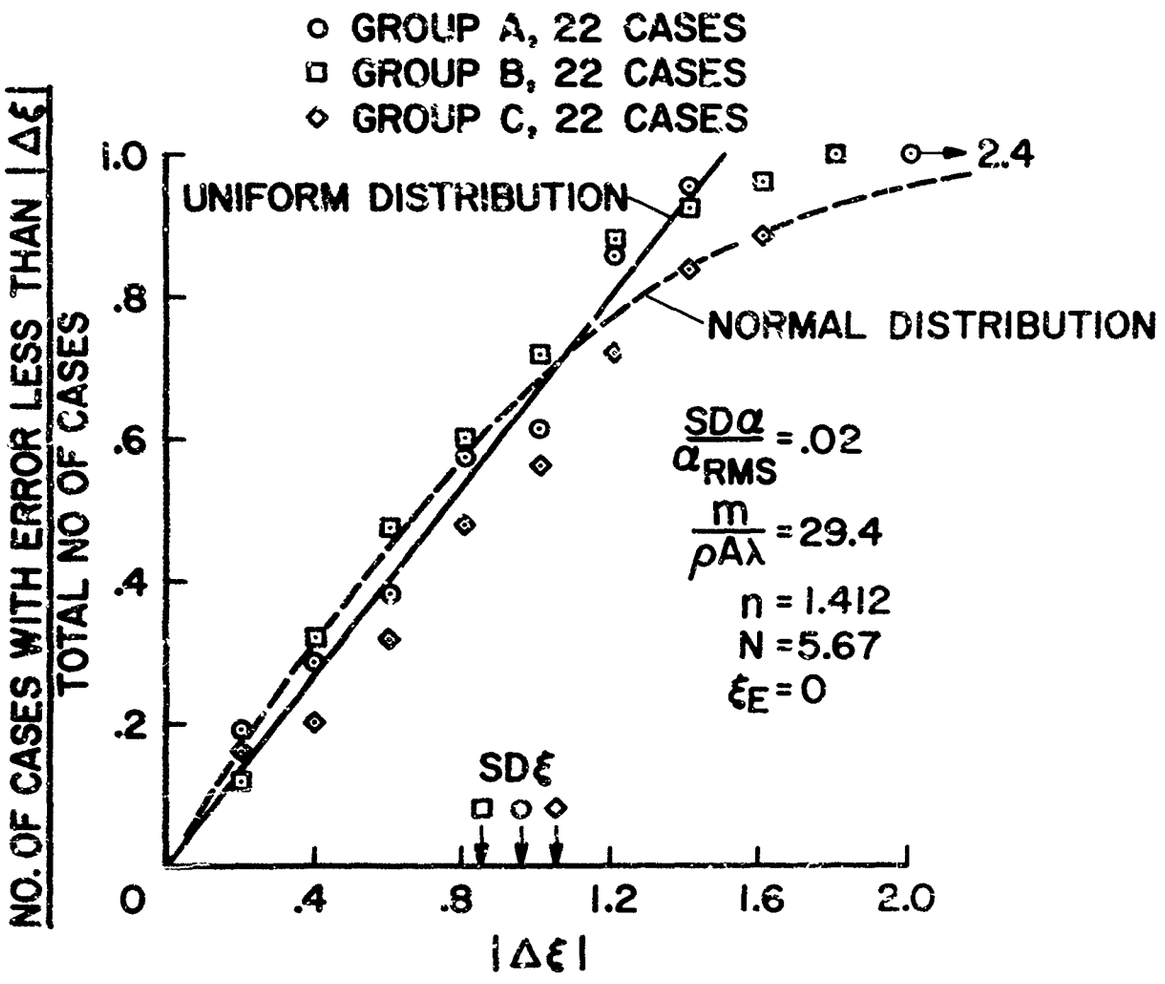

Figure 1.- Comparison of results from three groups of 22 trajectories each.

NATIONAL AERONAUTICS AND SPACE ADMINISTRATION
AMES RESEARCH CENTER, MOFFETT FIELD, CALIFORNIA

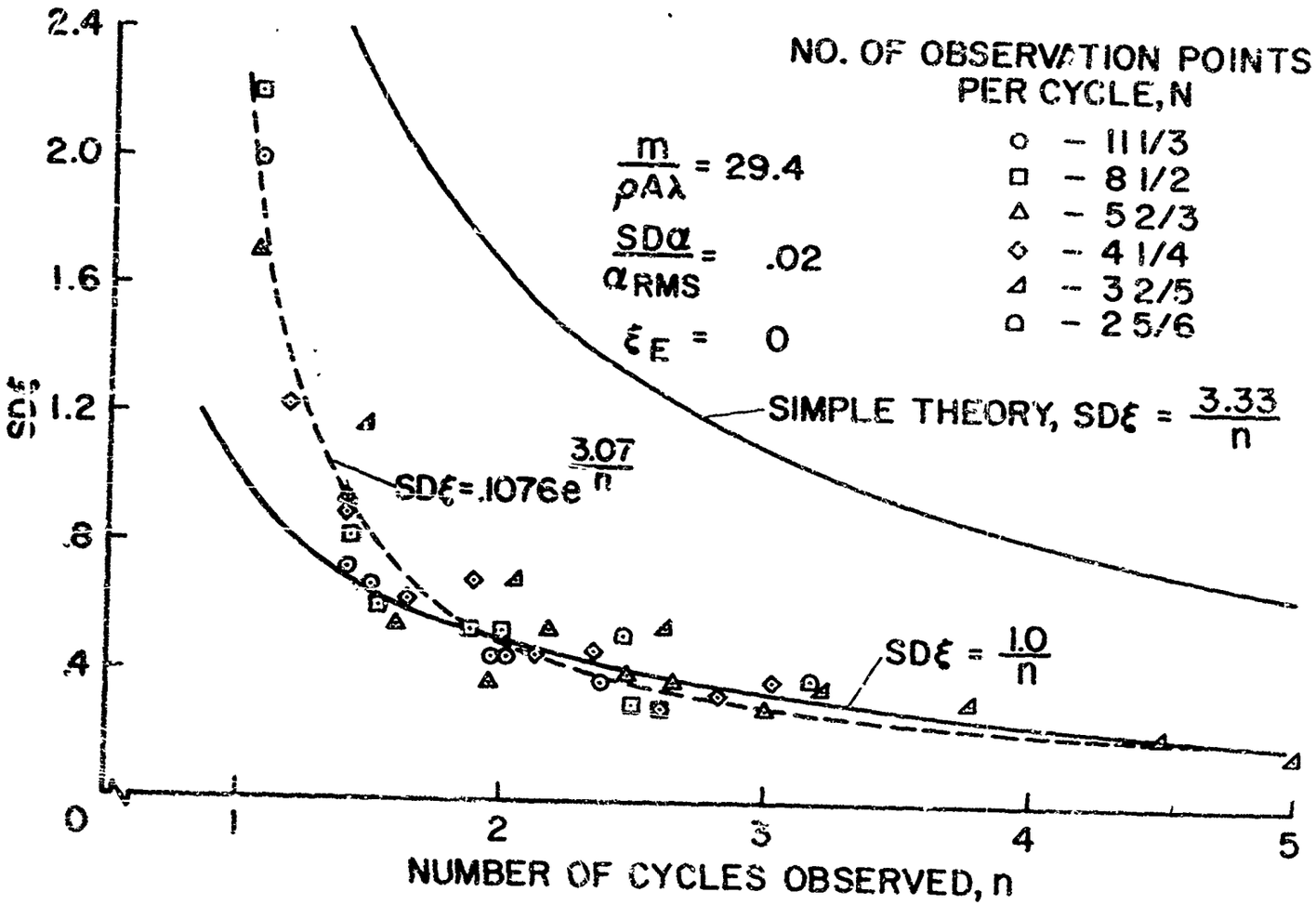

Figure 2.- Effect of n and N on the standard deviation in the dynamic stability parameter.

NATIONAL AERONAUTICS AND SPACE ADMINISTRATION
AMES RESEARCH CENTER, MOFFETT FIELD, CALIFORNIA

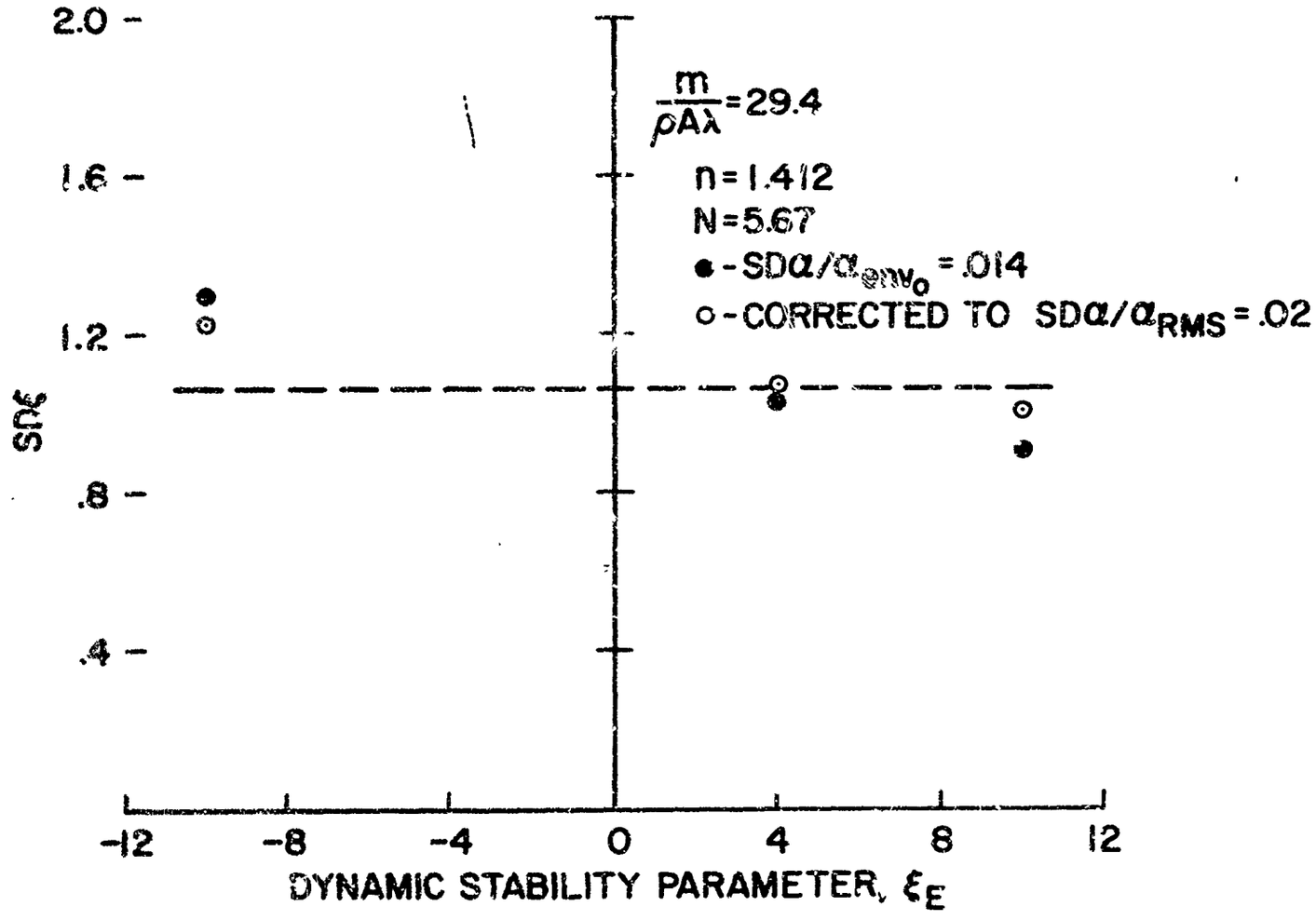

Figure 3.- Effect of the absolute level of the dynamic stability parameter on SDξ.

NATIONAL AERONAUTICS AND SPACE ADMINISTRATION
AMES RESEARCH CENTER, MOFFETT FIELD, CALIFORNIA

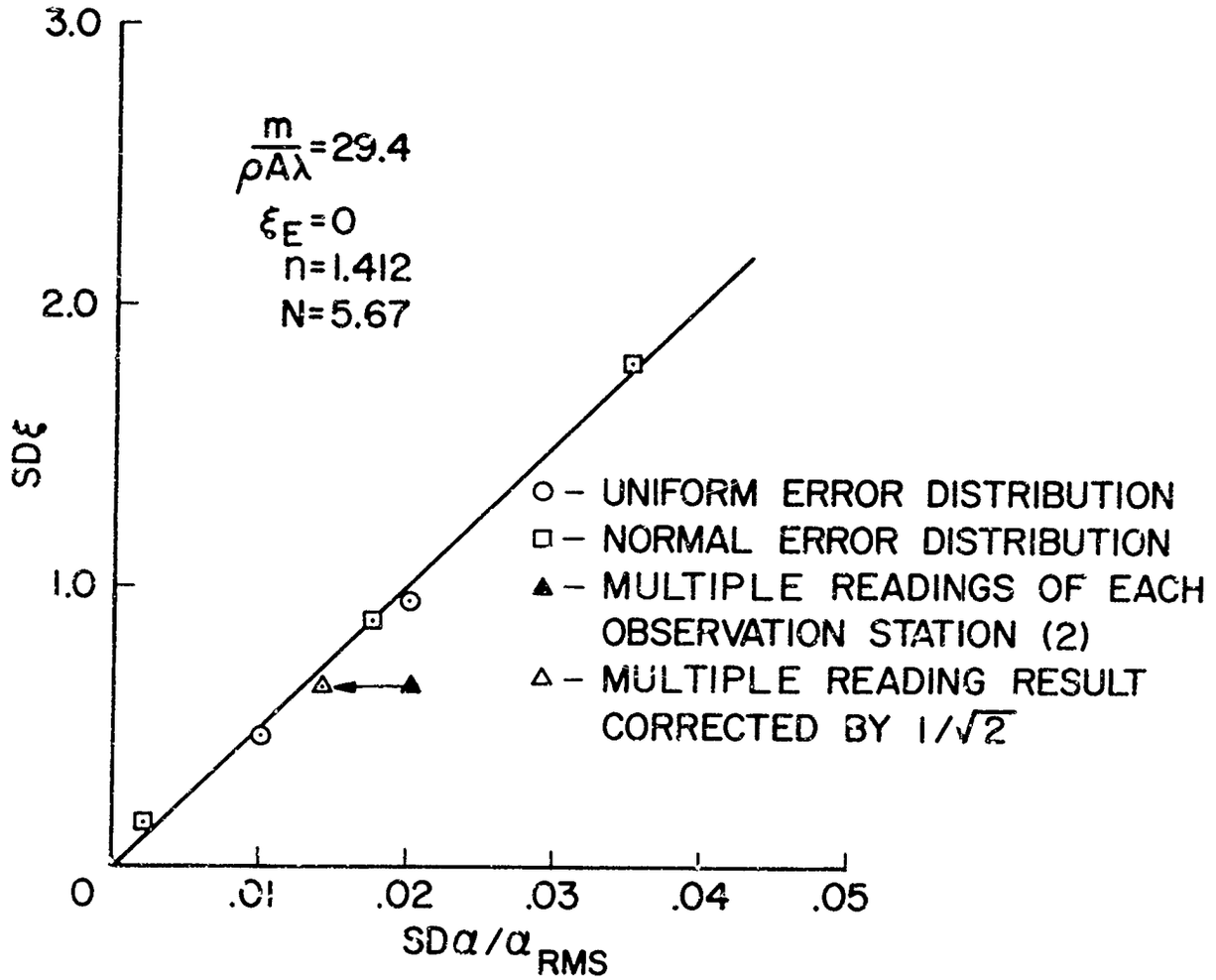

Figure 4.- Effect of SDα on SDξ.

NATIONAL AERONAUTICS AND SPACE ADMINISTRATION
AMES RESEARCH CENTER, MOFFETT FIELD, CALIFORNIA

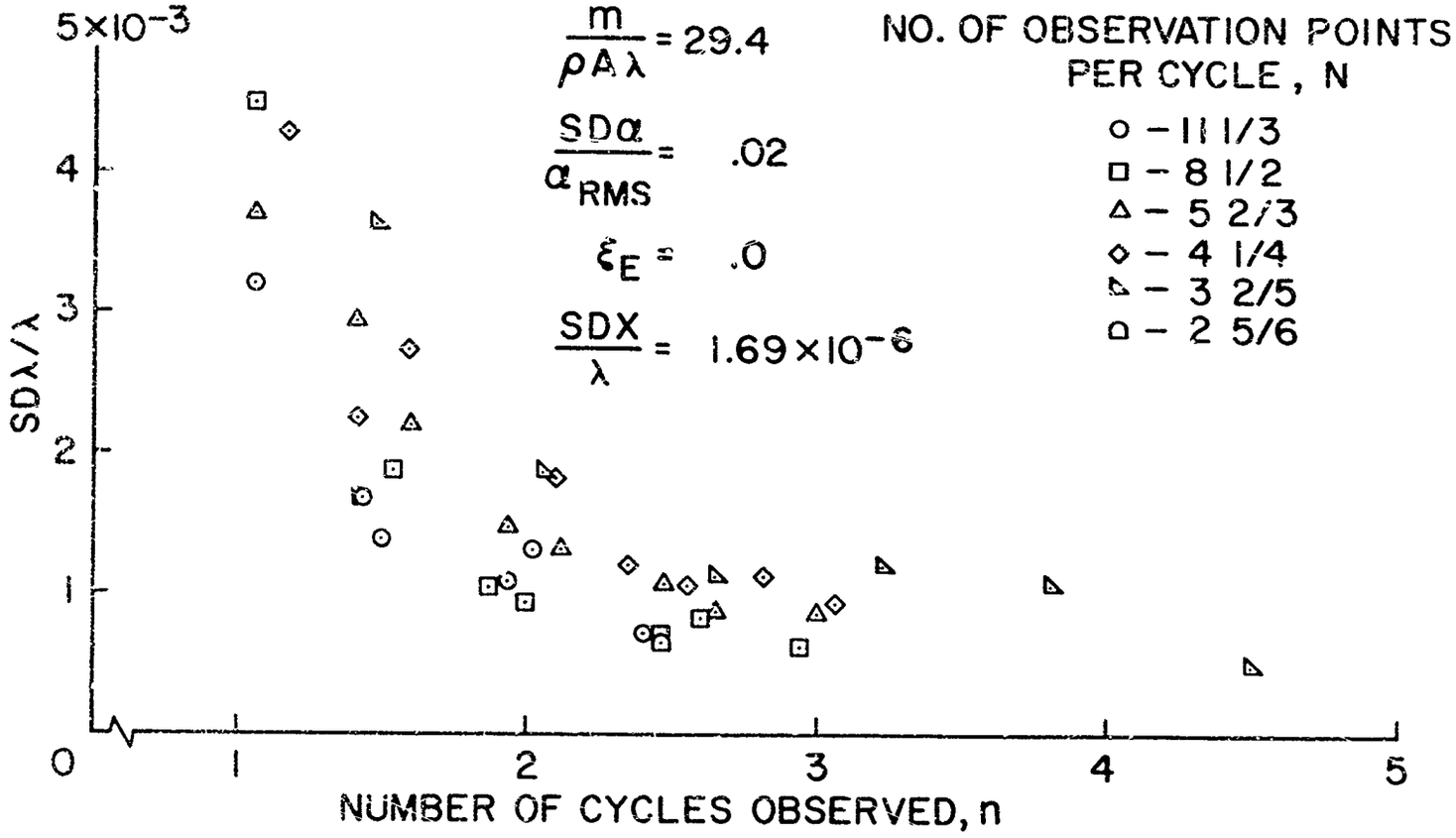

Figure 5.- Effect of n and N on the standard deviation in the wave length.

NATIONAL AERONAUTICS AND SPACE ADMINISTRATION
AMES RESEARCH CENTER MOFFETT FIELD CALIFORNIA

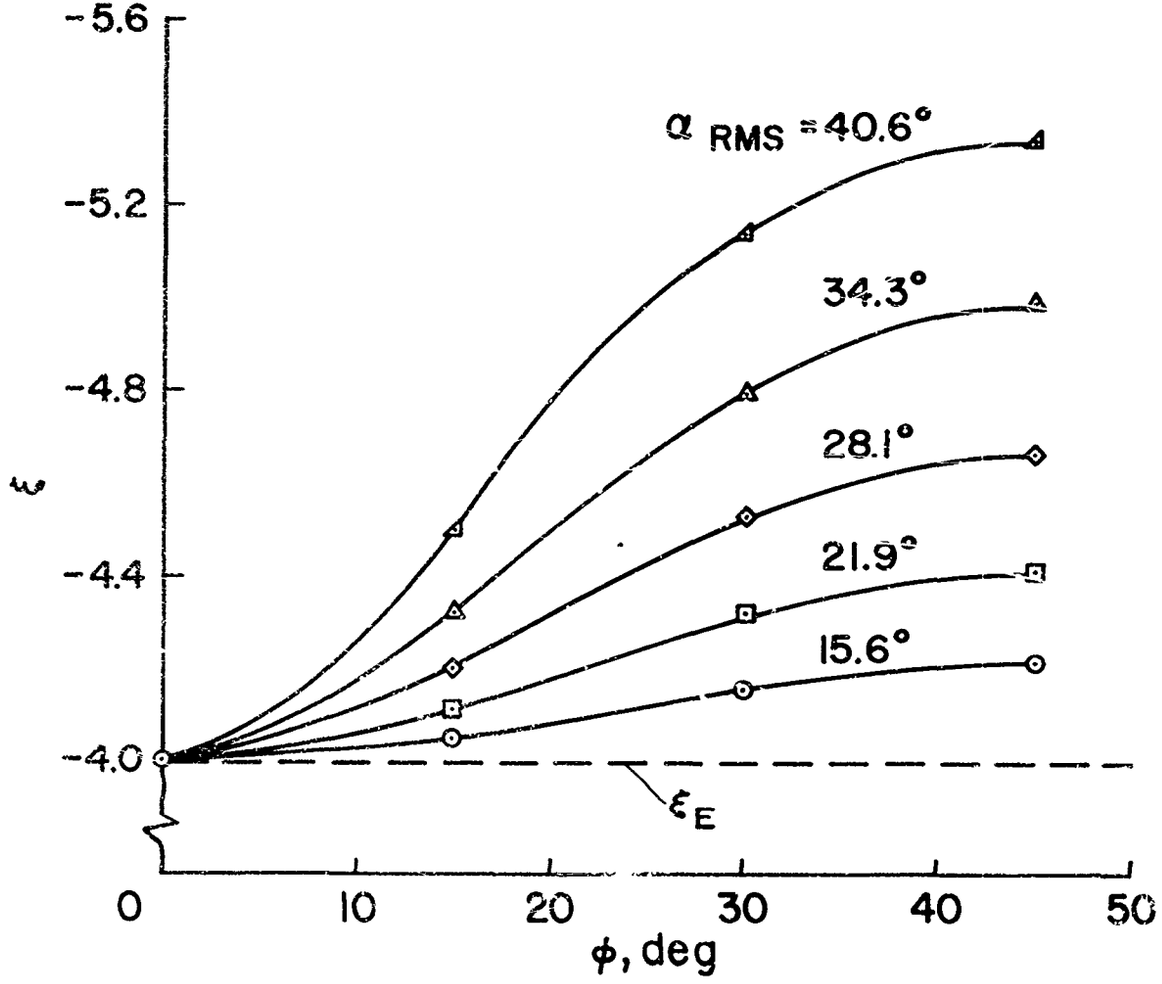

(a) ξ (exact) = -4.0

Figure 6.- Errors induced in the dynamic stability parameter by small angle assumption.

NATIONAL AERONAUTICS AND SPACE ADMINISTRATION
AMES RESEARCH CENTER, MOFFETT FIELD, CALIFORNIA

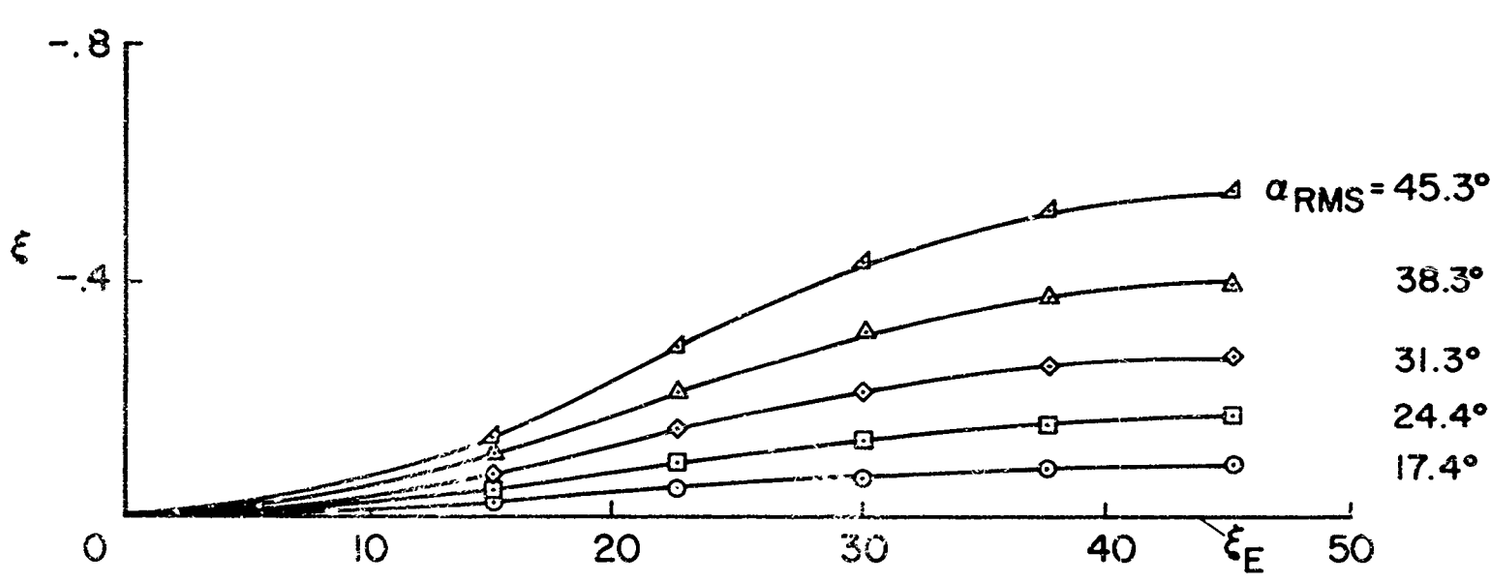

(b) ξ (exact) = 0

Figure 6.- Continued.

NATIONAL AERONAUTICS AND SPACE ADMINISTRATION
AMES RESEARCH CENTER, MOFFETT FIELD CALIFORNIA

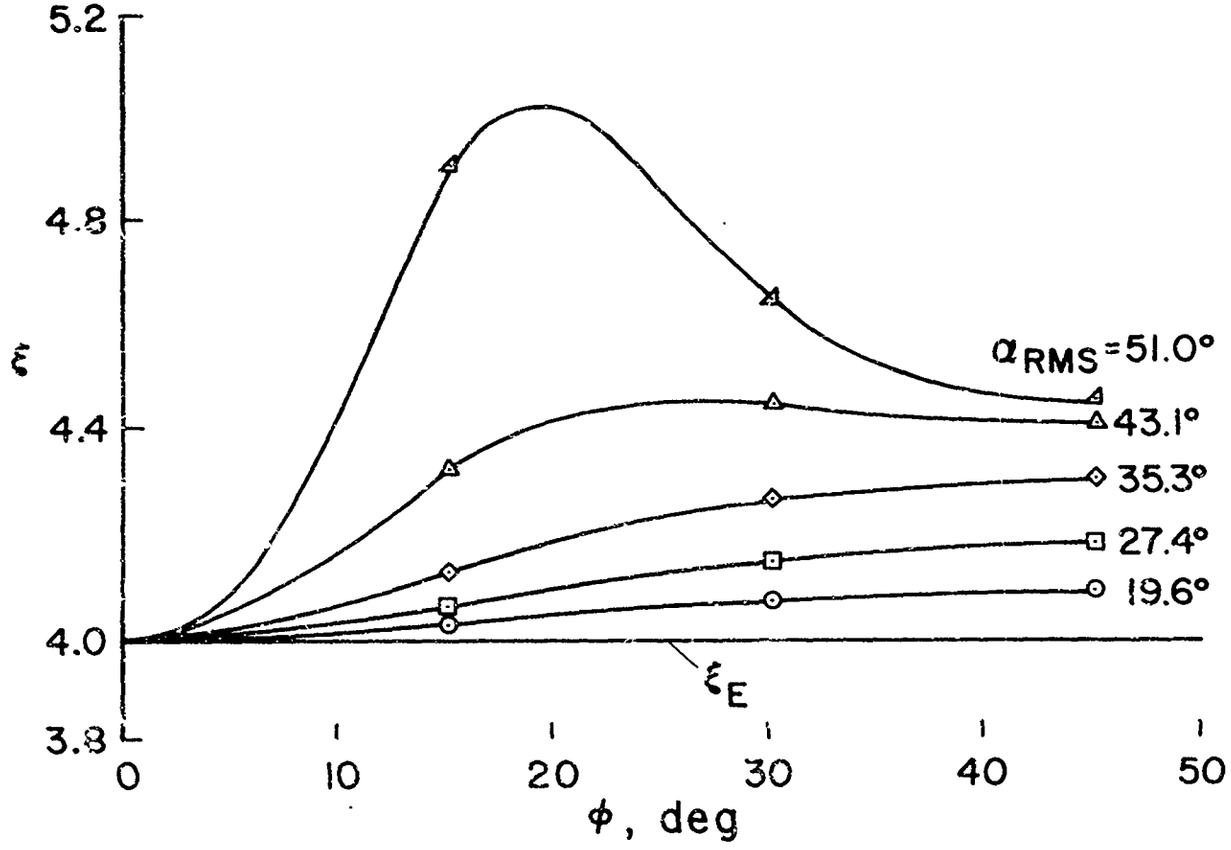

(c) ξ (exact) = 4.0

Figure 6.- Concluded.

NATIONAL AERONAUTICS AND SPACE ADMINISTRATION
AMES RESEARCH CENTER, MOFFETT FIELD, CALIFORNIA

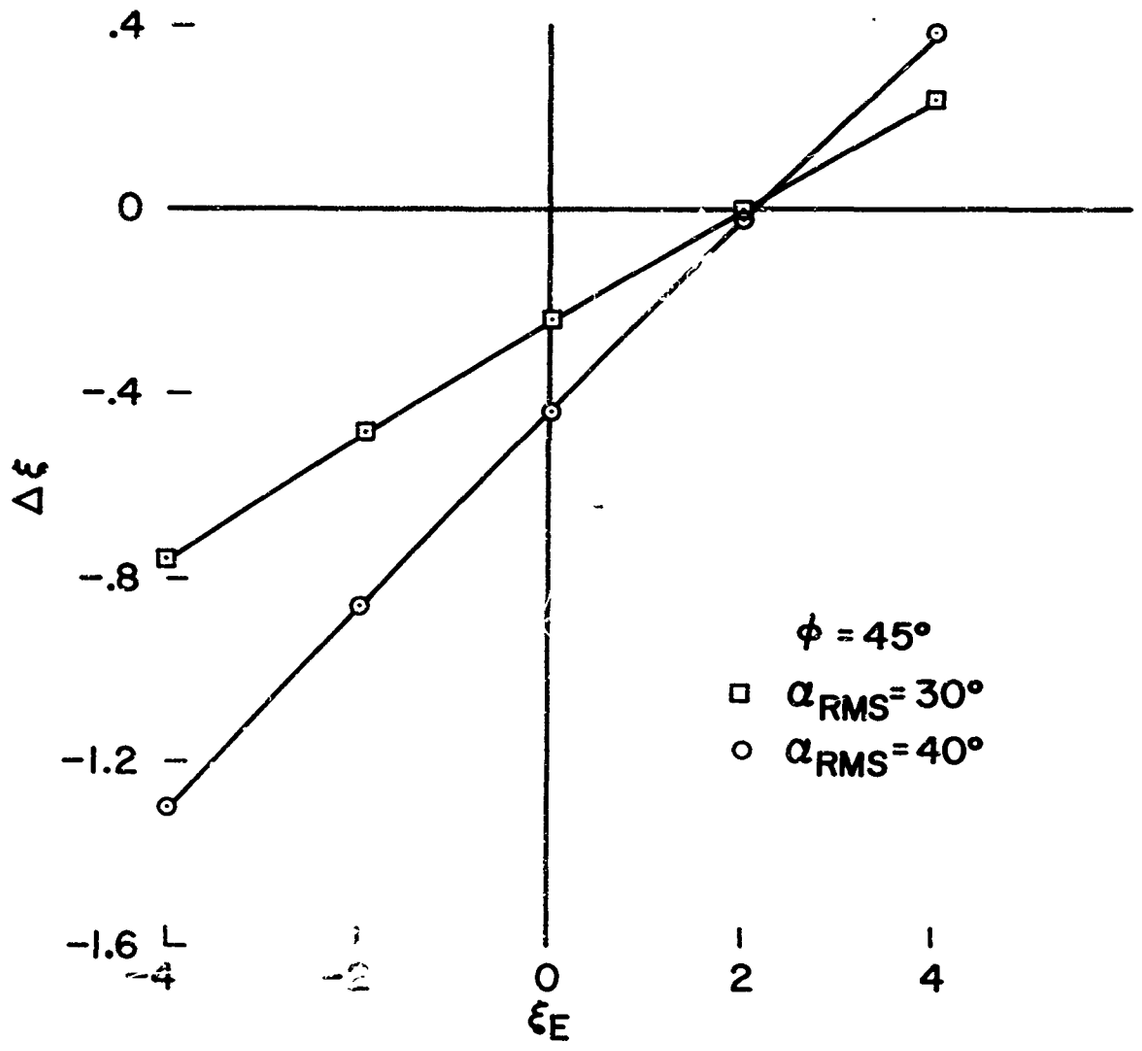

Figure 7.- Cross plot showing effect of the absolute level of the dynamic stability parameter on induced errors.

NATIONAL AERONAUTICS AND SPACE ADMINISTRATION
AMES RESEARCH CENTER, MOFFETT FIELD, CALIFORNIA

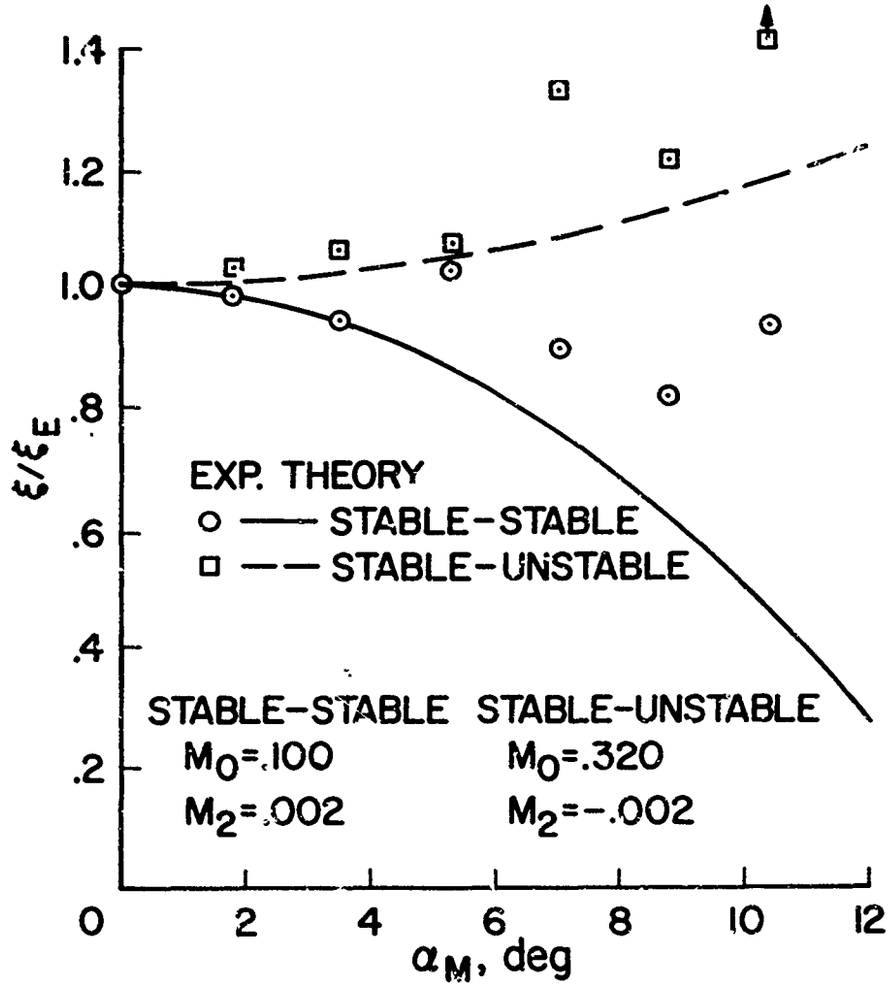

Figure 8.- Effect of nonlinearities in the restoring moment on deduced values of the dynamic stability parameter.

NATIONAL AERONAUTICS AND SPACE ADMINISTRATION
AMES RESEARCH CENTER, MOFFETT FIELD, CALIFORNIA

DISCUSSION

Lars Ericsson:

Your formula for the standard deviation shows a beneficial effect of increasing your range length and it also shows that making your model lighter improves accuracy.

G. Chapman:

Yes.

Lars Ericsson:

I would like to comment on the last method, that is, making your model light. Our experience with the Polaris re-entry body is that you have to be very careful and try to avoid going that route if at all possible. When you make the model light you decelerate the re-entry body in your test maybe ten times as fast as in real life. The Polaris re-entry body had characteristics that change drastically with Mach number (at transonic and subsonic speeds)--that is during one cycle of oscillation in the range the model decelerated through a Mach number range of maybe 0.1 or 0.2. For that amount of Mach number variance the aerodynamic characteristics changed quite drastically.

G. Chapman:

Yes, this is true. You have to apply this type of analysis in light of practical considerations. We at Ames have had similar experience with the Apollo abort system firing through the transonic range and when you get to cases as complicated as this you usually have to use an integral approach such as Jaffe's of JPL or something of this type.

C. Welsh:

What were your final conclusions on the number of points per cycle required? This is a function of your error but I never determined from the slides what the final conclusion was.

G. Chapman:

There is a beneficial effect of getting more data points per cycle but it was generally smaller than the other considerations. We covered from 2.5 points per cycle up to 11.5 points per cycle and in general you have a systematic increase but in doing the statistical analysis on this there were places where the results overlapped and in general it was sort of lost in the statistical scatter. Scatter of the statistical results were approximately, given in the written version, ±15 percent. It is there; you do get a beneficial effect of having more points per cycle but I

think it is small and it is nice when you have a facility as long as yours. You don't have to worry about this thing.

C. Welsh:

Well, this was the point here. It would seem from your data there and as you pointed out that the difference between 2 and 11 may not be so significant but this again I think is tied to the amount of error in the individual measurements of α and β.

G. Chapman:

Oh, we considered quite a range of angle errors. We showed normalized error standard deviations of 0.02, something like this, so for a 10 degree run this corresponds to 2/10 of a degree reading error standard deviations which means if you are using a normal distribution or a uniform error distribution you have a maximum error of approximately half a degree. We feel for our high speed results we can get well within this. Of course, this doesn't consider nonrandom errors. I mean you may have reference systems that are not aligned properly and these are very difficult to take into consideration; but we bring out a few of these in the written version just to indicate that you have to worry about these type of things. It is something that is difficult to handle and you can't handle it in the statistical manner.

C. Welsh:

We had tried this in a crude sort of manner of simulating errors in which we tried to simulate just a random type distribution of errors. What we would have indicated is that once you got above about 12 points per cycle (we used as many as 43) the curve was fairly flat and once you started below 12 this curve then started up and very rapidly as you indicate.

G. Chapman:

I read your paper--yes--the one presented to the Ballistic Range Association in Europe last year?

C. Welsh:

Yes.

G. Chapman:

Yes, I read the paper and we had a couple of disagreements but that wasn't one of them. We didn't consider above 12 points per cycle because--well, in general, our biggest facility at Ames is 200 foot range. We have 24 stations and in general we try to stay greater than the 1 1/2 cycles. You showed that one cycle of motion was sufficient; however, the type of error distribution you used

precluded any trim interfering in your error analysis and therefore we sort of feel that we have to stay larger than 1 1/2 cycles of motion. So for the facilities that we are considering; this analysis is sufficient although we are going to extend this to a larger number particularly since we have pop forward techniques now that can use the same type of analysis. Lionel Levy may show some results later on today. I think he is possibly going to show some motion pictures of tests where you can get an equivalent flight path of up to 10,000 feet for each second of flight in one of these pop not a pop forward technique just a vertical flow facility.

G. Chrusciel:

This is a question that has been bothering me a little bit that is using the standard data reduction techniques for unusual configurations. If you have a vehicle which exhibits say very large drag changes with angle of attack and you use the standard data reduction technique you could attribute large errors in the damping coefficient because of this. Would you care to comment?

G. Chapman:

I tend to agree with you--we really haven't investigated this effect but I have a feeling that large values of drag change with angle of attack is just like a q variation over the trajectory; it is going to have an effect and like I say there are many problems that I haven't considered here. I got into this problem through the backdoor and I am just starting to consider some of these various problem areas.

BALLISTIC RESEARCH LABORATORIES

FREE FLIGHT WIND TUNNEL TECHNIQUES AT THE BALLISTIC RESEARCH LABORATORIES

Anders S. Platou

Exterior Ballistics Laboratory
Ballistic Research Laboratories

Preprint of Paper
To be presented at the 2nd Technical Workshop on Dynamic Stability Testing,
20-23 April 1965, Arnold Engineering Development Center,
Arnold Air Force Station, Tennessee

ABERDEEN PROVING GROUND, MARYLAND

FREE FLIGHT WIND TUNNEL TECHNIQUES AT THE BALLISTIC RESEARCH LABORATORIES

A. S. Platou
Exterior Ballistics Laboratory
Ballistic Research Laboratories

During the past year and a half the BRL has been developing a wind tunnel free flight technique which can be used to obtain aerodynamic force and moment data on various configurations. This technique, which we are developing for our hypersonic tunnel, will be a valuable testing addition to our facilities. The principle of the technique is the same as that used at the Jet Propulsion Laboratory in that a model is launched at low velocity upstream into the high speed flow. The launch velocity must be such that the deceleration due to drag keeps the model trajectory in the wind tunnel test rhombus and permits at least the beginning and end of the flight to be photographed with a high speed camera. To date we have successfully launched two configurations--a 7/8-inch diameter aluminum sphere for checking a drag coefficient, and a low moment of inertia 10° half-angle plastic cone weighted with a frustrum of lead to determine its dynamic stability. The BRL system differs from the JPL system in that we are using a launcher which will permit launching several models without shutting down the wind tunnel, and the optical system is a two view system permitting orthogonal views of the model to be recorded.

THE LAUNCHER

The launcher is a water cooled one-inch inside diameter tube approximately 16 inches long (Fig. 1). The rear ten inches are used for holding the saboted reserve models, while the forward portion of the tube is used for launching each model. Doors are used to protect the models before launch from the hot air stream and to prevent a resonant shock and the resulting high temperature from occurring in the launch tube (Ref. 1). Two retractable pins are used to hold the models in position prior to launching and to prevent the reserve models from moving forward until the launching of the front model is accomplished.

To launch a model with this launcher, three sources of pressurized air are required. The feed air is applied continuously throughout the test to the rear of the feed piston, Fig. 1. Its pressure is adjusted so that it is always higher than the launch air which is applied directly behind the front model. The launch air pressure is adjusted prior to launch to provide the desired model launch velocity. An automatic sequence of events is started when air is applied to the door and pin cylinder. This opens the door, raises the front pin, and lowers the rear pin, thereby permitting the launching of the front model. After launch, the door cylinder air is reversed, which closes the doors, moves the pins back to their original position, and cuts off the launch air. The feed air then moves the next model into launch position. This sequence of events is tied in to the camera timing sequence, and occurs automatically in a few seconds.

With this launcher, models are usually launched with the launcher pointing directly upstream, and the initial model angle of attack has been due to flow asymmetries directly in front of the launcher. With the low moment of inertia cones this has worked well, for initial flight disturbances up to 10° or 12° are necessary for dynamic stability measurements. For other types of measurements involving high moment of inertia models it may be necessary to launch the model at an angle of attack or employ vertical air jets to pitch the model to an angle of attack during the launch. Vertical air jets have been built into our launcher, but have not yet been used.

THE OPTICAL SYSTEM

The dimensions of the usable portion of the tunnel flow which can be photographed with the orthogonal optical system is approximately 12 inches in diameter and 27 inches long between the nozzle exit and the diffuser scoop. However, the usable tunnel flow also extends upstream of the nozzle exit along Mach lines, and even though this region cannot be photographed it can be used in many cases for the mid portion of the model flight.

The orthogonal optical system is arranged, Fig. 2, so that both a side view and a top view of the test section are superimposed onto the frames of a 35mm half frame Fastax camera. A series of mirrors including a half silvered mirror are used to direct the optical paths into the camera in such a way that the upstream direction of the model in the two views is in opposite directions on the film frames, Fig. 3. In this way it is possible to distinguish the two model views in each frame. The views obtained are silhouettes of the model against a front-lighted white screen. The screens, one for each view, are mounted approximately three feet from the centerline of the tunnel on the opposite sides from the camera. Each screen contains lines marking the tunnel centerline, the center of the main tunnel windows, and two lines a known distance apart which are used as a calibration distance.

The resolution of the optical system is limited by the resolution of the high speed camera which is approximately 20 lines per millimeter. This resolution limits the accuracy of film measurements to .002 inch in the film plane, or approximately .05 inch in the center test section plane. As a result, considerable scatter is present in the measured model coordinates, Figure 4, and we must resort to least square smoothing techniques to improve the data accuracies, Figure 5. The smoothing increases the coordinate accuracies to approximately .01 inch. The film is being read on a Telereadex Type 29E machine, and the data are being reduced by the BRL Computing Laboratory using the high speed BRLESC computer.

With the present optical system the top view optical path must pass through a window in the top of the plenum chamber which is only 15 inches in diameter and located 4-3/4 inches downstream of the main window centerline. This limits the top view to approximately 2/3 of the test section length. Also, with the present optical system it is necessary to run an alignment check on the mirrors before each test period. For these reasons we plan to change to a two camera system--one for each orthogonal view--where the timing marks on the two films can be the same, thereby relating the frames on the two films.

The data from the first flights are being read and reduced while this paper is being prepared, so that the aerodynamic data are not yet available. The data will be available at the time of the meeting and will be shown at that time. The dimensions of the models used on the first flights are shown in Fig. 6. The tunnel conditions used for the flights are M = 6.0, P_o = 300 psia, T_o = 500°F, and R_e = .40 x 10^6 per inch.

REFERENCE

1. Vrebalovich, T. "Resonance Tubes in a Supersonic Flow Field" JPL Technical Report 32-378, June 1962.

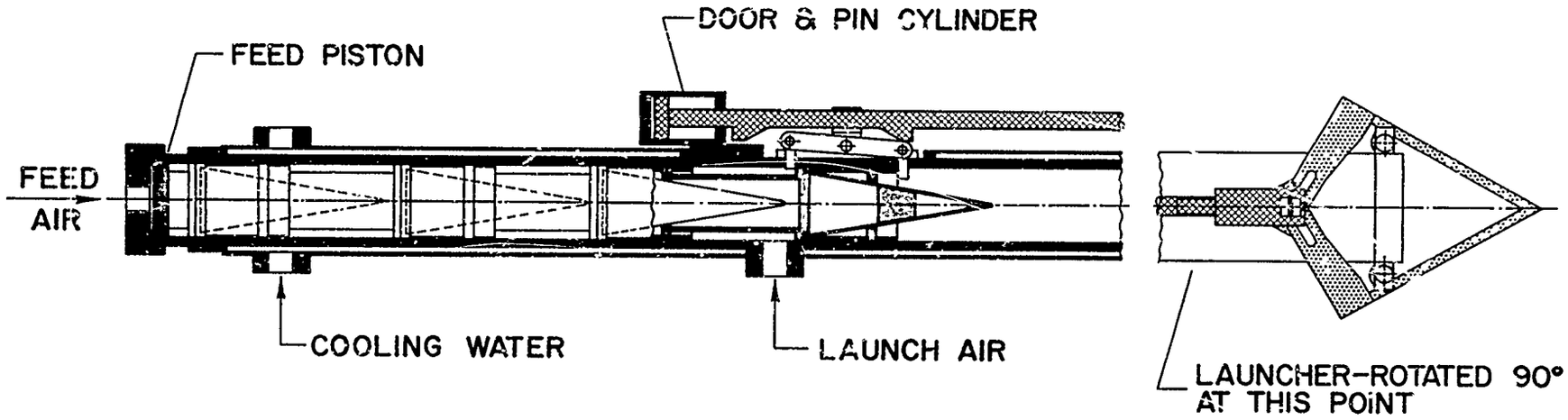

WIND TUNNEL FREE FLIGHT LAUNCHER

Fig. 1

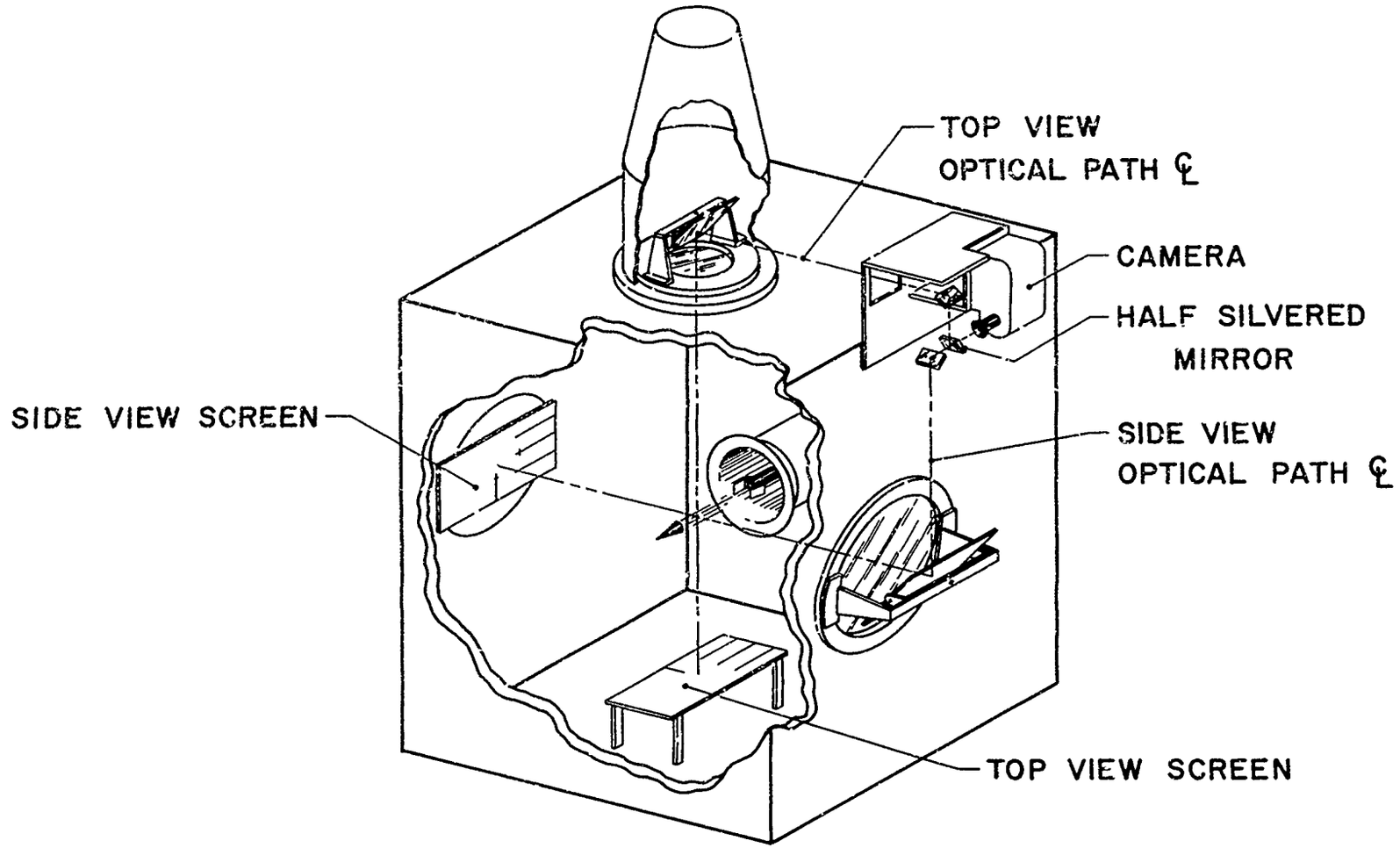

FREE FLIGHT OPTICAL SYSTEM

FIG. 2

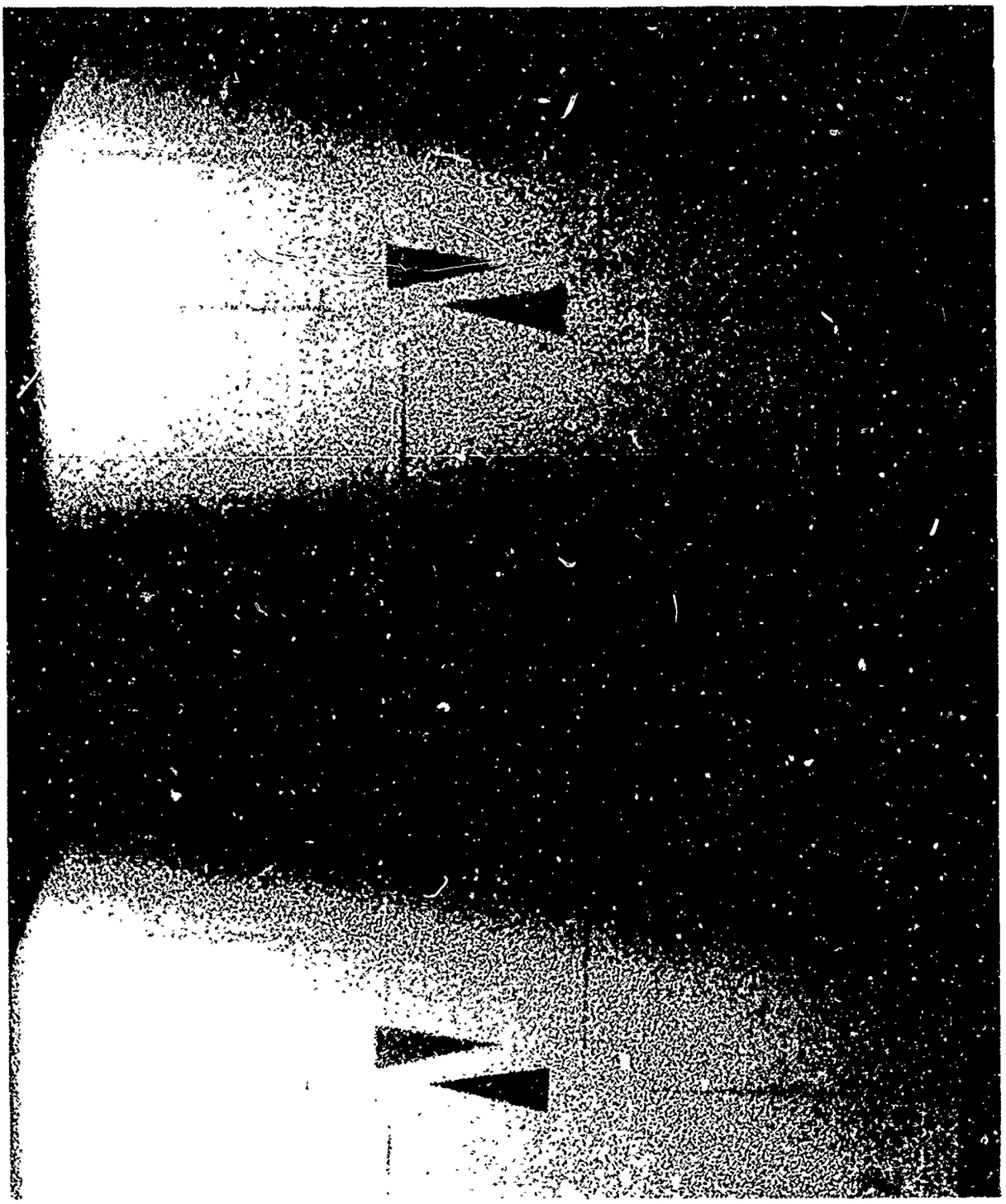

FIG. 3 Two frames from the high speed 35mm film used in the orthogonal viewing system.

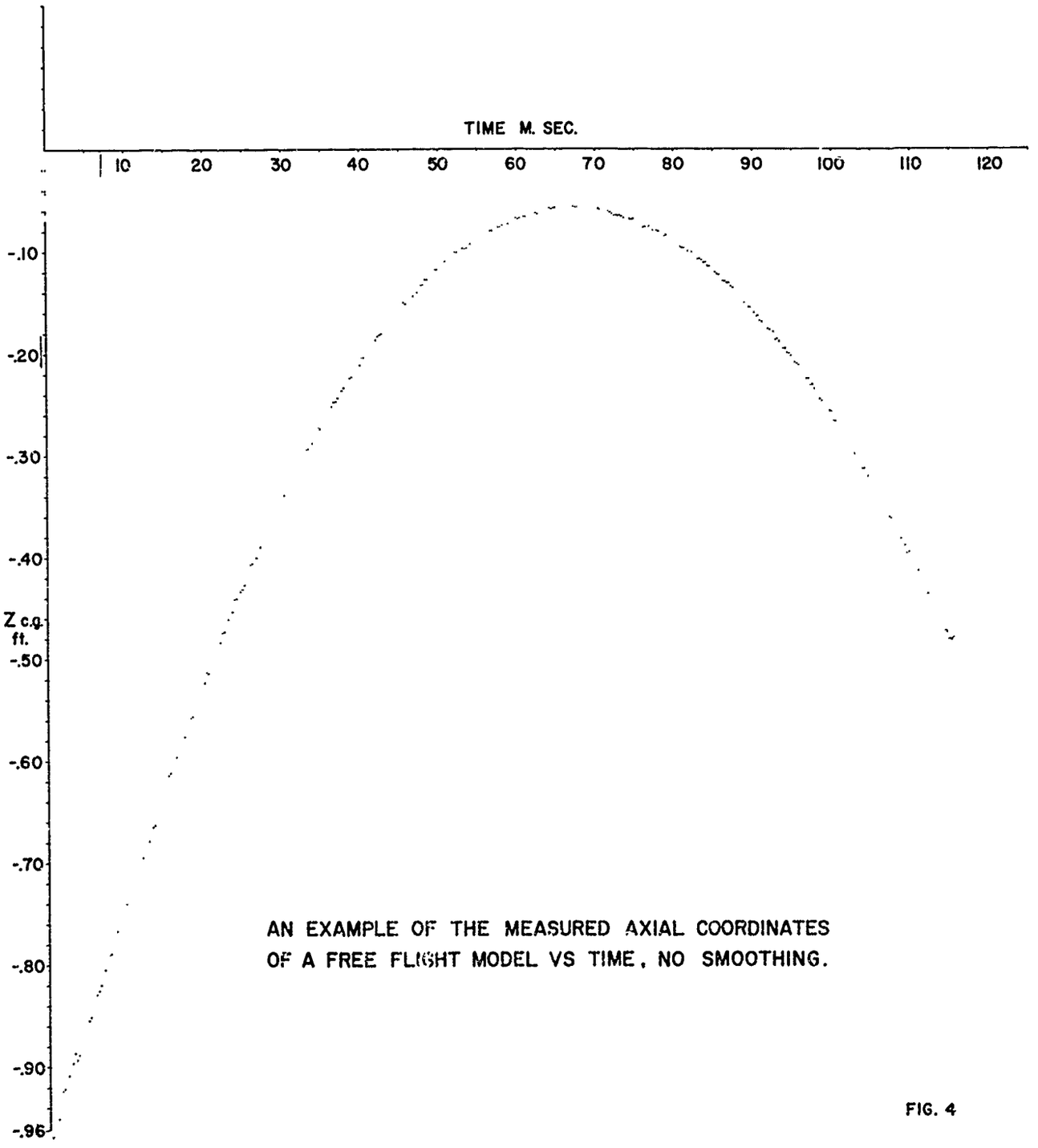

AN EXAMPLE OF THE MEASURED AXIAL COORDINATES OF A FREE FLIGHT MODEL VS TIME, NO SMOOTHING.

FIG. 4

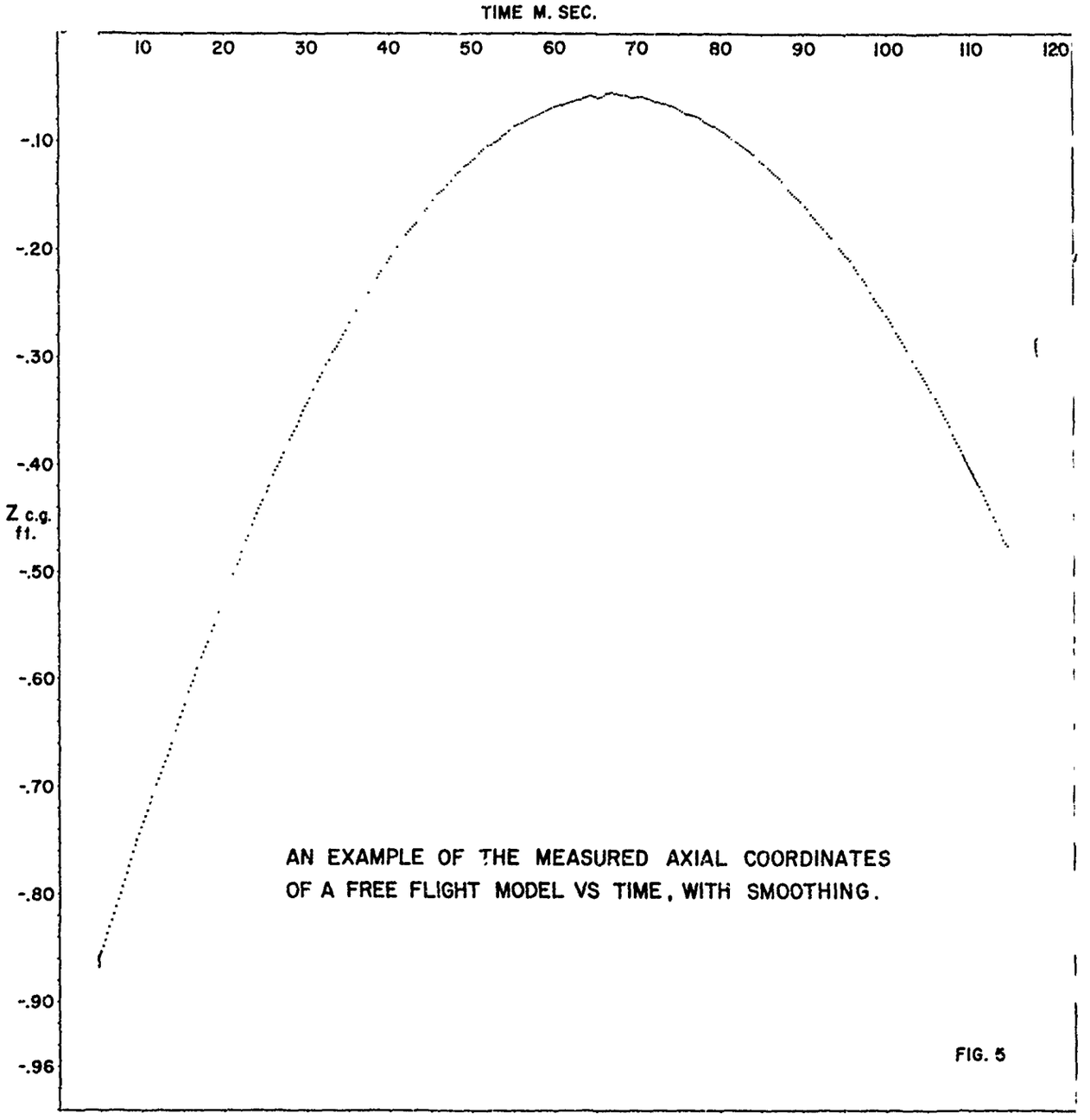

AN EXAMPLE OF THE MEASURED AXIAL COORDINATES OF A FREE FLIGHT MODEL VS TIME, WITH SMOOTHING.

FIG. 5

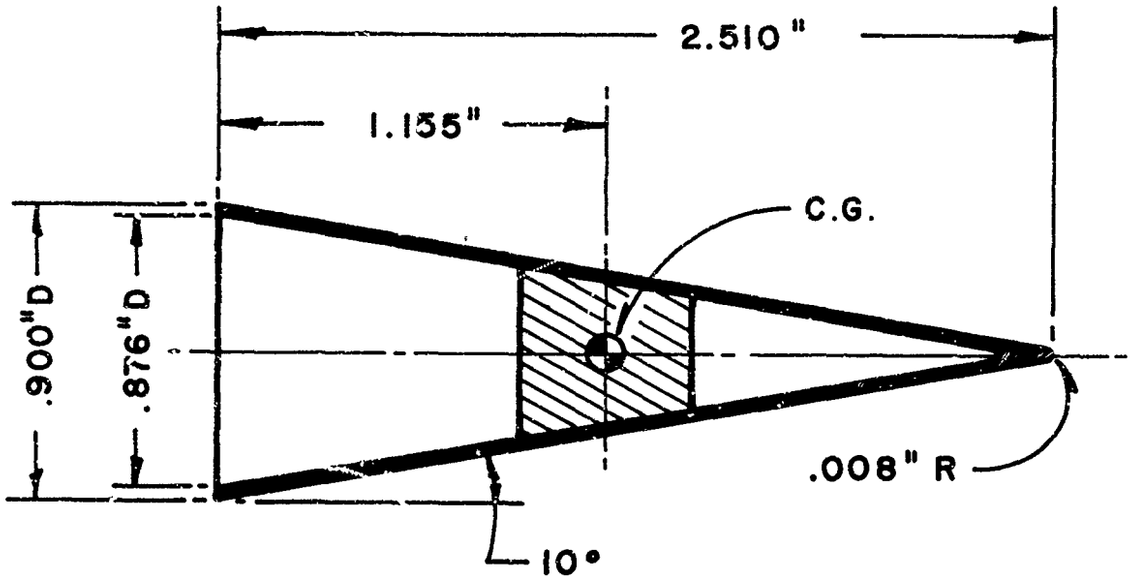

CONE

M = .038 LBS.

I c.g. = $.23 \times 10^{-6}$ SLUG FT.^{2}

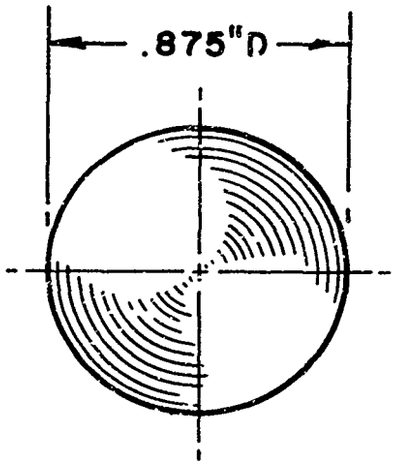

SPHERE

M = .037 LBS.

FREE FLIGHT MODELS

FIG. 6

DYNAMIC STABILITY TESTING WITH MAGNETIC BALANCE SYSTEMS*

Eugene E. Covert, Alan Copeland, Timothy Stephens

INTRODUCTION

For the last four and one-half years, members of the staff of the Aerophysics Laboratory of the Massachusetts Institute of Technology have been studying magnetic suspension and balance systems for use with wind tunnels. One of the principle purposes of these studies, which have been sponsored by the Fluid Mechanics Branch of Aerospace Research Laboratories, USAF has been to determine limiting factors in the performance and application of this kind of a balance system.

Without going into a detailed history of suspension by means of ferromagnetism it is worth noting that ultra centrifuges with a magnetically suspended rotor were first constructed at the University of Virginia by Holmes and Beams in the late 1930's. The first successful suspension of a wind tunnel model was accomplished at ONERA in France by Laurenceau and Tournier (Ref. 1). These results stimulated activities at our Laboratory. As a result of preliminary calculations in early 1958, we were convinced that the ONERA system could be used for general aerodynamic purposes. Subsequently John Chrisinger undertook a more detailed study as a thesis for the degree of Aeronautical Engineer, which was completed in May 1959 (Ref. 2). During the same period Parker and Kulthau at the University of Virginia undertook the construction of a magnetic suspension system for dynamic stability measurement. The principles of this balance were worked out and verified by Parker in 1959 (Ref. 3).

Parker's work stems from the background of magnetic suspension of ultra centrifuges at the University of Virginia and represents a line of development that not only is independent of the French and MIT development, but also was directly aimed at the problem of dynamic stability. R. Zapata, formerly with Parker's group, and T. Dukes have in the last 18 months,

* These studies were carried out under Contract AF 33(615)-1470 with the Aerospace Research Laboratories, United States Air Force, at the Massachusetts Institute of Technology, Aerophysics Laboratory.

completed a magnetic suspension system that has been used at the Gas Dynamics Laboratory, Princeton, to measure the fluid mechanical properties in the wake of spheres.

These systems have several common characteristics. The models must have a magnetic moment, although the direction and distribution of the magnetic moment, may vary for each of the several different models. This magnetic moment may be a part of the model (i.e., the model is a permanent magnet), the magnetic moment may be induced by a set of coils designed for that purpose, or the magnetic moment may be induced by the suspension fields themselves. The magnetic forces depend on the magnetic moment M and the gradient of the magnetic field, i.e.,

$$\vec{F} = \int_{\substack{\text{magnetized} \\ \text{volume}}} (d\vec{M} \cdot \nabla)\vec{B} \qquad (1)$$

Similarly the torques can be computed by an equally well-known formula

$$\vec{T} = \int_{\substack{\text{magnetized} \\ \text{volume}}} d\vec{M} \times \vec{B} \qquad (2)$$

The suspension system must be capable of producing the magnetic fields and gradients of magnetic fields to provide the forces and torques. If the system is to be in equilibrium then the applied magnetic forces and torques must just balance the forces and torques caused by gravity, aerodynamics pressure distribution and inertial effects (if the model is in motion). The equilibrium is brought about by a set of model position sensors whose output is used to control the electric current in the coils that produce the magnetic fields. Figure 1 shows a schematic diagram for a five degree of freedom system, where coil configuration is similar to the early ONERA units. Note there are five independent units consisting of position sensing elements, control networks and power supplies (not shown), and coils. Each unit is used to control one of the five degrees of freedom. In this case they are forward and aft lift, forward and aft lateral force, and drag.

In the MIT system, each control computes the integral of model position, model position and rate of model position as well as model acceleration, model acceleration rate and the rate of model acceleration rate. The latter three computations are quite obvious since a change in current corresponds to a change of force in the model. The first three are necessary to reduce drift and the change of model position under load. See Ref. 4 for a complete description of the MIT system.

Now this leads to an unusual situation. A model suspended by a magnetic suspension system appears to be free floating. But it is not. The model is actually fixed rigidly to a position that is identified with a reference voltage in the integrator. It is desirable to control the model to 10^{-3} inch, which can be done if care is taken. Figure 2 helps to convey the idea of how solidly the model is fixed. The model is seen from the diffusor inlet plane. The film was exposed for 0.2 seconds with f 2.8 lens. There is no indication of blurring. One other piece of information is considered pertinent. This information is contained in Fig. 3, and shows the repeatability of the measurement of aerodynamics drag as represented by the drag coefficient of a cone cylinder cone model. The absolute value of the drag coefficient for this configuration has been estimated to be in substantial agreement with the data.

BASIC IDEAS FOR FORCED OSCILLATION TECHNIQUES

Our approach to the application of magnetic balance system to the measurement of dynamic stability parameters is based upon the relatively rigid control over the position of the model. This control provides not only the opportunity to control the mean position of the model in the wind tunnel but also provides the opportunity to move the model about that mean position. The motion itself may be forced in any way that one desires. We have found the two extremes of sinusoidal motion and random motion to be useful. In regard to the former, we have been able to control the location center of rotation. In particular we can cover the range from pure pitching motion to pure plunging motion by controlling the phase difference between the forward and aft lift excitation. The motion is monitored

by three solar cell arrays that are located axially along the model. Pure pitching motion causes the signal of the fore and aft cells to indicate the same amplitude but 180 degrees out of phase, while the center cell indicates no motion. Pure plunging motion is indicated when all three cells indicate the same phase and amplitude. The drag control system, ideally, holds the model in the same longitudinal position throughout this process.

In the second class of excitation a random signal (at least it is random over a wider band width than the system will pass) is used to excite the lift system. These motions then combine pitching and plunging. In either the random excitation or the pitching and then the plunging excitation it is possible to isolate C_{M_q} from $C_{M_{\dot{\alpha}}}$. If these excitations are applied in the yaw plane one can measure C_{N_r} and $C_{N_{\dot{\beta}}}$, as well as C_{ℓ_r}.

It is possible to generalize either of these motions into the pitch and yaw planes instead of individual planes. However, we have not yet attempted this generalization.

In addition to the plane motions, there is the possibility of spinning about the longitudinal body axis. This spin is either at a constant rate, for nonwinged airframes or for a rocking type of motion. These controlled motions provide a means of determining C_{ℓ_p} and C_{N_p}.

It is one thing to be able to apply one of several kinds of motions that should lead to the measurement of dynamic stability data. However, a second problem is the data handling. As will be seen below, the reduction of the data from random excitation is recorded on a strip recorder, manually transferred to punched cards and processed by an automatic computing machine.

The roll data and the pitch data may either be recorded on the strip recorder or by means of a measurement of a phase change using an electronic counting circuit.

SPECIFIC TECHNIQUES

We shall discuss three techniques that have been tried. The first consists of a forced oscillation technique for measuring the sum C_{M_q} and $C_{M_{\dot{\alpha}}}$ and a suggestion for the measurement of $C_{M_{\dot{\alpha}}}$. The latter stability

parameter was not measured because our system is insufficiently powered. The second consists of the random excitation. Third, the problem of damping in roll will be discussed.

In applying a forced motion to the model, we can measure the damping by measuring a change in phase of the motion. This process is simplified if the motion has the same amplitude in the wind-off and wind-on conditions. Under these circumstances the dynamics of the control system need not be considered. This may be seen from the following equation. For the wind-off, the motion of the model is governed by the equation

$$I\ddot{\theta}_0 + D_E\dot{\theta}_0 = M_{A_0} e^{-i\omega t} \tag{3}$$

Here I is the moment of inertia in pitch, D_E is the eddy current damping, θ is the pitching variable, ω is the excitation frequency and M_{A_0} is the applied moment. With the wind-on the equation becomes:

$$I\ddot{\theta}_1 + (D_A + D_E)\dot{\theta}_1 + M_\alpha \theta = M_{A_1} e^{-i\omega t} \tag{4}$$

D_A is the aerodynamic damping, $D_A = qSl\,(C_{M_{\dot{\theta}}} + C_{M_{\dot{\alpha}}})$, M_α is the slope of the aerodynamic pitching moment curve. Recall that the solution to Eq. (3) is

$$\theta_0 = -\frac{M_{A_0}}{(I\omega^2)^2 + (\omega D_E)^2}\,(I\omega^2 - i\omega D_E)e^{-i\omega t} \tag{5}$$

The phase shift between a reference point of the applied moment, which will be discussed below, and the solution is

$$\phi_0 = \tan^{-1} - \frac{D_E}{I\omega} \tag{6}$$

Similarly

$$\theta_1 = \frac{M_{A_1}\left\{M_\alpha - I\omega^2) + i\omega\,(D_E + D_A)\right\}}{(M_\alpha - I\omega^2)^2 + \omega^2\,(D_E + D_A)^2}\,e^{-i\omega t} \tag{7a}$$

and

$$\phi_1 = \tan^{-1} \frac{(D_E + D_A)\omega}{M_\alpha - I\omega^2} \tag{7b}$$

Equation 6 can be used to compute D_E and then Eq. (7b) can be used to compute D_A i.e.,

$$D_E = -I\omega \tan \phi_0 \tag{6a}$$

so

$$D_A = I\omega \tan \phi_0 + \frac{M_\alpha - I\omega^2}{\omega} \tan \phi_1 \tag{7c}$$

If it happens that $M_\alpha \sim I\omega^2$ the measured value of ϕ_1 is more accurate. Note that the aerodynamic moment slope M_α must be known. The key in the use of this technique is the ability of the system to make the motion be sinusoidal, i.e., θ_0 and θ_1 are sinusoidal although the total applied moment M_A may not itself be constant. This nonconstant applied moment is a reaction that can arise from other constraints that are naturally in the system. Those constraints include changes in the magnetic moment and nonlinear interaction gradients caused by the control system. $M_A(t)$, the actual applied moment, was represented by $M_A e^{-i\omega t}$ for simplicity. Nevertheless, as $M_A(t)$ is periodic, and θ_0 and θ_1 are sinusoidal, Eqs. (6a) and (7c) may be used. The applied moment must be periodic so the phase shift can be measured.

Figure 4 shows the data Lee Tilton (Ref. 5) obtained in the 4x4", M = 4.8 tunnel at the Aerophysics Laboratory. This data shows that for a ±1° motion about 0° angle of attack, the damping is unstable in that it takes energy from the air streams and puts it into the motion. This curve also shows the value of eddy current damping, which is less than 0.1 of the aerodynamic term. The calculated value (based on slender body theory) is also shown. The agreement is not spectacular but is considered satisfying. The model has a fineness ratio of 10, the nose is a 3 caliber 3/4 power with a 3 caliber cylindrical mid-section. The base is a 4:1 ellipse followed by a 20° semi-vertex angle cone.

In principle the damping due to $\dot{\alpha}$ may be computed from the plunging equation,

$$D_E \dot{\alpha}_0 = M_{A_0} e^{-i\omega t} \tag{8a}$$

$$(D_E + D_A)\dot{\alpha}_1 + M_\alpha \alpha_1 = M_{A_1} e^{-i\omega t} \tag{8b}$$

If there is any eddy current damping, it must be estimated from (8a), and

$$D_A = \frac{M_\alpha}{\omega} \tan \phi_1 - D_E \tag{8c}$$

Again ϕ is the phase change from same reference point on M_{A_1} and the same point of the sinusoidal curve of $\alpha(t)$. As indicated above no attempt was made to measure $C_{M_{\dot{\alpha}}}$ because of the inability to excite an appreciable value of $\dot{\alpha}$, as well as the one-sidedness of our forcing function of plunging motion.

Note in passing that if one monitored side force and yawing moment that the deviations C_{Y_q} and C_{N_q} could be determined if the configuration possessed the proper kind of asymmetries. Similarly by excitation in the yaw plane one could in principle infer C_{N_r} and $C_{N_{\dot{\beta}}}$ and C_{ℓ_r} if the roll components were properly calibrated.

The second technique that we have considered for the measurement is based upon the ideas of system identification (cf. Ref. 6 and 7). In Ref. 7 these techniques have been applied to the problem of determining the aerodynamic characteristics of several different shapes. The procedure is perfectly general and can be used to provide information about nonlinear aerodynamic systems as well as linear systems. The nonlinear developments are based upon Volterra's series expansion (Ref. 9). This implies that the nonlinearities can be expanded in a power series. This is not a serious restriction below the stall.

The procedure itself is based upon the idea of an integral representation of the moment and in the wind tunnel, pitch relation; that is

$$M(t) = \int_{-\infty}^{\infty} \mathscr{L}_m (t - \tau)\theta(\tau)\, d\tau$$

$\mathcal{O}_m$ is some kind of kernel which can be convolved with the pitch angle, θ, to give the aerodynamic moment[1].

The usefulness of this form is completely obvious. $\mathcal{O}_m$ can be so defined that it includes the aerodynamic moment and it automatically includes the time delays or derivative effects. Further, at each Mach number $\mathcal{O}_m$ is in a form that is applicable to trajectory analysis merely by determining the proper value of the product of dynamic pressure and reference area.

The value of $\mathcal{O}_m$ can be computed by correlation techniques if a random, time stationary signal can be inserted into the θ control in the wind tunnel. Then the crosscorrelation of the moment with the pitch angle input, is just $\mathcal{O}_m$, i.e.,

$$\lim_{T\to\infty} \frac{1}{2T} \int_{-T}^{T} M(t)\theta(t-\lambda)dt = \lim_{T\to\infty} \frac{1}{2T} \int_{-T}^{T} dt \int_{-\infty}^{\infty} \mathcal{O}_m(t-\tau)\theta(\tau)\theta(t-\lambda)d\lambda$$

---

[1] It is easy to illustrate the existence of an integral representation. For example consider the differential equation

$$(M_q + M_{\dot{\alpha}})\dot{\theta} + M_\alpha \theta = M(t)$$

By application of Cauchy's theorem (cf. Morse and Feshback, Methods of Theoretical Physics Chap. IV) on the complex t plane

$$\frac{d^n\theta}{dt^n} = \frac{n!}{2\pi i} \oint \frac{\theta(\tau)}{(t-\tau)^{n-1}} d\tau \qquad \tau > t$$

Hence one integral form is

$$M(t) = \oint \left(\frac{1}{2\pi i}\right) \left[\frac{1!(M_q + M_{\dot{\alpha}})}{(t-\tau)^2} + \frac{M_\alpha}{(t-\tau)}\right] \theta(\tau)d\tau$$

A second form using Fourier Series (cf. Lighthill-Fourier Analysis and Generalized Function p. 35)

$$M(t) = \int_{-\infty}^{\infty} \left[(M_q + M_{\dot{\alpha}})(t-\tau) + M_\alpha\right] \theta(\tau)\, d\tau$$

If θ is random and time stationary, then

$$\lim_{T\to\infty} \frac{1}{2T} \int_{-T}^{T} \theta(\tau)\,\theta(t-\tau)\,d\tau = \delta(t-0)$$

Hence

$$\mathscr{L}_m(\lambda) = \lim_{T\to\infty} \frac{1}{2T} \int_{-T}^{T} M(t)\,\theta(t-\lambda)\,d\lambda$$

In using this approach one must be sure that the random signal is time stationary, i.e., its statistical properties are not dependent upon time. If this is not the case errors can occur. Figure 5 taken from Ref. 6 shows the result of using a nonstationary source of random signal. On the other hand Judd (Ref. 10) has used turbulence in the wind tunnel to serve as a random excitation and the calculated $\mathscr{L}_m$ agrees well with the measured value (Ref. 6).

Finally it is possible to measure damping in roll with the magnetic balance system. This is done by forcing the model to roll at a known rate ($p\,\frac{b}{2v} \sim 0.2$) and then turning off the roll forcing function and recording the roll velocity as a function of time. The damping roll is determined from the logarithmic decrement. We are using an alternate current technique for generating the rolling moment. It is possible to use d.c. (See Ref. 11). A current loop in the model (which acts like a rotor) is driven by two fields in quadrature (Fig. 7).

Figure 8, which shows the model in the tunnel is part of a program (Ref. 12) to learn how to apply the magnetic balance to problems of roll damping that is sponsored by AFCRL. The raw data includes eddy current damping which is measured with the wind-off at low pressures (0.1 psia). This data has been subtracted from that given in Fig. 9, which is therefore only C_{ℓ_p}.

CONCLUDING REMARKS

We conclude that magnetic suspension and balance systems can be used to infer dynamic stability data from wind tunnel measurements. This technique has been demonstrated for linear process and offers the possibility of providing aerodynamics coefficients in a form that is well adopted to trajectory calculations.

REFERENCES

1. Fournier, M. and Laurenceau, P., Suspension Magnetique dunc Maquette en Soufflerie, LaRecherche Aeronautique, No. 59, July-August 1957, pp. 21-27.

2. Chrisinger, J.E., Design of a Magnetic Wind Tunnel Balance, Thesis fo. Degree of Aeronautical Engineer MIT, June 1959.

3. Parker, H.M. and Jenkins, A.W.,"A Magnetic Suspension System with Orthogonal Force", Journal of Applied Physics, Vol. 30, No. 5, p. 458, April 1959, p. 258S.

4. Tilton, E.L., et al., "The Design and Initial Operation of a Magnetic Model Suspension and Force Measurement System", Journal of Royal Aeronautical Society, November 1963.

5. Tilton, E.L., Dynamic Stability Testing with a Wind Tunnel Magnetic Model System, S.M. Thesis MIT Department of Aeronautics, January 1963.

6. Gibson, J.E., Nonlinear Automatic Control, McGraw Hill Book Company, New York, 1963.

7. Lee, Y.W., Statistical Theory of Communication, John Wiley and Son, New York 1961.

8. Stephens, T., Determination of Nonlinear Aerodynamic Damping Effects with a Wind Tunnel Magnetic Model Suspension System, S.M. Thesis, MIT Department of Aeronautics Thesis, June 1964.

9. Volterra, V., Theory of Functional and of Integral and Integro-Differential Equation, Chap. I, p. 21, Dever, New York.

10. Judd, M., Measurement of Stability Derivatives from Response to a Randomly Varying Aerodynamic Force, University of Southampton ARC 24970, February 1963.

11. Procedures for Controlling of Roll with Magnetic Balance Systems, MIT Aerophysics Laboratory Report 78, (To be published).

12. Copeland, A., Proposed M.S. Thesis, MIT Department of Mechanical Engineering.

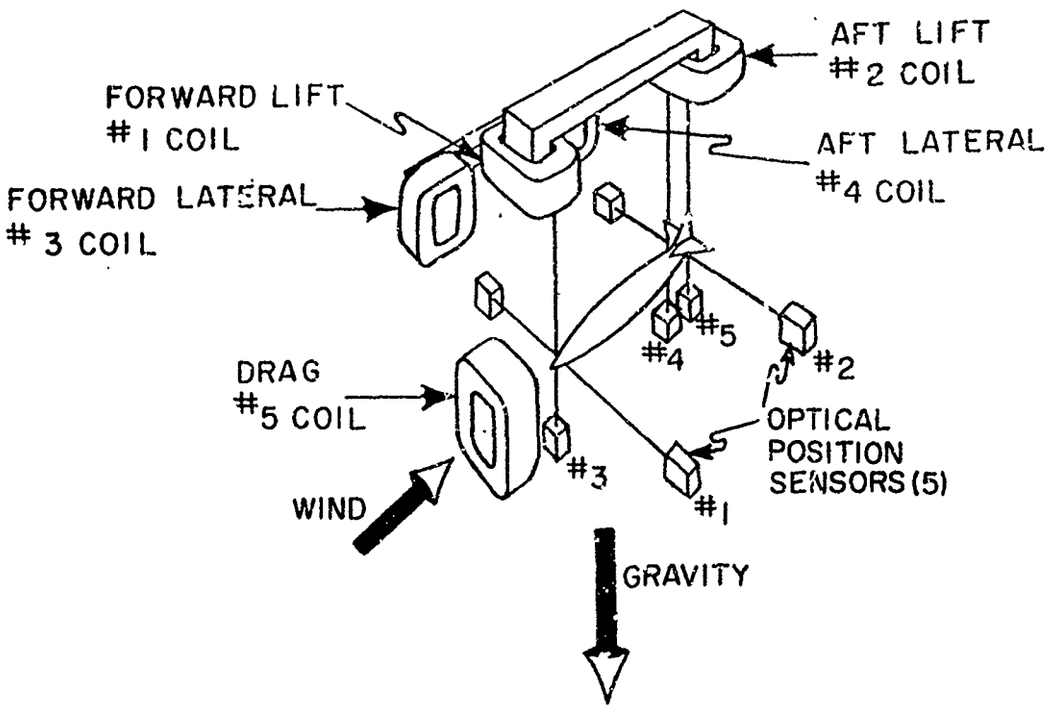

Figure 1. Magnet configuration showing model and optical position sensors

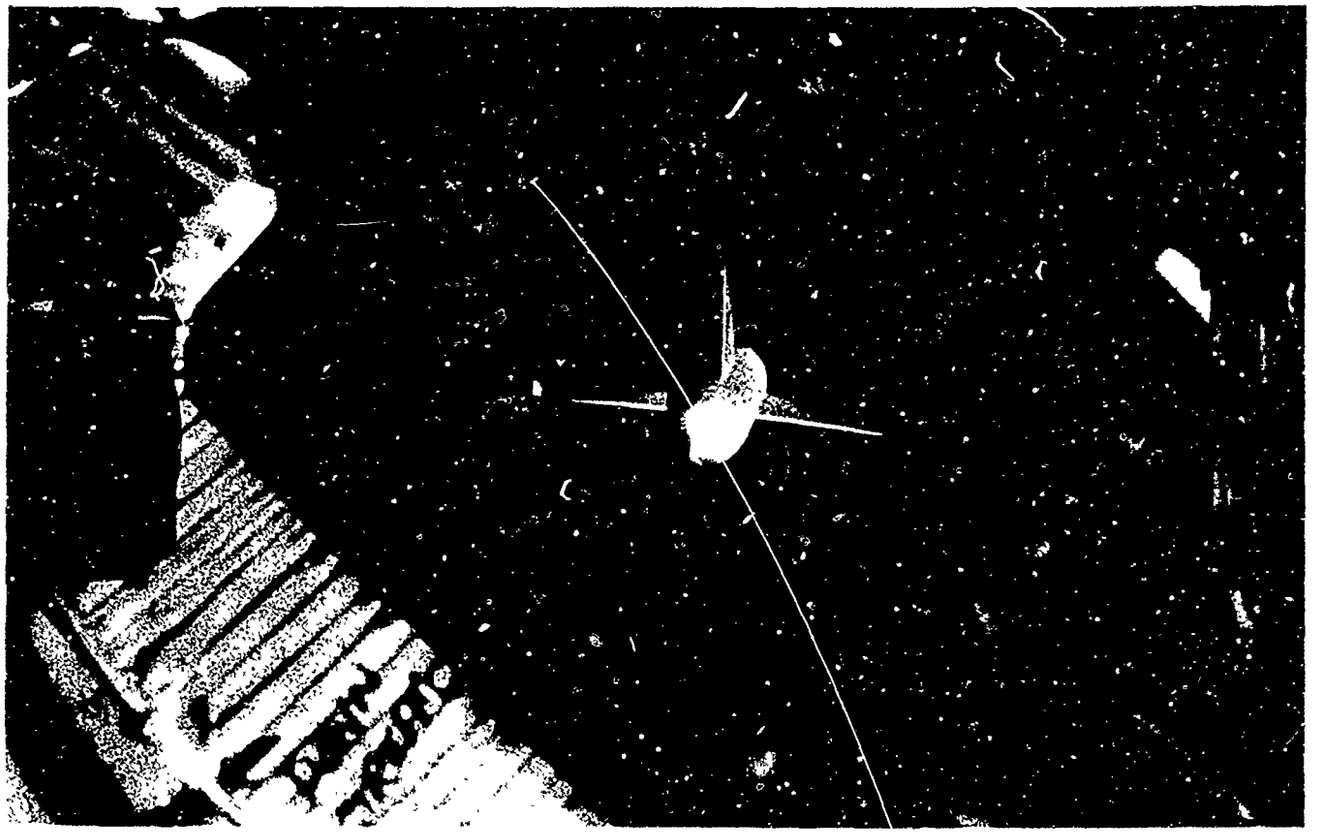

Figure 2. Photograph of model suspended in wind tunnel

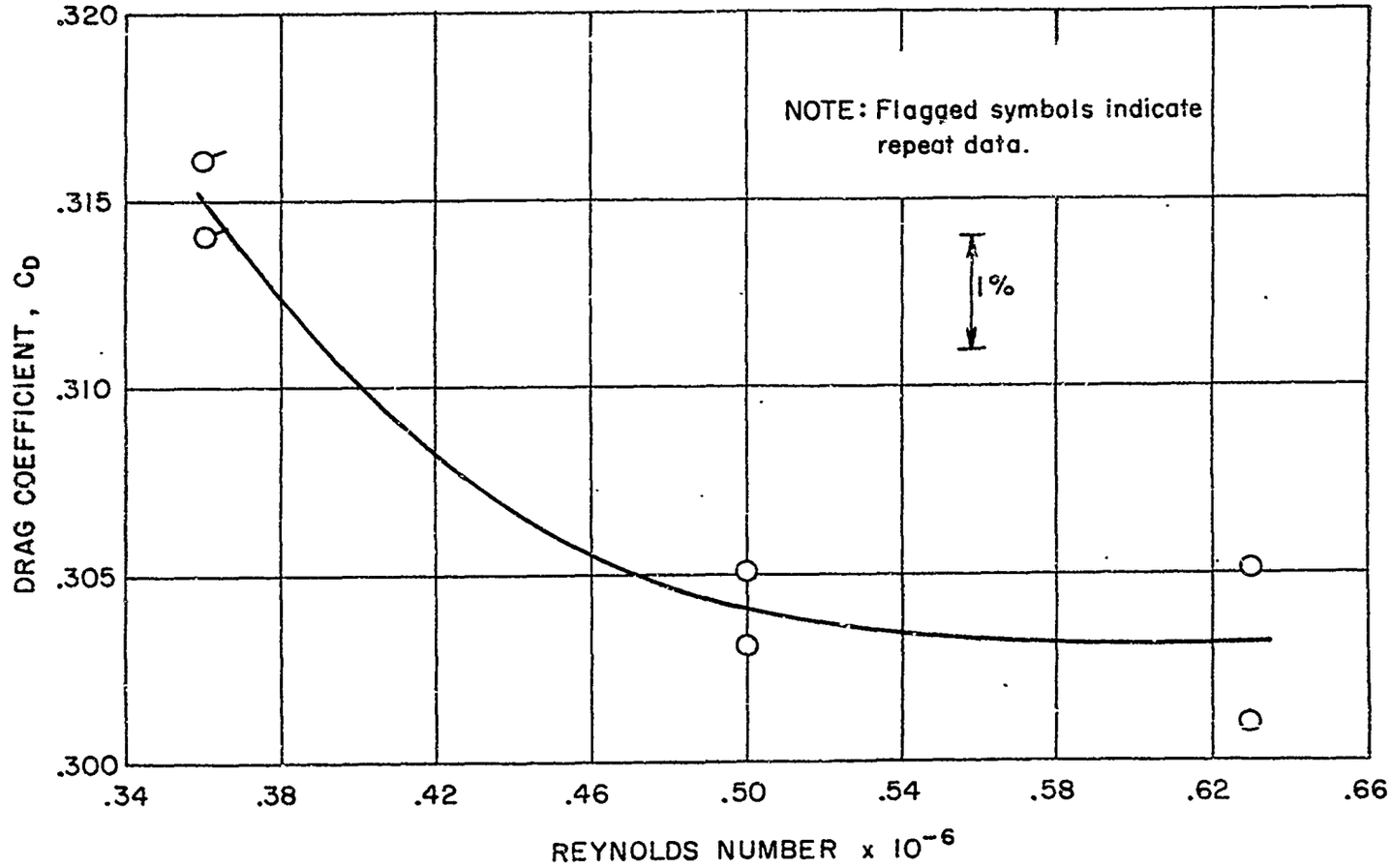

Figure 3. Drag coefficient at zero geometric angle of attack vs. Reynolds number

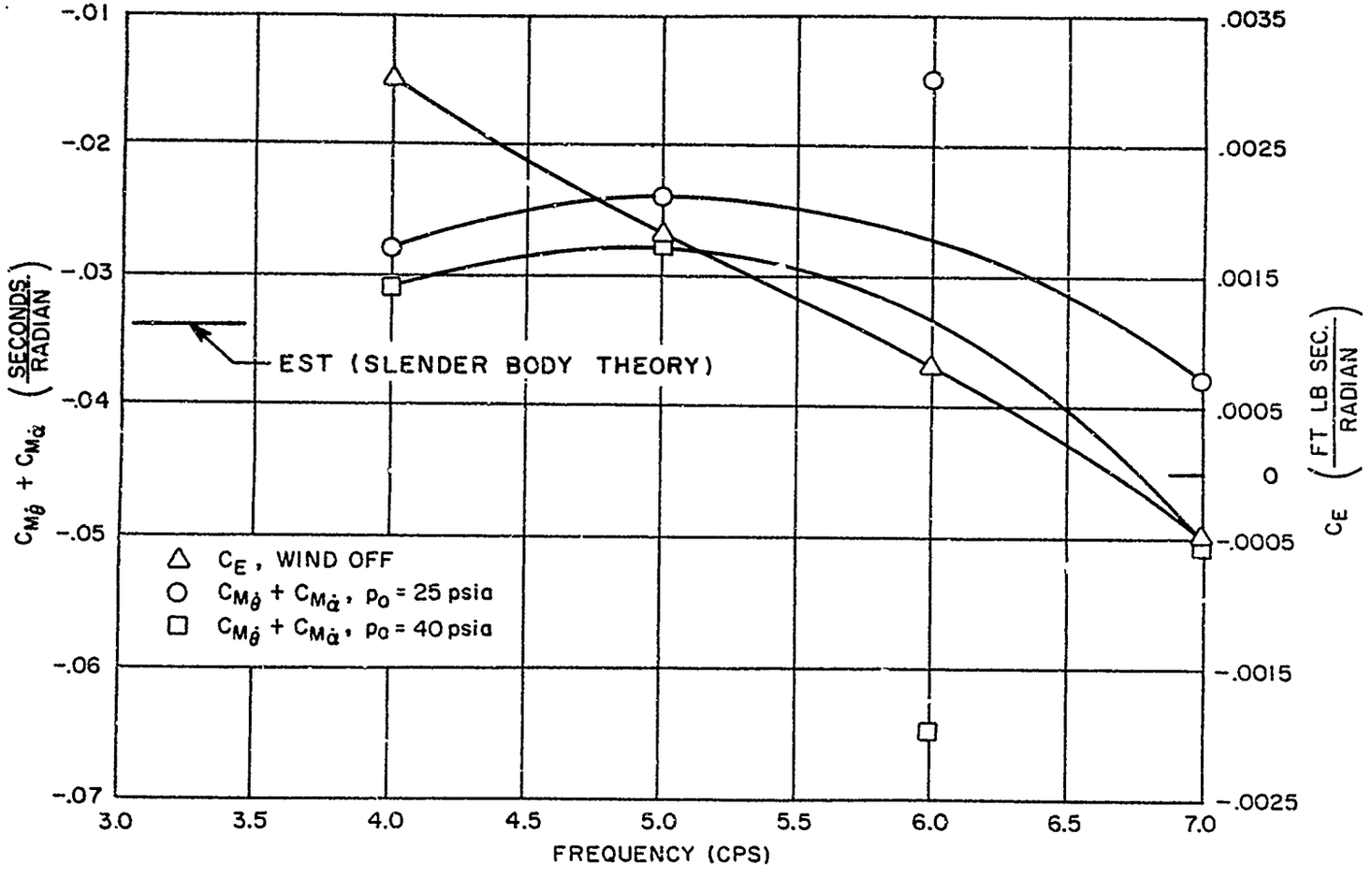

Figure 4. Variation of damping with frequency

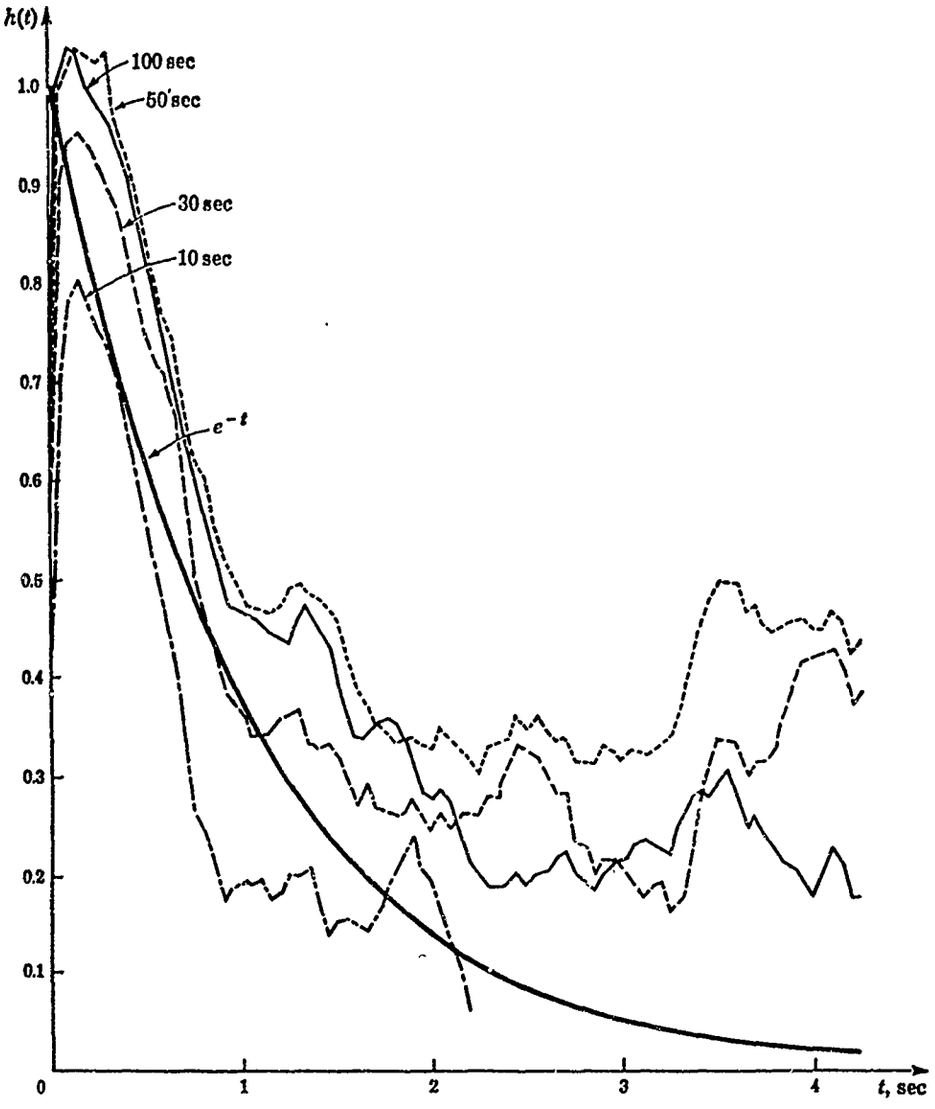

Figure 5. Approximation of the weighting function e^{-t} by correlation techniques (results for data intervals of 10, 30, 50, and 100 sec with a sampling interval of 0.05 sec are shown).

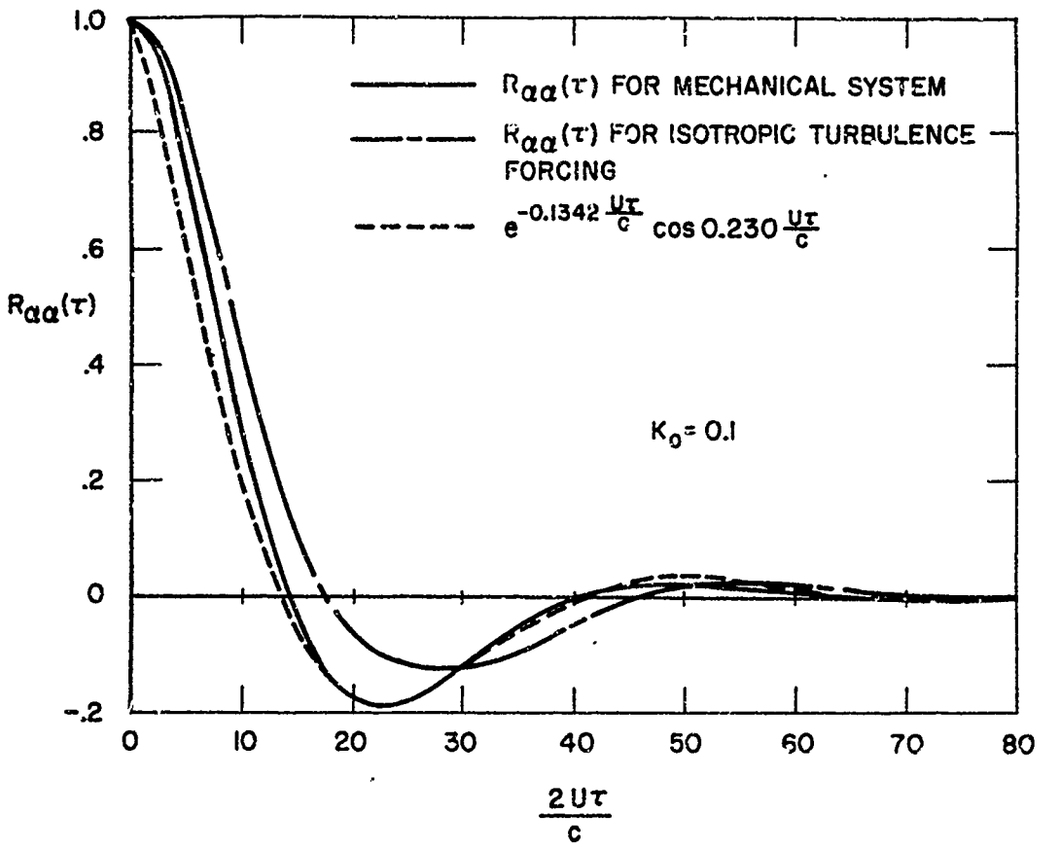

Figure 6. Auto-correlation functions of responses at $K_0 = 0.1$

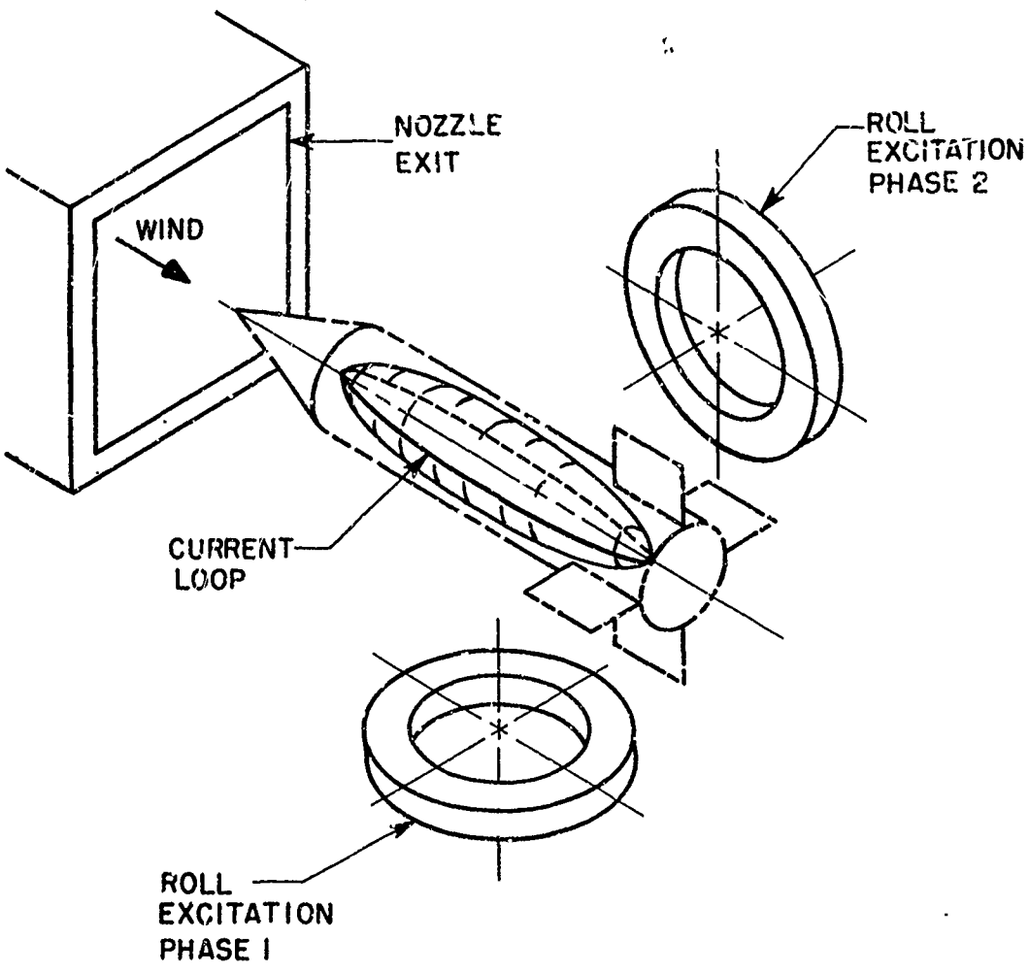

Figure 7. Alternating field roll control system

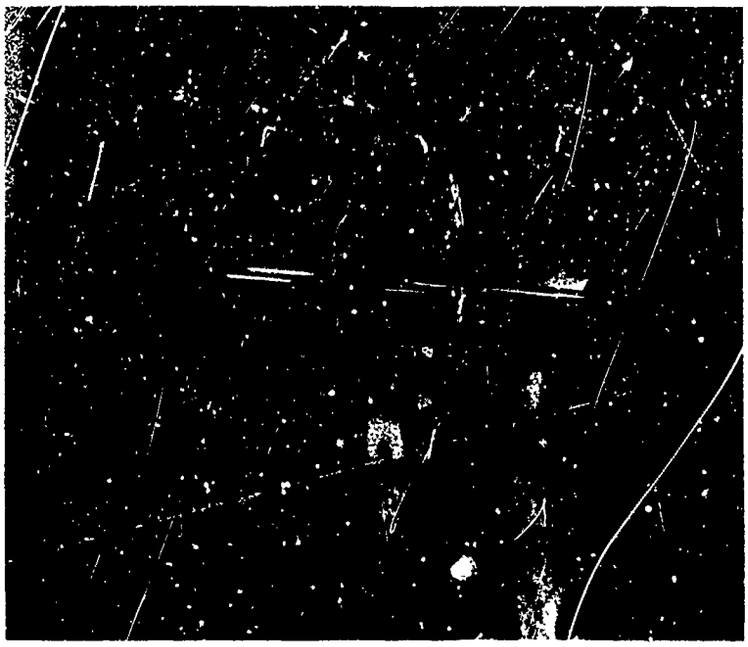

Figure 8. Roll model in the wind tunnel

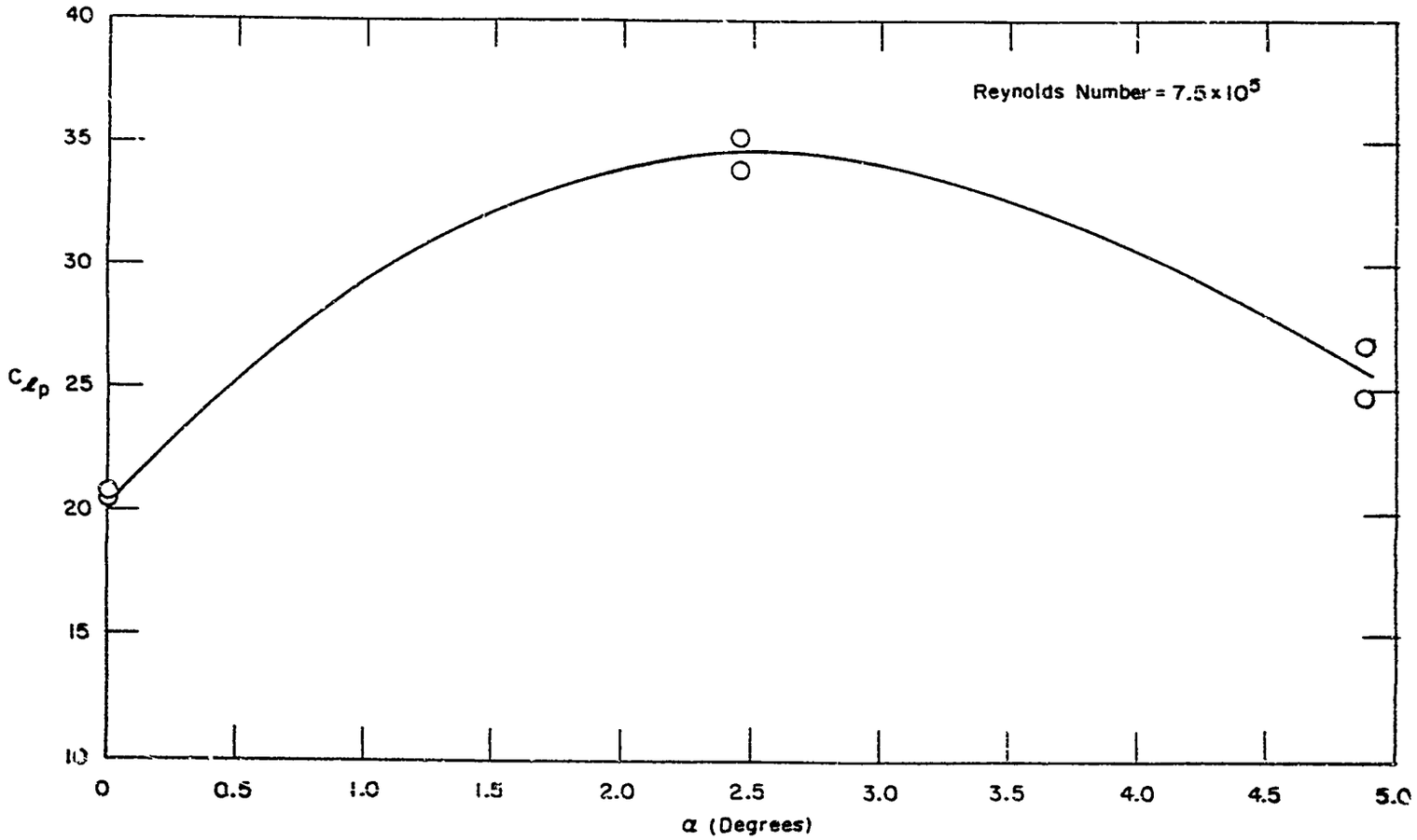

Figure 9. Roll damping coefficient vs angle of attack at M = 4.25 for the Iroquois model

DISCUSSION

Prof. Kuethe:

We are carrying out a similar study in the 4 x 4 inch supersonic tunnel at The University of Michigan. The model is in a strong magnetic field normal to the wind direction. An alternating current passing through a coil within the model causes it to oscillate about an axis normal to the magnetic and flow fields. The electromagnetic damping with an aluminum model was prohibitively high compared with the expected aerodynamic damping. The model we are presently testing is constructed of plexiglass and the tare damping is down to a usable value at Mach numbers around 4 and probably higher. I would like to ask whether you have experienced the same difficulty with high eddy current damping.

Dr. Covert:

On this slender model at low total pressures the eddy current damping looks like it will be about 25 to 30 percent of the aerodynamic damping.

Prof. Kuethe:

Is it the same wind on and wind off?

Dr. Covert:

Well, we make it be the same wind on and wind off by this calibration technique except for air bearing friction. We support the model on this air bearing system in the position that it would be in during the wind tunnel operation. We unhook the control system so that we can apply the same current in each coil that we measured during the wind tunnel operation and then since the only difference between these two cases is that one time the wind is on and the other time the wind is off; hopefully, the amount of eddy current damping is the same in each of these cases.

Prof. Kuethe:

The definitions of $C_{m_q} + C_{m_{\dot{\alpha}}}$ vary somewhat and I am wondering if the model used has a fairly high dynamic stability?

Dr. Covert:

The model I showed, has no fins on it at all. It is just a body of revolution and that one had a 3/4 power ogive on the nose, a cylindrical midsection, a 4 to 1 elliptical afterbody feeding into a cone. We have not tried to get any damping in pitch data with finned model. The reason that this is not as complete as one would like it is that what we were supposed to be doing is finding out what the limitations of this kind of an instrument are and so

we always try at least in our own minds to find the harder cases to study. The assumption being that if you can do it on a hard case you can do it on an easy case. Now there may be a pitfall here and there. The thing that we are trying to do with the pitching models is to measure a change in phase and we would like to get down to few degrees. The facts of life are that we have not been able to consistently measure below about 5.2 degrees change, but this seems to be enough at least for the kind of models that we are talking about. Now it may be that if we went to a higher Mach number and had a different configuration particularly some of the cone-cylinder-flare models we would be in difficulty. We can't say because we haven't done it yet.

C. J. Schueler:

If I recall the French system, they have the problem of insertion and removal of the model during tunnel start and stop. I wonder how you accomplished this or do you have sufficient capacity in your system?

Dr. Covert:

Our system has sufficient capacity, but this is not a problem. We have been able to start the tunnel; in fact, one of the things that we routinely do as a matter of course is to measure the current in the various systems as the starting shock goes downstream because we are interested in what starting loads really turn out to be, and the thing that so far we have learned is that they are never quite what you think. They seem to be strongly dependent on a configuration that you have, strongly dependent on how the valve opens any particular day, and they are a little bit dependent on individual nozzles. We have some nozzles that seem to start cleanly and others that seem to start with a big x shock. According to the theory, a shock configuration that is a x like should cause a vortex, and there is. The models will spin up and then they will spin for a while and after a while they will damp out. When we first put in this finned model the other day we were somewhat concerned about maybe it would start spinning so fast that we would get a spin instability. There are certain odd instabilities that can arise at certain frequencies so we really faced that starting problem with a great deal of trepidation, but so far it turned out to be not something to worry about. I have a starting load slide that I just happen to have in my pocket if you want to take two minutes? This is a well behaved start on a very slender model and what it indicates is that the start just follows the p_o. There doesn't seem to be a great deal of refraction. Any other questions? This is time in seconds and the ordinate scale is not really quite labeled correctly; this is really drag current corresponding to the steady state. If you put an impact probe in, each one of these peaks is when the shock comes down. It strikes the model a couple of times before it finally goes on by. Then after the tunnel starts then there is a gradual increase in pressure to the steady state; but

in this case there doesn't seem to be a factor of more than about two or three on this slender model. On blunter models this ratio can be as high as four or five.

J. Grimes:

Did you run into the plunging and heaving type of phenomena that we had on the Bicknell "66"? (A Delta wing, "T" Tailed configuration).

Dr. Covert:

We would like to plunge something someday. The reason we haven't gone into the plunging and heaving at all is because our system is so arranged that the only force downward is the gravity. The magnetic field only works upwards. At any frequencies that we can get where the model is actually plunging, the reduced frequency is so low that it is just a quasi-steadyeffect. One of the things that we think that this kind of balance system offers is the opportunity to separate pitching and plunging because you have control over motion. One of the advantages of doing the statistical system is that it includes both at once, automatically.

J. Grimes:

Thank you.

M. Fink:

This is more a comment than a question. You mentioned starting loads. We have had quite large starting loads not only on drag but on lift and pitching moment for the winged models that were tested in the program I described yesterday. For some of the models tested before we found that we lost flexures on the forced oscillation balance with amazing regularity. We put in a pneumatically operated device which supports the back end of the model and keeps it from pitching and putting loads on the flexures during the tunnel start and stop. For those of you who have dynamic stability balances and have tested only wingless re-entry vehicles, in the future, you may find yourself going into testing of winged vehicles. I'll give this as a bit of advice that the starting loads on lift and pitch can be startling rather than starting.

Dr. Covert:

We happen to have a schlieren of one start where the flow was essentially started on top and there was a normal shock at the bottom so the model sort of experienced a strong lift and pitch under these circumstances.

INSTRUMENTATION AND TECHNIQUES USED AT THE NAVAL ORDNANCE LABORATORY FOR THE DETERMINATION OF DYNAMIC DERIVATIVES IN THE WIND TUNNEL

by

Frank J. Regan

U. S. Naval Ordnance Laboratory

White Oak

Silver Spring, Maryland

ABSTRACT

The Naval Ordnance Laboratory's effort in developing and improving instrumentation for the measurement of roll damping, pitch damping, and Magnus effects is reviewed. Wind tunnel free-flight launch system, pitch damping model support with E-coil and air bearing and E-coil and ball bearings, roll damping support with air bearing, and highly sensitive Magnus balances are discussed. A brief outline is given of the techniques of data reduction. Data obtained with this instrumentation are compared with data from other sources. A motion picture of some wind tunnel free-flight trajectories is presented.

INSTRUMENTATION AND TECHNIQUES USED AT THE NAVAL ORDNANCE LABORATORY FOR THE DETERMINATION OF DYNAMIC DERIVATIVES IN THE WIND TUNNEL

I. INTRODUCTION

Over the past several years there has been an increasing awareness of the importance of dynamic derivatives. Many flight difficulties of projectiles, bombs, rockets and ballistic re-entry bodies are directly attributable to incomplete knowledge of the forces and moments caused by the rate of change of body angular position. Facilities such as tracking ranges, ballistic ranges, wind tunnels and shock tunnels have been used to grapple with the many problems associated with the measurement of these effects.

This paper summarizes the techniques used at the Naval Ordnance Laboratory in making dynamic stability measurements in its wind-tunnel facilities. The stability derivatives which have been measured include the damping-in-pitch derivative, $C_{m_q} + C_{m_{\dot{\alpha}}}$, the damping-in-roll derivative, C_{ℓ_p}, and the Magnus derivatives expressed variously as C_{y_p}, C_{n_p} or $C_{y_{p\alpha}}$, $C_{n_{p\alpha}}$.

In the past at NOL, damping-in-pitch measurements were made by the free oscillation technique using a model mounted by ball bearings on a transverse support through the center of gravity. The damping derivative was obtained from high-speed motion pictures. The ease and accuracy of this technique have been greatly improved by employing air bearings to reduce friction, and an E-core transducer to directly read data. Air bearings have also proven valuable in roll-damping measurements. The wind-tunnel free-flight technique has been developed for cases where supports may cause serious flow interference.

The measurement of Magnus derivatives presents special problems in measuring small yaw forces in the presence of large lift forces. The sensitive balances required are particularly susceptible to induced vibrations. Special

balances have been developed which work in spite of these difficulties.

II. PITCH DAMPING

A. Free Oscillation Technique

Of all the dynamic effects being measured at the present time, the greatest interest is undoubtedly in pitch damping. The various techniques nearly always involve oscillatory motion around a fixed axis. In this case one obtains the combination of derivatives $C_{m_q} + C_{m_{\dot{\alpha}}}$. Attempts have been made to develop wind tunnel supports to separate the translatory derivatives from the rotational derivatives with varying degrees of success (see refs. (1) and (2)).

The free oscillation technique has been used extensively at NOL (see Figs. 1 and 2). In this method the model is mounted on a transverse support through the center of gravity. The model is connected to this rod by means of ball bearings or an air bearing. The model is held at an angle of attack, and upon release undergoes a damped oscillatory motion. This motion is assumed to be described by the following equation:

$$\ddot{\alpha} - \left[\frac{\left(C_{m_q} + C_{m_{\dot{\alpha}}}\right) QSd^2}{2VI}\right] \dot{\alpha} - \left[\frac{C_{m_\alpha} QSd}{I}\right] \alpha = 0 \qquad (1)$$

For the case of light damping (damping ratio less than 0.1), equation (1) has the following approximate solution:

$$\alpha = \bar{\alpha} \cos \sqrt{-\frac{C_{m_\alpha} QSd}{I}}\, t \qquad (2)$$

where

$$\bar{\alpha} = \bar{\alpha}_o \exp \left\{ \frac{\left(C_{m_q} + C_{m_{\dot{\alpha}}}\right) QSd^2}{4VI}\, t \right\} \qquad (3)$$

The barred quantities in the above expression are the amplitude of the envelope of the oscillations with the subscript o indicating initial conditions. In the case of nonlinear damping the decay envelope is divided into n increments: 0, 1, 2, ..., i, ... n. The relationship between the angle of attack at the beginning and end of the i+1 increment is from equation (3):

$$\bar{\alpha}_{i+1} = \bar{\alpha}_i \exp \left\{ \frac{\left(C_{m_q} + C_{m_{\dot{\alpha}}}\right) QSd^2}{4VI} \left(t_{i+1} - t_i\right) \right\} \tag{4}$$

Equation (4) may be solved for the pitch-damping derivative as,

$$C_{m_q} + C_{m_{\dot{\alpha}}} = f\left(\tilde{\bar{\alpha}}_i\right) = -\left(\frac{4VI}{QSd^2}\right) \frac{1}{\left(t_{i+1} - t_i\right)} \ln\left(\frac{\bar{\alpha}_i}{\bar{\alpha}_{i+1}}\right) \tag{5}$$

where

$$\tilde{\bar{\alpha}}_i = \frac{\bar{\alpha}_{i+1} + \bar{\alpha}_i}{2} \tag{6}$$

Use of E-Core Transducer

Until recently the oscillatory motion of the wind-tunnel model was recorded on movie film at 70 frames per second. However, except for certain special tests, the motion is now "read" by an E-core electromagnetic variable reluctance transducer mounted within the model. Reference (2) describes the earlier application of this device at AEDC.

Figure 3 is a drawing of the E-core used at the Naval Ordnance Laboratory in the measurement of aerodynamic pitch damping. Figure 4 is a photograph of the core alone. It will be noted that two E-cores are fixed to the nonrotating transverse model support shaft. The E-core housing is fitted as an integral part of the model and, therefore, shares its oscillatory motion. The inner portion of the housing is eccentric with the model support shaft. Hence, as the model (and the housing) oscillate, the air gap between the E-core and the housing changes. This change in air gap will now be

shown to be related to the change in reluctance of a magnetic circuit and the change in self-inductance of an electric circuit.

In Figure 3 it will be noted that there is an excitation winding in the center leg of the E-core. From Ampere's cicuital law (ref. (3)), it can be shown that the magnetic flux linking each side leg of the E-core is,

$$\Phi = \frac{N^2 i}{R_\ell + R_h + lg/\mu Ag} \tag{7}$$

where Φ, N, i, R_ℓ, R_h, lg, μ and Ag are the magnetic flux, number of wire turns, the excitation current, the reluctance of the side leg, the reluctance of housing, the length of the air gap, the permeability of air and the effective cross-sectional area of the air gap, respectively.

From Faraday's law the induced emf can be related to the time rate of change of current i as:

$$E = -\frac{d\Phi}{dt} = -\frac{d\Phi}{di}\frac{di}{dt} = -L\frac{di}{dt} \tag{8}$$

The above equation demonstrates that the induced emf, E, is related to the time rate of change of the excitation current and self-inductance, L. Since L is equal to $d\Phi/di$, it is clear from equation (7) that any changes in L can only come from changes in the air gap, lg.

Figure 4 illustrates the original E-core and a later improved design using a wire-wound teflon bobbin. In the original E-core, a fish paper underlayment was used. This design had the disadvantages of frequent electrical shorts because of inadequate protection to the wire and the requirement of tedious manual winding. These difficulties were satisfactorily overcome by means of the teflon bobbin. The unit was assembled on a 0.25-inch shaft and potted (see Fig. 2). A more detailed discussion of the NOL E-core transducer is given in reference (4).

The E-core is calibrated with the model in the wind-tunnel pitch-damping calibration rig (Fig. 1). As the model is manually rotated through angular increments, calibration counts are recorded on magnetic tape. A sample calibration curve is shown in Figure 5. Upon completion of calibration, the model is ready for testing. During the test, the E-core transducer "reads" the damped oscillatory motion. The electrical signal is sampled 300 times per second and recorded in digital form on magnetic tape. A typical angle of attack versus time record is given in Figure 6. A comparison between pitch-damping coefficients obtained for the biconic model of Figure 1 using both the E-core and photographic technique is given in Figure 7. The results agree very well.

Use of Air Bearings

In spite of the greatly improved data acquisition capability of the support utilizing the E-core, the load transmission was carried out by ball bearings. While these bearings have been generally satisfactory, they only last a few runs. Bearing wear becomes evident by an increase in friction. Any frictional rise becomes especially intolerable in light load applications--usually at high Mach numbers. It was therefore decided to construct an air bearing for use in pitch-damping model supports. The support presently being evaluated is shown in Figure 8. It will be noted that this support contains a stationary E-core and a rotating housing. Bearing air is admitted through one side and exits from both sides of the support rod. Presently, this design is undergoing bench tests. Air bearings are discussed further below in connection with roll-damping tests.

B. Free-Flight Technique

Supersonic Wind-Tunnel Launcher

It is clear that no matter how carefully supports are designed, they introduce an artificiality into the test. It was for this reason that studies have been carried out to determine the advantages of flying a model in a wind tunnel. While such a technique is not new (see ref. (5)), it has recently received renewed attention (ref. (6)).

NOL is developing launch systems for all of its wind-tunnel facilities. The launcher for the supersonic tunnels is shown in Figure 9. This device consists of an air cylinder into which is admitted a regulated air supply driving forward a piston and piston rod. Attached to the other end of the piston rod is the launch head and model (Fig. 10). As the piston comes to an abrupt stop at the end of its travel, an inertial mass in the launch head moves forward, permitting the sabot fingers to snap open, and release the model.

It is necessary to know the relationship between the cylinder air pressure and launch head speed in order to keep the model trajectory at all times within the viewing area. This relationship is obtained as follows: Four permanent magnets are imbedded in the piston rod. As the piston rod exits the cylinder, these magnets in sequence pass a sensor. Signals from this sensor are recorded as pulses on an oscilloscope. Knowing the distance between the pulses, the sweep rate of the oscilloscope and the distance between the magnets, it is a simple matter to calculate the speed of the model. Thus for each Mach number a simple relationship is found between launch speed and the corresponding driving pressure.

In passing, it should be pointed out that the launch head contains an air motor capable of imparting a spin rate to the model at launch. Up to the present, no launches of spinning models have been attempted.

Hypersonic Wind-Tunnel Launcher

Free-flight experiments have also been carried out in the NOL Hypersonic Tunnel No. 4 at Mach 18. Figure 11 illustrates the essentials of the system. The launcher is removed from the test section until flow is established. Then the model, mounted on the launcher, is slid into the flow along the rails of the injector mechanism. A solenoid valve admits air from the regulator into an air cylinder which in turn drives forward a flexible cable enclosed in a guide tube. The model, attached to a guide at the opposite end of the cable, is injected into the flow.

Test Results

The free-flight models used in the supersonic tunnels were cones of 9° half-angle, machined from magnesium to a wall thickness of 0.007 inches (see Fig. 10). Model weighting was accomplished by bonding balls of hevimet to the cone walls.

Model motions are recorded by a 16 mm Eastman high-speed camera running at 3,000 frames per second. The camera initiates model launch at preselected values of film footage. Consideration is being given to taking pictures in mutually perpendicular planes simultaneously. Figure 12 shows a typical record of the free-flight model's oscillatory motion.

The measured damping derivative $C_{m_q} + C_{m_{\dot{\alpha}}}$ of the 9° cone is compared with Van Dyke's second order theory of reference (7) in Figure 13. The agreement is excellent.

The cone axial force coefficient (Fig. 14) has also been obtained using the wind-tunnel free-flight technique with a non-oscillating model. The result is in excellent agreement with ballistics range data.

Several runs have been made in Hypersonic Tunnel No. 4 at Mach 18 with a variety of very small models shown in Figure 15. The flared cone models of 10 and 20 degrees half-angle used had an aluminum nose and teflon afterbody. The model length was approximately 0.819 inches. A "ring wing" model was also flown. These models were cones of 10° half-angle with steel noses and aluminum wings. Figure 16 is a record of the oscillatory motion of this model in flight. Teflon spheres (0.183-inches diameter) were flown for drag measurements. The technique is very promising. It will be fully exploited when the present conical nozzle and 5-inch diameter viewing ports are replaced with a contoured nozzle and large test section windows. For the purpose of testing in low density flows, there is always the difficulty of manufacturing models with a small moment of inertia.

III. ROLL DAMPING

A. Description of Technique

The essentials of a roll-damping test are as follows: The model, attached to the rotating shaft, is spun by a sliding vane air motor. When the required spin rate has been achieved, a magnetic clutch disconnects the motor from the bearing, shaft and model unit. A magnetic tachometer provides an analog signal equal to the spin rate. This signal, together with time, is recorded on magnetic tape to provide a roll decay history. A digital computer program reduces these data to give the damping-in-roll derivative, C_{ℓ_p} as a function of the spin parameter, pd/2V.

The data reduction assumes that the spin decay is described by the following equation:

$$\dot{\bar{p}} - \left(\frac{C_{\ell_p} QSd^2}{2VIx} \right) \bar{p} = 0 \qquad (9)$$

where $\bar{p}$ is the spin parameter, pd/2V. Equation (9) may be integrated and solved for the roll-damping derivative, C_{ℓ_p} to give

$$C_{\ell_p} = - \left(\frac{2VIx}{QSd^2} \right) \left(\frac{1}{t} \right) \ln \left(\frac{\bar{p}_o}{\bar{p}} \right) \qquad (10)$$

where V, Ix, Q, S and d are the free-stream velocity, the axial moment of inertia, the dynamic pressure, the reference area and the reference length, respectively. Nonlinearities in roll damping (C_{ℓ_p} a function of $\bar{p}$) are handled in a fashion analogous to equation (5). The roll history is divided into n sub-intervals over which the damping mechanism is assumed linear. For a typical (i+1)th interval equation (10) becomes:

$$C_{\ell_p}(\bar{p}_i) = - \left(\frac{2VIx}{QSd^2} \right) \frac{1}{(t_{i+1} - t_i)} \ln \left(\frac{\bar{p}_i}{\bar{p}_{i+1}} \right) \qquad (11)$$

where

$$\bar{p}_i = \frac{\bar{p}_{i+1} + \bar{p}_i}{2}$$

B. Use of Air Bearings in Roll-Damping Tests

A recent development in roll-damping measurements is the replacement of ball bearings with air bearings. For full details, the reader is referred to reference (9). The air bearing is shown schematically in Figure 17. A single air source supplies air for both the journal and thrust surfaces. The air exhausts through radial holes through the bearing cover. All bearing surfaces are bronze-covered while all inner housing surfaces are hardened. The bearing gap is about 0.002 inches.

Bench tests (see Fig. 18) show that the logarithmic decrement of spin rate varies very little with load when an air bearing is used. This is an important characteristic for wind-tunnel tests since the drag and lift forces produce bearing loads during the run which are absent when the tare run is taken afterwards. The friction of a good ball bearing changes with load, and with wear, and makes it difficult to obtain accurate tare readings. However, ball bearings are still necessary under high load conditions (i.e. 100 lbs. if applied directly to the bearing).

In wind-tunnel evaluation tests the Basic Finner model was used because of the availability of roll-damping data. Figure 19 gives a comparison of roll-damping data obtained in the wind tunnel using an air bearing and in a free-flight aeroballistic range. It will be noted that the 5° angle of attack wind-tunnel data agree best with the range measurements. This seems reasonable in view of the likelihood of small angle of yaw occurring during a range flight.

IV. MAGNUS BALANCES

Dynamic forces and moments strongly influence the stability of spin stabilized projectiles. Of great importance are the cross derivatives C_{n_p} and C_{y_p} generally referred to as

Magnus force and moment derivatives (see ref. (10)).

Figure 20 shows the assembled Magnus balance and AN Spinner model. Some of the mechanical features of the balance are shown in Figure 21. Note that the model is attached to the balance by means of two ball bearings. Angular rate is measured by a magnetic tachometer located at the forward portion of the balance. Spin is imparted to the model by means of an air turbine located aft of the rear gage section. A passage through the sting provides air to spin the model drive turbine. In operation the model is spun to the required rate, the air supply is terminated, and gage readings are sampled and recorded on magnetic tape. Data reduction is accomplished exactly as in a static-stability test. Results are presented as side force and moment coefficients, C_y and C_n, versus spin parameter.

At present, four Magnus balances of this design have been constructed--three for the NOL supersonic tunnels and one which was used for an NOL test in the 7 x 10-foot DTMB transonic facility.

The problem encountered in constructing these balances is to provide sufficient sensitivity in yaw without greatly reducing balance stiffness. Figures 22 and 23 show the top and side views of the forward gage section of a Magnus balance, respectively. As the balance is subject to yaw loads, a secondary bending is induced in the eccentric column. Thus, this unit acts as a mechanical amplifier. The sensitivity of the yaw gages is about 9 times that of the pitch gages. This design then represents a threefold increase in sensitivity over the older and more conventional NOL steel Magnus balances. An additional factor of 3 was obtained by making the balance of aluminum instead of steel.

The Magnus data of Figure 24 are typical. These data are plotted versus the spin parameter, pd/2V. For comparison purposes it should be noted that the normal force coefficient is 1.3, or about 10 times the value of the side force, or Magnus, coefficient. With this balance, Magnus forces and moments can be measured at small angles of attack, of the order of 2 to 5 degrees.

REFERENCES

(1) Thompson, J. S. and Fail, R. A., "Oscillatory Derivative Measurements on Sting Mounted Wind Tunnel Models," Royal Aircraft Establishment Report No. 2668, 1962

(2) Welsh, C. J. et al, "Dynamic Stability Tests in Hypersonic Wind Tunnels and at Large Model Amplitudes," AEDC-TR-59-24, 1959

(3) Reitz, J. R. and Milford, F. J., "Foundations of Electromagnetic Theory," Addison-Wesley Publishing Company, Reading, Mass., 1960

(4) Regan, F. J., Ogan, R. and Holmes, J., "Variable Reluctance Transducer for Use in Wind Tunnel Pitch-Damping Measurements," NOLTR 65-9, in publication

(5) Orlik-Ruckemann, K. J., "Wind Tunnel Measurements of Dynamic Derivatives," Second Edition, National Research Council of Canada, 1963

(6) Jaffee P., "Obtaining Free-Flight Dynamic Damping of an Axially Symmetric Body in a Conventional Wind Tunnel," Technical Report 32-544, Jet Propulsion Laboratory, 1964

(7) Tobak, M., "Derivatives of Cones at Supersonic Speeds," NACA TN 3788, Sep 1956

(8) Nicolaides, J. D. and Boltz, R. E., "On the Pure Rolling Motion of Winged and/or Finned Missiles in Varying Supersonic Flight," BRL Report 799

(9) Regan, F. J. and Horanoff, E., "Wind Tunnel Model Support Using a Gas Bearing," NOLTR 65-14, in publication

(10) Platou, A., "Magnus Characteristics of Finned and Non-Finned Projectiles," AIAA Journal Vol. 3, No. 1, Jan 1965

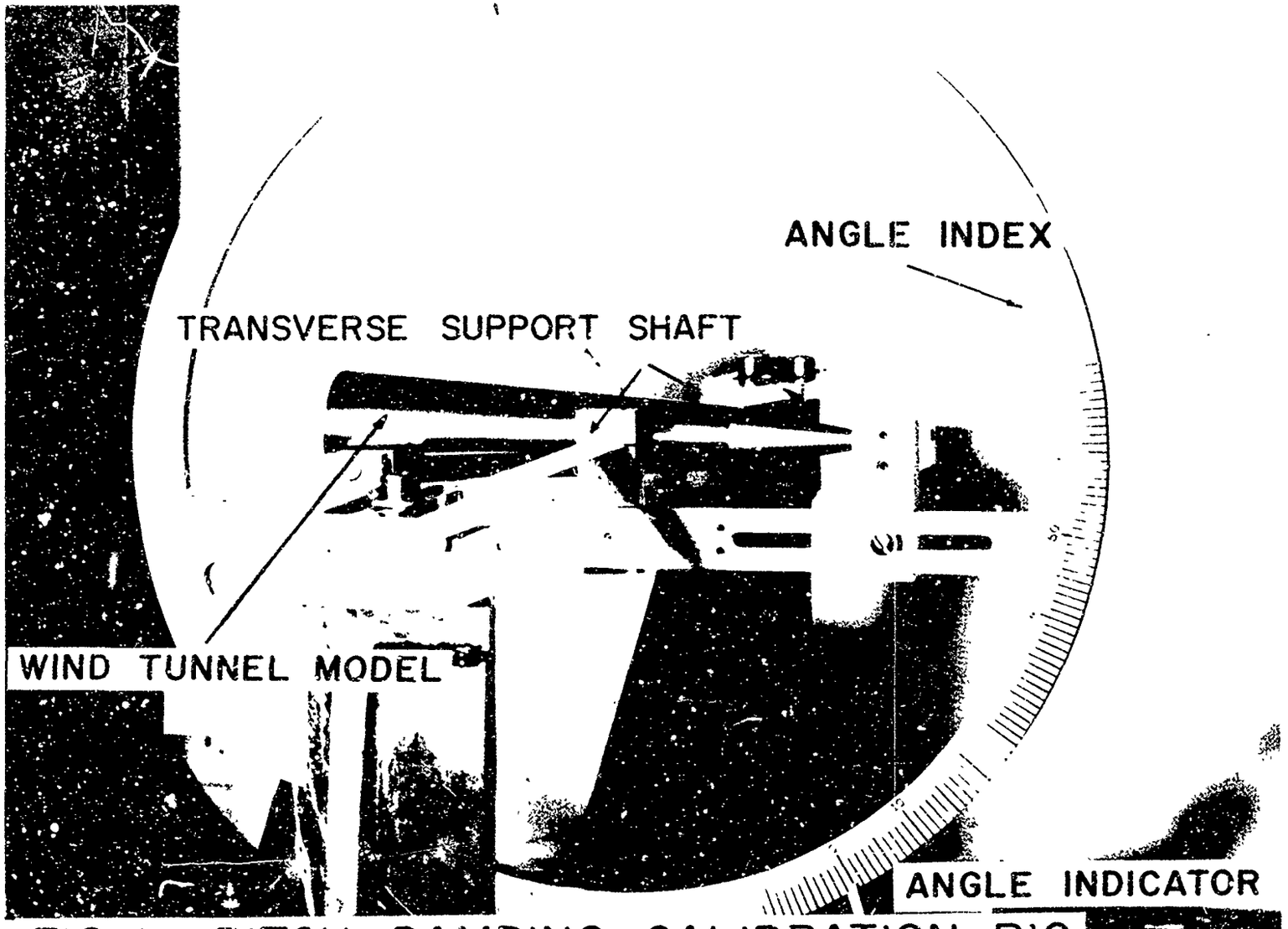

FIG. 1 PITCH-DAMPING CALIBRATION RIG

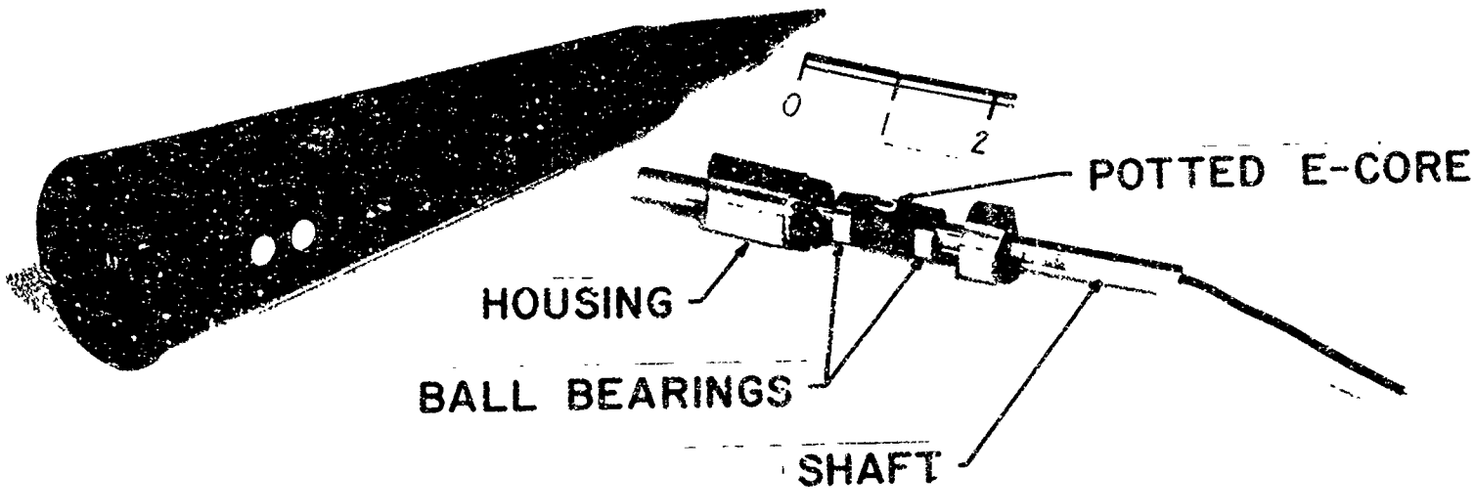

FIG. 2 MODEL & INSTRUMENTED SUPPORT SHAFT

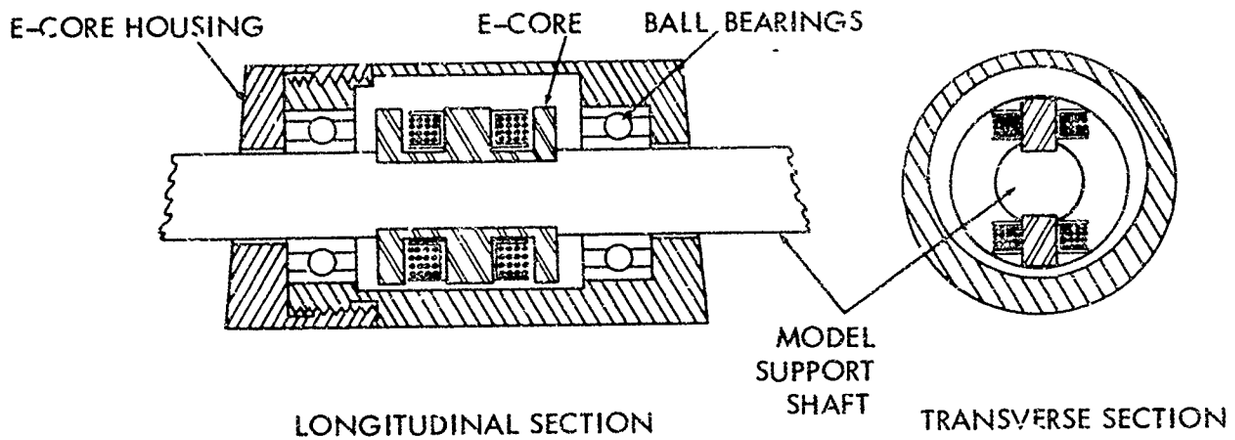

FIG. 3 CROSS-SECTIONS OF E-CORE

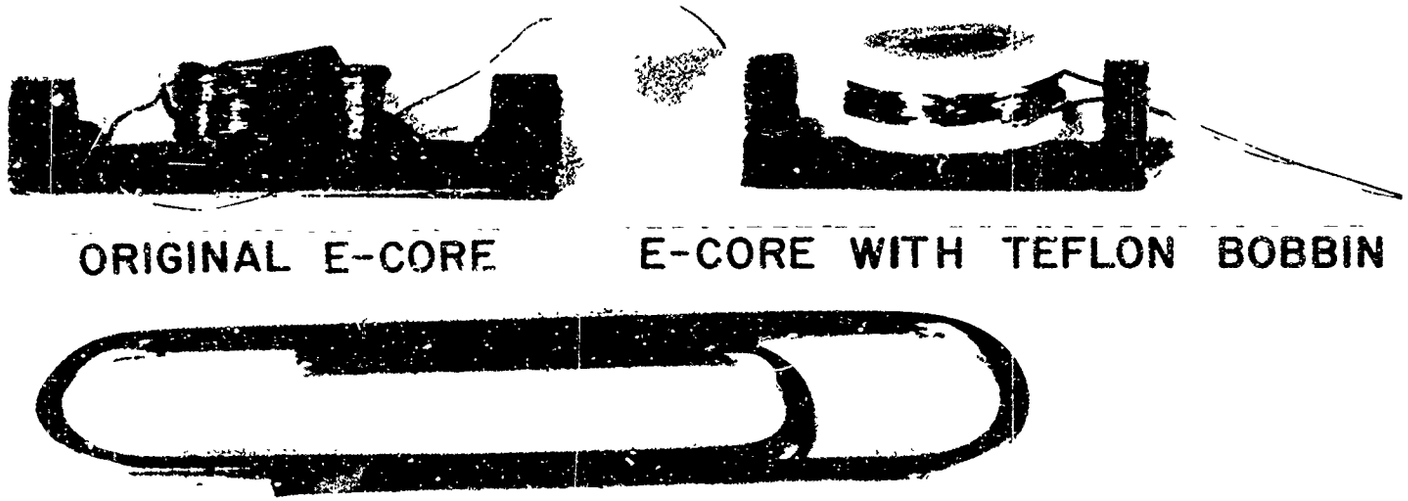

FIG. 4 E-CORE DEVELOPMENT

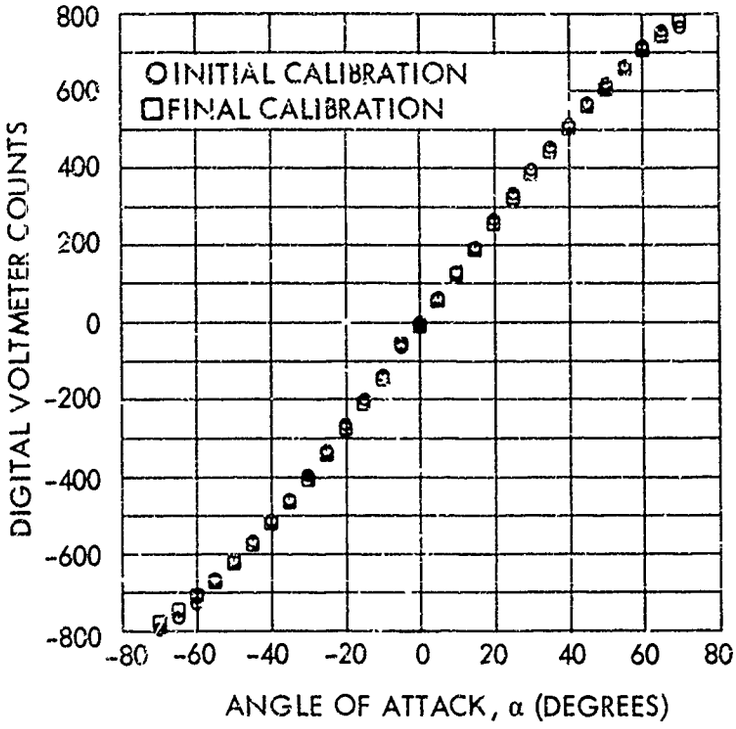

FIG. 5 E-CORE CALIBRATION - DIGITAL VOLTMETER COUNTS VERSUS ANGLE OF ATTACK

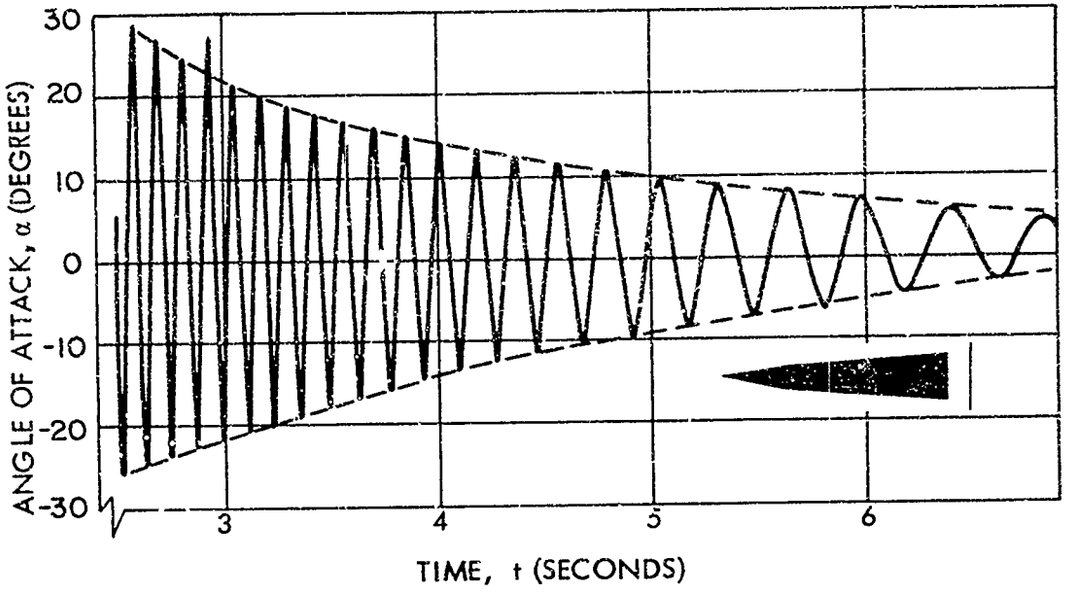

FIG. 6 E-CORE RECORD OF MODEL OSCILLATORY MOTION

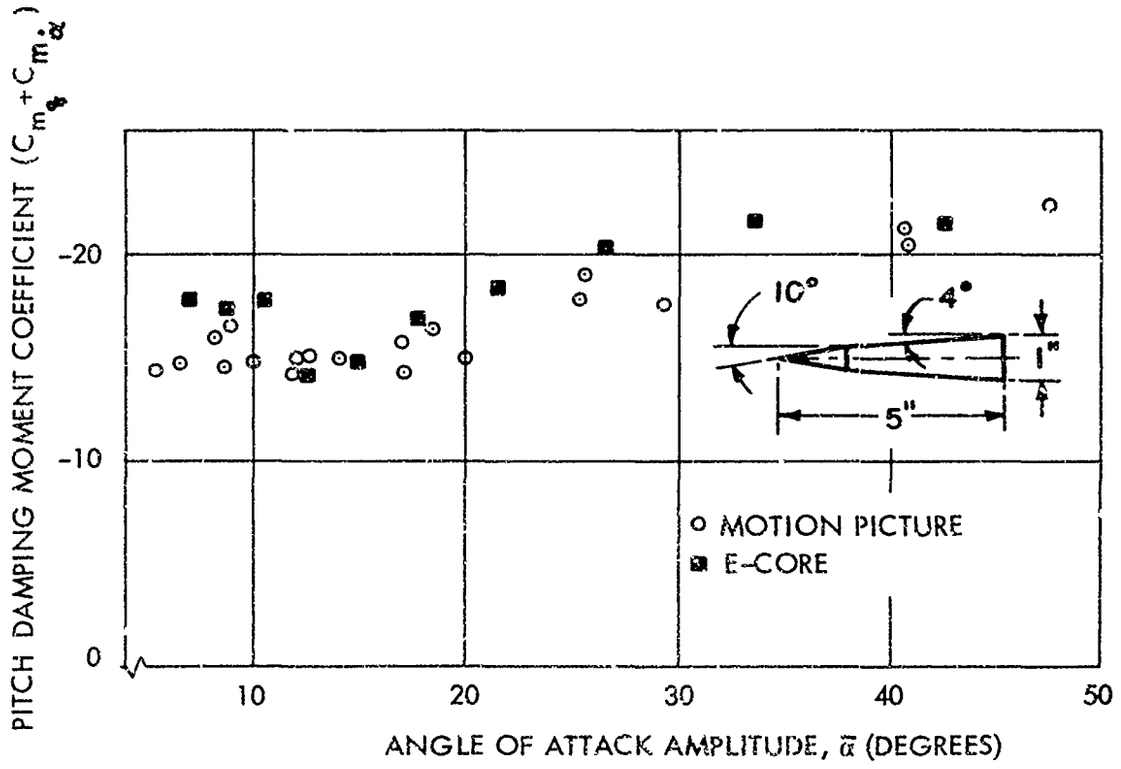

FIG. 7 PITCH DAMPING MOMENT COEFFICIENT VERSUS ANGLE OF ATTACK AT A MACH NUMBER OF 2.28

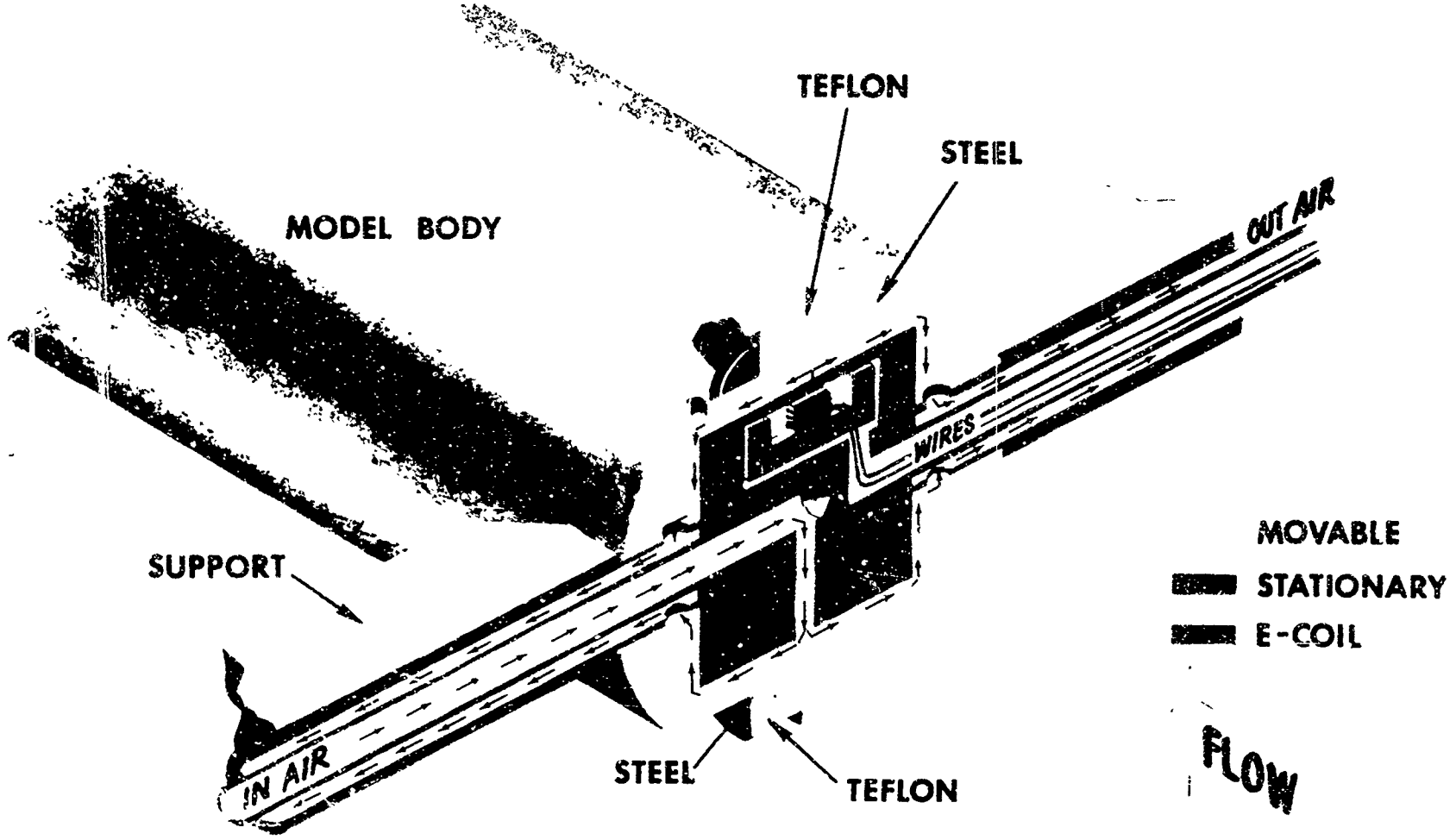

FIG. 8 PITCH DAMPING AIR BEARING WITH ELECTRICAL READOUT

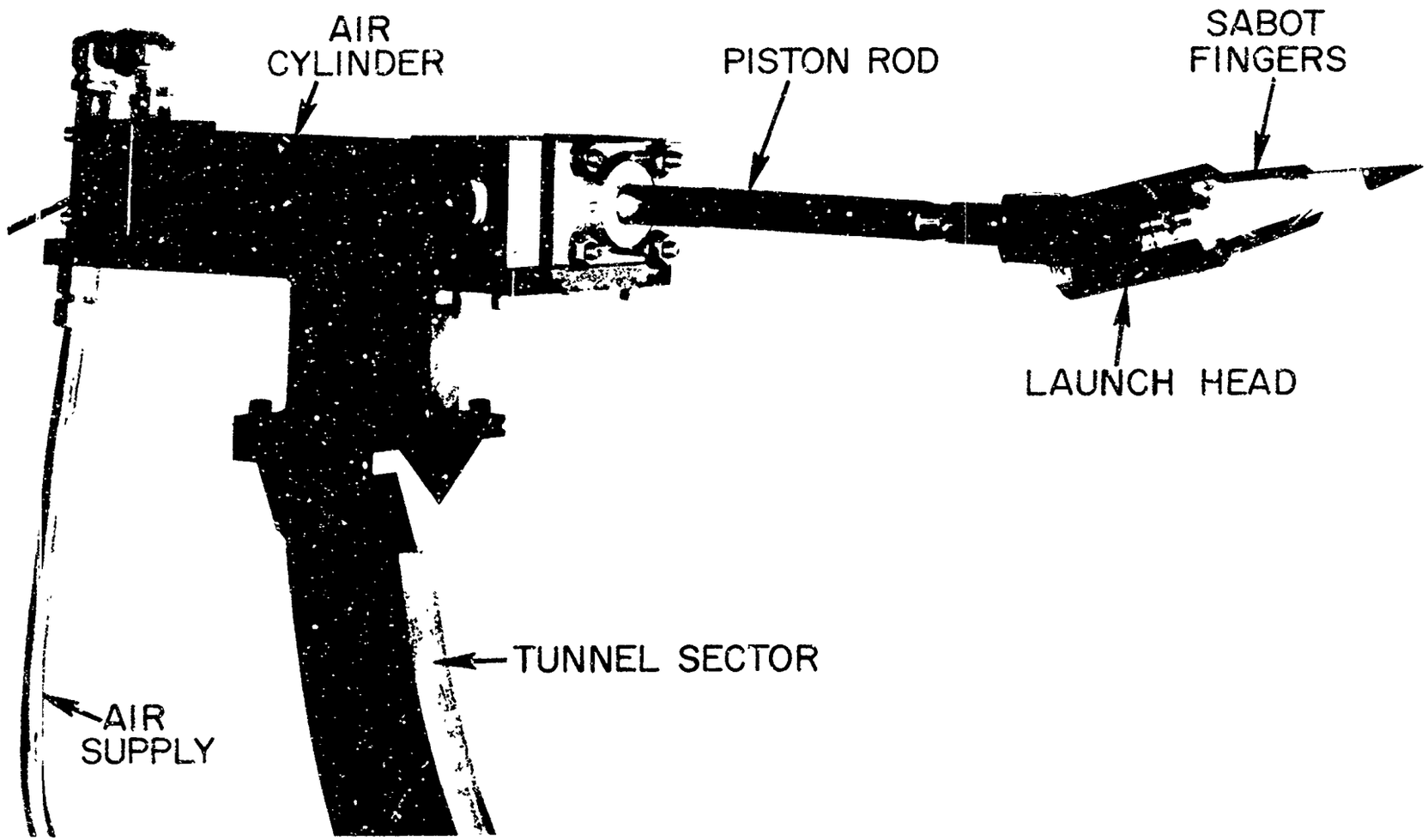

FIG. 9 SUPERSONIC WIND TUNNEL FREE FLIGHT LAUNCH SYSTEM

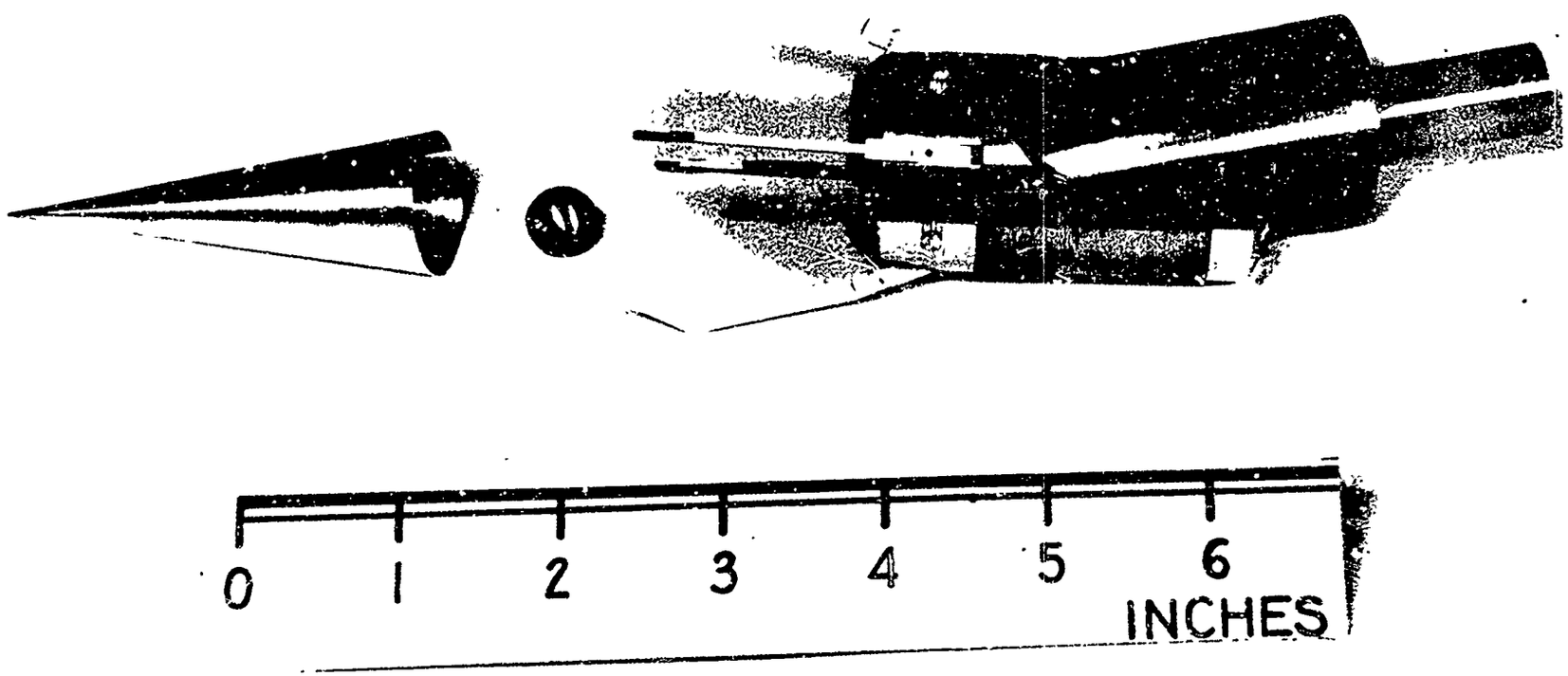

FIG. 10 MODEL, BALLAST & LAUNCH HEAD USED IN SUPERSONIC TUNNELS

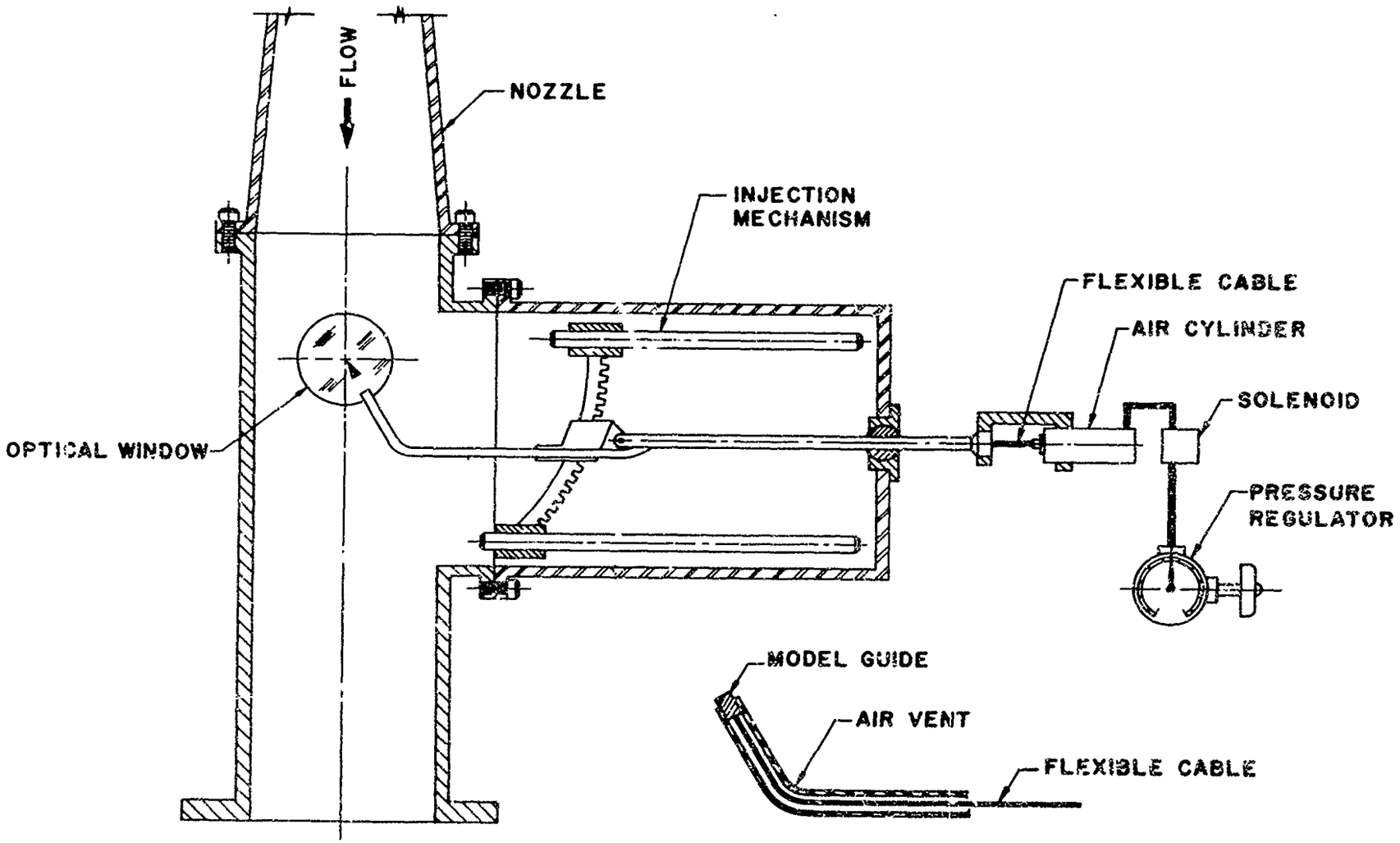

FIG. 11 MACH 18 FREE FLIGHT LAUNCHER
HYPERSONIC TUNNEL NO. 4

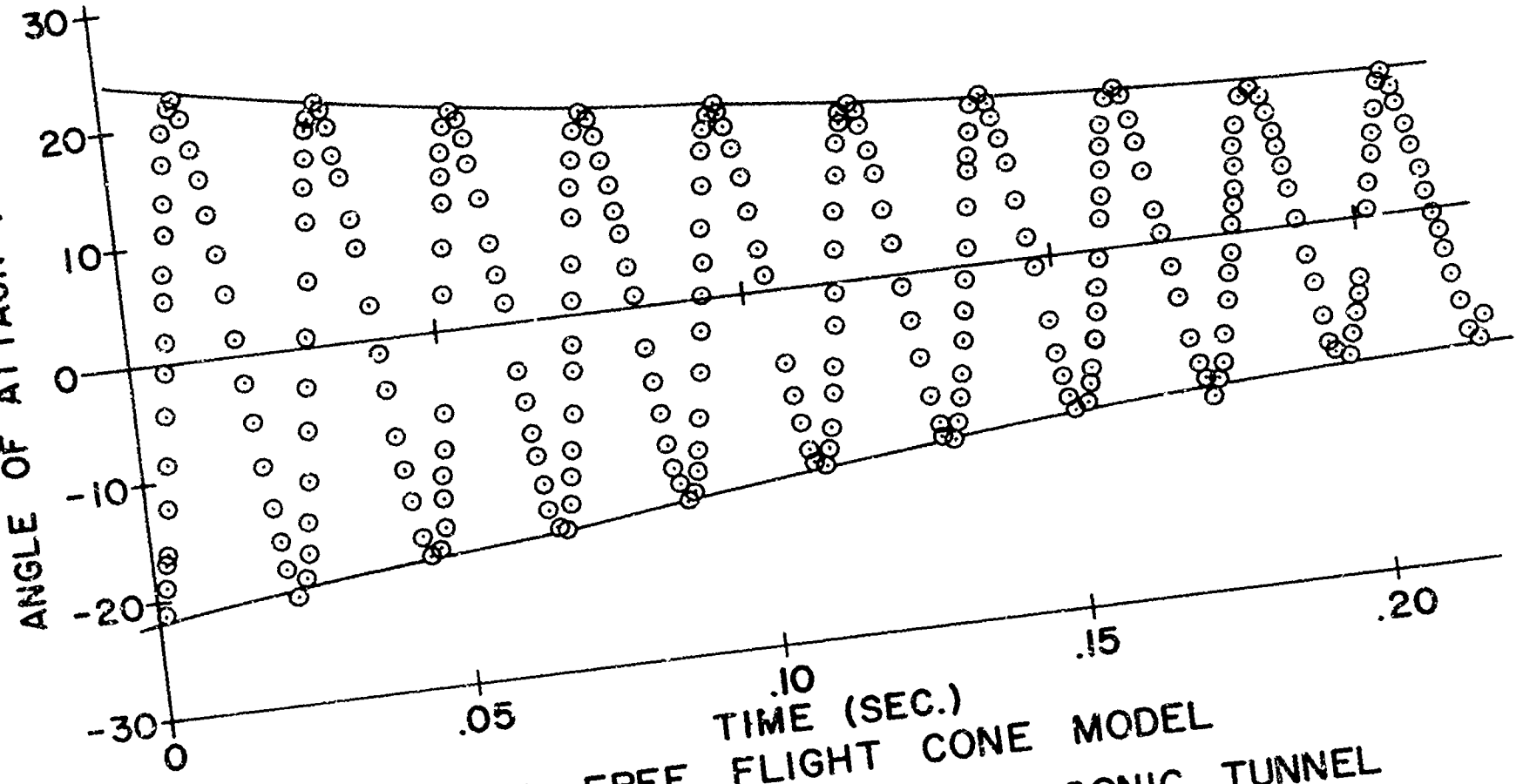

FIG. 12 TYPICAL FREE FLIGHT CONE MODEL OSCILLATIONS IN THE SUPERSONIC TUNNEL

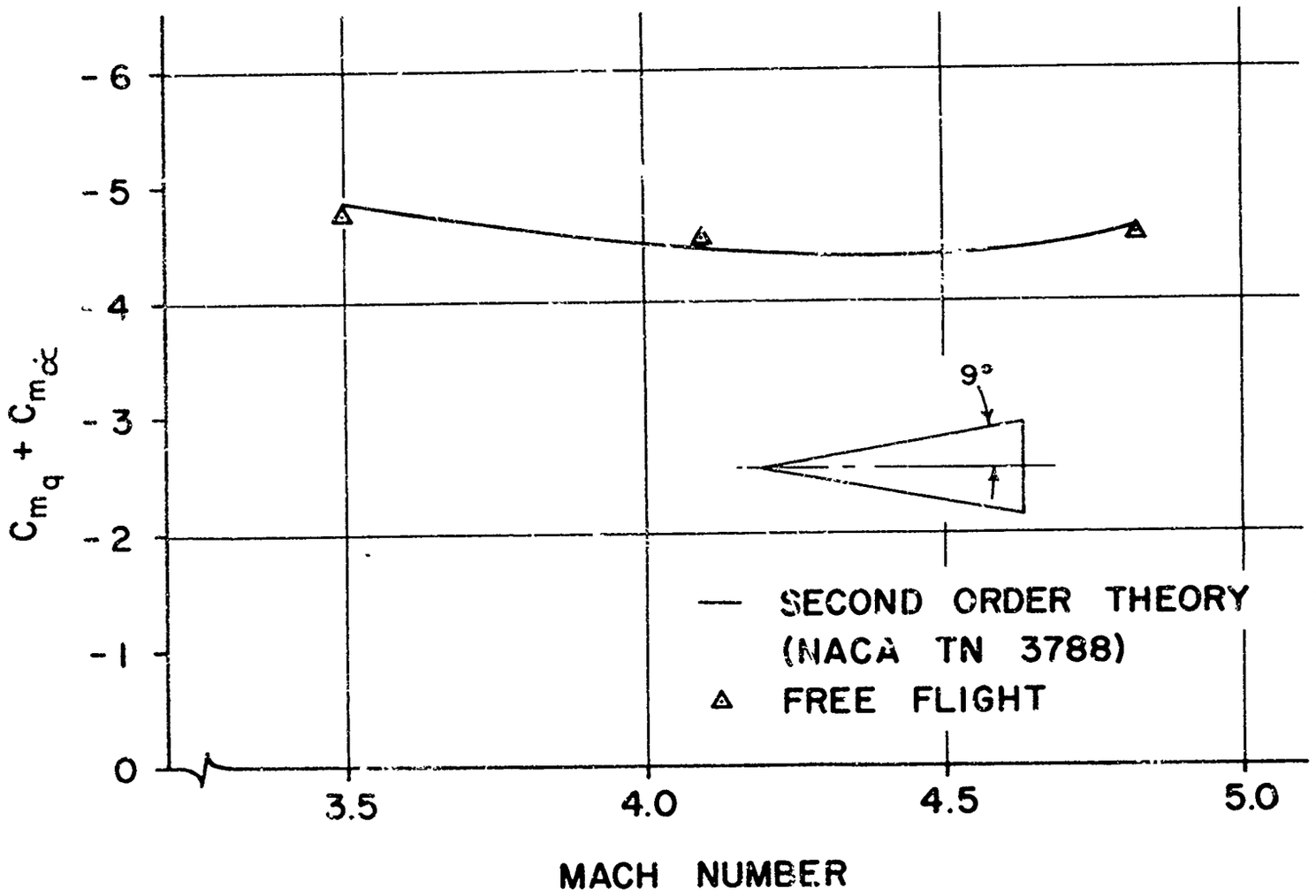

FIG. 13 COMPARISON OF FREE FLIGHT PITCH DAMPING DERIVATIVES WITH SECOND ORDER THEORY FOR A CONE

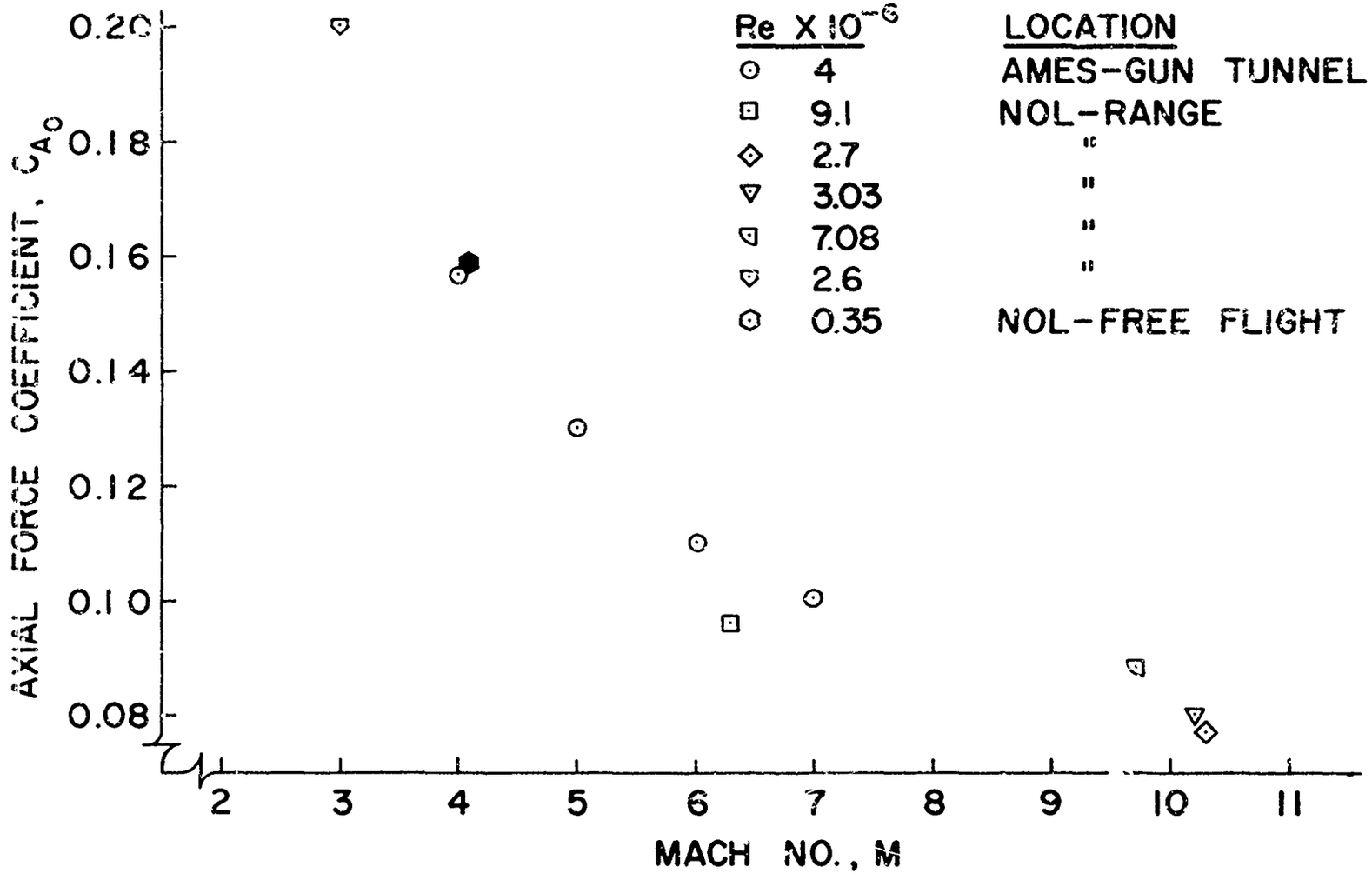

FIG. 14 INTER-FACILITY COMPARISON OF AXIAL FORCE COEFFICIENT VERSUS MACH NUMBER FOR A 9° HALF ANGLE CONE

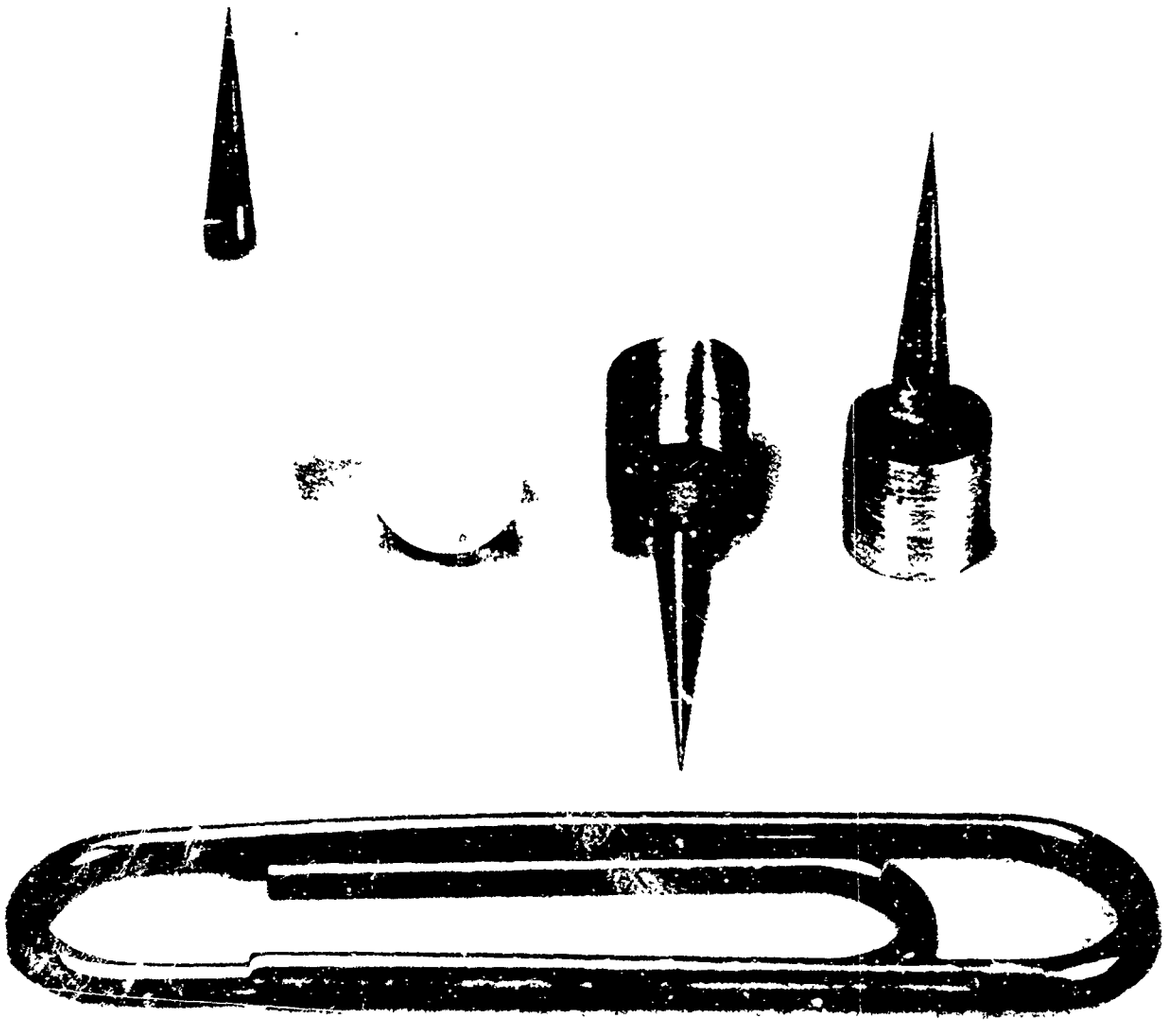

FIG. 15 HYPERSONIC TUNNFL NO. 4 FREE FLIGHT MODEI S

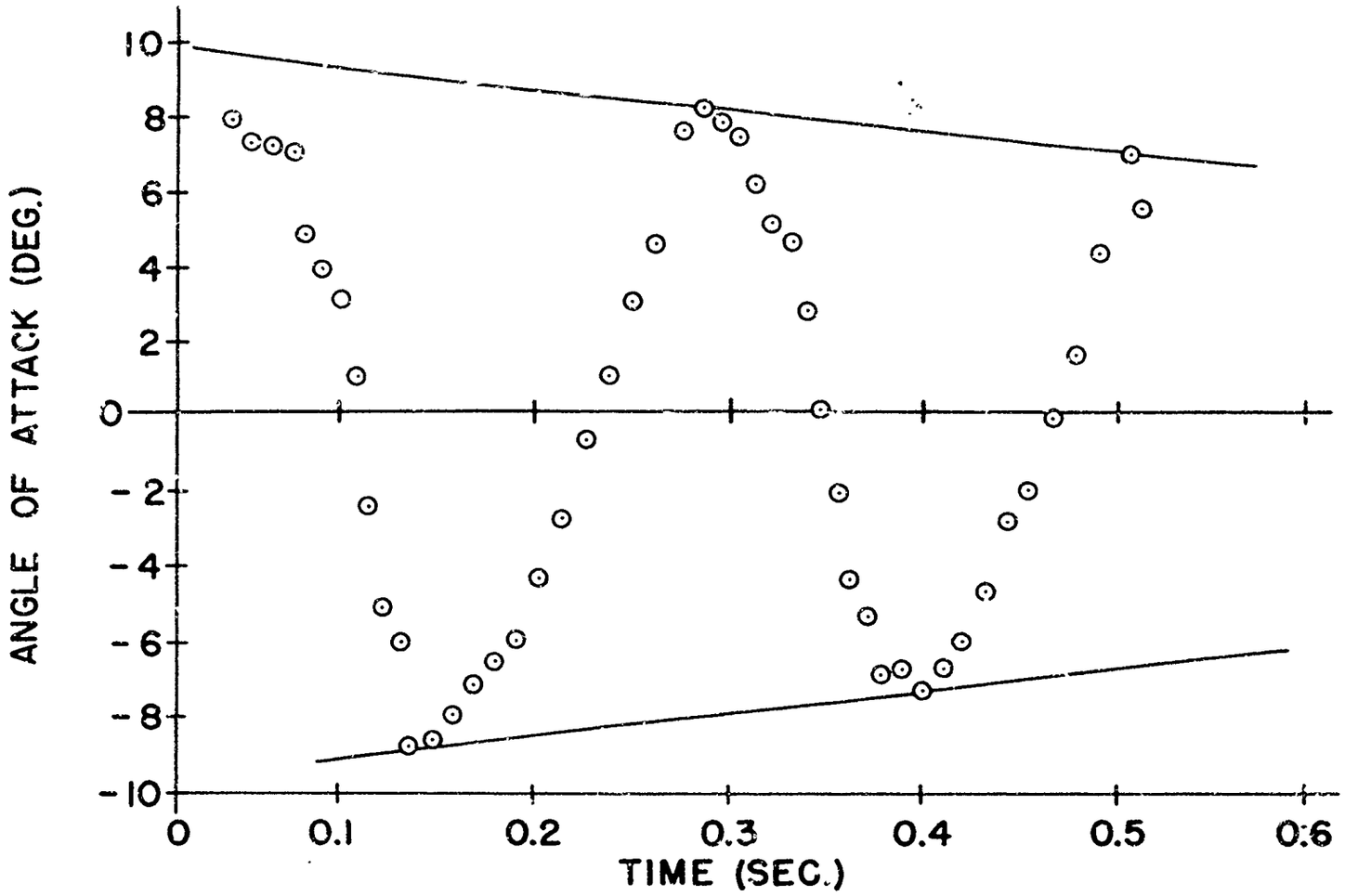

FIG 16 TYPICAL FREE FLIGHT OSCILLATIONS OF RING WING MODEL IN HYPERSONIC TUNNEL AT MACH 18

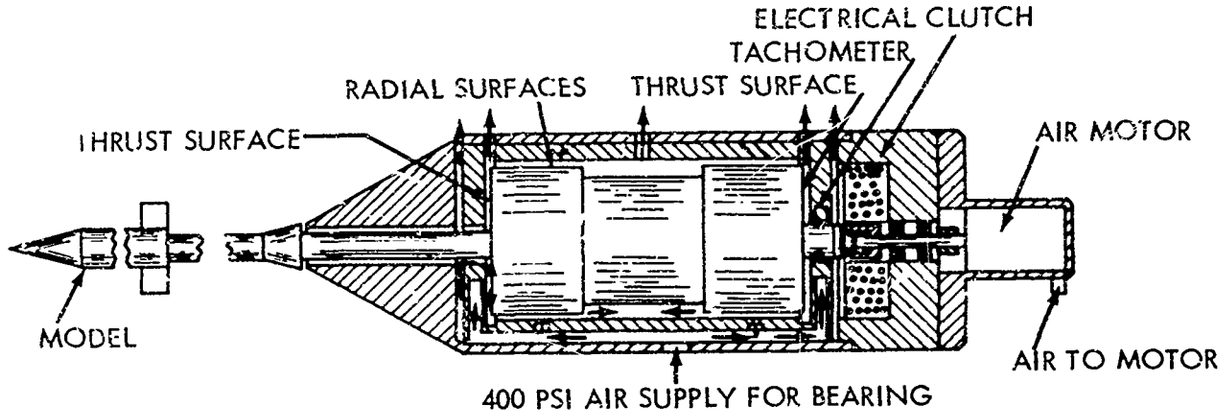

FIG. 17 AIR BEARING ROLL DAMPING MECHANISM

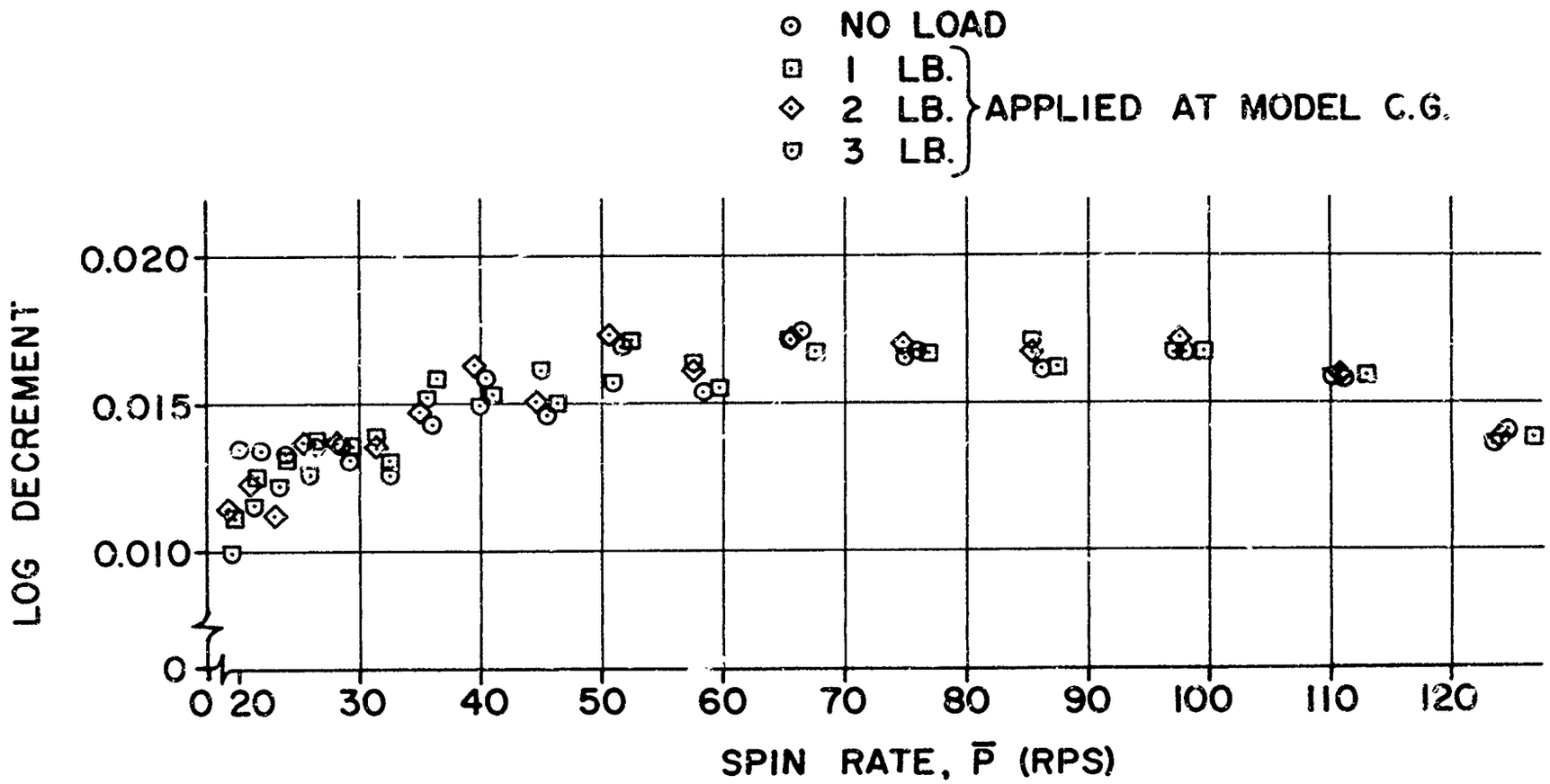

FIG. 18 LOG DECREMENT VERSUS SPIN RATE FOR AN AIR BEARING UNDER VARYING LOADS

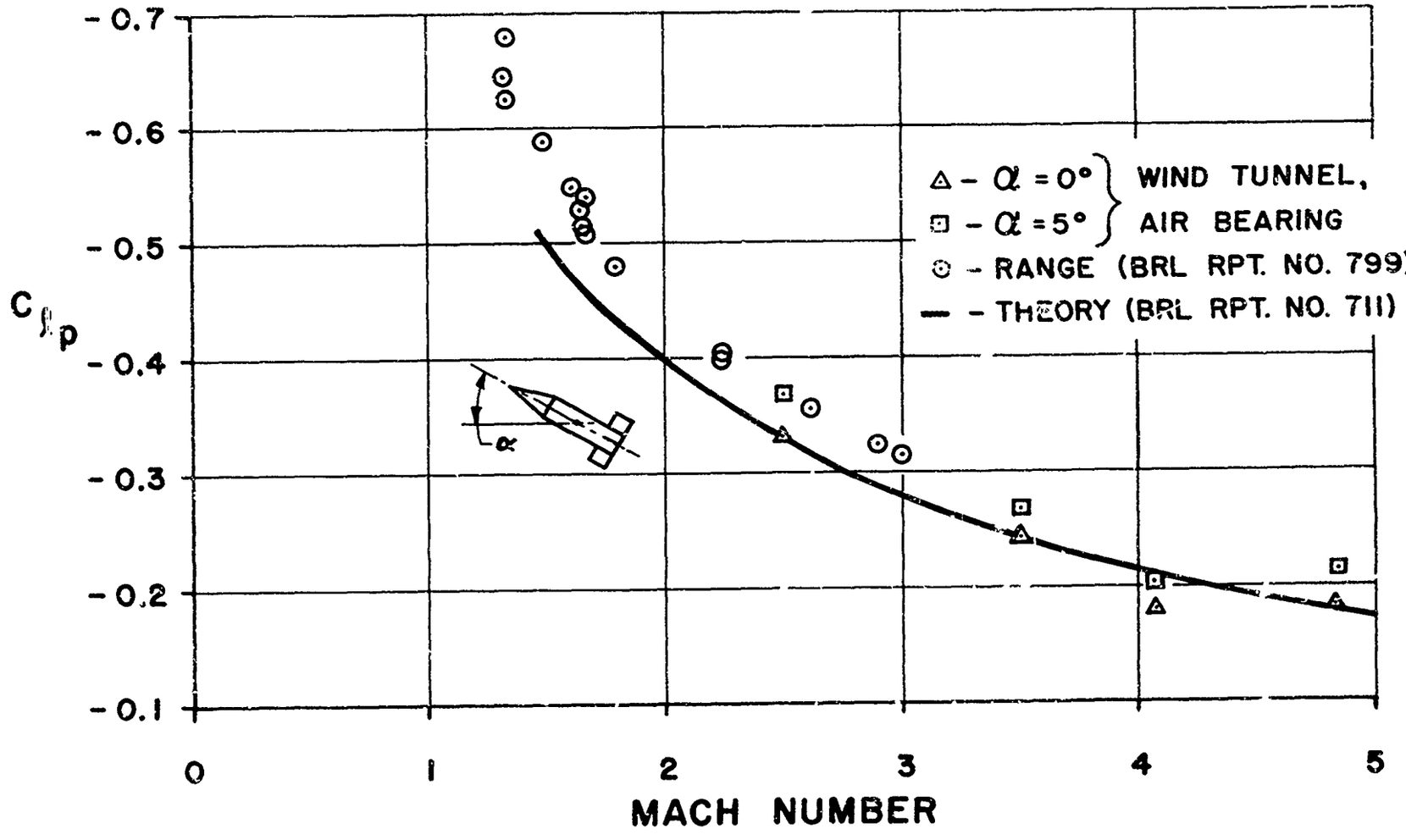

FIG. 19 ROLL DAMPING COEFFICIENT VS. MACH NUMBER FOR BASIC FINNER

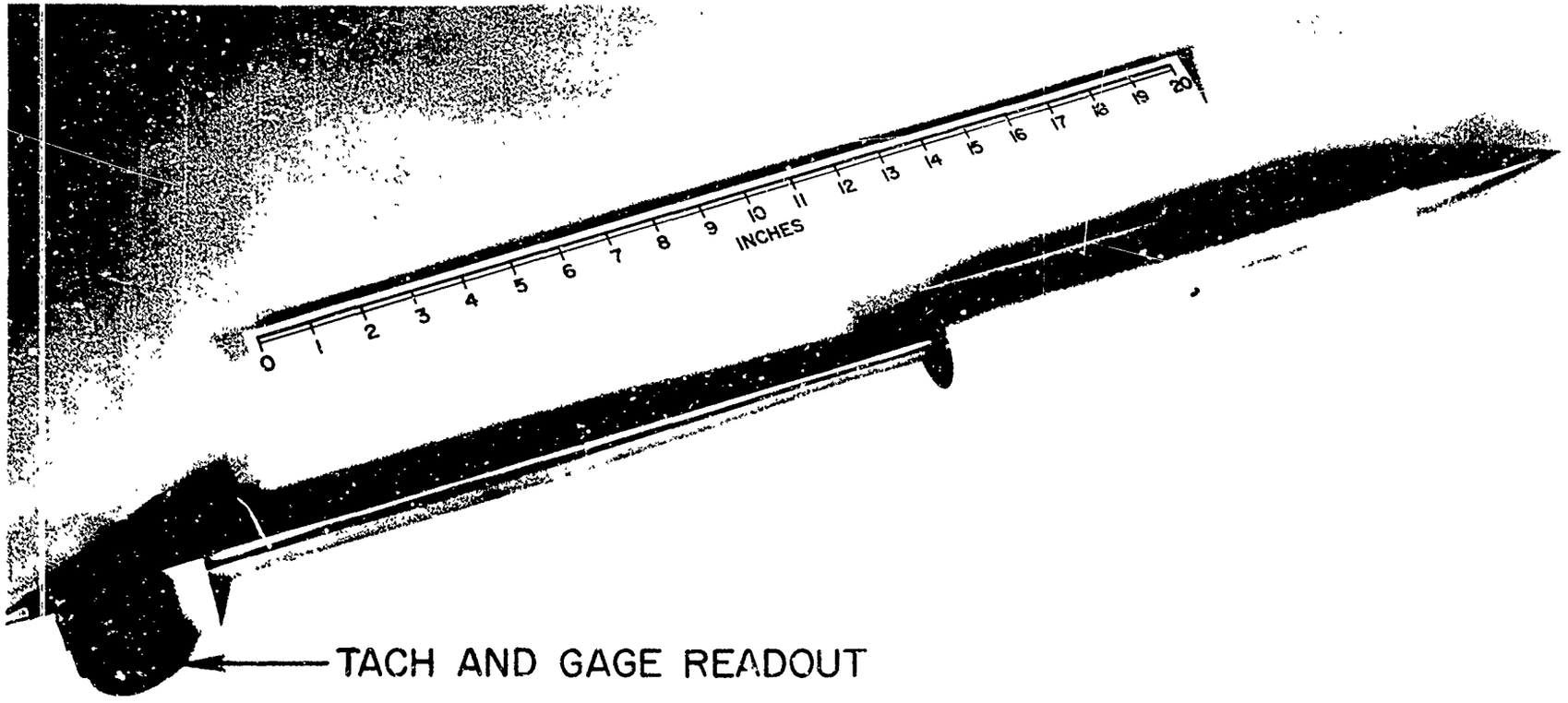

FIG. 20 AN SPINNER MODEL ON MAGNUS BALANCE

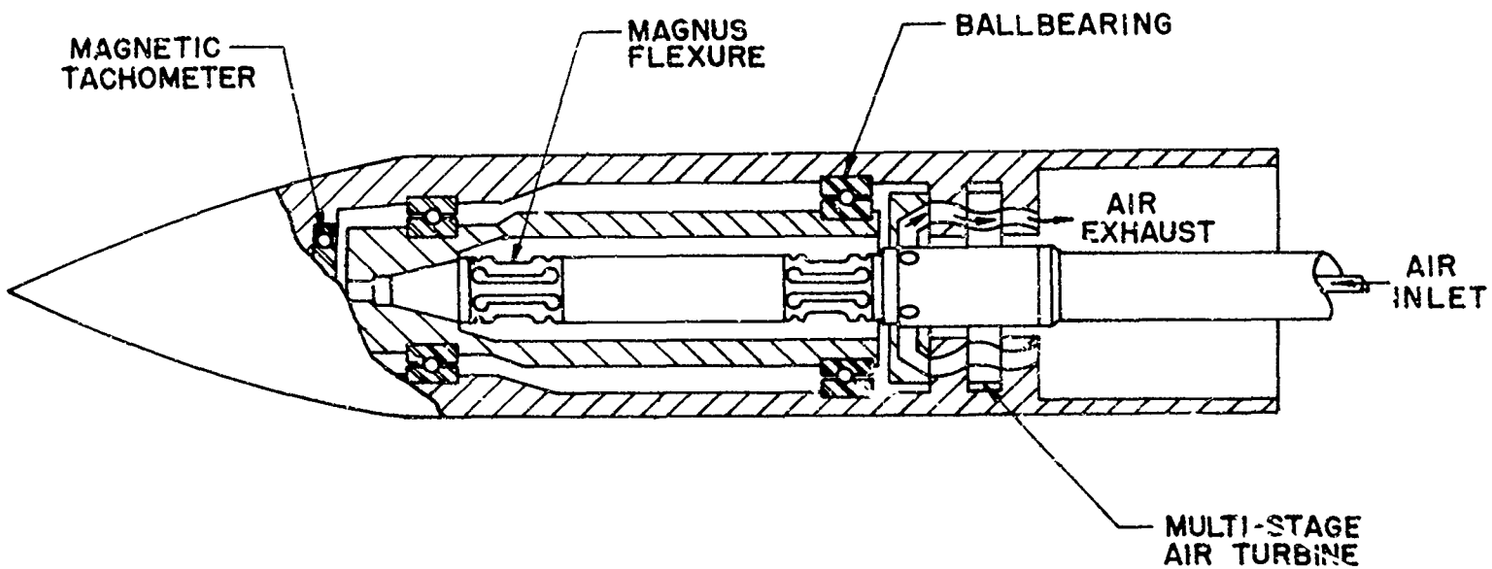

FIG. 21 MAGNUS BALANCE DETAILS

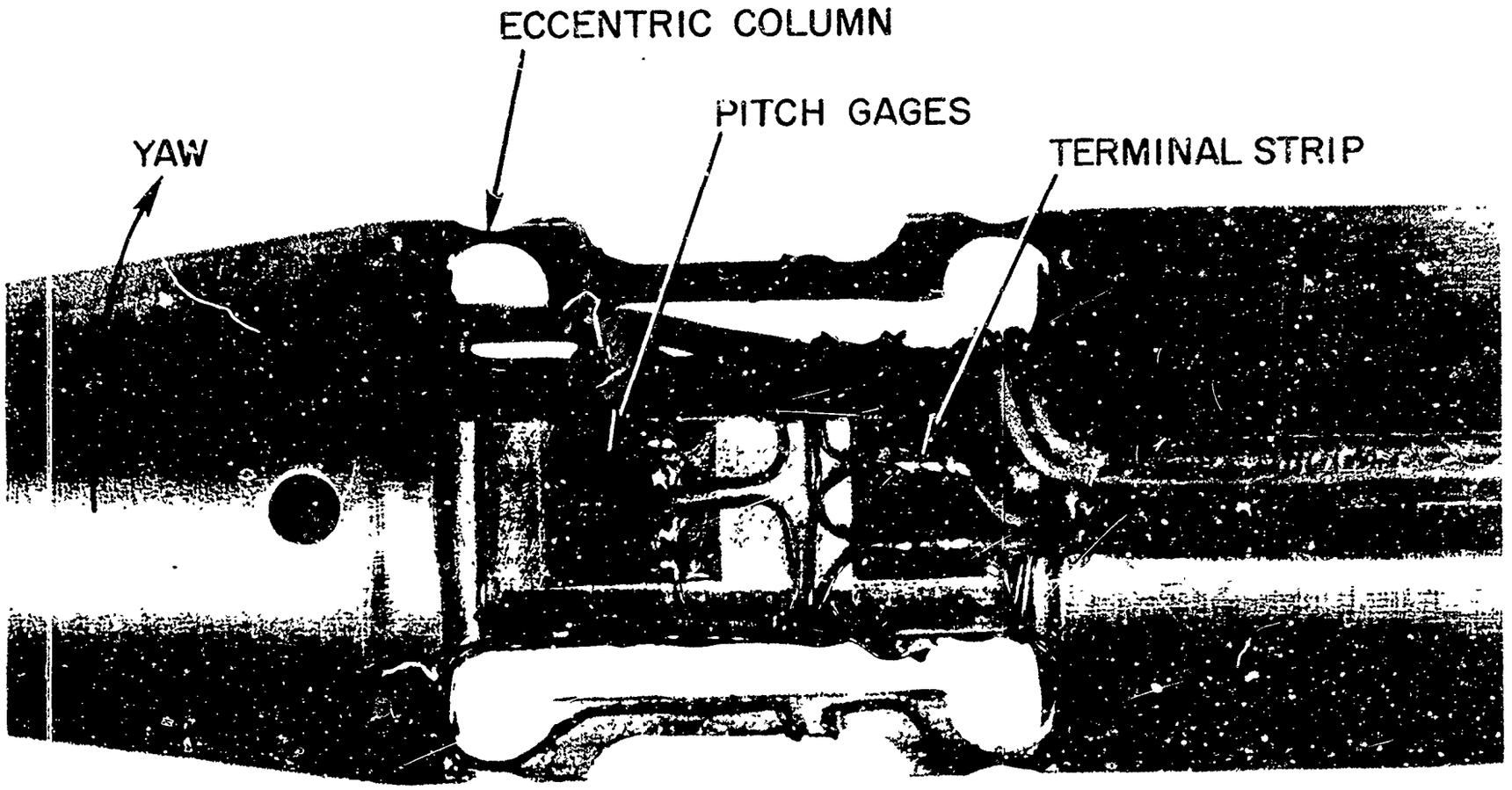

FIG. 22 TOP VIEW OF MAGNUS BALANCE

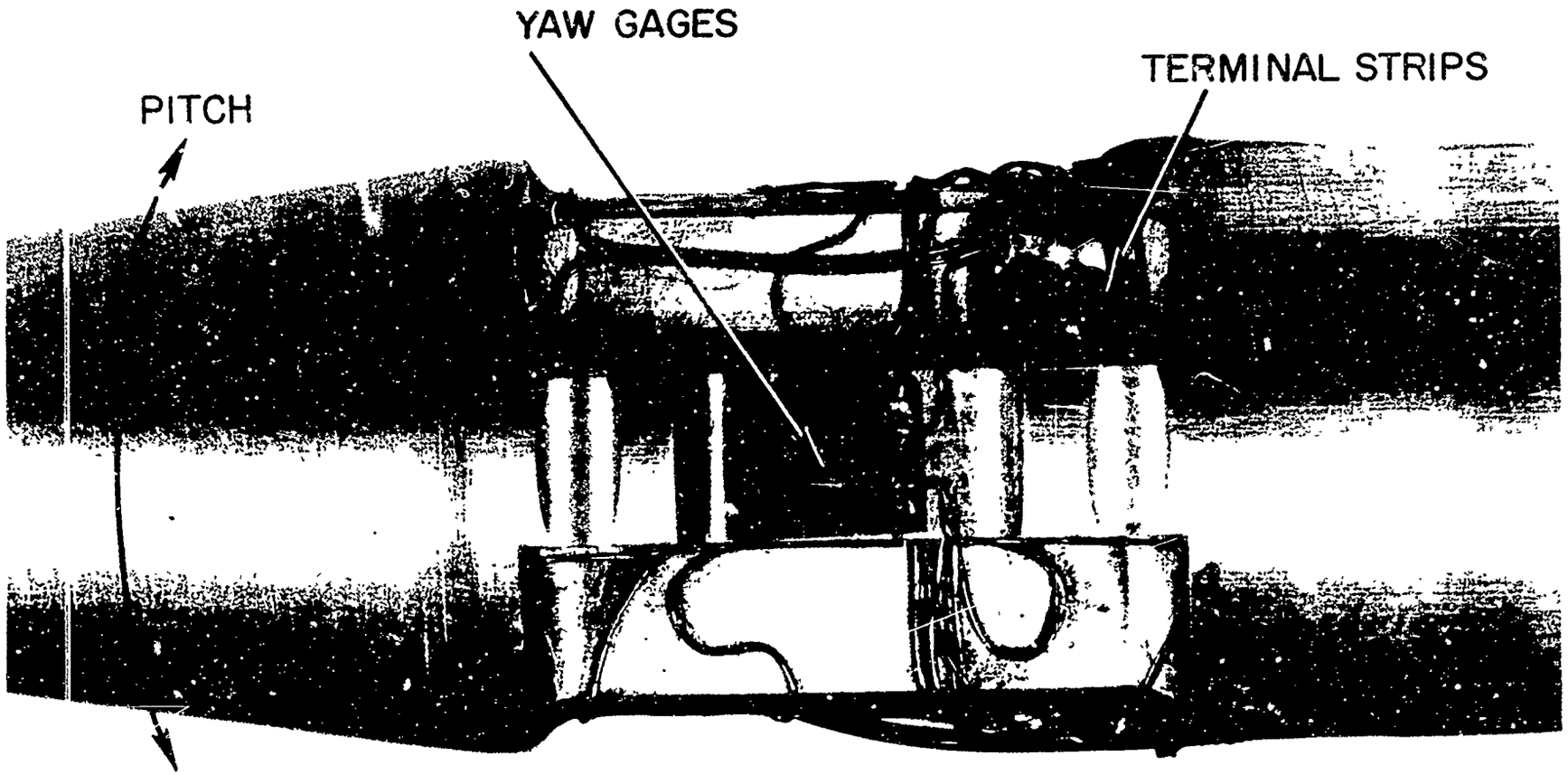

FIG. 23 SIDE VIEW OF MAGNUS BALANCE

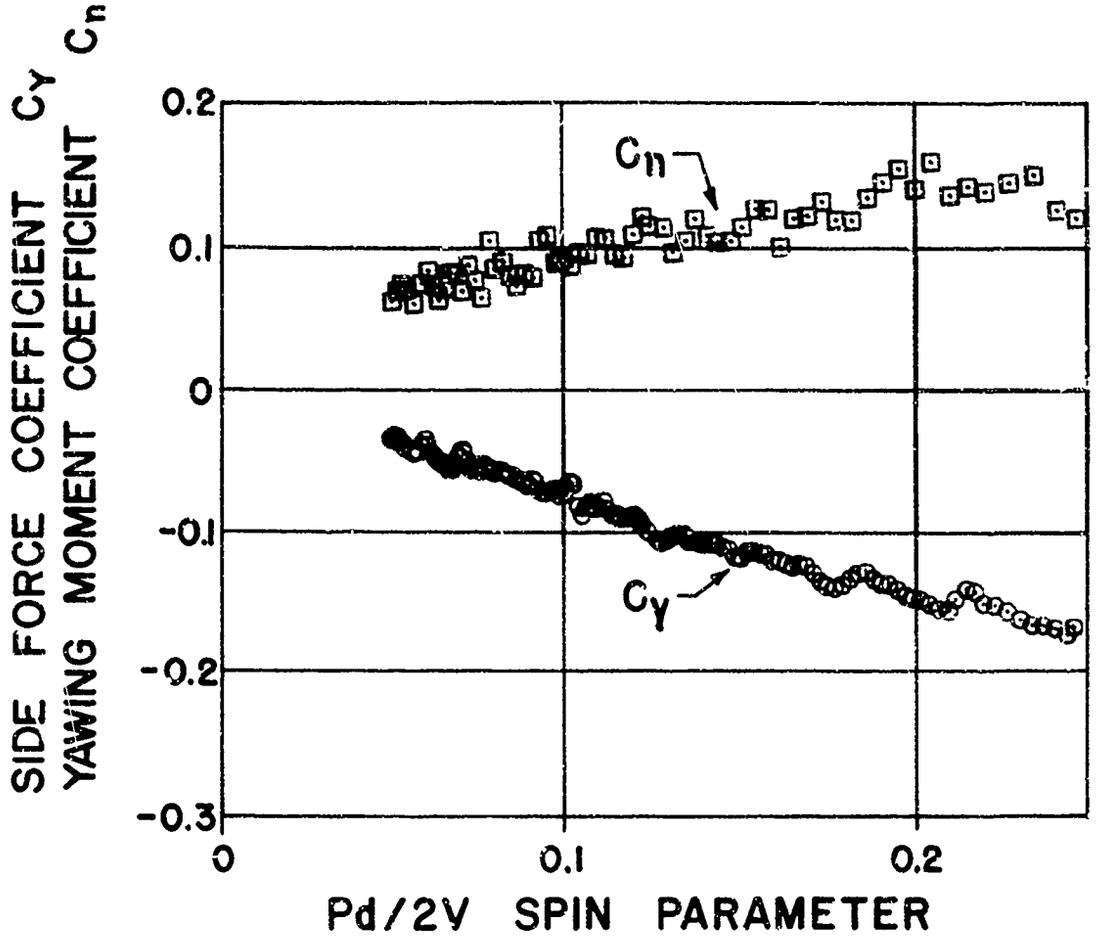

FIG. 24 SIDE FORCE AND YAWING MOMENT COEFFICIENTS VERSUS SPIN PARAMETER AT A MACH NUMBER OF 0.8 AND AN ANGLE OF ATTACK OF 14 DEGREES FOR THE AN SPINNER

DISCUSSION

A. Platou:

I was interested in some of your Magnus measurements and also on what you plan to do in the future on it. I was wondering if you have any plans for running any configurations with fins such as the basic spinner?

F. Regan:

Yes, we do; but it isn't the basic spinner at present. We have plans to run a bomb, a cruciform bomb, a bomb with a cruciform tail taking Magnus data on this using these balances.

A. Platou:

I would be interested in seeing this data once you get it. I would like to compare it with some of the theories which Benton and I have come up within the last year or so on Magnus forces with fins.

V. Peterson:

I think on your second slide or so I was curious of a result where you showed a typical angle of attack history with quite variable frequency. I was wondering if the dynamic pressure was variable there or what was going on. Do you recall that?

F. Regan:

Yes, I recall the slide. I don't think the dynamic pressure was varying. I would explain it as nonlinearities in the static pitching moment of the biconic. In other words, the frequency is higher when the model is moving through large angles then it decreases as it moves to lower angles.

V. Peterson:

I think the results showed it was opposite from that.

F. Regan:

It was? No, I don't think so.

C. Schueler:

I thought possibly Mr. Platou was going to comment on his use of solid state strain gages for measuring Magnus force. I would like to ask him whether he would mind commenting on using those gages versus a kind of a new adjustment to the gage section. Second, I would like to ask what was the rpm rate for your Magnus model?

F. Regan:

Up to about 500 rps.

C. Schueler:

So you don't really need bearing cooling.

A. Platou:

On the use of solid state strain gages for measuring Magnus forces and moments, I would say that using the solid state strain gages makes the manufacture of the beam much simpler since it just means making a four component strain gage balance; that is two pitching moments, for the pitching forces, and two yawing moments for the yawing forces. It is not necessary to go to the thin gage section such as NOL has. Of course, now, in using the solid state strain gages it requires a little bit more finesse in temperature compensating; however, by being a little bit more particular and taking a little more time, you can temperature compensate the solid state strain gages. I would also like to mention that we have taken just a conventional beam and used conventional gages on it and then amplified the signal using solid state amplifiers and this too seems to be ample for getting Magnus moments.

INFLUENCE OF BOUNDARY-LAYER TRANSITION ON DYNAMIC STABILITY AT HYPERSONIC SPEEDS*

by

L. K. Ward

ARO, Inc.

SUMMARY

The results of a brief investigation of the effects of boundary-layer transition on the damping characteristics of a 10-deg half-angle cone are presented. The data were obtained in the Gas Dynamic Wind Tunnels, Hypersonic (E) and (C) of the von Kármán Gas Dynamics Facility. The tests were conducted at Mach numbers 5, 6, 7, 8, and 10 at Reynolds numbers, based on model length, ranging from 2 to 15 million. The data were measured at model oscillation amplitudes of about ±1.8 deg using free oscillation and forced oscillation cross flexure pivot balances.

Results obtained at all Mach numbers tested show that the damping derivatives are maximum when transition is near the model base. In addition, the results show the trend of increasing dynamic stability with Mach number when the product of the free-stream Mach number and the cone half-angle is greater than one, as some theories predict.

*The research reported in this paper was sponsored by the Arnold Engineering Development Center, Air Force Systems Command, United States Air Force, under contract AF 40(600)-1000 with ARO, Inc. Further reproduction is authorized to satisfy the needs of the United States Government.

CONTENTS

ILLUSTRATIONS

NOMENCLATURE

A	Base area, reference area, ft^2
C_m	Pitching-moment coefficient, pitching moment/$q_\infty Ad$
C_{m_α}	Rate of change of pitching-moment coefficient with angle of attack $(\partial C_m/\partial\alpha)_{\alpha \to 0}$, 1/rad
C_{m_q}	$\left[\partial C_m/\partial(qd/2V_\infty)\right]_{q \to 0}$
$C_{m_{\dot\alpha}}$	$\left[\partial C_m/\partial(\dot\alpha d/2V_\infty)\right]_{\dot\alpha \to 0}$
	Damping-in-pitch derivatives, 1/rad
d	Model base diameter, reference length, in. or ft
ℓ	Actual model length, in.
ℓ_s	Model surface length, in.
M_∞	Free-stream Mach number
p_b	Model base pressure, psia
p_∞	Free-stream static pressure, psia
q	Pitching velocity, rad/sec
q_∞	Free-stream dynamic pressure, psfa
Re_ℓ	Reynolds number base on model length
V_∞	Free-stream velocity, ft/sec
x_{cg}	Distance from model nose to pivot axis, in.
x_t	Model surface distance to beginning of transition, in.
α	Angle of attack, deg
$\dot\alpha$	Time rate of change of angle of attack, rad/sec
δ	Cone semi-vertex angle, rad or deg
θ	Oscillation amplitude, deg

ψ	Model nose radius to base radius ratio
ω	Oscillation frequency, rad/sec
$\frac{\omega d}{2V_\infty}$	Reduced frequency parameter, rad

INTRODUCTION

During the past several years increased emphasis has been placed on obtaining dynamic stability measurements, especially at hypersonic speeds. The means for obtaining dynamic stability measurements at these speeds has been provided at several of the ground test facilities throughout the country.

Comparisons of dynamic stability derivatives obtained from theoretical predictions, ground test results, and flight data for the cone-cylinder-flare-type re-entry vehicle have not been good. The discrepancies may be attributed to limited theoretical methods, the inherent nonlinear characteristics of this type configuration, and inadequate methods for treating the region of flow separation ahead of the flare. The more recent generation of re-entry vehicles (cones or blunted cones) have, in most cases, simplified the aerodynamists' problems in the application of theories and, in addition, have yielded better correlation between flight, ground test, and theoretical values.

The purpose of this paper is to present the results of dynamic stability tests that were conducted at Mach numbers 5 through 10 on a 10-deg half-angle cone, to discuss the noted effects of boundary-layer transition on dynamic stability, and to compare the experimental results with several theories.

APPARATUS

The tests were conducted in the VKF Gas Dynamic Wind Tunnels, Hypersonic (E) and (C). Tunnel E is a 12 in. intermittent tunnel operating at Mach numbers 5 through 8, and Tunnel C is a 50 in. Mach 10 continuous flow tunnel. A description of the tunnels and airflow calibration information may be found in Ref. 1.

The balance used in the Tunnel E tests was a small amplitude, free oscillation balance. A low amplitude, forced oscillation balance was used in the Tunnel C tests. Further information on the balances may be found in Refs. 2 and 3 along with data reduction procedures.

Three similar 10-deg half-angle cone models were used in the tests. A 4-in. base diameter model was tested at Mach numbers 5 and 6, a 5-in. base diameter model at Mach numbers 6, 7, and 8, and a 10-in. base diameter model at Mach 10. The model geometry is shown in Fig. 1.

RESULTS AND DISCUSSION

The results of the Tunnel E tests are presented in Fig. 2 as the damping-in-pitch derivatives ($C_{m_q} + C_{m_{\dot{\alpha}}}$), the static stability parameter (C_{m_α}), and the model base pressure ratio (p_b/p_∞) versus Reynolds number. Boundary-layer transition measurements presented were obtained from shadowgraph pictures.

The Mach number 5 and 6 data (Figs. 2a and b) show that the damping-in-pitch derivatives are maximum and the slope of the pitching-moment curve is minimum when the beginning of boundary-layer transition is at the model base. Shadowgraph pictures have confirmed that boundary-layer transition is near the model base when the base pressure ratio (p_b/p_∞) first becomes a minimum. These results are in agreement with the lower Mach number results reported by Uselton in Ref. 2.

The Mach number 7 and 8 data (Figs. 2c and d) show the same Reynolds number trend; however, the maximum and minimum values of dynamic and static stability, respectively, occur at Reynolds numbers that are slightly higher than those at which the beginning of transition is at the model base.

The Mach 10 data, obtained in Tunnel C and shown in Fig. 3 as the damping-in-pitch derivatives versus Reynolds number, show the same trend as the Mach 8 data. The maximum Reynolds number point unfortunately represents the maximum Reynolds number available in Tunnel C with this model. This also was the case in Tunnel E with the Mach 8 data (Fig. 3).

Additional tests were conducted in Tunnel E using a 2.6-in. base diameter cone to obtain shadowgraph pictures. The data obtained at Mach 6 at a Reynolds number of 8 million and at angles of attack up to 10 deg are presented in Fig. 4 as the ratio of transition length to cone surface length versus angle of attack. As angle of attack is increased up to about 3 deg, the beginning of transition on the leeward side moves rapidly toward the nose (about 1.5 in. per degree), whereas on the windward side no appreciable movement of transition location is noted. Jack and Moskowitz (Ref. 3) found similar results using a 5-deg half-angle cone at Mach number 3.12. A further increase of angle of attack up to 10 deg shows no appreciable change in transition location on either side; however, the boundary-layer thickness at the beginning of transition did increase with angle of attack on the leeward side. Separation caused by crossflow is possible

at the higher angles; however, as the damping data were obtained at oscillation amplitudes less than 3 deg, crossflow effects should not be important in these data.

It has been shown that the damping-in-pitch derivatives and the slope of the pitching-moment curve are influenced by boundary-layer transition. The present theoretical predictions of cone damping should not be expected to predict this maximum level of damping but rather should be compared to values obtained when either a near full turbulent or full laminar boundary layer is present at the maximum oscillation angle to be tested. The laminar boundary case is that condition where the boundary first becomes laminar.

The results of the present tests are shown in Fig. 5 as the damping-in-pitch derivatives versus Mach number. The lower experimental values are data from Figs. 2 and 3 and were obtained with either nearly full-turbulent flow or when the flow was believed to be fully laminar. Excellent agreement is noted between the Mach 5 data and Tobak's potential flow theory. Good agreement is also obtained with the Newtonian theory at Mach numbers near $M_\infty\delta = 1$ (when $M_\infty\delta = 1$, Mach angle $\approx$ cone angle). Fink's shock expansion method and Brong's flow field analysis predict the trend of the damping-in-pitch derivatives increasing with Mach number above $M_\infty\delta = 1$, which was found in the experiments, but fail to predict the magnitude.

The upper experimental curve shows the maximum values of the damping derivatives for this oscillation amplitude ($\vartheta \approx 1.8$ deg). Note that the increasing Mach number trend is apparent in these data also.

CONCLUSIONS

Dynamic stability tests were conducted at Mach numbers 5 through 10 using a 10-deg half-angle cone. Data were obtained at model oscillation amplitudes of about 1.8 deg at zero angles of attack. Conclusions based on these data are as follows:

1. The damping-in-pitch derivatives are a maximum when the beginning of boundary-layer transition is near the model base.

2. The trend of increasing dynamic stability with Mach number above $M_\infty = 6$, tha is predicted by some of the more recent theories, was confirmed by the experimental data.

REFERENCES

1. Test Facilities Handbook (5th Edition). "von Karman Gas Dynamics Facility, Vol. 4." Arnold Engineering Development Center, July 1963.

2. Uselton, B. L. "Investigation of Sting Support Interference Effects on the Dynamic and Static Stability Characteristics of a 10-Deg Cone at Mach Numbers 2.5, 3, and 4." AEDC-TDR-64-226 (AD450660), November 1964.

3. Jack, John R. and Moskowitz, Barry. "Experimental Investigation of Temperature Recovery Factors on a 10-Deg Cone at Angles of Attack at a Mach Number of 3.12." NACA TN 3256, July 1954.

4. Tobak, Murray and Wehrend, William R. "Stability derivatives of Cones at Supersonic Speeds." NACA TN 2788, September 1956.

5. Private Communications from Mr. E. A. Brong, Re-Entry Systems Department, General Electric Company.

6. Fink, Martin R. and Carroll, J. B. "Hypersonic Static and Dynamic Stability at Wing-Fuselage Configurations." UAC Report C910188-17, January 1965.

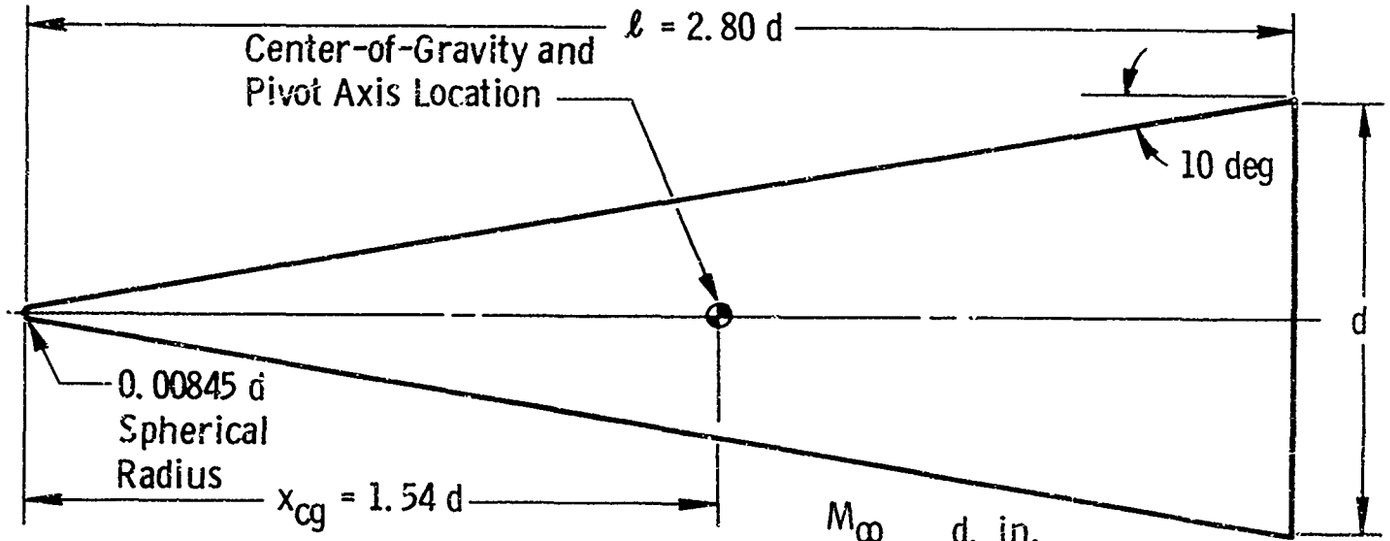

$x_{cg}/\ell = 0.55$

$r_n/r_b = 0.0167$

M_∞	d, in.
5	4
6	4, 5
7	5
8	5
10	10

103512

Fig. 1 Model Geometry

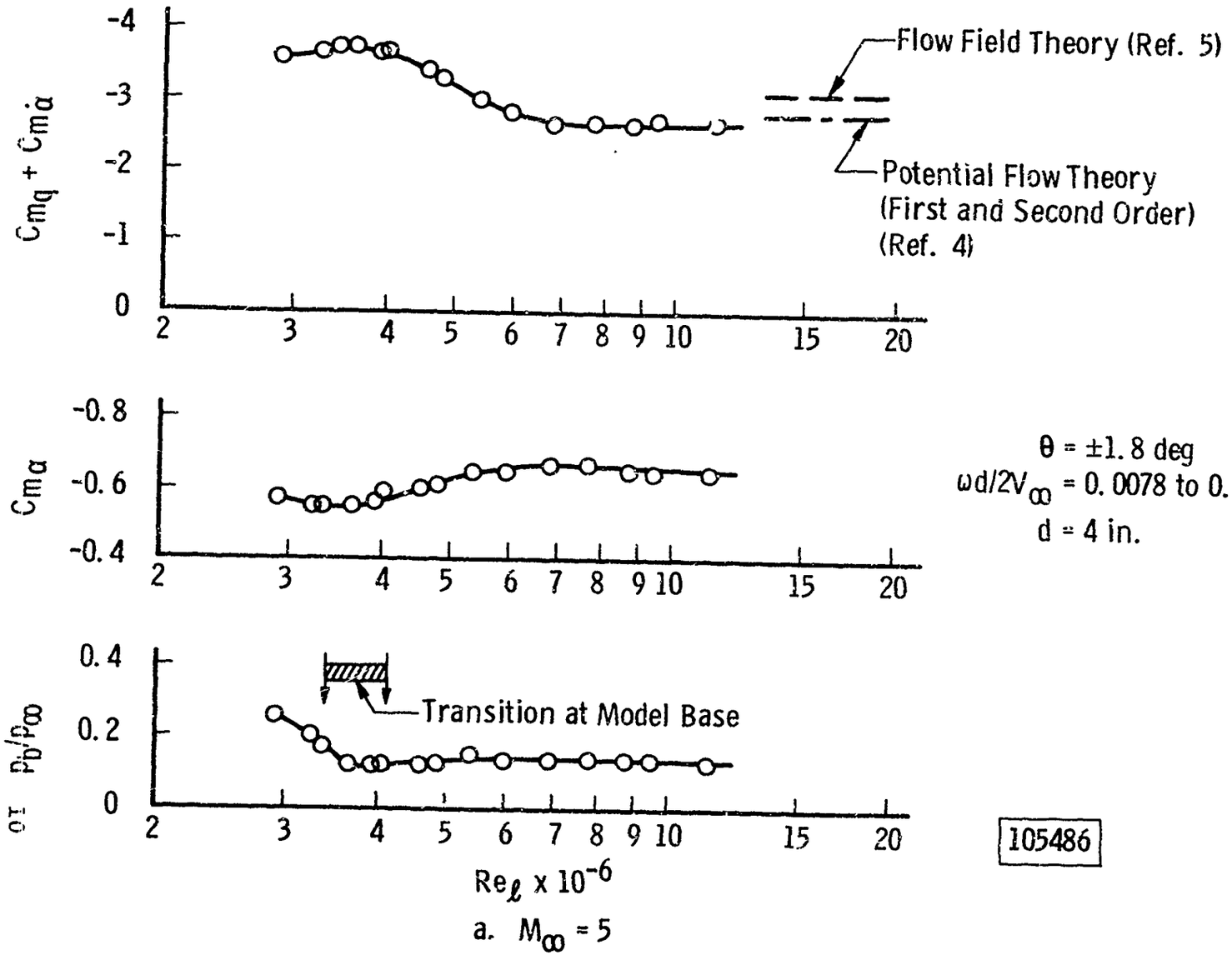

a. $M_\infty = 5$

Fig. 2 Effect of Reynolds Number on Dynamic and Static Stability

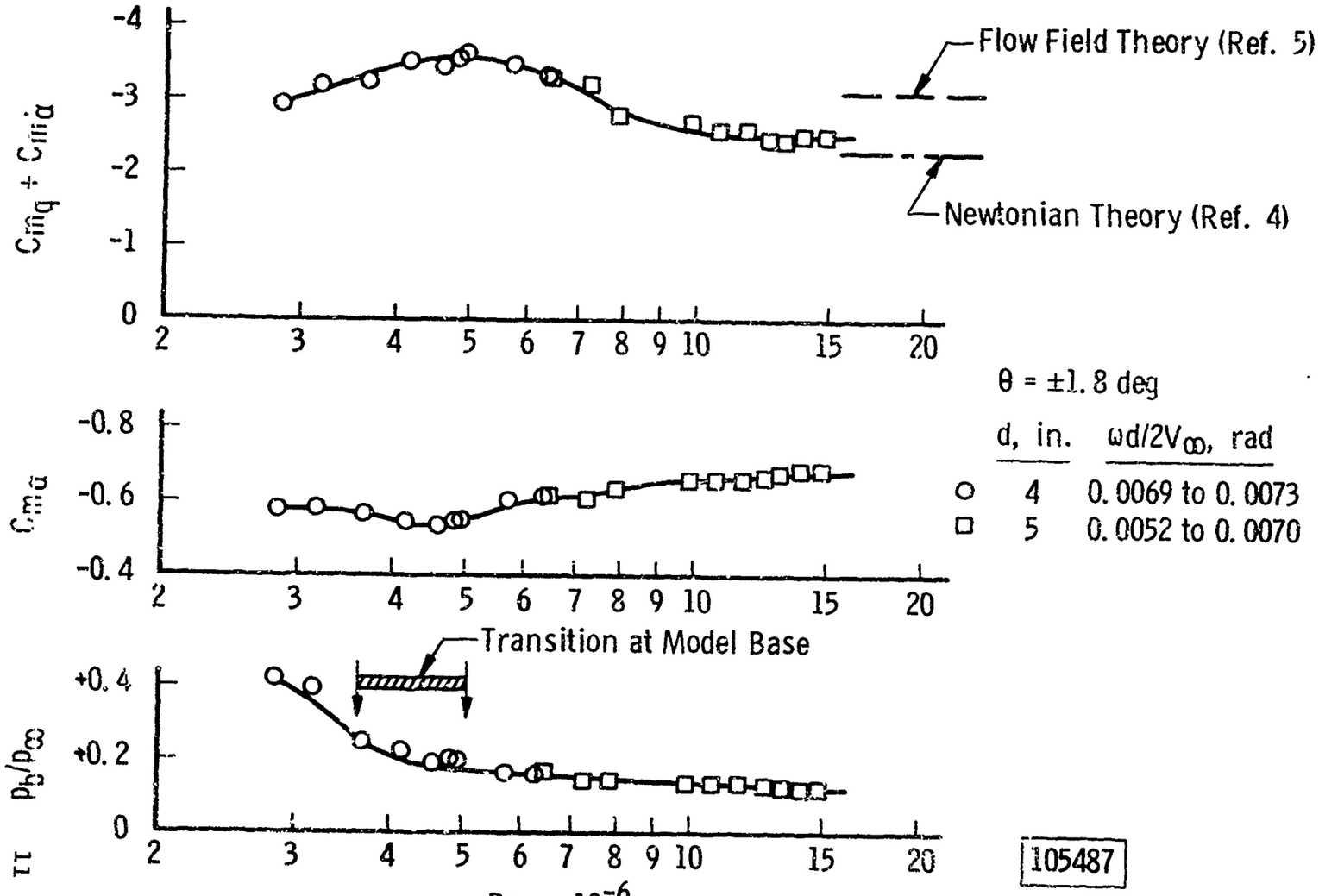

b. $M_\infty = 6$

Fig. 2 Continued

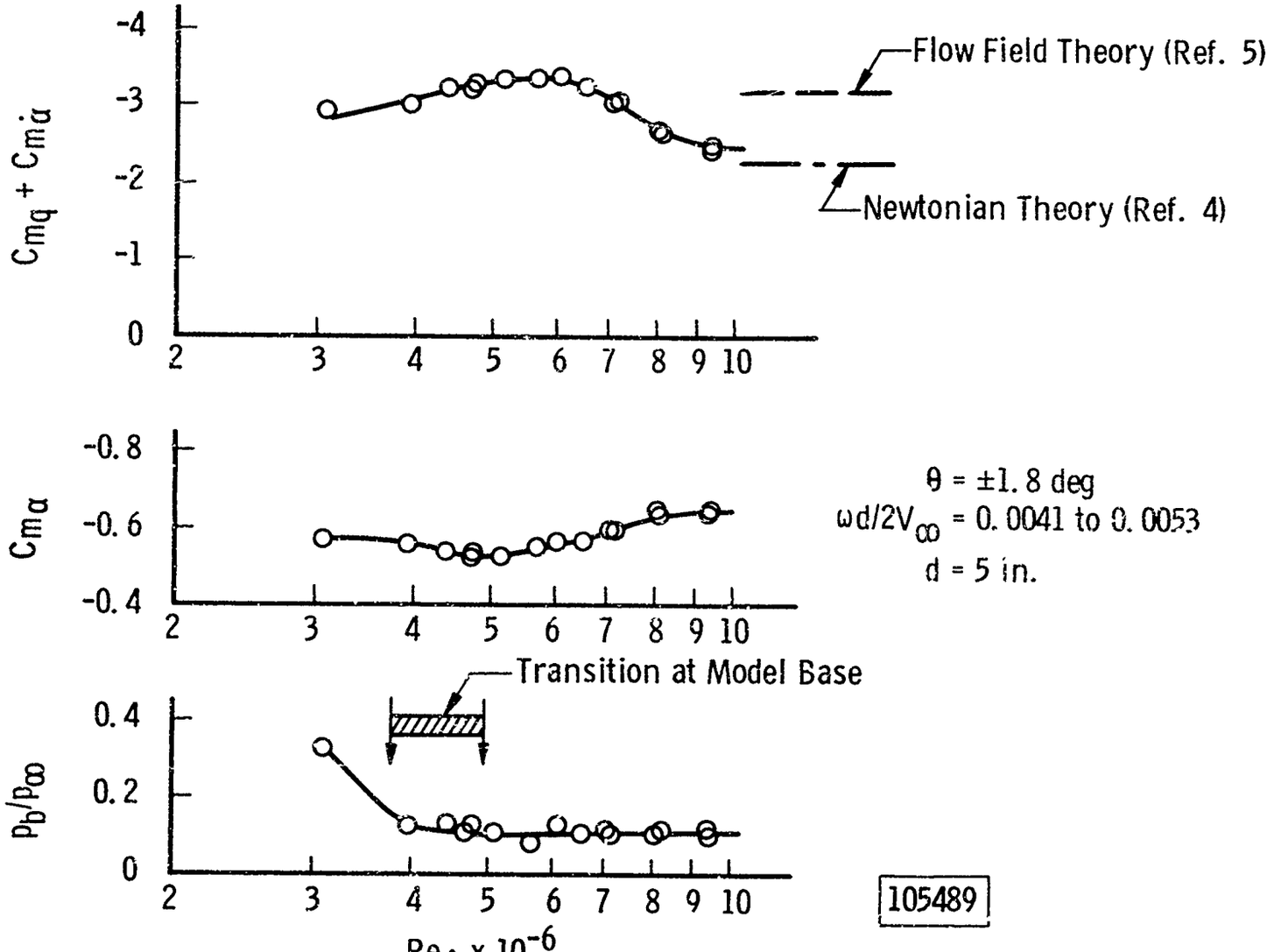

c. $M_\infty = 7$

Fig. 2 Continued

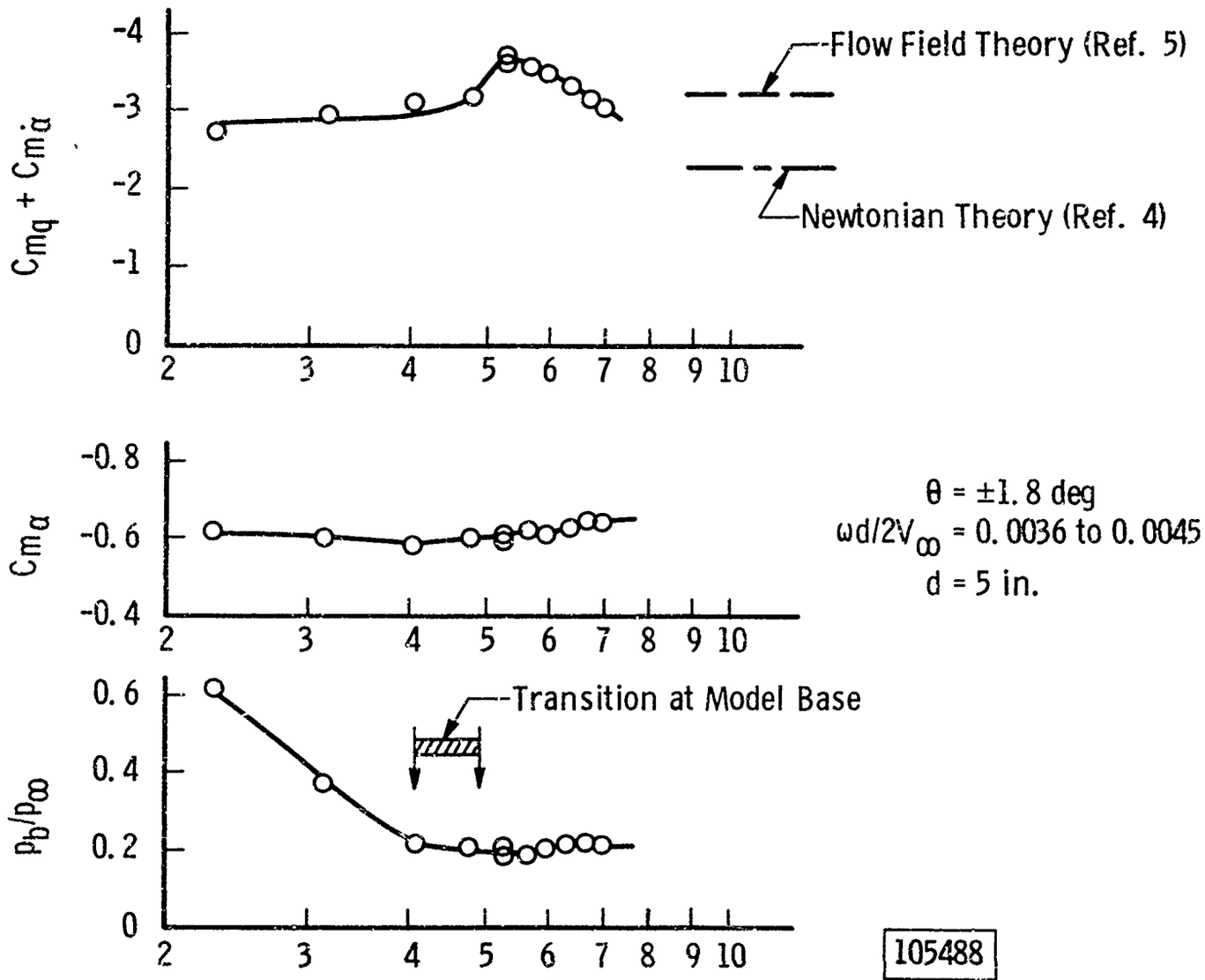

d. $M_\infty = 8$

Fig. 2 Concluded

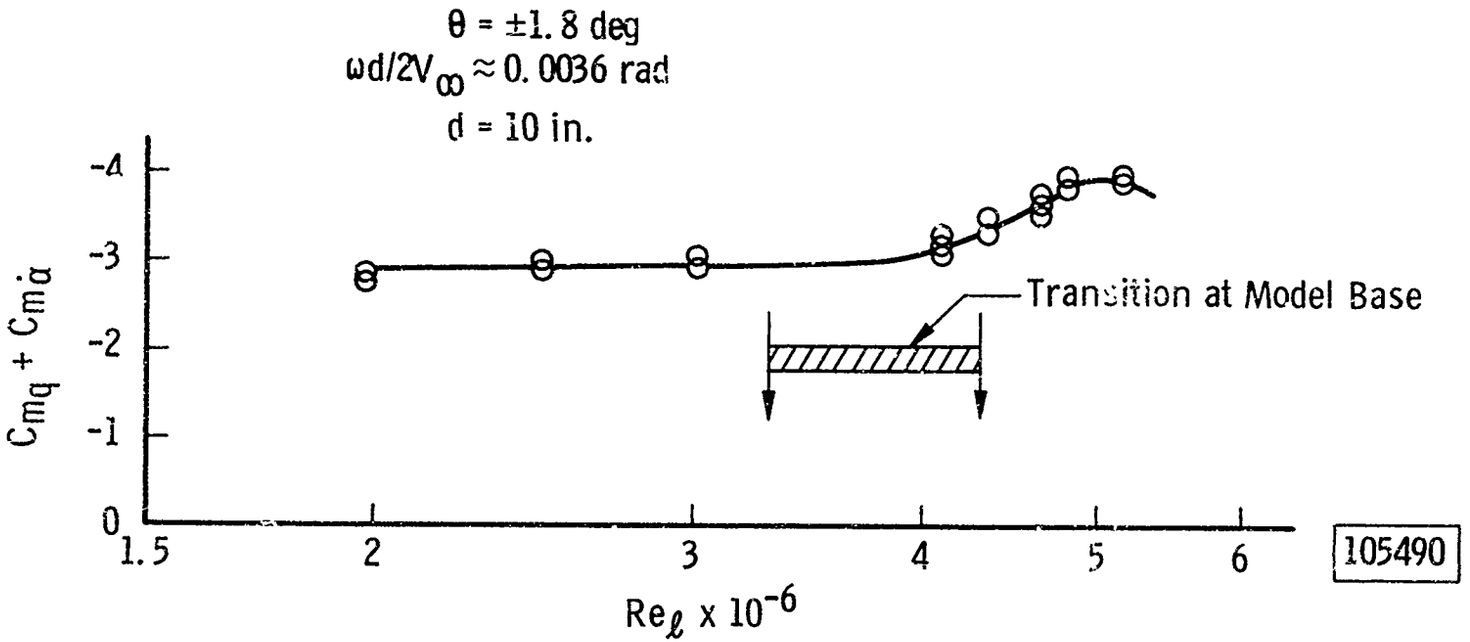

Fig. 3 Effect of Reynolds Number on Dynamic Stability, $M_\infty = 10$

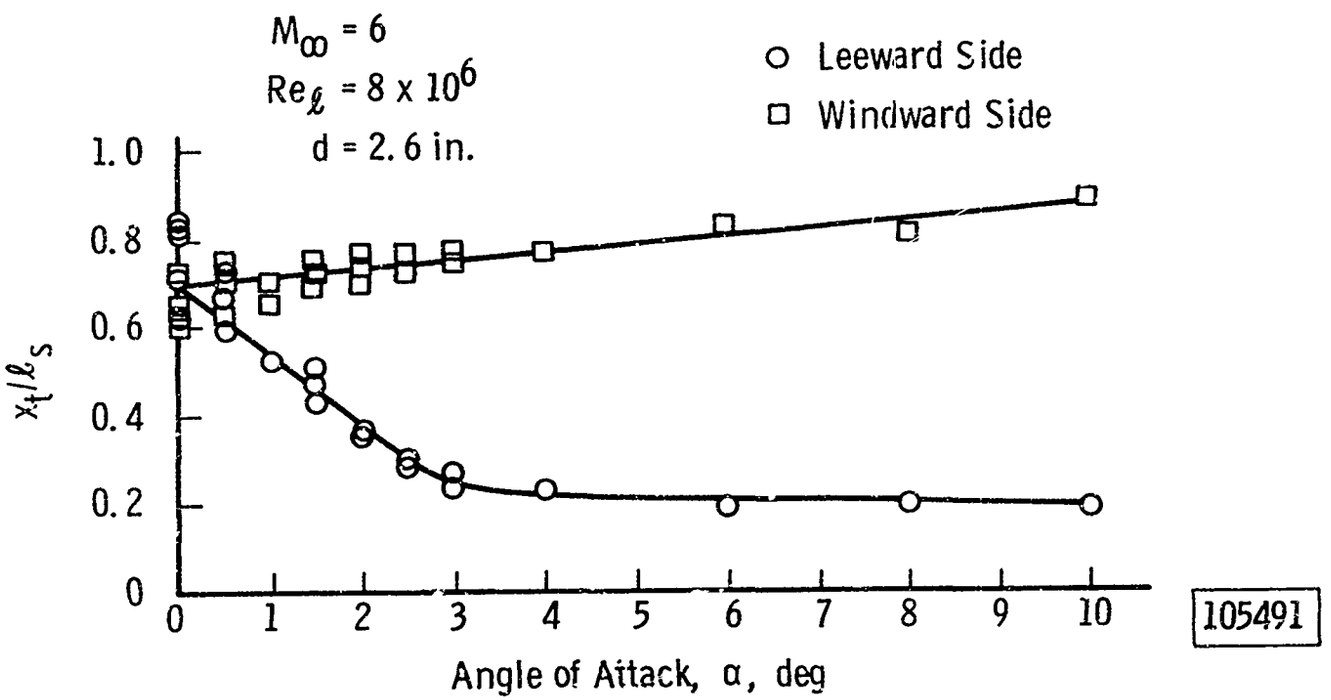

Fig. 4 Effect of Angle of Attack on Transition Location

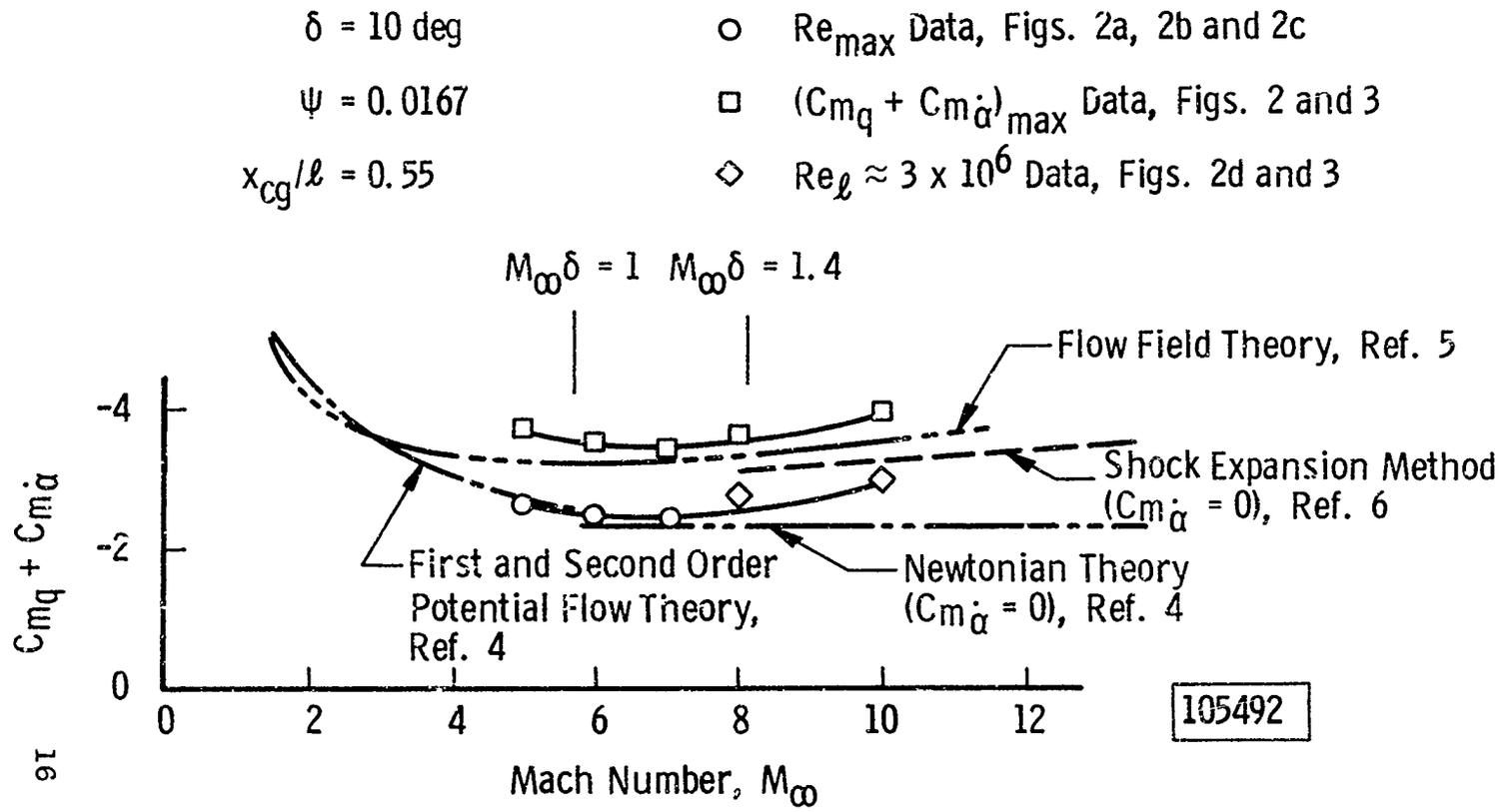

Fig. 5 Damping-in-Pitch Derivatives versus Mach Number

DISCUSSION

Lars Ericsson:

Did you have a flat base model for these transition measurements?

L. K. Ward:

Yes, the base was flat.

Lars Ericsson:

Have you made any measurements or are you planning to make any to investigate the effect of base roundness, i.e., find out if and how amplifying this transition effect?

L. K. Ward:

Well, we don't have any plans to do this on this particular configuration. We are developing a free flight technique where we plan to do some work with rounded bases; although, I could say previous tests that we have run in Tunnel C with a rounded base model (corners rounded) have shown that rounding the edge did show a drop off in the pitch derivatives. In other words, this is a destabilizing effect. Now these were taken with a sting supported system, but they were at low amplitudes and we do show the effects.

Lars Ericsson:

What about transition--did you have one type of boundary layer or did you have transition near the base?

L. K. Ward:

The most predominate effect was found at the very low Reynolds number where the flow was full laminar.

Brian Quinn:

I was just wondering when you refer to transition you are actually referring to some place downstream of which the boundary layer was fully turbulent--is that right--or is it quasi-turbulent, quasi-laminar?

L. K. Ward:

Well, this is a hard area to define. I am trying to do this with shadowgraph pictures and the point that I have chosen, I would say, is the point of the beginning of transition.

J. Arnaiz:

You have a lot of good static stability data there, also, although you didn't discuss it at great length. I was wondering if you could comment on any relationships you have found in this relative to transition and also relative to the various theories?

L. K. Ward:

Well, relative to the theories, we did compare some of these data with theory and I think the agreement was fair. It was not as good agreement as we found with the pitch derivative. Now as to the effect or the reason for the drop-off--is this what you are asking?

J. Arnaiz:

No specific question.

L. K. Ward:

Well, I have made some first order approximations as to reasons why the derivatives change when moving through this transition point and so far I haven't found a good reason. That obviously is why I didn't comment on it before but this could be attributed to a skin friction change from a turbulent to a laminar case and we plan to do some more work on this and get a better correlation with theory.

Prof. Kuethe:

I have some appreciation, I think, for the difficulties of transition measurements and I am impressed by the fact that you can get consistent measurements with different models. My question pertains more to some papers that were given in the ablation session than to yours. In those papers it was remarked that the transition jumped suddenly from off the base to the nose with the blunted models and I wondered if this is a characteristic of the bluntness. In a paper just published (R. J. Santor, J. P. DeCarlo, and D. T. Torrillo, "Hypersonic Boundary Layer Transition Data for a Cold-Wall Slender Cone," Jour. AIAA, Vol. 3, No. 4, pp 758-760, April 1965) measurements on smooth and rough cones of various degrees of bluntness indicate just this behavior, the jump becoming more sudden as the bluntness increases, independent of the roughness of the cone surface. Our work on transition on a sphere in simulated hypersonic flow (Roger Dunlap and A. M. Kuethe, Jour. Aero, Sci. Vol. 29, No. 12, pp. 1454-1461, Dec. 1962; and A. M. Kuethe, Takao Ishii and James L. Amick, Phys. Fluids, Vol. 7, No. 8, pp 1198-1200, Aug. 1964) shows that the boundary layer forward of the sonic line is extremely sensitive to slight surface roughness. Therefore, as the bluntness increases transition could be tripped by the roughness near the nose; the boundary layer would then be turbulent everywhere behind the nose region. On an

ablating body, the ablation would presumably cause a roughening of the surface. In regard to this hypothesis I would like to ask whether there are data other than that referred to above on the effect of bluntness on transition.

Mr. Potter:

I am unable to answer your question, Prof. Kuethe, with regard to movement of transition with ablation existing, but without ablation there are abundant records of "slow" movement forward of transition on blunted conical and hemisphere-cone-cylinder bodies as either roughness height or Reynolds number increased. There also are records wherein a more abrupt movement of transition is evident. Of course, it is apparent that nose blunting produces a layer of lower local Mach number along a body, with the thickness of this layer depending on the degree of blunting. Now, it seems to be established that, for local Mach numbers greater than, say 3, the boundary layer stability improves as local Mach number increases. Thus, one may conjecture that blunting, and consequent lowering of local Mach number, creates a boundary layer which is more sensitive to the destabilizing effects present, such as roughness or mass ejection. Because the local Reynolds numbers also are reduced by the blunting, this train of thought is inconclusive, but it may be interesting to some of the audience. Professor Kuethe's point is most interesting and I cannot confirm or deny his hypothesis.

SC-R-65-907

SANDIA CORPORATION REPRINT

DYNAMIC STABILITY DERIVATIVES FOR A 10° BLUNT CONE AT MACH NUMBERS FROM 0.5 TO 21

by

E. C. Rightley

April 1965

ABSTRACT

Static and dynamic stability coefficients of a 10° blunt cone were measured in six wind tunnels. These data show fair correlation between tunnels and with applicable theory.

TABLE OF CONTENTS

LIST OF ILLUSTRATIONS

NOMENCLATURE

C_m Pitching moment coefficient, $\frac{\text{Pitching moment}}{q_\infty S d}$ dimensionless

C_{m_α} Slope of pitching moment curve, $\frac{\partial C_m}{\partial \alpha}$, per degree

C_{m_q} Damping derivative due to pitching velocity, $\frac{\partial C_m}{\partial\left(\frac{qd}{2V}\right)}$, per radian

$C_{m_{\dot\alpha}}$ Damping derivative due to rate of change of angle of attack, $\frac{\partial C_m}{\partial\left(\frac{\dot\alpha d}{2V}\right)}$, per radian

d Base diameter, ft.

f Frequency of model oscillation, cycles/sec.

I Moment of inertia of model, slug-ft.^{2}

M Free stream Mach number

q Pitching velocity, rad/sec.

q_∞ Free stream dynamic pressure, lb/ft^2

R Reynolds number, $\frac{\rho V d}{\mu}$, dimensionless

S Reference area, $\frac{\pi d^2}{4}$, ft^2

t Time, seconds

V Free stream velocity, ft/sec.

α Angle of attack

μ Free stream viscosity, slug/ft-sec.

NOMENCLATURE (continued)

θ Amplitude of model oscillation, degrees

ρ Free stream density, slug/ft^3

ω_R Reduced frequency, $\frac{\pi fd}{V}$, dimensionless

DYNAMIC STABILITY DERIVATIVES FOR A 10° BLUNT CONE AT MACH NUMBERS FROM 0.5 TO 21

INTRODUCTION

An aerodynamic shape of interest to Sandia Corporation is a cone with a 10-degree half angle and a spherical nose with a ratio of nose to base radius of 0.188. Static and dynamic stability tests of this configuration were conducted in several wind tunnels at Mach numbers from 0.5 to 21. The tunnels used were:

1. Cornell Aeronautical Laboratory 8-foot Transonic Tunnel
2. Ling-Temco-Vought 4-foot High Speed Tunnel
3. Fluidyne Engineering Corporation 20-inch Hypersonic Tunnel
4. Jet Propulsion Laboratory 21-inch Hypersonic Tunnel
5. Sandia Corporation 18-inch Hypersonic Tunnel
6. Ling-Temco-Vought 13-inch Hypervelocity Tunnel

This paper presents the results from the tests in the various tunnels in an attempt to show where correlation exists from one to another. A secondary purpose is to compare the results with applicable theory.

TEST TECHNIQUE

Experimental Apparatus

A general description of the models that were used is given in Figure 1. Model A was tested at all the facilities, with the three center-of-gravity locations shown used in the dynamic stability tests. The base diameter of Model A was 9.80 inches in the tests at Cornell Aeronautical Laboratory and at the Ling-Temco-Vought 4-foot tunnel, 5.097 inches in the tests at the Jet Propulsion Laboratory 21-inch tunnel, 3.00 inches at the Fluidyne 20-inch tunnel and at the Sandia 18-inch tunnel, and 1.960 inches at the LTV 13-inch tunnel. Dynamic tests were conducted on Models B and C at the JPL 21-inch tunnel, and the results for the forward center of gravity are reported here allowing a limited study to be made of the effect of nose bluntness and base rounding. The base diameters for both of these models were 5.250 inches.

Test Conditions

A free-oscillation ball-bearing dynamic rig was used at the Cornell Aeronautical Laboratory transonic tunnel and at the Ling-Temco-Vought high speed tunnel, References 1 and 2. The rig allows model oscillation of about ±10 degrees from the tunnel centerline. The results from these tests represent average pitch damping derivatives computed from the data collected while the amplitude of model oscillation decreased from ±6 or 7 to ±3 or 4 degrees. The Mach number range at CAL was from 0.5 to 1.3 while

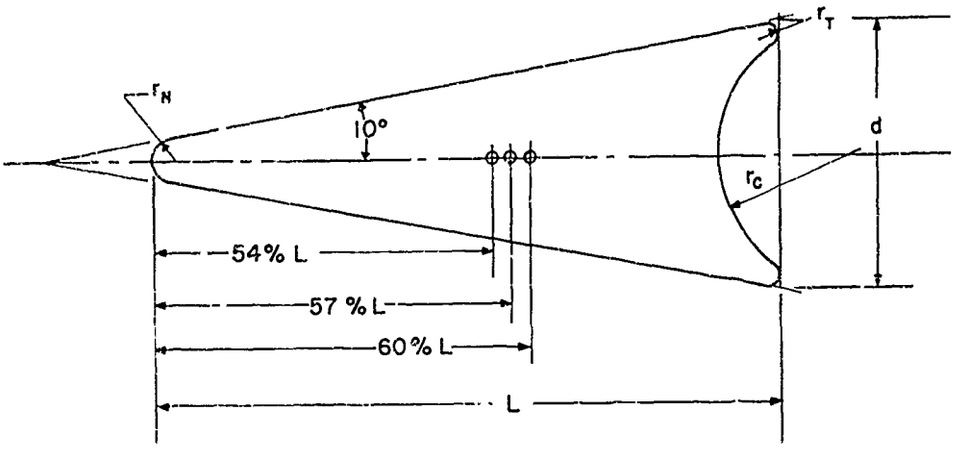

FIGURE 1. CONE MODELS

MODEL A BLUNT NOSE-CONCAVE BASE	MODEL B SHARP NOSE-FLAT BASE	MODEL C BLUNT NOSE-FLAT BASE
$L/d = 2.44$	$L/d = 2.84$	$L/d = 2.44$
$r_N/d = 0.094$		$r_N/d = 0.094$
$r_T/d = 0.045$		
$r_c/d = 0.515$		

the Reynolds numbers, based on model base diameter, varied from 2.2 X 10^6 to 3.1 X 10^6 and the reduced frequency was from .0040 to .0072. The Mach number range, Reynolds number range, and the reduced frequency at the LTV 4-foot tunnel were 1.6 to 4.8, 6.0 X 10^6 to 11.8 X 10^6, and .0044 to .0083 respectively.

Dynamic tests were performed at Mach numbers of 6 and 8 at the Jet Propulsion Laboratory 21-inch tunnel using the sting-mounted JPL gas-bearing rig. The results included here are the average stability derivatives reduced from the data from the JPL tests while the amplitude of model oscillation was decreasing from approximately ±5 to ±2 degrees. The Reynolds numbers varied from 0.9 X 10^6 to 1.4 X 10^6 while the reduced frequency was .0020 to .0034.

A side-mount, air-bearing rig was used at the Fluidyne Engineering Corporation 20-inch hypersonic tunnel (Reference 3) at Mach numbers of 11 and 14. The air bearing is located outside the flow of the open-jet tunnel, and the model is attached to it by a transverse rod which rotates with the model. The stability derivatives reported here were determined from the model motion which followed release of the model at an angle of attack of approximately 5 degrees. The tests were conducted at Reynolds numbers of 0.3 X 10^5 to 1.7 X 10^5 and reduced frequencies of .00037 to .00073.

Both a dynamic stability and a three-component force test were performed in the hypervelocity tunnel at Ling-Temco-Vought (Reference 4). For the dynamic test, the blunt cone model was mounted on a free-oscillation

flexure rig which limited the model displacement to ±2 degrees. These tests were at Mach numbers of 14, 17, and 21; Reynolds numbers from 1.1×10^5 to 2.1×10^5, and reduced frequencies from .014 to .018.

A three-component force test to determine static stability was conducted at Mach numbers of 5.3 and 7.6 in the Sandia Corporation 18-inch hypersonic tunnel at Reynolds numbers varying from 2.1×10^5 to 3.3×10^5 (Reference 5).

Data Reduction

The stability derivatives were calculated from the following equations (Reference 6):

$$C_{m_q} + C_{m_{\dot{\alpha}}} = - \frac{4VI}{q_\infty Sd^2} \frac{\text{LOG}_e \left(\theta_1/\theta_2\right)}{t_1 - t_2}$$

$$C_{m_\alpha} = - \frac{4\pi^2 If^2}{q_\infty Sd}$$

The tare damping in the dynamic rigs was accounted for by comparing the model oscillations with the tunnel operating and with wind off in the tests at Cornell Aeronautical Laboratory and in the two tunnels at Ling-Temco-Vought. The damping of the air bearing at Fluidyne was determined prior to the test by mounting the bearing in a horizontal position and noting the oscillations of a pendulum attached to it. A calibration sphere was used on the gas-bearing rig at JPL with the tunnel operating, but the data from this test was not available at the time that this paper was written.

The static stability derivatives from the force tests were determined by making a linear fit to the C_m versus angle-of-attack points in the vicinity of zero angle of attack. In the tests at the Sandia 18-inch tunnel, the linear fit was established in the angle of attack range of -6 to +6 degrees. The linear fit in the tests at the LTV hypervelocity tunnel was made over the entire angle-of-attack range, -6 to +20 degrees.

RESULTS

The experimental results from the tests in the various facilities are shown in Figures 2, 3, and 4. Figure 2 includes results from tests of Model A with the center of gravity located at 54% of the actual model length aft of the blunt nose while the results with the center of gravity at 57% and 60% are shown in Figures 3 and 4, respectively.

The stability derivatives, both static and dynamic, were computed over the applicable Mach number range from Tobak and Wehrend's first and second order potential flow theory for a sharp 10-degree cone (Reference 7), and are included in the figures. The derivatives also were calculated for the forward center-of-gravity location by the Newtonian method as described in Reference 8, and they are indicated in Figure 2.

For the forward center of gravity location, the dynamic stability results shown in Figure 2 appear to correlate adequately up to about Mach 8. At the high Mach numbers, the results indicate either dynamic instability or very low dynamic stability. The instability was noted in the tests in

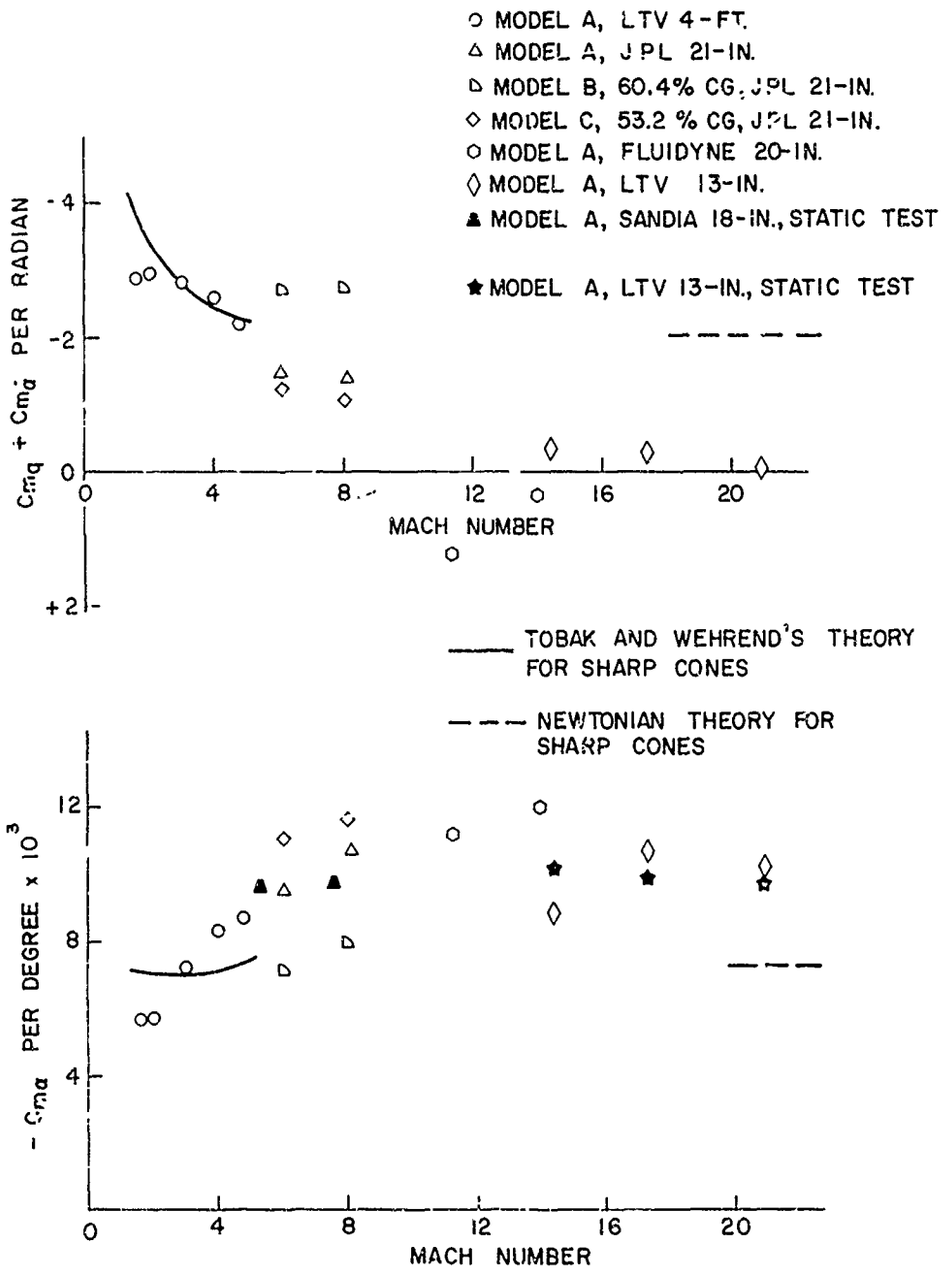

FIGURE 2. STABILITY DERIVATIVES, MODEL A, 54% C.G.

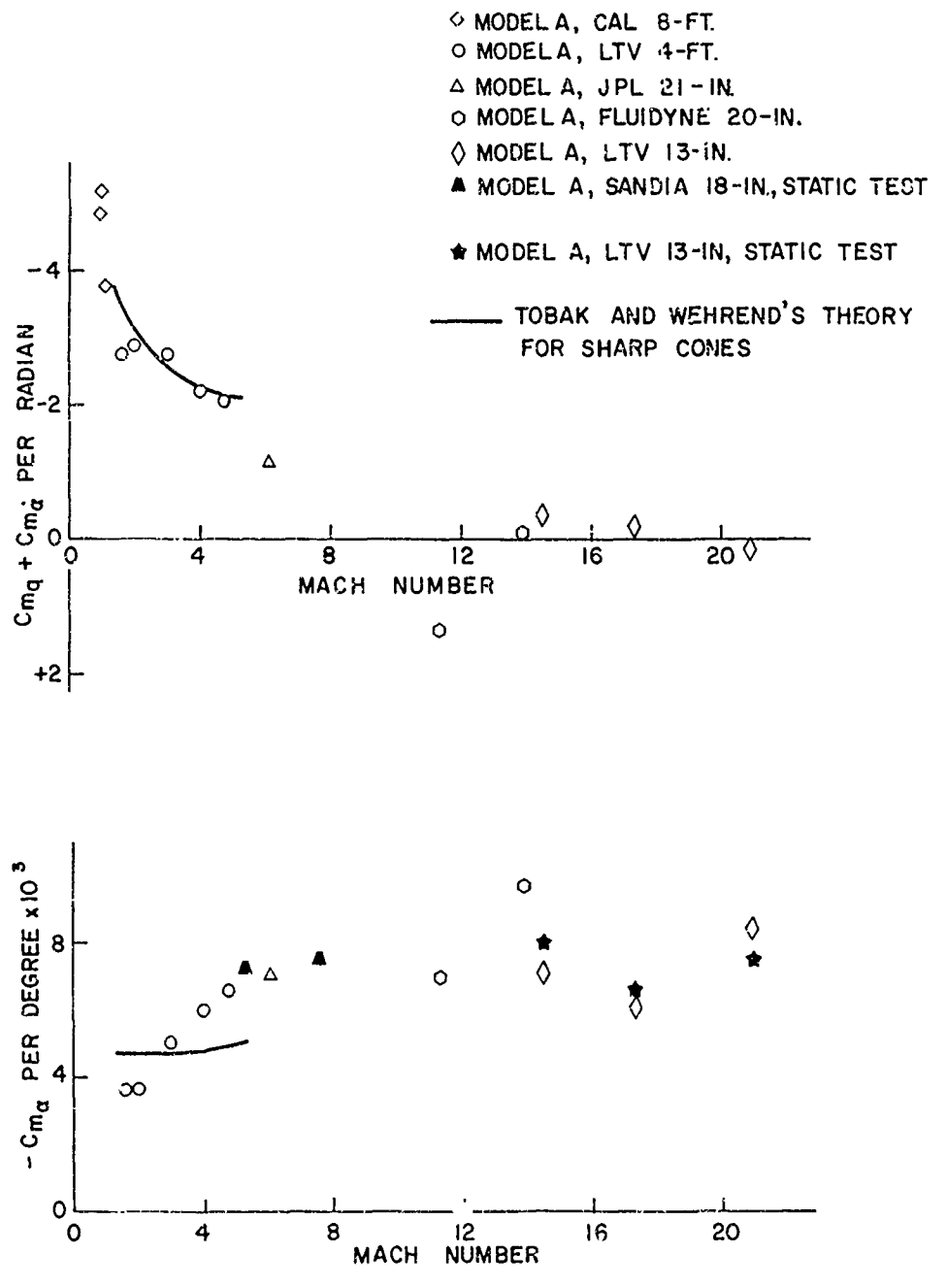

FIGURE 3. STABILITY DERIVATIVES, MODEL A, 57% C.G.

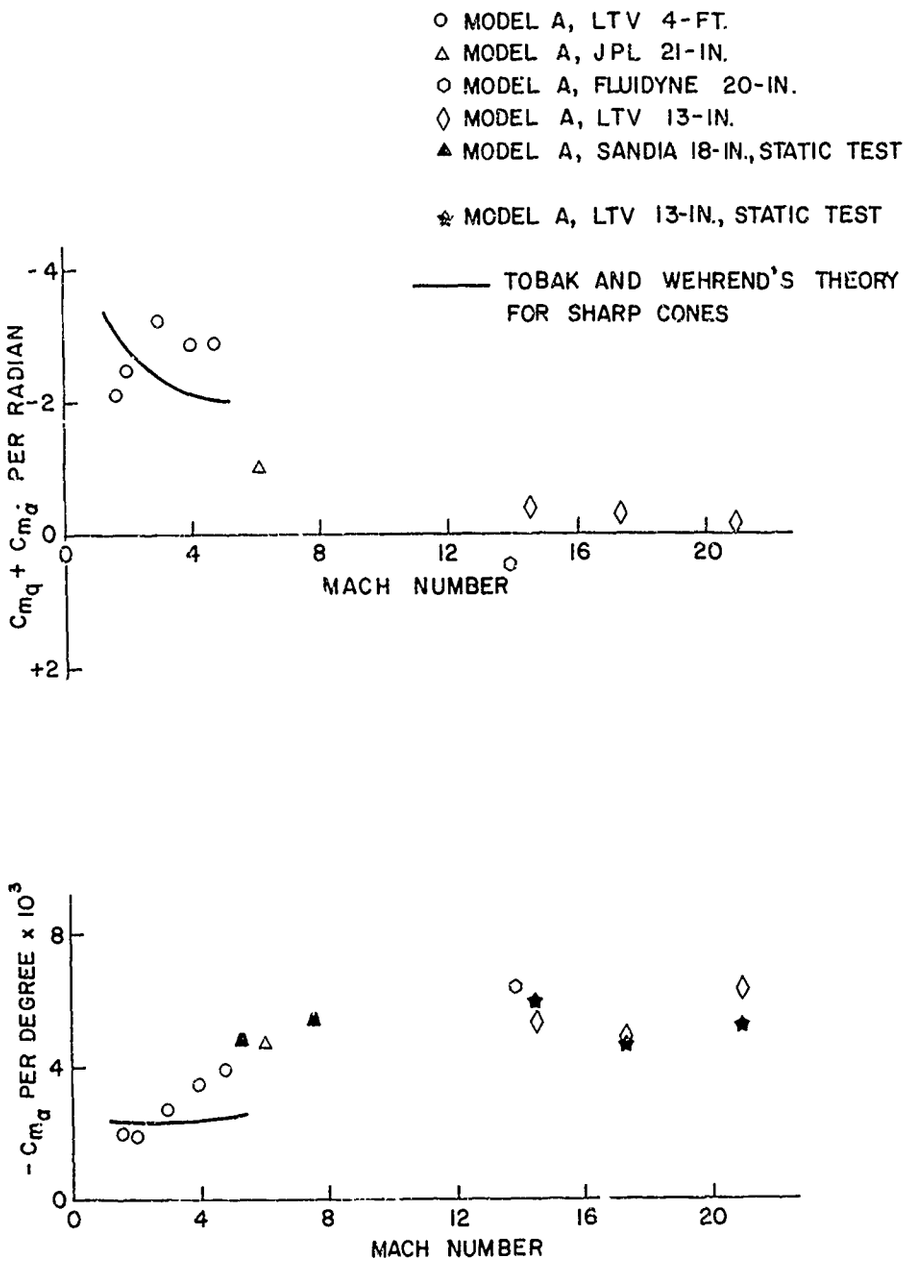

FIGURE 4 STABILITY DERIVATIVES, MODEL A, 60 % C.G.

which the model was mounted to an air bearing by a strut entering the side of the model, and the precise effect of this side strut has not been determined.

The static stability derivatives correlate quite well up to the hypervelocity regime where the results may reflect the effect of oscillation frequency. The static derivatives appeared to approach a value considerably greater than that predicted by Newtonian theory for a sharp cone.

The effect of nose bluntness is evident for the forward center of gravity location at Mach numbers of 6 and 8. It apparently reduces dynamic stability while increasing static stability. At lower Mach numbers the effect seems much less, at least with respect to dynamic stability, since the results for the blunt cone agree so well with the Tobak and Wehrend theory for sharp cones.

The results indicate that base rounding does not seem to have much effect on either dynamic or static stability.

CONCLUSIONS

Static stability derivatives obtained from force tests correlate fairly well with those obtained from dynamic stability tests.

There is fair correlation among the tunnels on static stability results.

Nose bluntness increases the static stability while decreasing the dynamic stability.

The dynamic stability derivatives, as predicted by Tobak and Wehrend's theory, show good correlation with the results.

Newtonian theory predicts more dynamic and less static stability than the data indicates.

A reasonable trend in dynamic stability results is indicated except for the data from the side-mounted air-bearing rig which is low.

Not much effect of center-of-gravity location is shown on the dynamic stability while there is the expected large effect on static stability.

REFERENCES

1. Reid, C. F., "Dynamic Stability Tests of a Sandia Blunted Cone Shape at Transonic Speeds," CAL 110-143, Cornell Aeronautical Laboratory, Inc., May 1964.

2. Ziegler, C. E., "A Dynamic Stability Test of a Sandia Corporation Blunted Cone Configuration in the LTV High Speed Wind Tunnel in the Mach Number Range of 1.6 to 4.8," HSWT Test 157, Ling-Temco-Vought, Inc., July 1964.

3. Rainer, C. W., "Dynamic Stability Tests of a Blunted Cone Model at Mach 11.5 and 14," Fluidyne Project 0405, Fluidyne Engineering Corp., August 1964.

4. Lindsey, J. L., "LTV Hypervelocity Wind Tunnel Force and Dynamic Stability Test of a Blunted Cone Model," HVWT Test 25, Ling-Temco-Vought, Inc., November 1964.

5. George, O. L. Jr., "Static Stability and Axial Force Tests of Three Slender, Blunted Cones at Mach number of 5.3 and 7.6," SC-TM-64-1655, Sandia Corp., March 1965.

6. Rowe, Paul W., "An Introduction to Aerodynamic Stability," SC-TM-220-56(51), Sandia Corp., February 1957.

7. Tobak, Murray and Wehrend, William R., "Stability Derivatives of Cones at Supersonic Speeds," NACA TN 3788, September 1956.

8. Gilmore, A., Seredinsky, V., and MacKenzie, D., "Investigation of Dynamic Stability Derivatives of Vehicles Flying at Hypersonic Velocity," ASD-TDR-62-460, Grumman Aircraft Engineering Corp., September 1963.

DISCUSSION

Lars Ericsson:

I couldn't see on your slide if you showed any effect of this dome, the base roundness.

E. Rightley:

Well, with only two points it is pretty hard to draw any definite conclusions; but what was shown on the slide was apparently a slight reduction in dynamic stability and a somewhat larger increase in the static stability. As to whether you could assign that to the doming effect or the dome of the base or that concave part I don't know. I guess I should point out that there wasn't much effect shown in the concave part on any of the tests except the one at FluiDyne because with the sting entering in the back, a large part of the concave feature was missing in the model.

Lars Ericsson:

I agree. I don't think the concave part is important at all, but the radius of curvature at the shoulder is. If you recall, Dr. Murphy showed yesterday undamping data for another cone with a dome shaped base. The explanation could be an apparent curvature effect in the wake; that is, the flow will attach on the downward going side producing a negative force. This gives a statically destabilizing and dynamically destabilizing effect. One has to be very careful when attempting to measure this effect because there is bound to be a sting interference problem. I think you have to worry more probably about the sting effect than about the side mount effect.

Bill Weaver:

I noticed that in the last two slides you showed the static derivative between Mach numbers 16 and 20 from the force measurements and from data derived from dynamic tests. You are dropping in static stability between these Mach numbers--what reason can you give for this?

E. Rightley:

I don't think I have any reason--did they drop consistently in the last two?

Bill Weaver:

I believe in the last two showed a definite drop at about Mach 17. There was a fairly straight line out to there and then it went back up at Mach 20.

E. Rightley:

Yes, this is indicated. I have no explanation for that.

A. Platou:

On this business of using rounded bases or just even a small radius at the shoulder of the base, I would like to throw in a word of caution. We at BRL have found that in some cases for dynamic stability measurements that rounding the base has caused some difficulty and also in my own experience in measuring Magnus forces and moments I have found in some cases that just the slight rounding of the base can change the Magnus force from a positive force to a negative force. There can be some difficulties here so I just wanted to throw in this word of caution.

Bass Redd:

One question that I have--did the FluiDyne test actually diverge or did this damping become unstable once you removed your bearing damping?

E. Rightley:

No, it actually diverged. When the models were released from 5 degrees the amplitude built up to almost 11 degrees. I have to say in all fairness that in the FluiDyne test when the model was released at 15 or in some cases at 30 degrees it converged, but at Mach number 11 as I recall it converged to around 11 or seemed to be trying to approach 11 degrees. Since the bearing friction is in there I don't know if that angle really means anything. At Mach 14 it would converge more so. It converged readily from 15 degrees, for instance, towards an angle somewhat less than 10. And at Mach 14 when it was released at 5 degrees, it couldn't seem to make its mind for a while but finally it did start to diverge.

EFFECT OF A HEMISPHERICAL AFTERBODY ON THE DYNAMIC STABILITY OF A SLENDER CONE (WIND TUNNEL FREE-FLIGHT TECHNIQUE)

by

Bain Dayman, Jr.

Jet Propulsion Laboratory

California Institute of Technology

Pasadena, California

ABSTRACT

The use of a free-flight technique, either in a ballistic range or a wind tunnel, is required in order to determine the effect of afterbody shape on dynamic stability. If it is assumed that the afterbody can have an effect, then the use of a sting (a form of an afterbody) would not be a valid approach. Afterbody-shape effect data have been obtained in ballistic ranges. The wind tunnel free-flight technique was used to extend this investigation to a ten-degree (half-angle) sharp-nose cone. At M = 2 and 4 and an oscillation envelope of 18 degrees there was no noticeable effect of a hemispherical afterbody addition on the dynamic stability or the drag of a flat-base cone. However, the static stability with the hemispherical afterbody was substantially larger than that of the flat-base configuration.

It is the general feeling that the base shape does affect the dynamic stability (that is, pitch damping) of axially symmetric bodies - especially in the transonic and low supersonic regimes. For example, the addition of a spherical segment to the flat base of a slender body would be expected to appreciably degrade the dynamic stability. In order to investigate this phenomena in a realistic, non-interference manner in a wind tunnel, the use of the wire-release, free-flight technique was applied to standard cones: 10^{o} half-angle, sharp-nose cones with cg's at 53% of the length from the nose. The tests were performed at M = 2 and 4, laminar or turbulent cone boundary layers (at $\alpha = 0^{o}$), on cones with either flat or hemispherical bases. For the most part, the models were launched at about 25^{o} angle-of-attack, and the 10^{o} decay during the useful trajectory resulted in an average oscillation envelope of about 18^{o}. At M = 4, additional launches were made at 33^{o} angle-of-attack which yielded an average oscillation envelope of about 27^{o}.

In none of these flights could any effect of the hemispherical afterbody on the pitch damping be observed. Figure 8* shows the $C_{m_q} + C_{m_{\dot{\alpha}}}$ of these cones. One could hypothesize that the lack of effect is due to the rather large angle of oscillation. But, as has been shown in several other papers, the damping during the lower local angle of attack regions dominates the average effective damping during the complete oscillation cycle.

Figure 3 indicates no noticeable effect on the total drag due to the addition of a hemispherical afterbody. In contrast to the lack of effect on either the pitch damping or the drag, there is a substantial effect of a hemispherical afterbody on the static stability. In Figure 4 one can see the effect of oscillation envelope on the pitching moment slope of the flat-base cones. A variation in the oscillation envelope from 0 degrees to 18 degrees causes a large increase in the pitching moment slope. An additional increase of similar magnitude occurs at an 18^{o} oscillation envelope when a hemispherical base is added to the originally flat-base cone. This effect is especially large when the static margin of about 13% of the model length for the flat-base cone is considered.

---

*Figure numbers refer to those in the next paper--Free Flight Dynamic Stability Testing at High Amplitudes of Oscillation by Bain Dayman, Jr.

FREE-FLIGHT CONE DYNAMIC STABILITY TESTING

AT

HIGH AMPLITUDES OF OSCILLATION

Bain Dayman, Jr.

August 1964
Jet Propulsion Laboratory
California Institute of Technology
Pasadena, California

INTRODUCTION

This paper presents a summary of information from several published reports and tests recently completed which deal with the measurement of dynamic stability of cones at high amplitudes of oscillation by use of wind tunnel free-flight techniques. The techniques of testing and data reduction are very briefly mentioned as they have been described in adequate detail elsewhere. However, considerable damping data are included in order to fully document the value and consistency of the results.

TESTING TECHNIQUES

The cone models (0.5 to 1.0 inch diam.) are constructed of thin plastic or metal (aluminum or magnesium) shells and are ballasted with either lead or gold cores.

The models are launched into free-flight trajectories across the viewing area of the wind tunnel by either of two ways. They can be supported on a vertical wire (at any desired initial angle of attack) at the upstream edge of the viewing window and released into flight by rupturing the wire at a notch within the model. Models can be propelled against the airstream by a pneumatic launch tube located downstream of the window, giving trajectories both upstream and downstream across the window. Two basic methods are used for supporting the model on the launcher. Up to moderate angles of attack (< 40 deg) they can be supported on a wedge within the model base. For high angles of attack (up to 120 deg) the models can be supported in a cradle and are launched in a manner similar to that used by a shot-putter at a track meet.

The model motion is recorded on high-speed (2000-5000 frames/sec) half-frame 35 mm motion picture film using conventional high-speed cameras. Back-light (either silhouette or schlieren) is used to outline the model. Although steady light can be used, in order to eliminate model motion during film exposure (60 μ sec or longer), use is made of multi-flash (500-1000 flashes) short duration (2 μ sec) strobe light, synchronized to the camera. Even though the model motion is normally confined to the vertical plane and, consequently, requires only a single camera, a second one is used to record the motion in the horizontal plane.

Each model has many cycles of oscillation during its viewing-window trajectory (with a large number of high quality pictures being obtained for each cycle) and the motion is appreciably damped. Figure 1 presents a typical angle-of-attack history for a cone during a dynamic stability test. In Figure 2 the oscillation amplitude of another run is plotted aginst the relative airstream distance in the manner used for data reduction.

For further details on model design and construction along with additional information on the launching equipment and data acquisition, References 1-3 will be quite helpful. Data reduction methods are described in Reference 4.

EXAMPLES OF DYNAMIC STABILITY DATA

Even though the sole purpose of the test may be for the measurement of model dynamic stability, the model drag and pitching moment slope are generally obtained during the data reduction. The effect of oscillation amplitude on drag is shown in Figure 3. Data from a recent test (wire-release, August 1964) are compared to the extensive data of Reference 5 where tests (gun-launch) were run during April 1964. The comparison is quite satisfactory for flat as well as hemispherical afterbodies on the sharp-nose, 10-deg half-angle cones.

Figure 4 shows the cone pitching moment slope as a function of Mach number. Contrary to the drag comparison, the effect of the hemispherical afterbody does appreciably affect the pitching moment. The cone tables of Reference 6 were used for the theoretical curve.

An example of a large amount of dynamic stability data (taken from Reference 5) is shown in Figure 5. The data consistency and repeatability are good. Also shown in this figure is the Newtonian solution for the damping coefficient at various amplitudes of oscillation. The increase of damping with oscillation amplitude for the theoretical case is quite small even though the increase is appreciable for Newtonian damping at increasing local angles of attack. Because the Newtonian solution is not sensitive to oscillation amplitude, the Newtonian case will be considered only at zero amplitude in the succeeding figures.

The effect of cone center-of-gravity location on the damping coefficient is shown in Figure 6. The experimental data behave in the manner predicted by the various theories -- Tobak (Reference 7) and Newtonian.

Figure 7 presents cone damping through a Mach number range ($2 < M < 6$) as a function of oscillation amplitude. At zero amplitude the comparison with Tobak is adequate but not ideal since the experimental and theoretical curves are not parallel.

Dynamic stability data from Reference 5 are transferred to the conditions of the August 1964 free-flight test for presentation in Figure 8. Here again the recent data compare favorably with the previous data. The hemispherical afterbody on the cone models does not affect the damping, with or without boundary layer trip. The trip has been shown (Reference 5) to give turbulent cone boundary layer and wake at zero angles of attack.

Limited tests were performed at $M = 6$ in order to compare the damping of cones with different apex angles. In Figure 9 the comparison of trends with Newtonian is shown to be quite good.

At $M = 2$ and 4 several flights were made with flat-based cones blunted to a nose radius to base radius ratio of 0.2. This amount of blunting did significantly decrease the damping, even more so than predicted by Newtonian theory (see Figure 10). The location of the model center of gravity, in respect to the base, was the same for the blunted and sharp cones.

SUMMARY

Enough dynamic stability data for slender cone models have been presented in order to demonstrate the usefulness of this aspect of free-flight testing in conventional wind tunnels. Data were obtained for cone angles of oscillation up to 30 deg amplitudes. Additional wire-release and gun-launch tests have been performed on a series of cone models up to initial oscillation amplitudes of 90 deg at M = 4, 6, 8. Preliminary data analysis indicates test results as good as those presented in this paper.

REFERENCES

1. Dayman, Bain Jr., "Simplified Free-Flight Testing in a Conventional Wind Tunnel", Technical Report No. 32-346, Jet Propulsion Laboratory, Pasadena, California, October 1962.

2. Holway, H. P., J. G. Herrera, and B. Dayman, Jr., "A Pneumatic Model Launcher for Free-Flight Testing in a Conventional Wind Tunnel", Technical Memorandum No. 33-177, Jet Propulsion Laboratory, Pasadena, California, March 1964.

3. Dayman, Bain Jr., "Definitive Interference-Free Experimental Studies of Vehicle Motion", AIAA Preprint 64-476, (Presented at the 1st AIAA Annual Meeting, Washington, D. C., June-July 1964).

4. Jaffe, Peter, "Obtaining Free-Flight Dynamic Damping of an Axially Symmetric Body (At All Angles of Attack) in a Conventional Wind Tunnel", Technical Report No. 32-544, Jet Propulsion Laboratory, Pasadena, California, January 1964.

5. Jaffe, Peter and Robert H. Prislin, "Effect of Boundary Layer Transition on Dynamic Stability over Large Amplitudes of Oscillation", AIAA Preprint 64-427, (Presented at the 1st AIAA Annual Meeting, Washington, D. C., June-July 1964).

6. Sims, Joseph L., "Tables for Supersonic Flow Around Right Circular Cones at Small Angle of Attack", NASA SP-3007, Washington, D. C., 1964.

7. Tobak, Murray and William R. Wehrend, "Stability Derivatives of Cones at Supersonic Speeds", NACA Technical Note 3788, September 1956.

NOMENCLATURE

A	model reference area, $\pi d^2/4$
B.L.	boundary layer
C_D	drag coefficient; $C_D = \frac{\text{Total drag}}{qA}$
C_m	pitching moment coefficient; $C_m = \frac{\text{Pitching moment}}{qAd}$
C_{m_α}	pitching moment slope per radian
$C_{m_q} + C_{m_{\dot\alpha}}$	dynamic damping-in-pitch coefficient per radian $C_{m_q} + C_{m_{\dot\alpha}} = \left[\frac{\partial C_m}{\partial(\frac{\theta d}{V})}\right] + \left[\frac{\partial C_m}{\partial(\frac{\dot\theta d}{V})}\right]$ (assumed constant over cycle)
d	model base diameter (reference length)
f	frequency of oscillation (cycles/sec)
HS	hemispherical
L	model length (for blunted models, length taken as that for sharp-nose model)
M	freestream Mach number
q	freestream dynamic pressure
r_B	model base radius
r_N	radius of nose bluntness
V	freestream velocity
X_{cg}	distance of center of gravity aft of nose (for blunted models from sharp nose before blunting)
X	model position relative to air flow
R_{d_∞}	freestream Reynolds number based on model base diameter

NOMENCLATURE (CONT.)

α	angle of attack
α_{env}	oscillation amplitude
$\bar{\alpha}_{env}$	effective (average) oscillation amplitude over a complete trajectory; $\bar{\alpha}^2_{env} = 2\delta^2$
δ	root-mean-squared angle-of-attack during a complete trajectory
σ	cone half-apex angle
$\dot{\theta}$	model angular velocity

SUMMARY OF AUGUST 1964 DATA

(All Wire-Release)

Run	N	α (deg)	d (in)	r_n/r_B	Afterbody Shape	B.L. Trip Diam. (in.)	X_{cg}/L	α_{env} range (deg)	$\bar{\alpha}_{env}$ (deg)	$C_{m_q} + C_{m_{\dot{\alpha}}}$	f (cps)	V (in/sec)	$\frac{fd}{V}$	R_{d_∞}
4	2	10	1.0	0	Flat	0.01	0.531	22-13½	18.4	-2.48	77	2.06×10^4	3.7×10^{-3}	0.20×10^6
5					HS		0.531	22-15	18.0	-2.48	87		4.2×10^{-3}	
6					Flat		0.532	21½-14	17.7	-2.42	77		3.7×10^{-3}	
7					HS		0.527	22½-12	18.5	-2.61	87		4.2×10^{-3}	
9						0	0.532	22½-15	19.4	-2.44				
11							0.529	21-14	17.3	-2.46				
12				0.2	Flat		0.526	22½-16	19.0	-1.76	92		4.5×10^{-3}	
18	4			0		0.02	0.531	24½-14½	19.3	-1.92	88	2.76×10^4	3.2×10^{-3}	0.35×10^6
21					HS		0.526	23-13	18.9	-1.90	90		3.3×10^{-3}	
23						0	0.532	20½-12½	17.2	-1.85				
24				0.2	Flat		0.524	16½-10	13.9	-1.34	102		3.7×10^{-3}	
26							0.526	21-12½	18.2	-1.29				
29				0	HS		0.528	32-21½	28.0	-2.15	90		3.3×10^{-3}	
30							0.529	30-20	26.4	-2.17				
22	6		0.5		Flat		0.514	24½-19	21.7	-1.88	130	3.50×10^4	1.9×10^{-3}	0.17×10^6
20		15					0.542	29½-22	25.7	-1.00	160		2.3×10^{-3}	
21							0.535	29-22	25.4	-1.02				

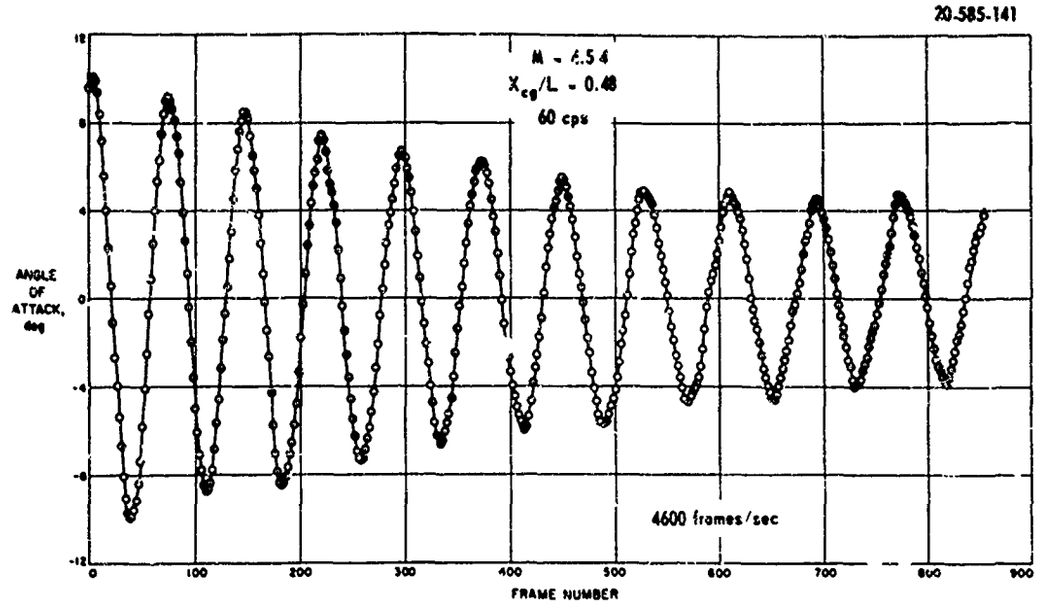

Fig. 1 Example of Gold-Core Cone Gun-Launch

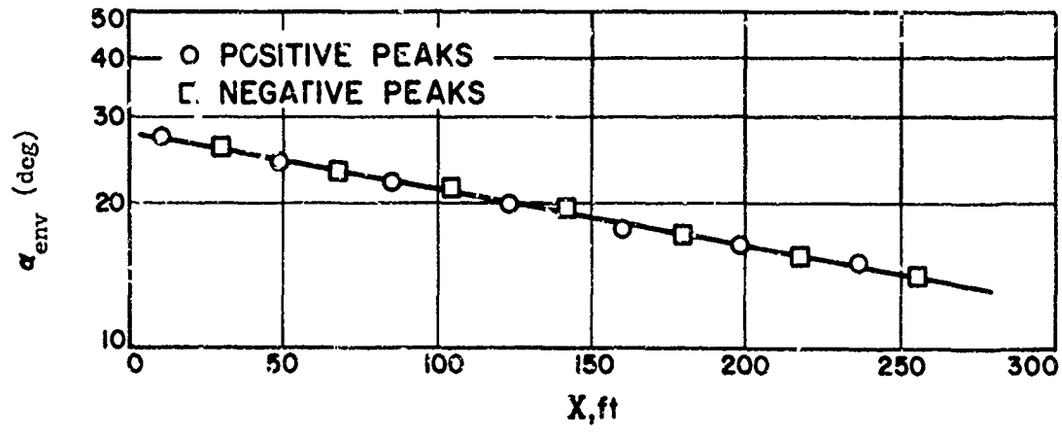

Fig. 2 Oscillation Envelope as a Function of Model Travel Relative to Air Flow

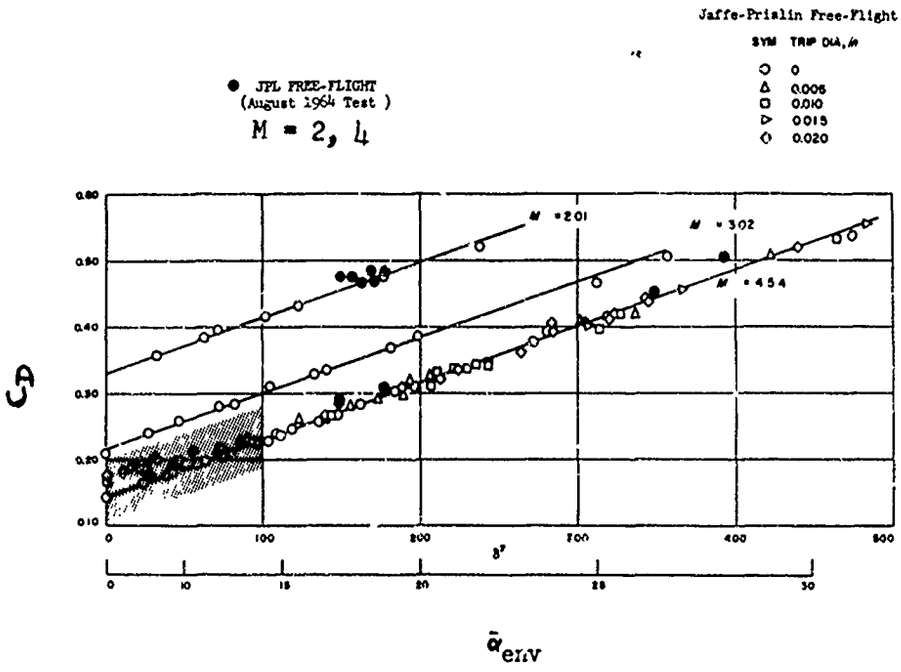

Fig. 3 Effect of Oscillation Amplitude on Cone Drag

$\sigma = 10°$

$r_N/r_B = 0$

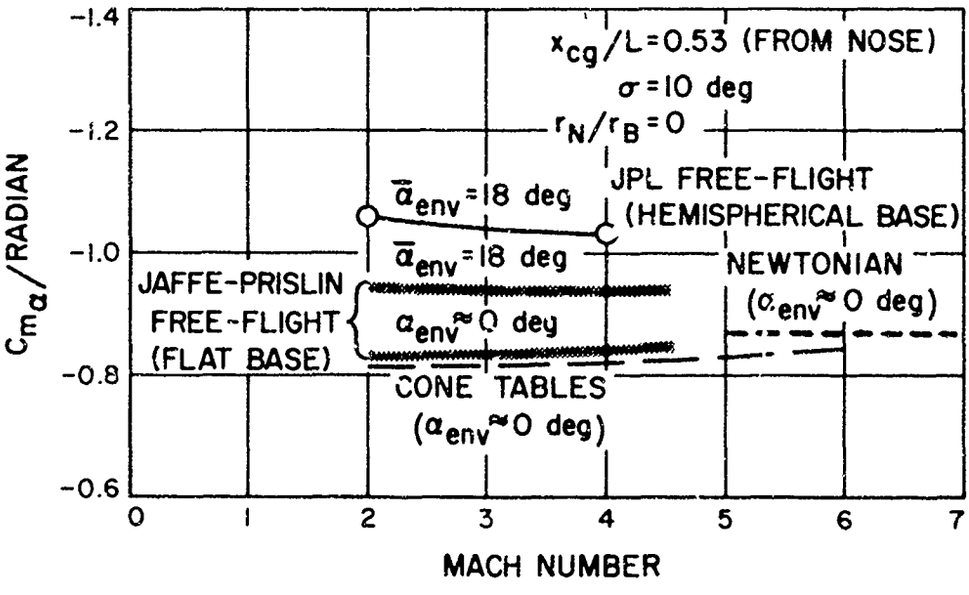

Fig. 4 Cone Effective Pitching Moment Slope

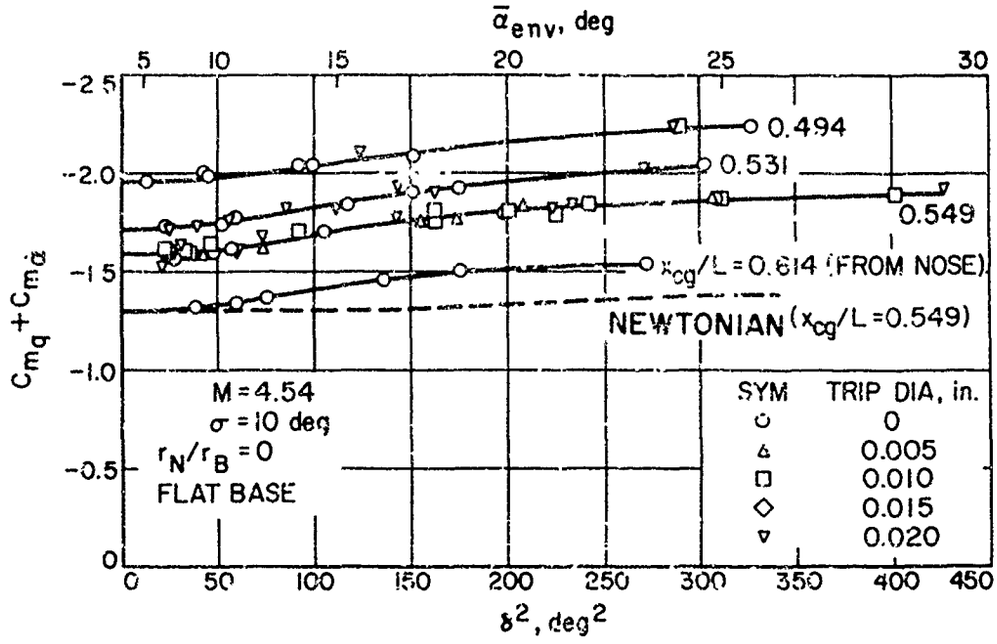

Fig. 5 Free-Flight Cone Dynamic Stability (Jaffe-Prislin)

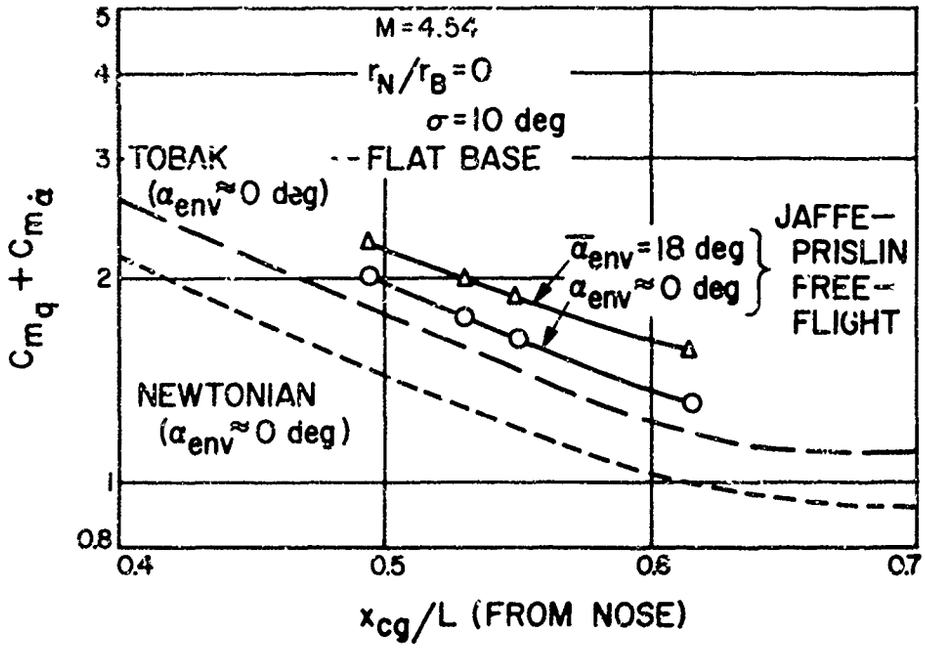

Fig. 6 Effect of Center-of-Gravity Location on Cone Dynamic Stability

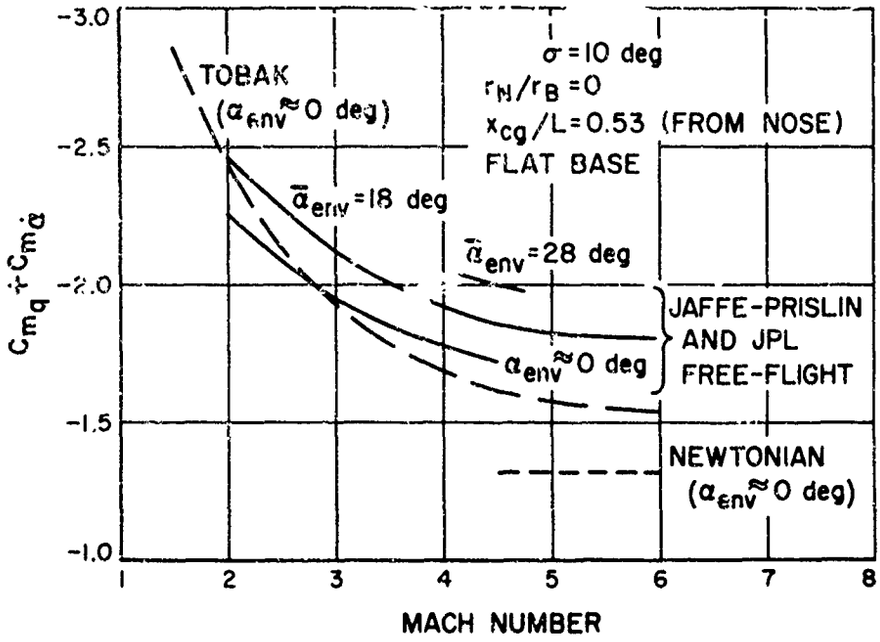

Fig. 7 Effect of Mach Number on Cone Dynamic Stability

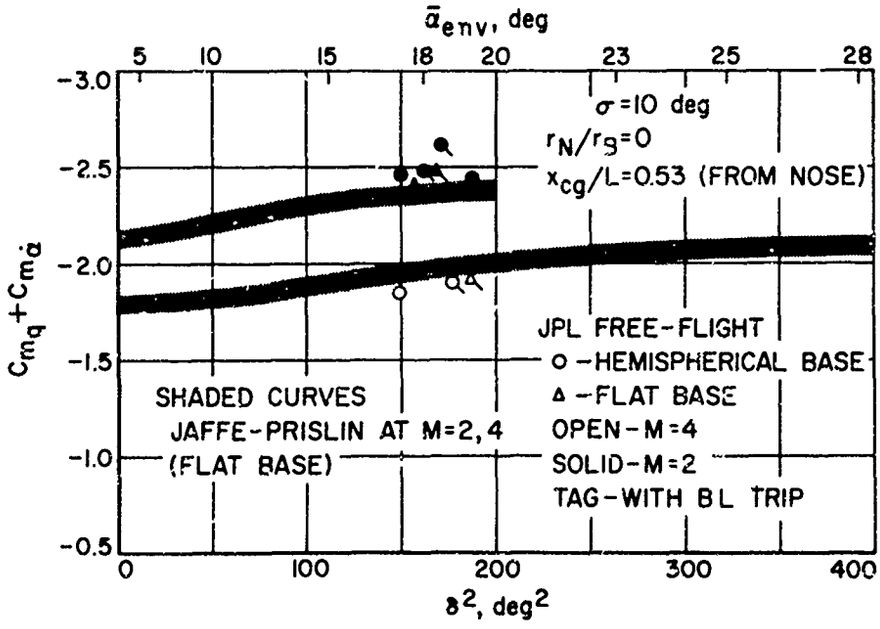

Fig. 8 Effect of Oscillation Amplitude on Cone Dynamic Stability

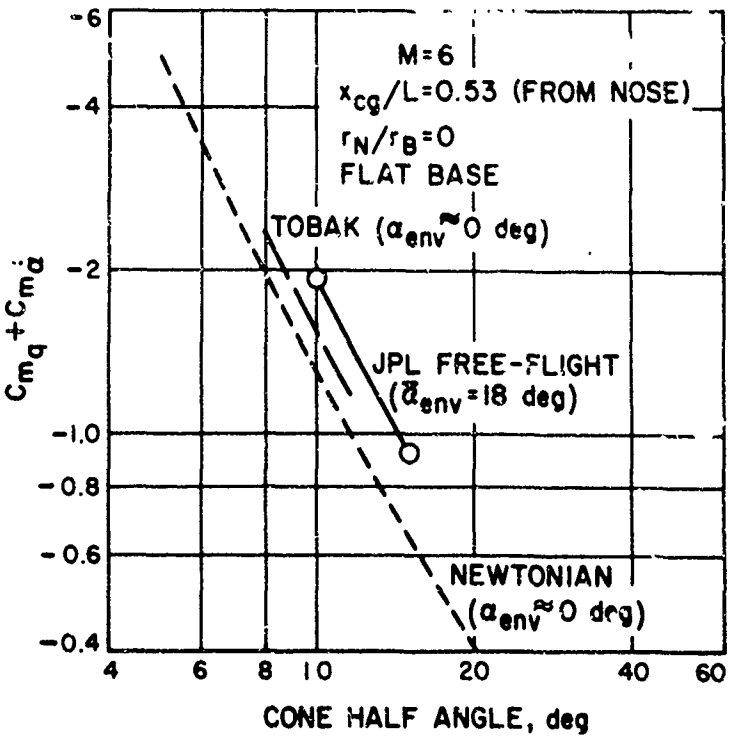

Fig. 9 Effect of Apex Angle on Cone Dynamic Stability

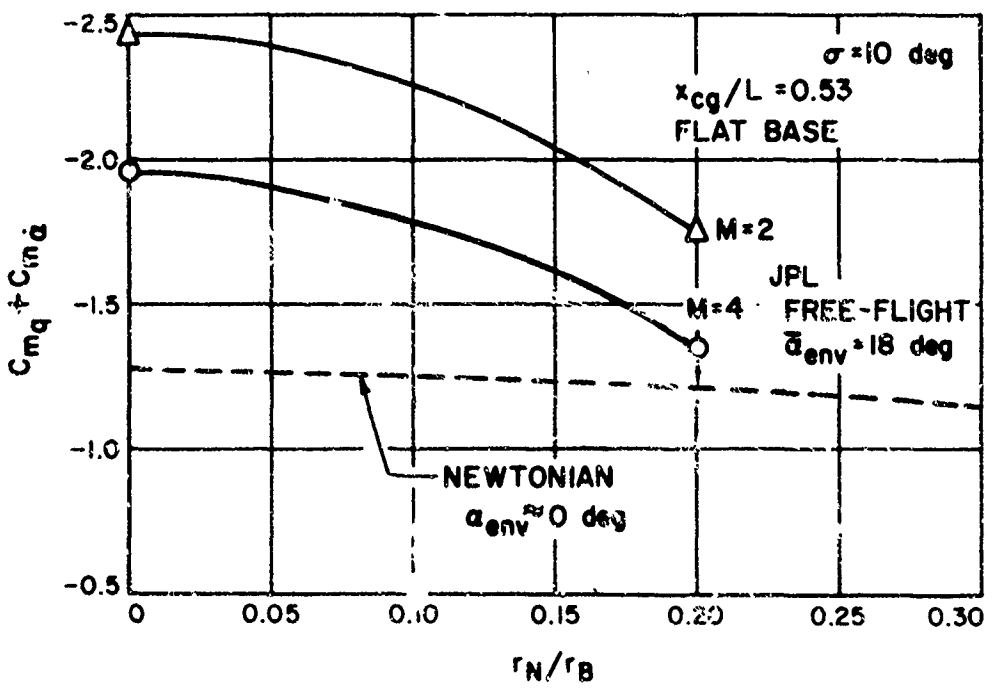

Fig. 10 Effect of Nose Bluntness on Cone Dynamic Stability

CONSIDERATION FOR FLOW HYSTERESIS
AND
MODEL WALL TEMPERATURE EFFECTS
ON THE
FLOW FIELD

by

Bain Dayman, Jr.
Jet Propulsion Laboratory
California Institute of Technology
Pasadena, California

A subject that has been one of the centers of attraction during this workshop is hysteresis of flow separation. At JPL we have been performing tests on a modified form of the Saturn-Apollo configuration. Two major results, neither being necessarily surprising, of this series of investigations are: the effects of hysteresis can be very large; and that an extremely important similarity parameter (one that has been virtually ignored during this meeting) is the ratio of model wall to freestream static temperature.

At zero angle of attack it is possible to alter the flow field about the model from nearly attached to entirely separated by varying the model wall temperature from free-stream static to adiabatic (see Figure 1). This effect has been investigated for Mach numbers from 5 to 9. The free-stream wall temperature was achieved by cooling the models with liquid Nitrogen. The drag coefficient can vary by a factor of about two as the flow goes from separated to attached and the center-of-pressure can change by about 20 percent of the base diameter.

High-speed schlieren movies (5000 frame/sec) indicate hysteresis in the flow (attached vs. separated) as the model oscillates. In the cases where the flow is completed separated at zero angle-of-attack, the flow has characteristics of attached flow at angles of attack above 4 or 5 degrees. The angle at which the flow changes its character depends upon whether the flow is going from attached to separated or vice versa. This phenomenom has been substantiated during subsequent sting-mounted force tests where the data were obtained while the model was being pitched toward and away from zero angle of attack (about two degrees per second).

I have tried to indicate that: hysteresis effects can be very large such as in the case of flow separation on an extreme vehicle configuration - and that the character of a flow-field about a model can be strongly influenced by the model wall temperature, thereby necessitating at least the consideration of this similarity parameter.

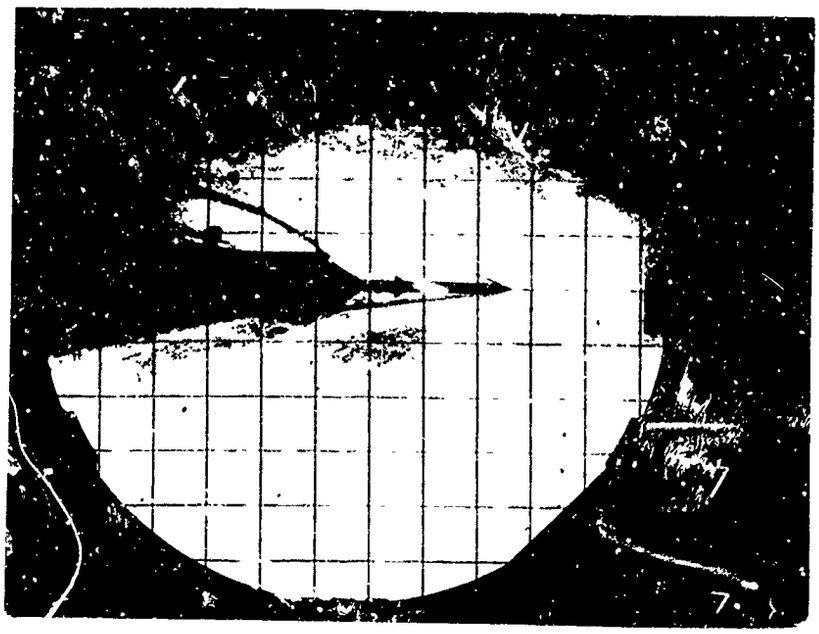

$T_w/T_\infty \approx 5.3$

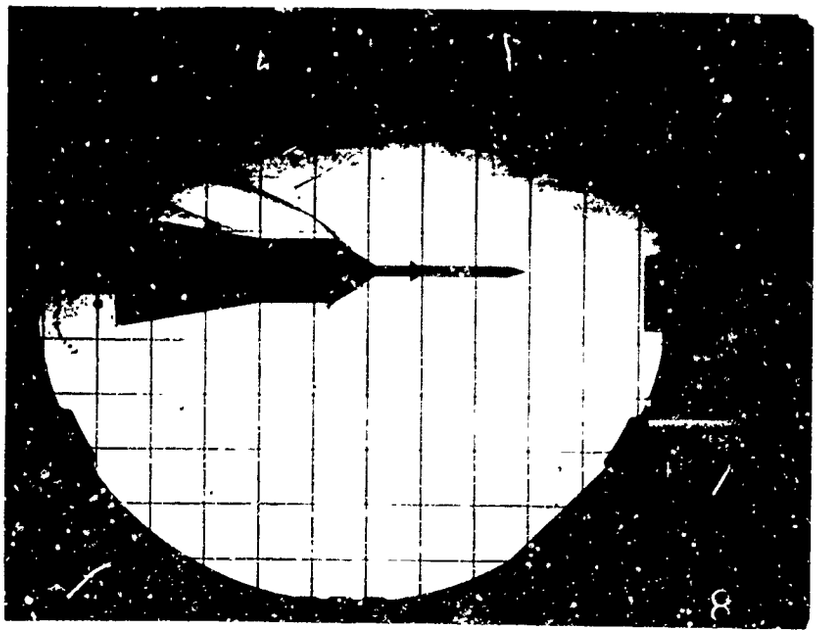

$T_w/T_\infty \approx 1.3$

Flow Field Variations Caused by Model Wall Temperatures

$M = 5 \quad \alpha = 0^\circ \quad R_{D_\infty} \approx 5\frac{1}{2} \times 10^5 \quad$ Alt $\approx$ 170,000 ft

DISCUSSION

Lars Ericsson:

I have a couple of questions; first about the base shape effect. I think you pointed out that it was a turbulent boundary layer and naturally you would not expect this base shape effect to be very dominant then. It would be very dominant when you have transition near the base and it would still be significant when you have laminar boundary layer.

Bain Dayman:

Regarding your comment on that cone--I don't know what you mean because the boundary layer on cones we had with the afterbodies were both laminar and turbulent at $\alpha = 0$.

Lars Ericsson:

I thought you said you tripped the boundary layer to get a turbulent boundary layer.

Bain Dayman:

When we didn't trip the boundary layer, it would stay laminar. The tagged symbols were tripped--(turbulent B. L.)--the untagged symbols were no trip (laminar B. L.).

Lars Ericsson:

Oh, and you still didn't get the effect.

Bain Dayman:

This is correct.

Lars Ericsson:

That dome shape--it still was a sharp shoulder wasn't it?

Bain Dayman:

No, it was very smooth.

Lars Ericsson:

Ok. Now I am confused. Thank you.

Bain Dayman:

That's all I wanted to do--confuse the issue.* Thank you.

Lars Ericsson:

As to this Saturn-Apollo launch configuration shape it looks very familiar to me--I worked on it for the last two years. When did you get this hysteresis and was that with the model cooled?

Bain Dayman:

No, the flow field hysteresis was mostly noticeable on the adiabatic model. The hysteresis is there on the liquid nitrogen cooled models but it doesn't make as dramatic schlieren pictures because the Mach number is higher or the Reynolds number is lower.

Lars Ericsson:

Which angles did you measure for starting separation and for reattachment?

Bain Dayman:

I had rather not comment until the pictures are studied more but it is somewhere between 3 and 5 degrees.

G. Chrusciel:

Had you any thought to testing this spherically base cone at lower Mach numbers, transonically where the effect is very pronounced?

Bain Dayman:

We would like to do it very much but it just turns out that for our particular facility, Mach 2 is the lower limit. If you launch these, you really ought to have orthogonal views in order to not distort any portion of the base shape for the launch. We prefer not to put slots, pins, etc. into the base for doing it. So if you launch it like a shot putter the chances of yaw are considerably higher than launching it with a pin hole or slot. We wire released these models in order to not disturb the shape of the base at all and the wires, when they break in the tunnel and

*The confusion was cleared up later in private discussion by Mr. H. Wiley, NASA Langley, who pointed out that Mr. Dayman's data was for a free flying body with 18 degrees angle of attack envelope. The base-rounding effect discussed earlier is restricted to low angles of attack. Even in planar motion the $\alpha = 0$ effects would probably be diluted enough when integrated over these magnitude amplitudes.

fold back, generate a shock pattern that can intersect the model flight path. As a consequence if we went down in Mach number Mach 1 1/2 would be the minimum but we would have to go down to a half inch diameter cones and I wasn't interested since we demonstrated the point that generalities should not be considered to be general.

G. Chrusciel:

I think that for most of the data shown the significant effect occurred right around Mach 1 and below with the dome shapes.

Bain Dayman:

During this meeting as well as previously we have heard that this effect occurs at higher Mach numbers than that.

R. Meyer:

Just to put this attached versus nonattached flow into perspective, along a typical boost schedule at what Mach number is this effect most significant. At low speeds your adiabatic wall temperature would be very close to free stream and at high speeds the necessities of material would dictate that you would have the cold wall case and so where does this become most significant in the flight article?

Bain Dayman:

I had rather not discuss the flight article--all I can say is that we investigated a model wall to freestream static temperature ratio of 1 to 1 1/2 which would more or less be applicable to the flight regime.

DYNAMIC STABILITY TESTING TECHNIQUES AT THE JET PROPULSION LABORATORY

BY

R. H. Prislin

Jet Propulsion Laboratory

California Institute of Technology

Pasadena, California

This paper presents a summary of information regarding two wind tunnel dynamic stability testing techniques employed at the Jet Propulsion Laboratory; the free-flight technique and the free oscillation technique. The free flight technique refers to actual unsupported model flights in the wind tunnel. The technique incorporates most of the advantages of a ballistic range while eliminating many of the difficulties and limitations. Details of alternate free flight launch techniques and free flight model design criteria are included in the text. The free oscillation technique consists of a model mounted on a bearing in the wind tunnel, free to oscillate in one plane. Through this procedure, large amounts of high quality data may be obtained in relatively short periods of time. The sting effects, inherent in this technique, may be assessed through complimentary use of the free flight technique. Data acquisition and reduction for both techniques are covered in some detail. In the case of the free flight technique, the discussion is limited to planar motion; however, this is a restriction which is possible to remove.

In addition, summary results from a test program designed to investigate the dynamic stability characteristics of sharp and blunted 10 degree cones are presented. This includes only portions of the available data, and in some cases the results are considered preliminary. However, the presented data do point out compatability between the two testing techniques as well as comparisons with theoretical results.

FREE FLIGHT TECHNIQUE

Two actual wind tunnel free flight launch techniques are employed. In both cases an attempt is made to restrict the model to planar motion, as this greatly simplifies the data reduction. In the ensuing discussion, it will generally be assumed this restriction has been met.

In the first technique the models are supported on a vertical wire at the upstream edge of the wind tunnel viewing window. They are released into a free flight trajectory by rupturing the wire at a notch located within the model. This release method allows complete flexibility in the model's initial angle of attack. If the wire hole is placed forward of the model's center-of-gravity, the model will remain in equilibrium before rupture of the wire, and the resulting motion will be planar.

The second method employs a pneumatic launch tube located downstream of the viewing window. This technique allows trajectories both upstream and downstream across the viewing window, effectively doubling the test time per run. The supporting piston is extended such that the model release occurs upstream of the tube bow shock. A set of pneumatic restraining fingers, opened just prior to model launch, provide support during tunnel starting. For flat-base models at angles-of-attack up to 30°, the model is mounted on a wedge fitting within the model base, thus receiving ample support to insure planar motion. In other cases a cradle support, contoured to the model base and side, has been used. This technique has not proved as reliable as the wedge support, resulting in non-planar motion more than half of the time. Launch velocities vary between 20-100 ft/sec, depending on model characteristics and tunnel conditions. Launch pressures for the required velocities are determined empirically. Further details on launching equipment for both techniques can be found in References 1 and 2.

The model motion is recorded with a high speed (4000-5000 frames/sec) 35 mm half frame motion picture camera. Though the model motion is normally confined to the vertical plane, a second camera is used to record the motion in the horizontal plane. This provides verification of planar motion and, in the case of non-planar motion, enough information to facilitate reduction. Back light, either silhouette or schlieren, is used to outline the model. At these frame rates, normal exposure times would be 60-80 μ sec. In order to eliminate model motion during exposure, a short duration, multi-flash strobe light is used. The flash duration can be set as low as 1.2 μ sec. A reluctance pickup on the camera sprocket synchronizes strobe flashes with camera shutter. By incorporating the strobe light tube into the wind tunnel schlieren light house, flow visualization is obtained and parallax distortions are eliminated. A typical run will result in 400 to 1000 frames of data. Angular data can be determined from the film with accuracies ranging from 0.1 to 0.25 degrees, depending on the particular model configuration and size.

Unlike a ballistic range, where the loadings can be as high as $\frac{1}{2}$ million g's, accelerations range from 10 to 100 g's, allowing a model construction designed to optimize the free flight motion for dynamic stability purposes. The dynamic stability coefficient obtained from the free flight technique is a function of the angular decay observed during the flight. Therefore, the accuracy of this coefficient is dependent upon the number of oscillation cycles viewed during the flight, the amplitude decay per cycle, and the ability to determine this decay. The number of cycles in a given distance is proportional to $\left[\left(\frac{-C_{m_\alpha}}{C_D}\right)\left(\frac{md^2}{I}\right)\frac{1}{d}\right]^{\frac{1}{2}}$ and the decay per cycle is approximately proportional to $(C_{mq}+C_{m_{\dot{\alpha}}})\left[(-C_{m_\alpha})^{-1}\left(\frac{d^3}{m}\right)\left(\frac{md^2}{I}\right)\rho\right]^{\frac{1}{2}}$

If the mass distribution remains fixed, such that md^2/I and d^3/m remain constant as the model diameter, d is varied, the number of cycles varies inversely with $d^{\frac{1}{2}}$ while the decay per cycle varies directly with $\rho^{\frac{1}{2}}$. Since a smaller geometrically similar model will have greater amplitude decay than a larger model, the diameter should be minimized subject to the constraints of photographic resolution and facility of launch. Once the diameter has been fixed, the total decay for the flight can be maximized only by maximizing the model m/I^2. This is accomplished by constructing the models of a dense inner core and a thin outside peripheral shell. The models tested range from 0.5 to 1.5 inches in diameter. Both magnesium shells with wall thickness as low as 0.007 inch and injection molded polystyrene models with 0.020" wall thickness have been used. Lead, because of its density, cost, and malleability is well suited for the core material. Components for typical models are shown in Figure 1. Table 1 provides representative values of model test characteristics for a 0.5 inch blunt cone and a 1.0 inch sharp cone, both gun launched. In general, a launch tube release provides in 8 to 12 cycles of data at 60 to 120 cps.

The coordinate system used for data reduction references the model's position to the moving gas media. X is the distance between the model and the media, and is the independent variable for the equations of motion. Assuming first-order linear aerodynamic coefficients ($C_m = C_{m_\alpha}\alpha$; $C_L = C_{L_\alpha}\alpha$; $C_D = C_{D_o}$) and small angular excursions, the equation describing planar angular motion becomes a second-order differential equation with constant coefficients. The solution to this equation is

$$\alpha = \alpha_o e^{\lambda x} \cos\left\{\left[\frac{-\rho A d}{2I} C_{m_\alpha} + \lambda^2\right]^{\frac{1}{2}} x\right\}$$ where

$$\lambda = \frac{\rho A}{4m}\left[C_{D_o} - C_{L_\alpha} + \frac{m d^2}{I}\left(C_{m_q} + C_{m_{\dot\alpha}}\right)\right]$$

Solving for the dynamic stability coefficient in terms of the amplitude envelope:

$$(C_{m_q} + C_{m_{\dot{\alpha}}}) \frac{md^2}{I} = \left(\frac{4m}{\rho A}\right)\left(\frac{\Omega}{n\pi}\right) \ln\left(\left|\frac{\alpha_n}{\alpha_o}\right|\right) + C_{L_\alpha} - C_{D_o}$$

where α_n is the amplitude at the nth half cycle and Ω is the experimental distance oscillation frequency. This $(C_{m_q} + C_{m_{\dot{\alpha}}})$ is an effective coefficient, remaining constant over the n half cycles.

In general, the restrictions imposed upon this solution cannot be met, and a more applicable solution is required. Reference 3 derives an unrestricted equation for the dynamic stability coefficient from energy considerations. Assuming that the pitching moment is a linear function of angle-of-attack during the flight, this equation becomes

$$(C_{m_q}+C_{m_{\dot{\alpha}}})\left(\frac{\pi}{2}\frac{md^2}{I}\alpha_o^2\right) = -\left(\frac{2m}{\rho A}\Omega\alpha_o\delta\alpha\right) - \int_{-(\alpha_o-\delta\alpha)}^{\alpha_o}\int_{\alpha}^{\alpha_o} C_L(\alpha_o^2-\alpha^2)^{\frac{1}{2}}\,d\alpha\,d\alpha \cdots \int_{-(\alpha_o-\delta\alpha)}^{\alpha_o} C_D(\alpha_o^2-\alpha^2)^{\frac{1}{2}}\,d\alpha$$

where $\delta\alpha$ is the decay for a half cycle and C_L and C_D are arbitrary functions of α. In the case where $C_L = C_{L_\alpha}\alpha$ and $C_D = C_{D_o}$, this becomes equivalent to the solution of the linear differential equation if the decay is small enough such that the approximation $-\ln\left(\left|\frac{\alpha_n}{\alpha_o}\right|\right) = \delta\alpha/\alpha_o$ is applicable. In general, this approximation over a half cycle is quite good (Figure 2). Therefore,

by extension a correction to the linear solution which will account for arbitrary lift and drag can be made by incorporating the terms determined from the energy solution. As an example, assume the lift and drag curves take the following form:

$$C_L = C_{L_\alpha}\alpha + k\alpha^3; \quad C_D = C_{D_o} + c_1\alpha^2 + c_2\alpha^4$$

Then the energy solution for $C_{m_q} + C_{m_{\dot{\alpha}}}$ becomes

$$(C_{m_q} + C_{m_{\dot{\alpha}}})\left(\frac{mk^2}{I}\right) = -\left(\frac{4n}{\rho h}\right)\left(\frac{\Omega}{\pi}\right)\left(\frac{\delta_E}{\alpha_o}\right) + \left(C_{L_\alpha} + \frac{3}{4}k\alpha_o^2\right) - \left(C_{D_o} + \frac{c_1}{4}\alpha_o^2 + \frac{c_2}{8}\alpha_o^4\right)$$

These corrections are based on an amplitude which changes during a flight; therefore, it is necessary to define a new amplitude value to be used in the computations and for data correlation purposes. The mean-square resultant angle-of-attack, δ^2, is defined as

$$\delta^2 \equiv \frac{\int_o^N \alpha^2 dN}{\int_o^N dN} \approx \frac{(\alpha_n^2 - \alpha_o^2)}{4\ln\left(\left|\frac{\alpha_n}{\alpha_o}\right|\right)}$$

The mean amplitude for the flight, $\bar{\alpha}_o$, will be defined in terms of δ^2:

$$\bar{\alpha}_o^2 = 2\delta^2 \approx \frac{(\alpha_n^2 - \alpha_o^2)}{2\ln\left(\left|\frac{\alpha_n}{\alpha_o}\right|\right)}$$

In the limit, as the decay approaches zero, $\bar{\alpha}_o = \alpha_o$. In the same manner that k^2 represents the mean angle-of-attack, $\bar{\alpha}_o$ best represents the mean amplitude. Including the lift and drag corrections and the mean amplitude into the linear solution, it becomes

$$(C_{m_{\dot{\alpha}}} + C_{m_{\dot{\alpha}}})\left(\frac{md^2}{I}\right) = \left(\frac{4m}{\rho A}\right)\left(\frac{\Omega}{n\pi}\right) \ln\left(\left|\frac{\alpha_n}{\alpha_o}\right|\right) + \left(C_{L_\alpha} \frac{\delta}{\pi} k \bar{\alpha}_o^2\right) - \left(C_{D_o} + \frac{C_L}{4} \bar{\alpha}_o^2 + \frac{C_2}{8} \bar{\alpha}_o^4\right)$$

The applicability of this equation was verified with an exact computer solution of the equations of motion. The analytical forms of the aerodynamic coefficients were entered into the program and the resulting motion computed. $(C_{m_q} + C_{m_{\dot{\alpha}}})$ was then calculated with the above solution using the computer decay. The deviation between this result and the input value of $(C_{m_q} + C_{m_{\dot{\alpha}}})$ was less than 1%.

It is generally recognized that the presence of a sting, no matter how small is likely to affect the base pressure and base heating of the test configuration. In turn, many aerodynamic measurements, including dynamic stability, may be materially affected by the base flow conditions. However, usual evaluation of data from "captive" type tests tends toward the assumption that support interference is negligible. The free flight technique offers a method to obtain support free data which may be used to check the validity of this assumption.

In addition, the free flight technique allows the extension of wind tunnel dynamic stability testing into areas difficult or impossible to match

with other techniques. Complete flexibility with initial angle of attack as well as the possibility of analyzing non-planar motion are available. Experiments can be conducted in a high oscillation frequency regime which cannot be matched in a captive free-oscillation test. At the present state of the technique development, free-flight dynamic stability coefficients are repeatable to $\pm$ 0.05.* This includes coefficients obtained in alternate wind tunnels at similar conditions. From a qualitative point of view, the technique allows the experimenter an opportunity to view actual flight motion and corresponding stability trends.

*Often repeatabilities are better than this figure. It is expected that additional technique developments will lower this tolerance.

FREE OSCILLATION TECHNIQUE

The models are mounted in the wind tunnel on a sting supported, low friction gas bearing. The bearing uses high purity gaseous nitrogen at 200 psi as a lubricant. At this pressure the bearing is capable of supporting radial loads up to 55 lb. The bearing exhaust is channeled to a point about 2 feet downstream from the model base. However, there is a small amount of leakage, resulting in some exhaust gas escaping through the model base. This leakage affects the model base pressure less than 5%. The maximum model angle-of-attack is limited by the sting to 20 (sharp cone) to 45° (highly blunted cone), depending on the configuration. The model may be remotely pitched to the desired angle-of-attack. The operation of the bearing is normally checked with a calibration sphere prior to recording any data. The calibration sphere mounted on the diameter, which contains an offset mass to provide a restoring moment, is allowed to oscillate until damped by the bearing friction and the aerodynamics. Since the aerodynamic effects are small as the sphere oscillates about a diameter, this damping history provides a qualitative measure of the condition of the bearing.

The data is collected through a system which uses an Optron Tracker*, a passive optical-electronic device which is designed to follow the motion of an object without physical contact. Figure 3 shows a cutaway schematic of the Optron Tracker. The tracker requires a target having a sharp delineation in brightness to provide contrast. This target is optically focused on a photocathode which emits an electron image towards and through an aperature into a photomultiplier section. The photomultiplier output is coupled to a differential amplifier which compares the output signal to a reference

---

*Manufactured by Optron Corporation, Santa Barbara, California

signal established with the sharp line of contrast centered on the aperature. Any deviation from this reference causes the differential amplifier output to become unbalanced and send a correction voltage to a deflection yoke. The deflection yoke repositions the electron beam so it is again centered on the aperature, thus forming a complete servo loop. A readout voltage can be sampled from the differential amplifier output. If the target is not on the model center of rotation, angular deflection will yield vertical displacement of the target, and the Optron Tracker Output will be a function of the model angle-of-attack. The Optron Tracker is calibrated statically by pitching the model to a known angle-of-attack and recording the Tracker output. The relationship between the voltage output and model angle-of-attack is quite linear between -25 and 25 degrees. Thus, the number of points necessary during a calibration is minimized.

The available output from the Optron Tracker is then a continuous analog record of the model angle-of-attack. All that is necessary in order to obtain dynamic stability is a record of the amplitude versus time history. Therefore, it is desirable to sample the Optron output only around peak angle-of-attack areas. This is accomplished as follows: zero voltage output, equivalent to zero angle-of-attack is sensed electronically. Using this, the time for each half oscillation cycle is measured. Every half cycle period is then used to predict the occurence of a peak two half cycles later (two to account for oscillation asymmetries). A sample of the Optron output is recorded 4.5 milliseconds prior to the predicted peak time, and every 0.5 milliseconds thereafter until 4.5 milliseconds after the predicted time (19 records). In general, this method will catch the peak, and in the cases where it does not, the 19 recorded values provide enough information to extrapolate the peak value. Applying the calibration to this data

and summing the half-oscillation cycle times yields the raw data, a time versus oscillation amplitude history. The number of amplitude points per run varies between 30 for a high damping, high tunnel density run, to as many as 1000 in the other extreme. Generally 3 or more runs are taken at each data point in order to provide a consistency check on the equipment operation as well as the results. The angular position of the model can be determined to better than 0.2 degrees. Part of this tolerance is due to difficulties in determining the actual angle-of-attack of the model during the calibration. The decay itself, upon which the dynamic stability coefficient is dependent, can be determined to about 0.1 degrees. Figure 4 shows an amplitude vs time plot obtained through the free oscillation technique.

Because of the physical size of the bearing, the free oscillation models are necessarily large, 4 to 5.25 inches in diameter, in comparison with those used in the free flight technique. This, in turn, leads to substantial loads on the model, and corresponding sting deflections as the model oscillates. It thus becomes necessary to record these deflections such that any effect may be determined. To this end the sting was instrumented with a full strain guage bridge (2 guages on top and 2 on the bottom) which provided a method to determine both loads and sting deflections. Output from the strain guage bridge was recorded simultaneously with the peak angular data, and in addition, was recorded continuously with an oscillograph. Figure 5 presents an oscillograph trace showing the Optron Tracker Output, the strain guage bridge output, and the triggering pulses corresponding to the initial scans of the nineteen records around each peak. Notice in this trace no phase shift or higher harmonic motion is observable.

The equation of motion,

$$I_{\dot{\alpha}} + M_D \dot{\alpha} + M_{\alpha} \alpha = I M_B$$

where

$$M_D = -(C_{m_q} + C_{m_{\dot{\alpha}}}) \frac{q_\infty A d^2}{V_\infty}$$

$$M_{\alpha} = C_{m_\alpha} q_\infty A d$$

M_B = bearing-damping moment (constant damping moment, opposing angular motion)

was solved assuming the coefficients remained constant over one cycle of oscillation. Again the resulting $(C_{m_q} + C_{m_{\dot{\alpha}}})$ is an effective coefficient, remaining constant over an oscillation cycle. The solution for the envelope angle at time t is

$$\alpha_t = \alpha_0 e^{\frac{-M_D}{2I} t} - \frac{M_B \tau^2}{4I\pi^2}\left[1 + e^{\frac{-M_D}{2I} t} + 2e^{\frac{-M_D}{2I}\tau/2}\left(\frac{1 - e^{\frac{-M_D}{2I}(t-\tau/2)}}{1 - e^{\frac{-M_D}{2I}\tau/2}}\right)\right]$$

In the limit, as $\frac{M_D}{2I}$ approaches 0,

$$\left[1 + e^{\frac{-M_D}{2I} t} + 2e^{\frac{-M_D}{2I}\tau/2}\left(\frac{1 - e^{\frac{-M_D}{2I}(t-\tau/2)}}{1 - e^{\frac{-M_D}{2I}\tau/2}}\right)\right] = \frac{4t}{\tau}$$

Therefore, as a first approximation,

$$\alpha_E \approx \alpha_0 e^{\frac{-M_D}{2I} t} \frac{-M_B t \tau}{\pi^2 I}$$

Solving this equation for M_D provides a better approximation for the bearing damping term, thus establishing an iterative procedure which may be used to obtain $(C_{m_q} + C_{m_{\dot{\alpha}}})$.

For the values of $\frac{M_D}{2I}$ which generally occur $\left(\frac{M_D}{2I} < 1 \right)$, this iteration converges quite rapidly (one iteration usually results in an error much less than 1%).

Values for M_B corresponding to various bearing radial loads can be determined experimentally through the use of a sphere with an off center weight (assuming the aerodynamic damping moment is negligible). The data is smoothed using a least squares technique before the above solution is applied. Resulting damping coefficients are, in general, repeatable to $\pm$ 0.04.

DYNAMIC STABILITY DATA

A series of tests designed to investigate the dynamic stability characteristics of a family of blunted 10 deg cones have been conducted in the Jet Propulsion Laboratory supersonic and hypersonic wind tunnels. The principal test parameters were Mach number, Reynolds number, oscillatory frequency, oscillatory amplitude, center of rotation, and bluntness ratio. Only a portion of the data from this program is presented here, and in some cases it is still considered preliminary. However, there is ample data presented such that both testing techniques are exemplified and compared. For the class of bodies tested with the free oscillation technique, the bearing damping was negligible in comparison to the aerodynamic dynamic damping. Therefore, the term M_B was set equal to zero in the reduction equations. Table 2 contains a summary of the tests and corresponding test parameters. The nomenclature of Table 2 is explained in Figure 6, which shows a typical model, with a contoured base and a bluntness ratio, r(nose)/d(base), of 0.094. Unless specified otherwise, all configurations had flat bases. Notice that for all blunt cones the center of gravity location is referenced in lengths of a hypothetical sharp cone from the hypothetical sharp nose.

Figures 7 and 8 show the effects of oscillation amplitude on the dynamic stability coefficient. Figure 7 contains free-oscillation and free flight data for the sharp cone configuration at several centers of rotation. Note, the free flight data was obtained at $M_\infty = 4.5$ and the free-oscillation data at $M_\infty = 6.0$. Both techniques indicate the same trend of increasing dynamic stability coefficient with increasing amplitude. The free-oscillation data begins to rise somewhat earlier (4 to 6 deg) than does the free flight data

(8 to 10 deg) but, thereafter the curves appear to remain parallel. The effect of amplitude on a blunted 10° cone is shown in Figure 8. This data, taken at $M_\infty = 6.0$ by the free-oscillation technique, indicates a greater change in the dynamic stability coefficient with amplitude than was seen with the sharp cone. For the 0.6 ℓ case, there is a 14% rise as the amplitude increases from 4 to 18 deg with the sharp cone, whereas, there is a 57% increase with the blunted cone. It should be noted, however, that in case of very blunt cones (r/d = 0.423) this trend reversed itself to the point where there is no discernable amplitude effect (Reference 4).

Figure 9 presents the effect of center of rotation on the dynamic stability coefficient at constant amplitude for the sharp cone. This figure includes free flight data taken at $M_\infty = 3.0$ and 4.5 and free-oscillation data taken at $M_\infty = 6.0$. The data are compared with Tobaks first and second order potential flow solution, applicable near 0 angle-of-attack (Reference 5). There is good agreement at all Mach numbers, the maximum deviation being on the order of 7%. This plot shows excellent correlation between the data obtained by the two alternate testing techniques.

The same type of data for a blunt 10 deg cone, r/d = 0.094, with a contoured base is shown in Figure 10. Again there are several Mach numbers and both free flight and free-oscillation data are presented. The data are compared with a curve calculated from the Newtonian impact Theory. The free flight and free-oscillating curves exhibit the same shape; however, the levels of the two curves differ by about 10%. No explanation for this inconsistency is apparent at this time. In the upper right of this figure is a summary of the effect of Mach number, for this blunt configuration, obtained from the free-flight data.

Figure 11 shows the effect of Mach number on dynamic stability for the sharp cone. Again, both free flight and free oscillation data are shown on this plot. The solid line represents Tobak's potential flow solution while the dashed line represents a shock expansion solution (Reference 6). Both theories agree with experimental data to better than 7%. Both theory and experiment show a pronounced drop in the coefficient in the region of $M_\infty = 2$ to 3, and both show an indication of a drop in the $M_\infty = 6$ to 8 region.

The effects of bluntness on dynamic stability from the free-flight data is shown in Figure 12 along with a curve from the Newtonian impact theory. The points at r/d = 0.2 and 0.3 are preliminary data and are not as reliable as the remaining points. The experimental data for the sharp cone (r/d = 0) is about 30% above the Newtonian. As the bluntness ratio increases the experimental and Newtonian curves tend to converge meeting near r/d = 0.3. Experimental data at r/d = 0.423 (Reference 4) also indicates good agreement with Newtonian, confirming the general trend.

NOMENCLATURE

A	model reference area, $\pi d^2/4$
a	model acceleration
c.g.	distance to the center of gravity from nose
C_D	drag coefficient; C_{D_o} = drag coefficient at zero angle-of-attack
C_L	lift force coefficient; C_{L_α} = lift force coefficient slope per radian
C_m	pitching moment coefficient; C_{m_α} = pitching moment coefficient slope per radian
C_{m_q}	dynamic damping in pitch coefficient per radian, $\left[\frac{\partial C_m}{\partial(\frac{\dot{\theta} d}{V})}\right]$ (assumed constant over a cycle)
$C_{m_{\dot{\alpha}}}$	$\left[\frac{\partial C_m}{\partial(\frac{\dot{\alpha} d}{V})}\right]$ (assumed constant over a cycle)
$(C_{m_q} + C_{m_{\dot{\alpha}}})$	dynamic stability coefficient (assumed constant over a cycle)
d	model diameter, reference length
I	model moment of inertia about a transverse axis at center of gravity
ℓ	length of sharp cone, 2.8356 d
M_∞	free stream Mach number
m	model mass
q_∞	free stream dynamic pressure
Re_d	Reynolds number based on model diameter and free stream condition
V_∞	free stream velocity
X	model position relative to media

α	angle-of-attack
α_o	initial oscillation amplitude
$\bar{\alpha}_o$	effective oscillation amplitude
α^2	root-mean-squared angle-of-attack
$\delta\alpha$	amplitude decay
θ	angle between freestream velocity vector and model centerline
ρ	gas density
τ	oscillation period, sec
Ω	oscillation frequency, rad/distance, x, traveled
ω	oscillation frequency rad/sec
$(\dot{})$	derivative with respect to time

Subscripts

o	conditions at time = 0
E	envelope
eff	effective
n	conditions after n half-angles of oscillation
∞	free stream conditions

TABLE 1

Configuration	Wall Material	dia (in)	c.g. (% ℓ)	m (slugs)	I (slug - ft^2)	a/g (α = 0° M_∞ = 4 q_∞ = 3 psi)	Flight time (sec)
Sharp Cone	Plastic	1.0	54.9	0.78 X 10^{-3}	0.10 X 10^{-5}	14.0	0.18
r/d = 0.3	Magnesium	0.5	66.0	0.20 X 10^{-3}	0.31 X 10^{-7}	37.0	0.12

TABLE 2

Configuration	Test No.	Mach No.	c.g. % ℓ aft of nose	Re/in x10^{-6}	$\omega d/_V$ x 10^2
A. FREE OSCILLATION					
sharp cone	21-176	6.0-8.0	60.4-66.2	0.04-0.20	0.25-0.55
r/d = 0.091	21-176	6.0-8.0	60.4-66.2	0.07-0.20	0.36-0.68
r/d = 0.094 - contoured base	21-176	6.0-8.0	60.6-66.5	0.02-0.28	0.17-0.53
sharp cone	20-577	2.0-4.0	60.4-66.2	0.04-0.29	0.21-0.95
r/d = 0.091	20-577	2.0-4.0	60.4-66.2	0.04-0.29	0.33-1.22
r/d = 0.200	20-577	2.0-4.0	60.4-66.2	0.04-0.29	0.36-1.22
r/d = 0.423	20-548	2.0-4.5	85.1	0.02-0.34	0.10-1.40
r/d = 0.423	21-134	6.0-8.0	85.1	0.03-0.23	0.07-0.70
B. FREE FLIGHT					
sharp cone (Ref. 7)	21-172, 20-555, 20-562, 20-585	2.0-4.5	49.4-61.4	0.17-0.34	0.94-1.99
r/d = 0.094 - contoured base	21-172	4.0-8.0	48.0-59.0	0.22-0.25	0.57-1.19
r/d = 0.1	20-598	4.0	54.7	0.28	1.44
r/d = 0.2	20-598	4.0	66.0	0.28	1.13
r/d = 0.3	20-598	4.0	66.0	0.28	1.19
r/d = 0.4	20-598	4.0	81.7	0.28	1.18

REFERENCES

1. Dayman, Jr., Bain, "Simplified Free-Flight Testing in a Conventional Wind Tunnel", Technical Report No. 32-346, Jet Propulsion Laboratory, Pasadena, California, October 1962.

2. Holway, H. P., J. G. Herrera and Bain Dayman, Jr., "A Pneumatic Model Launcher for Free Flight Testing in a Conventional Wind Tunnel", Technical Memorandum No. 33-177, Jet Propulsion Laboratory, Pasadena, California, March 1964.

3. Jaffe, Peter, "Obtaining Free-Flight Dynamic Damping of an Axially Symmetric Body (At all Angles of Attack) in a Conventional Wind Tunnel", Technical Report No. 32-544, Jet Propulsion Laboratory, Pasadena, California, January 1964.

4. Prislin, Robert H., "Captive Dynamic Stability Tests of Blunt Entry Configuration in the JPL Supersonic and Hypersonic Wind Tunnels", WT 20-548, Jet Propulsion Laboratory, Pasadena, California, May 1964.

5. Tobak, M. and W. R. Wehrend, "Stability Derivatives of Cones at Supersonic Speeds", NACA TN 3788, September 1956.

6. Saverwein, H., "Application of the Piston Analogy to the Calculation of Stability Derivatives for Pointed Axially Symmetric Bodies at High Mach Numbers", RAD-TM-61-40, October 1961.

7. Jaffe, Peter, and Robert H. Prislin, "Effect of Boundary Layer Transition on Dynamic Stability over Large Amplitudes of Oscillation" AIAA Paper No. 64-427, June 29, 1964.

FIGURES

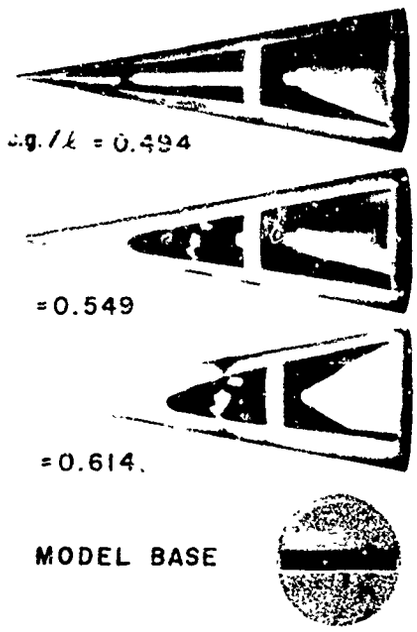

Figure 1. Typical Model Construction

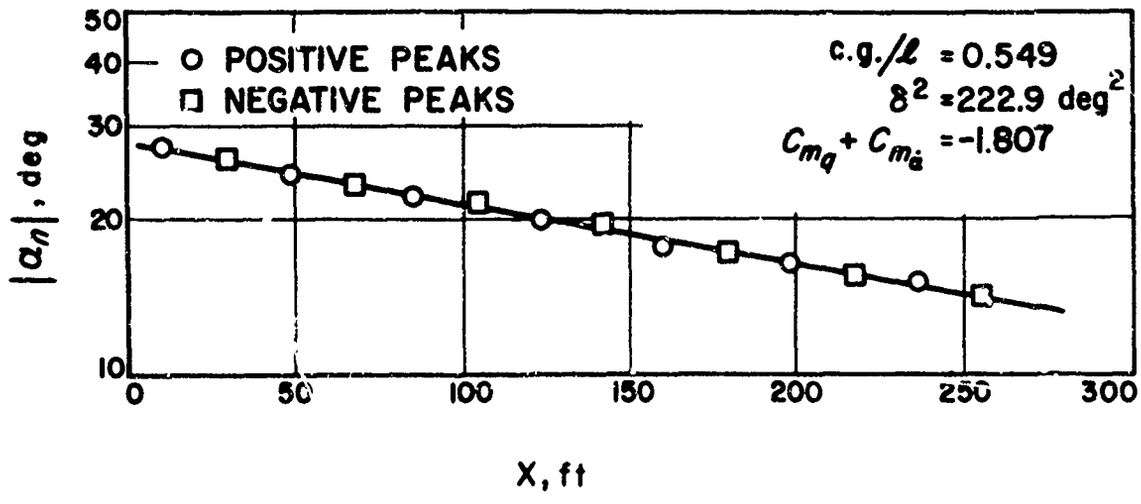

Figure 2. Free Flight Alpha Envelope vs Distance

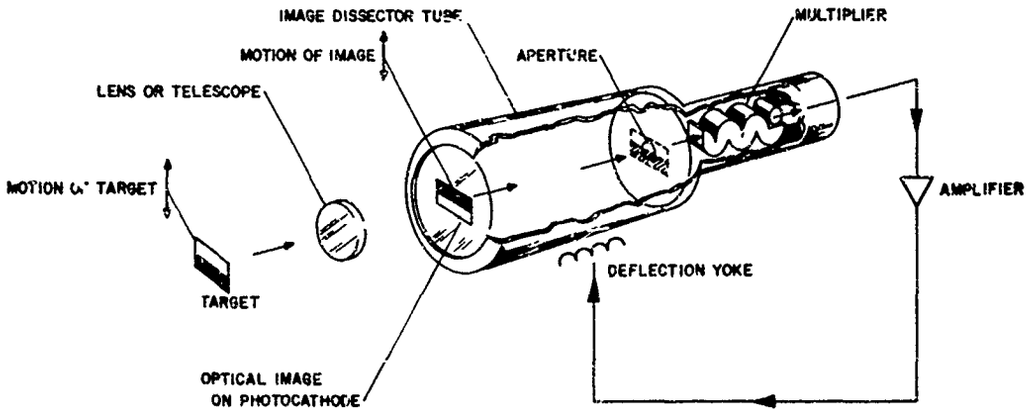

Figure 3. Cutaway Schematic of Optron Tracker

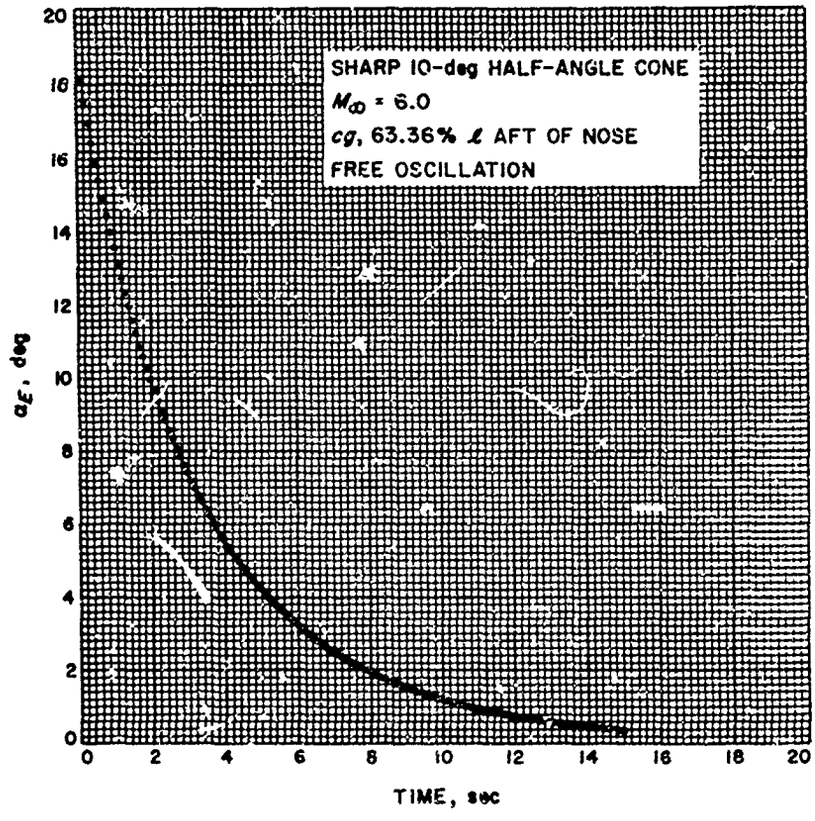

Figure 4. Free Oscillation Amplitude vs Time

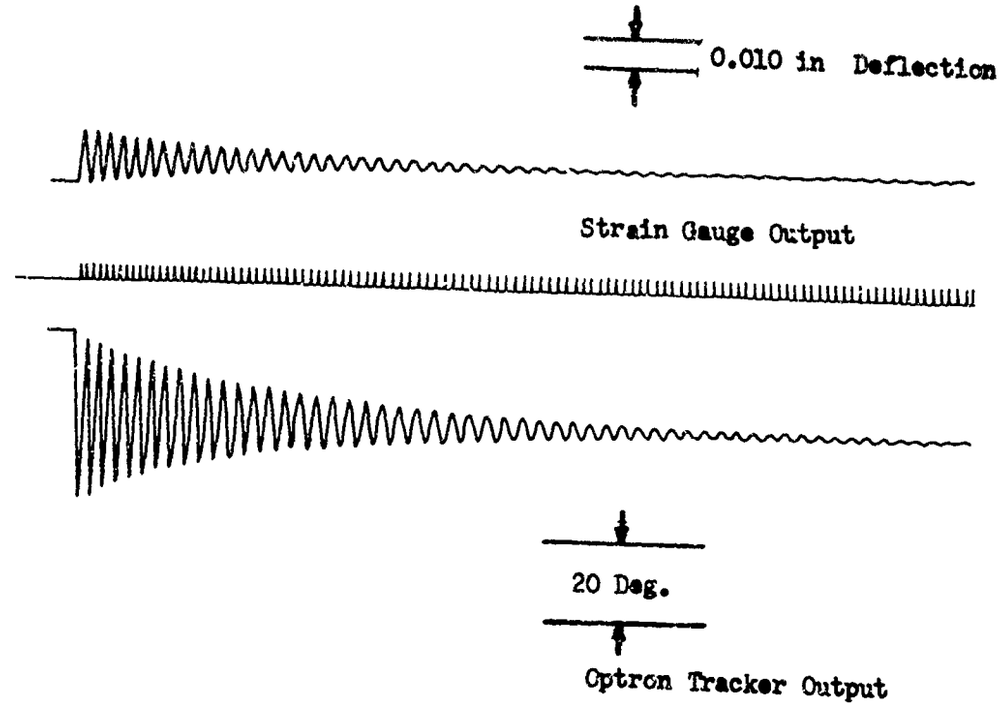

Figure 5. Oscillograph Trace of Optron and Strain Guage Output

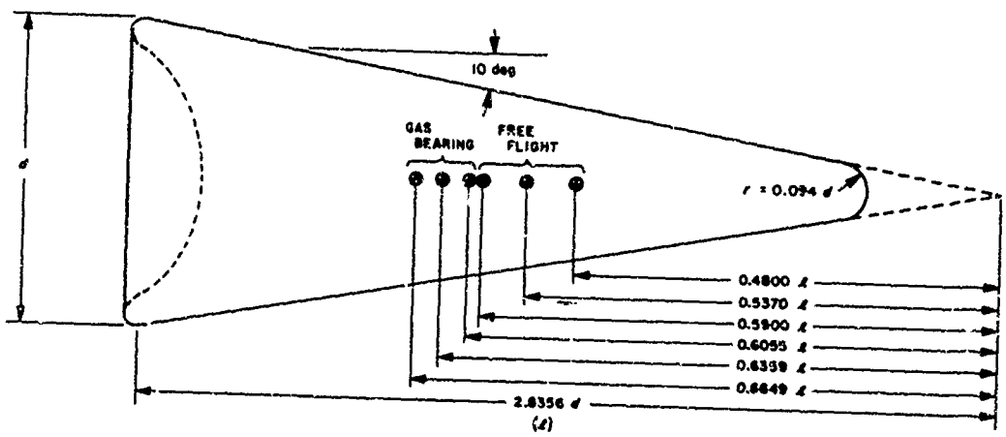

Figure 6. Typical Test Configuration

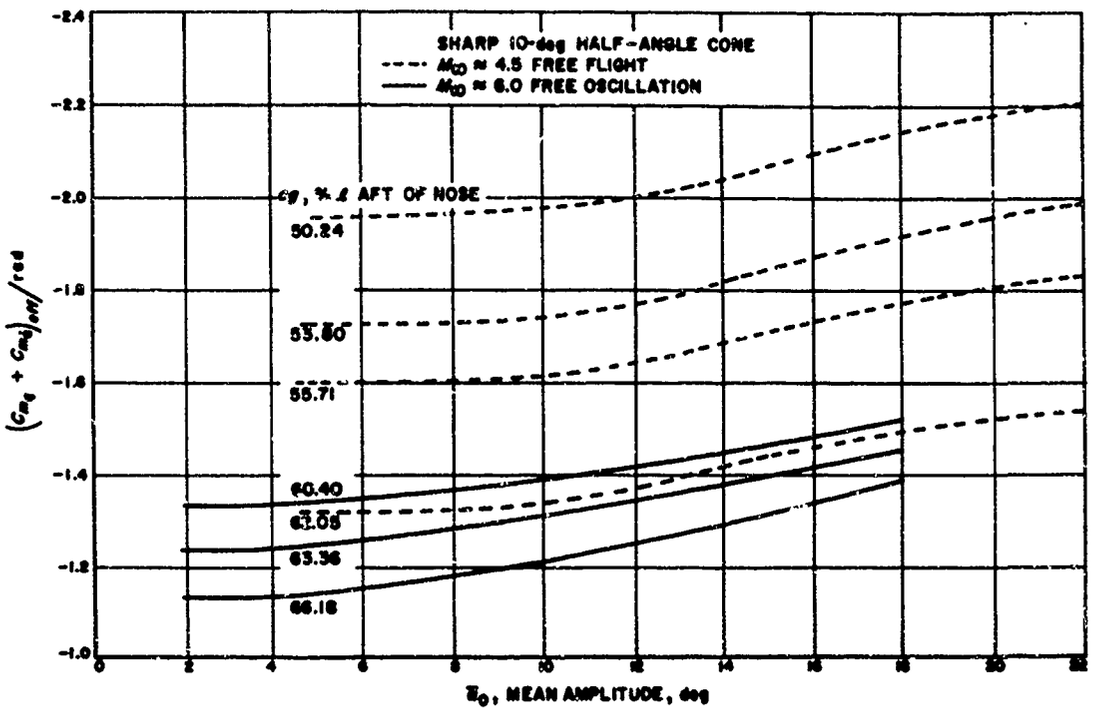

Figure 7. Effects of Oscillation Amplitude on Dynamic Stability for a Sharp Cone

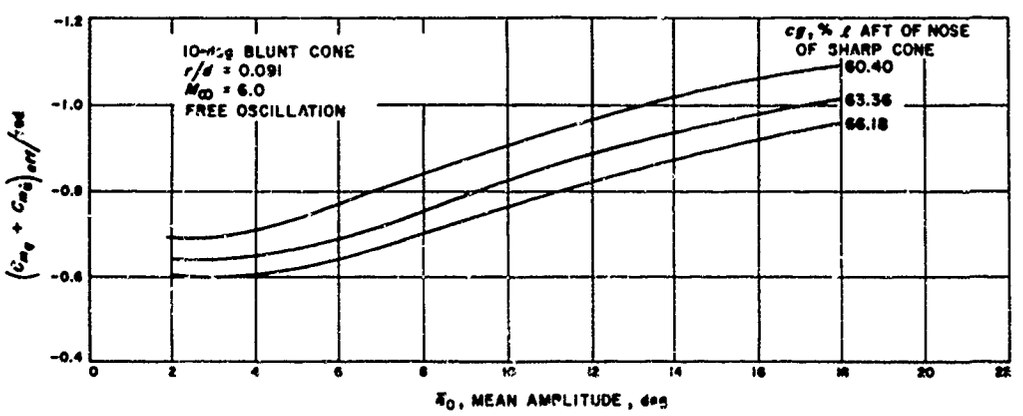

Figure 8. Effects of Oscillation Amplitude on Dynamic Stability for a Blunt Cone

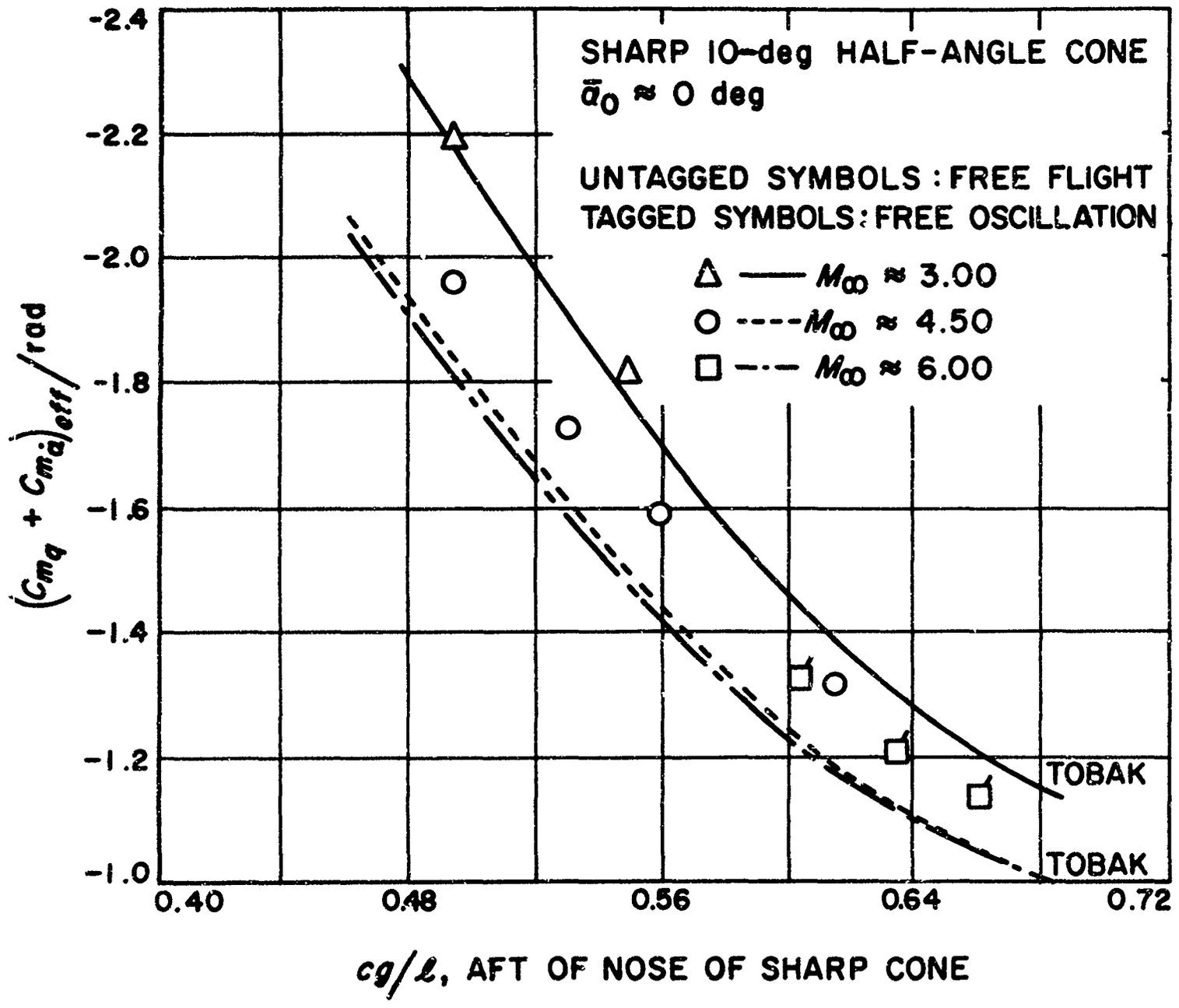

Figure 9. Effects of Center of Rotation on Dynamic Stability for a Sharp Cone

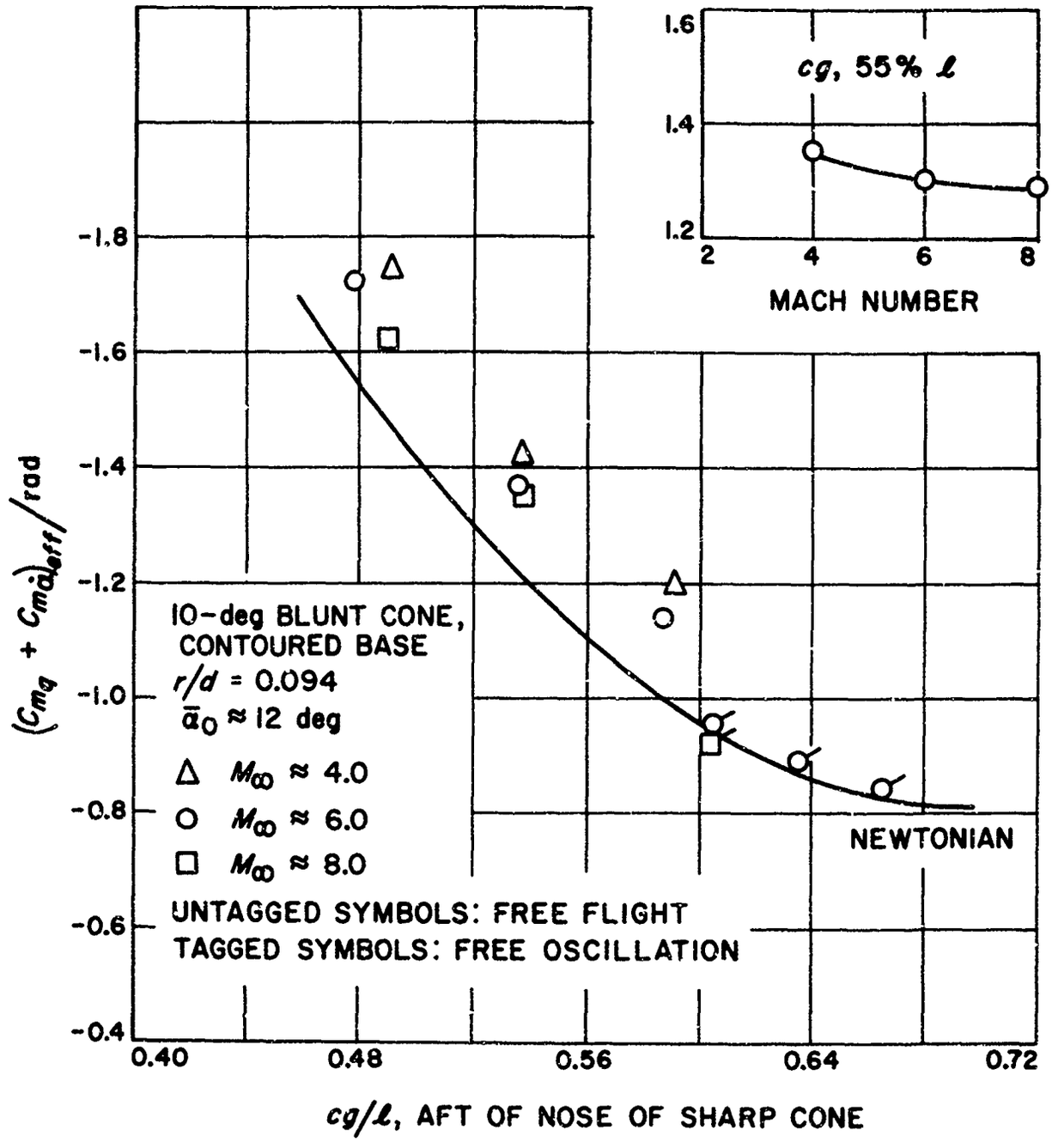

Figure 10. Effects of Center of Rotation on Dynamic Stability for a Blunted Cone

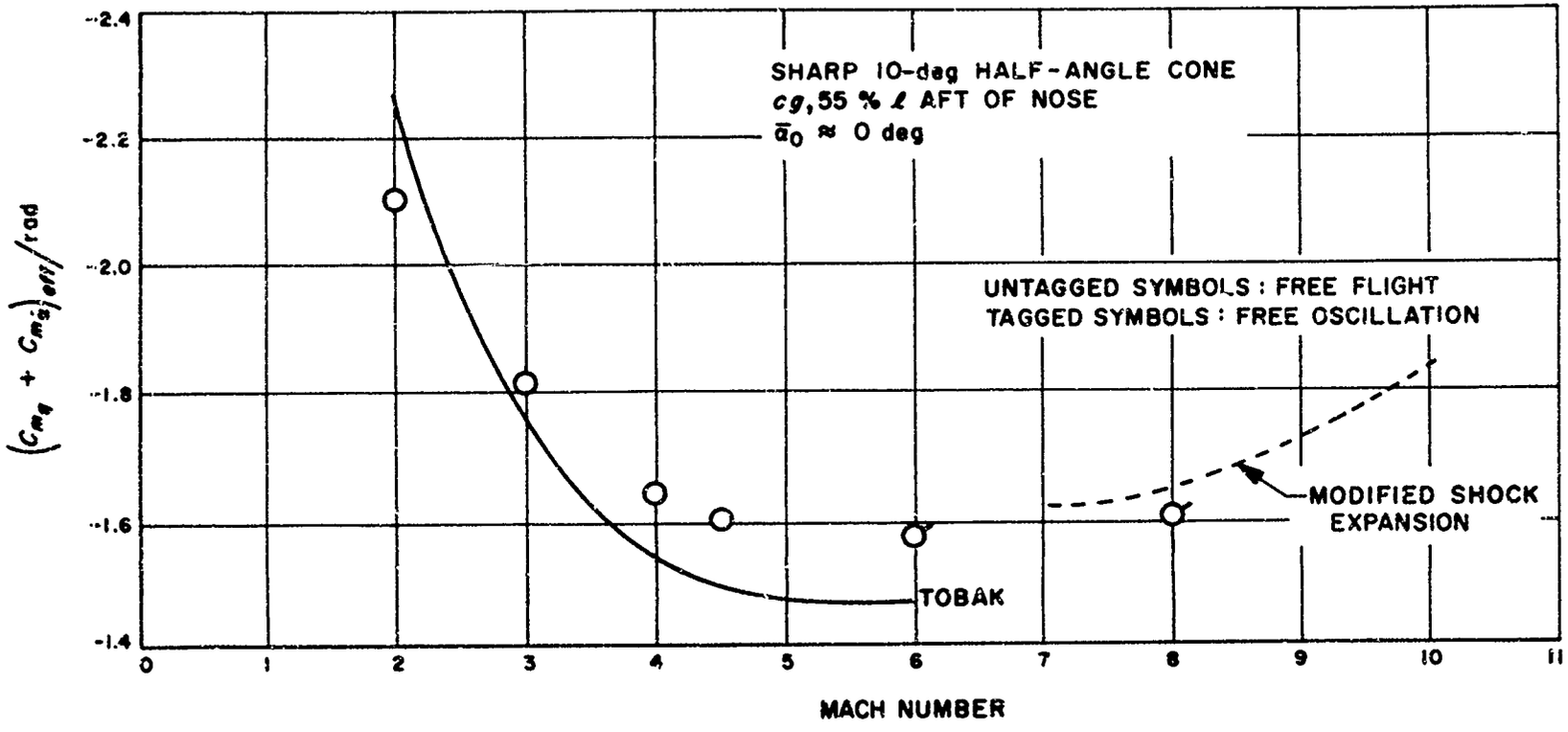

Figure 11. Effects of Mach Number on Dynamic Stability for a Sharp Cone

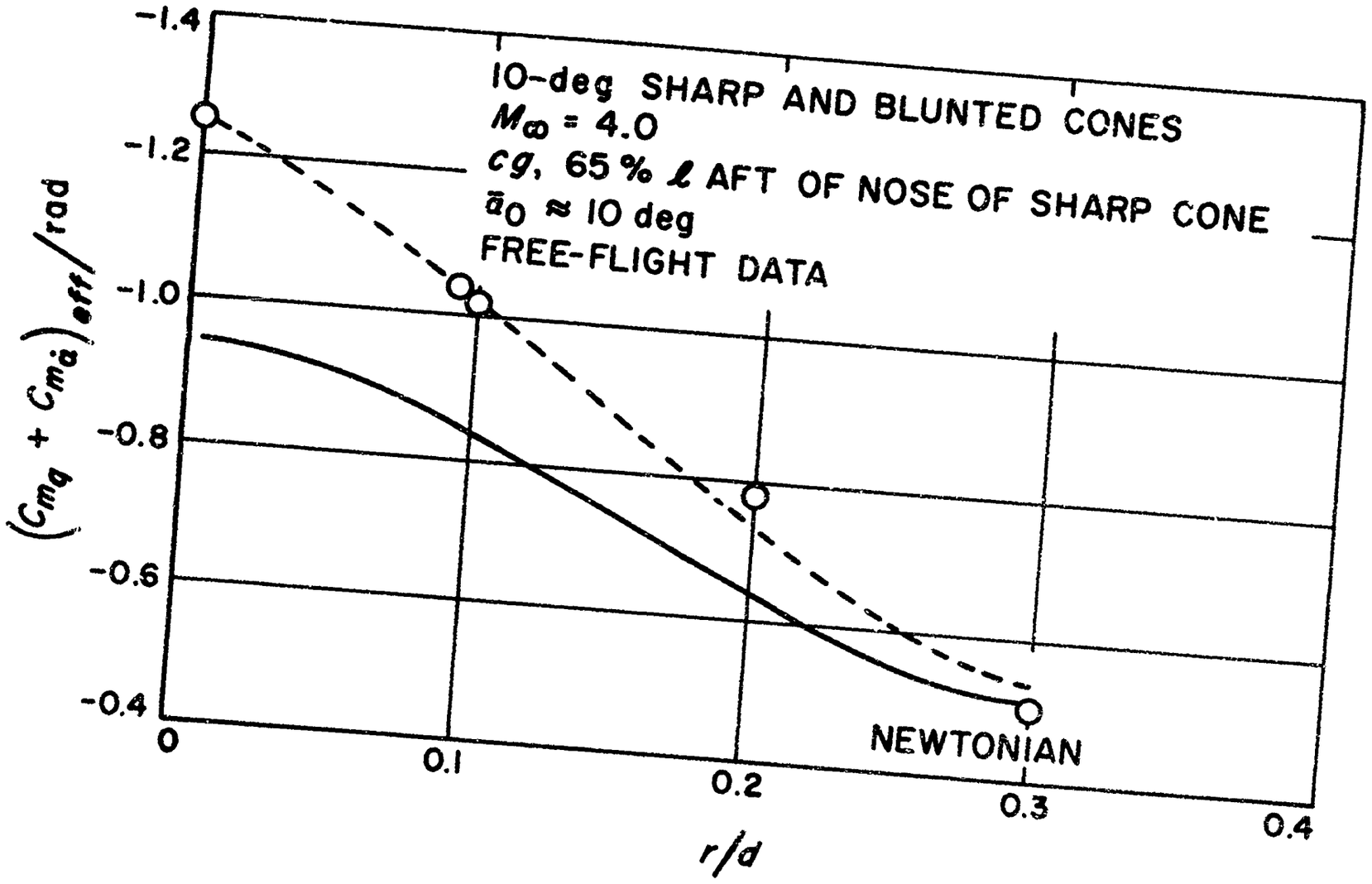

Figure 12. Effects of Bluntness on Dynamic Stability

DISCUSSION

M. Fink:

You mentioned the angle of attack effect being different at different Mach numbers. One of the slides in my talk yesterday showed a computed variation of damping in pitch with angle of attack and this did vary as a function of Mach number or Mach number similarity parameter. At the lower Mach numbers it was predicted to increase with increasing angle of attack-at the higher Mach numbers it first decreased then increased with increasing angle of attack. I don't remember exactly how it goes with what Mach numbers for a 10 degree cone but it may be that Mach 10 for a 10 degree cone is where it is fairly level for a while and then increases.

L. K. Ward:

This was a sharp cone?

M. Fink:

Yes. My axisymmetric results for non-zero angle of attack are only for sharp cones. This nonlinearity with angle of attack being different for different Mach numbers is something that does come out of the theory and something that has been shown. Data which I hadn't shown in a slide in my talk but which is in the written version of the paper includes the 20 degree Mach 8 AEDC data of a few years ago which does show the decrease of damping with increasing angle of attack over a moderate range of angle of attack.

P. Jaffe:

For Mr. Fink's benefit, this data is the effective constant coefficient whereas your computed data would be for the local values, and in using it this should be remembered. There isn't a direct connection unless you include some angular motion.

FREE-FLIGHT TECHNIQUE FOR MEASURING DYNAMIC STABILITY OF ABLATING MODELS

By Lionel L. Levy, Jr.

NASA, Ames Research Center,
Moffett Field, Calif.

An investigation to determine the effects of ablation on the dynamic stability of reentry vehicles has been initiated at the Ames Research Center. The investigation utilizes a free-flight technique in an arc-heated wind tunnel.

The wind tunnel is shown schematically in Figure 1. A vertical arc-heated wind tunnel is used so that the model weight can be balanced by the drag force and thus permit maximum viewing time through the test-section windows. The test gas, air, is heated by striking a dc arc between two water-cooled ring electrodes. To prevent overheating the electrodes, the arc is spun at high speeds by the magnetic field produced by coils surrounding the arc chamber. The air is expanded through a contoured nozzle (12-inch exit diameter) to produce the desired conditions in the open-jet test chamber. A contoured nozzle is used to provide the most uniform flow in the test chamber consistent with the minimum vertical gradient of dynamic pressure required to stabilize model motions in the vertical direction.

Of paramount importance to this investigation is the assurance of steady-state ablation for the full interval of flight. Thus, it is necessary to hold the model in the stream until steady-state ablation is established and then release it for free flight.

The mechanism used to hold and release the model is shown in Figure 2. A piece of monofilament line attached to the base of the model, and looped around a "hot wire," holds the model firmly against the bottom of a retractable tube. When it is desired to release the model, an electrical circuit is energized which heats the wire and severs the monofilament. At the same time the tube is retracted upward, leaving the model in free flight.

Free-flight motions of the model are recorded photographically by movie cameras placed to observe the motion in two orthogonal planes. The film speed is about 250 frames per second.

A representative frame from a film record of the model motion is shown in Figure 3. The test conditions were a total pressure of 6.8 atmospheres, a total enthalpy of 2100 Btu/lb (velocity approximately 10,000 ft/sec), a Mach number of 10, and a Reynolds number of 500 based on model diameter.

Successful flights to date include ablating and nonablating models of axisymmetric blunt-faced reentry vehicles. Flight times range from 2 to 4 seconds. The corresponding flight distance is approximately 10,000 feet for each second of flight and the models experienced about 3 cycles of oscillation per second of flight.

In the present data reduction procedure, time histories of model motions determined from movie film are punched on cards, processed by an IBM 7094 computer, and stored on tape. The taped information will be used as input to a 7094 program for solving the equations of motion. The latter program is in the formative stages.

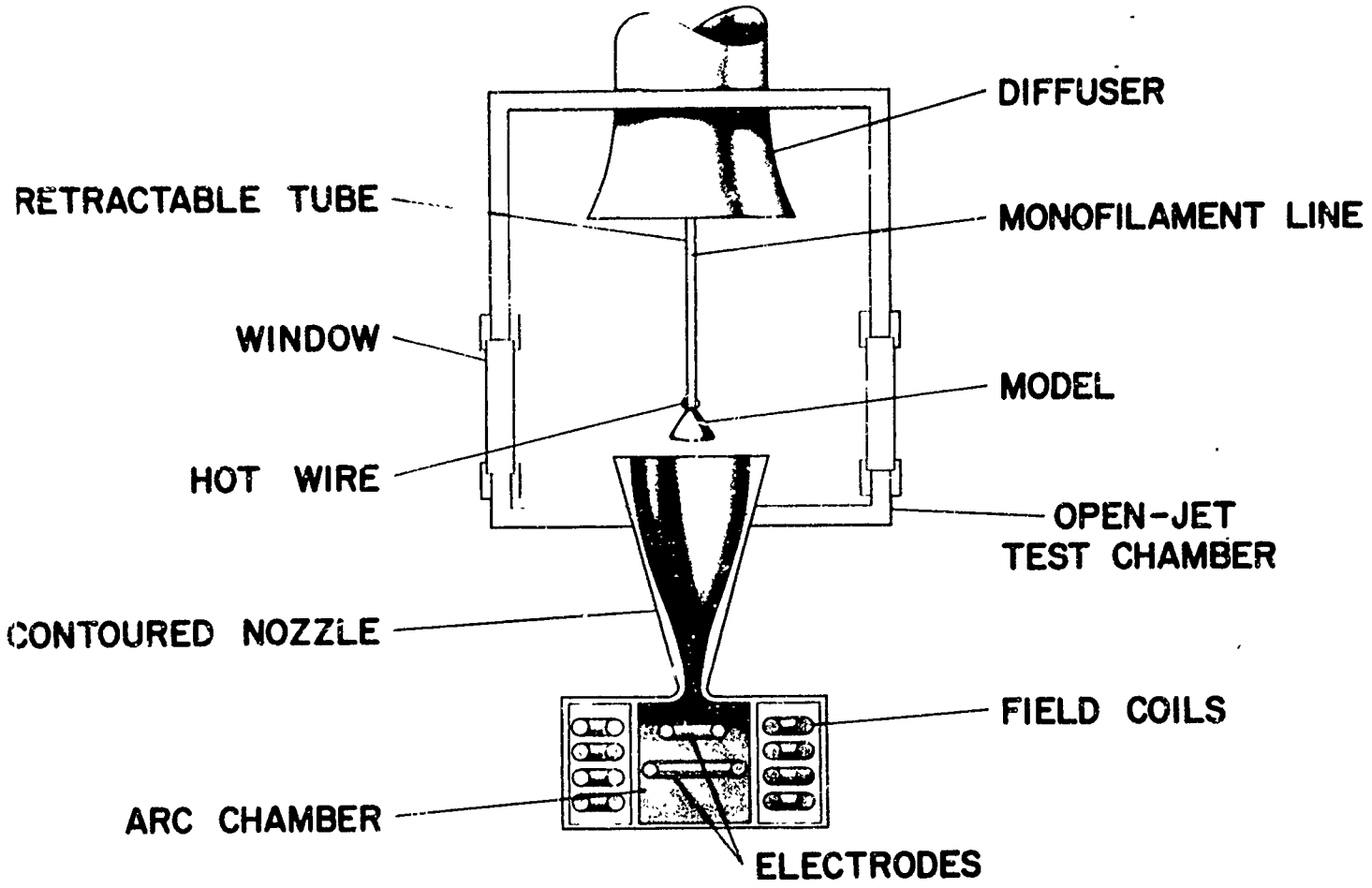

A-34069

Figure 1.- Sketch of Ames vertical arc-heated wind tunnel.

NATIONAL AERONAUTICS AND SPACE ADMINISTRATION
AMES RESEARCH CENTER, MOFFETT FIELD, CALIFORNIA

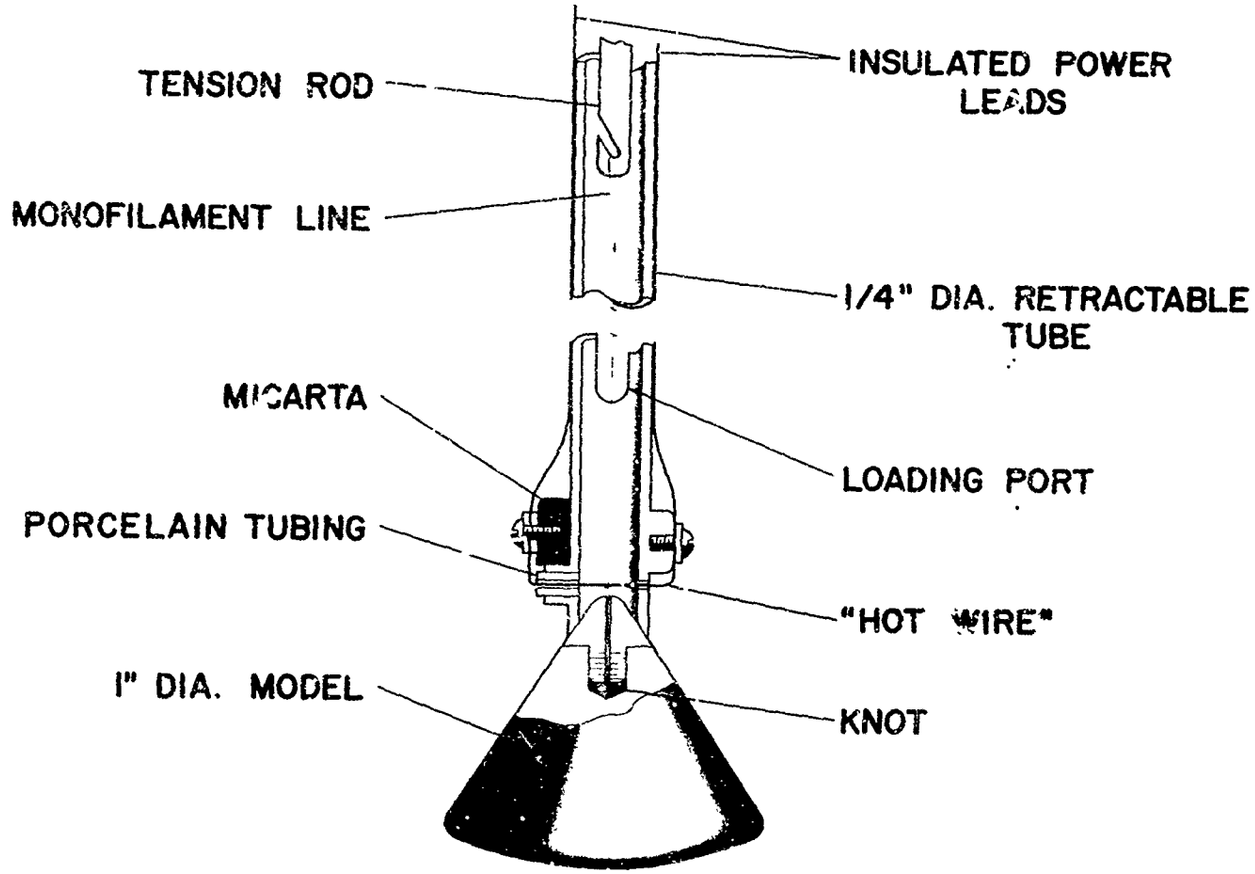

Figure 2.- Details of hot-wire release mechanism.

A-34070

NATIONAL AERONAUTICS AND SPACE ADMINISTRATION
AMES RESEARCH CENTER, MOFFETT FIELD, CALIFORNIA

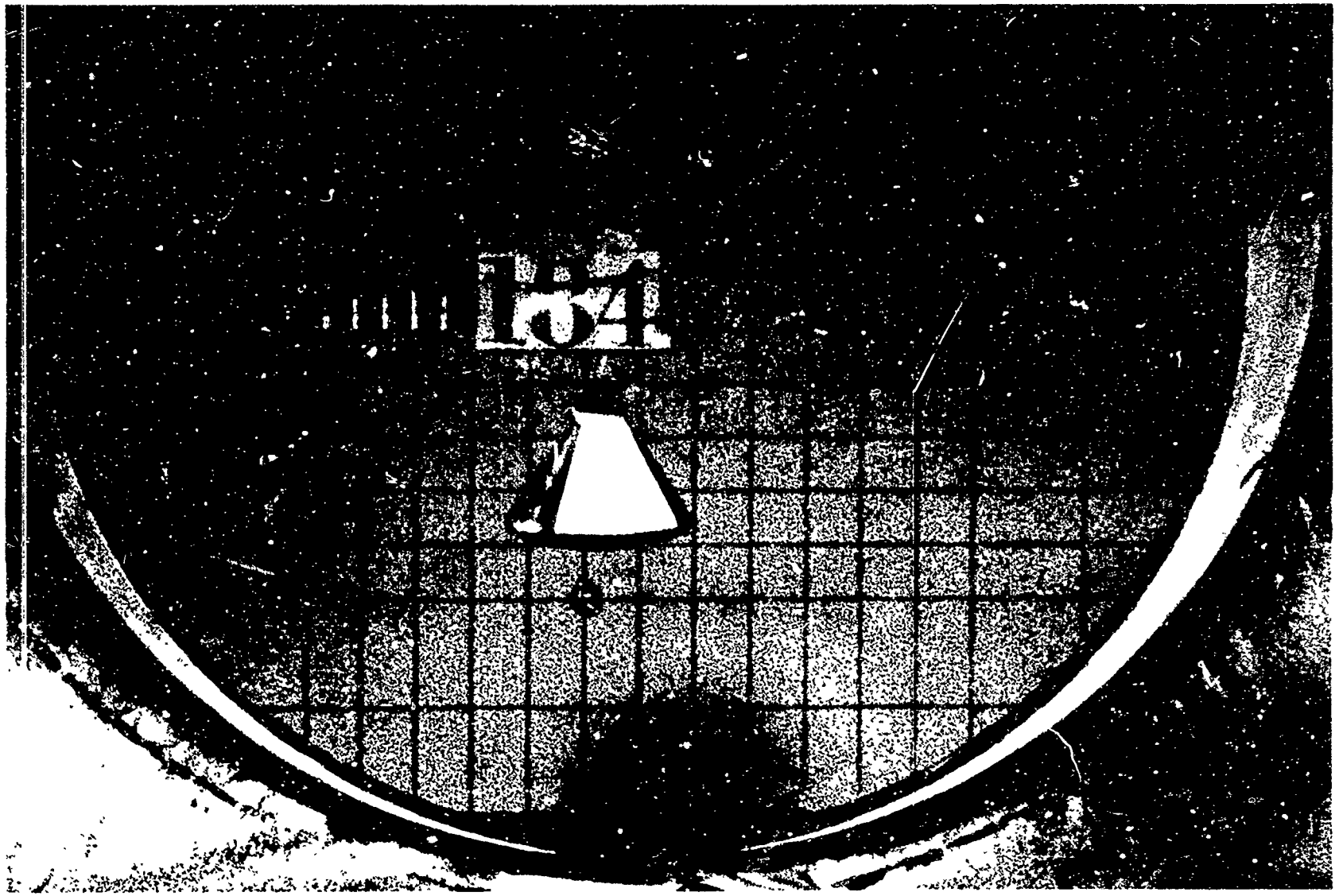

Figure 3.- Representative frame from film record.

NATIONAL AERONAUTICS AND SPACE ADMINISTRATION
AMES RESEARCH CENTER MOFFETT FIELD, CALIFORNIA

DYNAMIC STABILITY TESTING OF SPECIAL WEAPON SHAPES

(Interim Report—Limited Distribution Only)

by

James F. Reed

Sandia Corporation, Albuquerque, New Mexico

ABSTRACT

A brief resumé is presented of Sandia Corporation's experience in the field of wind tunnel dynamic stability testing over the past 17 years. Techniques employed, some of the problems encountered, and the peculiarities of performance of some of the special weapon shapes tested are discussed. Information on the correlation between data from different wind tunnels and between wind tunnel and flight data is also included.

APRIL 1965

Presented at: THE DYNAMIC STABILITY TESTING WORKSHOP,
ARNOLD ENGINEERING DEVELOPMENT CENTER,
APRIL 20-23, 1965,
TENNESSEE.

Issued by
Sandia Corporation,
a prime contractor to the
United States Atomic Energy Commission

TABLE OF CONTENTS

LIST OF ILLUSTRATIONS

LIST OF ILLUSTRATIONS (cont)

NOMENCLATURE

a	Speed of sound
CG	Model center of gravity, percent of length
C_m	Pitching moment coefficient, $\frac{m}{\bar{q}Sd}$
$-C_{m_\alpha}$	Static stability parameter, $-\frac{\partial C_m}{\partial \alpha}$, per degree
$-C_{m_q} + C_{m_{\dot{\alpha}}}$	Dynamic stability parameter, per radian $-\left[C_{m_q} + C_{m_{\dot{\alpha}}}\right] = -\left[\frac{\partial C_m}{\partial\left(\frac{qd}{2V}\right)} + \frac{\partial C_m}{\partial\left(\frac{\dot{\alpha}d}{2V}\right)}\right]$
d	Model diameter, in.
I	Model moment of inertia
M	Mach number, V/a
m	Pitching moment
P	Period of model oscillation
$\bar{q}$	Dynamic pressure, $1/2\ \rho V^2$
q	Model angular velocity
R_e	Reynolds number, $\frac{\rho Vd}{\mu}$
S	Model cross sectional area
$T_{\frac{1}{2}}$	Time to damp to one-half of original oscillation amplitude
V	Velocity
α	Angle of attack

NOMENCLATURE (cont)

$\dot{\alpha}$	Rate of change of α
ρ	Air density
μ	Air viscosity

DYNAMIC STABILITY TESTING OF SPECIAL WEAPON SHAPES

Introduction

Over the past 17 years, Sandia Corporation (an AEC weapons laboratory) has conducted more than 70 dynamic stability testing programs utilizing nearly 1900 hours of tunnel time in wind tunnels throughout the United States. Most of these tests were conducted under AEC Restricted Data security classification because of the shapes involved. Thus wide dissemination of test data was not possible. Recent reclassification of these shapes and aerodynamic characteristics make it possible to discuss some of our test methods and results.

This paper will present some of the testing techniques used and problems encountered, and some of the peculiarities of stability characteristics exhibited by special weapon shapes. In addition, some correlation will be presented on data between wind tunnels and between wind tunnel and free flight data.

Development of Testing Techniques

Background

The ballistic shapes shown in Figures 1 and 2 were dropped on Japan in August, 1945. The bombs, Fat Man in particular, were unstable in flight. The original design of Fat Man and Little Boy was developed by physicists with little help from anyone connected with aerodynamics. The tail assembly on Fat Man, for example, was modified to resemble a parachute at the suggestion of one of the aircraft bombardiers. This change reduced the dynamic instability to tolerable limits—less than ±30°.

As the international tension developed before and during the Korean War, more sophisticated warhead designs were developed and these designs required new ballistic shapes. Statically and dynamically stable bombs were needed to limit dispersion, to limit acceleration loads on components, and to increase reliability of fuzing systems. Wind tunnel tests were planned to study the subsonic and nearsonic stability characteristics of these bluff, low-fineness-ratio shapes.

Blimp Shapes

The first stockpile weapon produced by Sandia Corporation was a modification of the Fat Man called the Mark 3. The first completely new weapon can be seen in Figure 3. The basic shape was that of a modified Class C blimp. The blimp shape was modified by cutting a flat on the nose and adding 5° - 25° double wedge fins for the first implosion weapons. Design criteria in this case were quite simple: fit as large a bomb as possible into the B-29 bomb bay. For reasons of storage, the fins were not permitted to protrude beyond a box tangent to the major diameter of the weapon. This created problems with static stability. Because of the size criteria, the fineness ratio of the entire store was set at 2.13, creating problems with dynamic stability.

The double-wedge fins solved the static stability problems satisfactorily. Dynamic instability (oscillations diverged to ±30° between M = 0.84 to 0.95) was reduced to ±6° after many (over 150) drop tests and a series of wind tunnel tests by the addition of five thin spoiler bands along the bomb's length. The resultant shape was used for an improved weapon (Figure 4).

Testing Techniques

The first wind tunnel tests were conducted using a crude, three-degree-of-freedom, ball-bearing, free-oscillation rig in the Wright Air Development Center (WADC) 10-Foot Transonic Tunnel. Decisions were based upon observers' reports of model action. Motion pictures were taken, but the

delay in development prohibited their use in the test program. The rig had no deflector for cocking the model to a trim angle. No quantitative data were obtained in these tests.

The next step in testing techniques used a two-degree-of-freedom rig with remote hydraulic control to yaw, lock, release, and brake a model. Thin strain-gaged beams recorded pitch and yaw motion. The final version of this rig, which underwent considerable development over the years, is shown in Figure 5. This device has been the workhorse of Sandia's dynamic testing.

In addition to the one- or two-degree-of-freedom, ball-bearing, sting-mounted rig, typified by Dynamic Rig No. 4 in Figure 5, a number of other dynamic stability testing techniques have been tried by Sandia. These include:

free oscillation half-model using a splitter-plane,
free oscillation cross-flexure rig,
side-mount rig with one or two degrees of freedom,
gas-bearing rig (at JPL),
free-flight wind tunnel tests (at JPL),
free-flight ballistic range tests (at BRL),
free-flight and single-degree-of-freedom vertical tunnel tests (at WADC), and
three-degree-of-freedom spin-stabilized projectile tests (at MIT).

Wind Tunnel Correlation

Single-Degree-of-Freedom System -- Early in Sandia's testing program, a study was conducted to determine if a single-degree-of-freedom system would

be adequate.[2] Figures 6 and 7 show typical correlation between one- and two-degrees-of-freedom testing on Configuration 2. Data were obtained at the Cooperative Wind Tunnel on a 6.5-inch-diameter model.

The following data reduction technique was used in this and all wind tunnel tests reported here:[3]

static stability parameter, $-C_{m_\alpha}$

$$-C_{m_\alpha} = \frac{1}{57.3}\left[\frac{4I\pi^2}{P^2\bar{q}Sd} + \frac{I}{\bar{q}Sd}\left(\frac{\ell n\, 2}{T_{\frac{1}{2}}}\right)^2\right]$$

Usually for bluff bombs, the second term is small relative to the first and the static stability parameter equation reduces to

$$-C_{m_\alpha} \approx \frac{1.378\, I}{P^2\rho V^2 Sd}$$

dynamic stability parameter, $-\left[C_{m_q} + C_{m_{\dot\alpha}}\right]$

$$-\left[C_{m_q} + C_{m_{\dot\alpha}}\right] = \frac{m_q + m_{\dot\alpha}}{\frac{\bar{q}Sd^2}{2\bar{V}}},$$

where

$$m_q + m_{\dot\alpha} = \frac{2I(\ell n\, 2)}{T_{\frac{1}{2}}}.$$

Thus, the formula for dynamic stability parameter may be reduced to

$$-\left[C_{m_q} + C_{m_{\dot\alpha}}\right] = \frac{-5.544\, I}{\rho V Sd^2 (T_{\frac{1}{2}})}.$$

From the information presented in Figures 6 and 7 and from other similar correlations, Sandia engineers concluded that single-degree-of-freedom testing would suffice for low fineness ratio bluff shapes.

Sting and Model Frequencies -- During the same test program, a series of runs were made to determine the effect of sting natural frequency and model oscillation frequency on the stability parameters. Sting natural frequency was varied through the use of guy wires, and model frequency was changed by varying moment of inertia. The test was performed on four somewhat similar configurations with similar results. As can be seen from Figures 8 and 9 (Configuration 2), there is no ordered trend related either to changes in sting natural frequency from 15.3 to 11.6 cycles per second, or changes in model frequency from 2.7 to 9.8 cycles per second. The scatter shown appears to be almost all within the accuracy of the data. No data were taken on a resonant frequency condition, that one in which model frequency corresponds to sting natural frequency.

Reynolds Number -- In an effort to determine the effect of Reynolds number on stability parameters, Configuration 2 test data from five test programs were compared. (Four of the test programs were run in the Cooperative Wind Tunnel and one in the 8-Foot Transonic Tunnel at Langley Aeronautical Laboratory.[4]) The range of Reynolds numbers covered, based on model diameter, is shown in Figure 10. As can be seen from Figures 11 and 12, the trends of static and dynamic stability derivatives as functions of Mach number are quite similar. Although the Mach number at which stability derivatives show high rates of change apparently varied with the Reynolds number, this effect had little significance in the search for a stable configuration because the trends were similar. Reynolds numbers experienced by the full-scale vehicle ranged from approximately 5 to 30 x 10^6, depending on Mach number and altitude.

Model Unbalance -- For several years all free-oscillation testing done on a single-degree-of-freedom rig was performed in the pitch plane using carefully balanced models. Then in 1957, Sandia began to investigate the effect of

testing in the yaw plane with the model balanced about some point other than the center of rotation,[5] it was assumed that if the system were truly single-degree-of-freedom, it would make no difference.

The center of gravity was varied from 36.0 to 52.4 percent of model length while the center of rotation was maintained at 39.6 percent. Tests of several configurations were conducted in the Wright Air Development Center 10-Foot Transonic Tunnel; data are presented for two typical configurations. Figures 13 and 14 show the variation of static and dynamic stability parameters for a completely stable configuration. Figures 15 and 16 show the same for a model with a region of neutral dynamic stability about Mach 0.88. Again, there is no discernible trend and the data are in fair agreement.

Typical Single-Degree-of-Freedom Stability Patterns

Bluff special stores have exhibited many stability patterns. Some of these which have been observed during Sandia's experience in wind tunnel testing are shown in Figure 17. Traces (a) and (b) represent static stability with dynamic stability, and static stability with dynamic instability (at least as far as the limits of the rig). Trace (c) shows a case when the model is statically stable about 0° angle of attack, but statically unstable above 6°. Trace (d) shows trim of approximately 4° with dynamic stability about that point. Trace (e) indicates static instability against the 6° rig limit. Trace (f) shows static and dynamic stability about 0°, but dynamic instability when deflected. Trace (g) is from a model with essentially neutral dynamic instability about the release angle. Rig friction gradually damps the oscillations until the model becomes dynamically stable. Trace (h) shows neutral dynamic stability about ±3°. Model damps from ±6° and diverges from 0°. Trace (i) shows dynamic instability against the stops, whether the model is deflected or released from 0°.

Wind Tunnel–Free Flight Correlation

Sandia has performed a number of tests to correlate free flight ballistic performance with wind tunnel data on bluff shapes. The following technique was used for obtaining data from free flight tests. Stores released from bomber aircraft were allowed to fall freely. Atmospheric conditions were usually obtained using radiosonde balloons released just before or immediately following a drop. Data store velocities were obtained from Askania phototheodolite tracking cameras which followed the store trajectory. When dynamic stability information was desired, small rockets were used to deflect the store to an angle of attack at some predetermined time in the flight path. Roll, pitch, yaw, accelerations, and often pressure measurements were telemetered to ground stations from gyros and other instrumentation within the store.

Figure 18 shows a store of fineness ratio 4.8. Dynamic stability tests were conducted at Cornell Aeronautical Laboratory on a 3-inch-diameter model. Static force tests were conducted at the MIT Naval Supersonic Laboratory[6] on a 1.5-inch-diameter model. The composite results of C_{m_α} as a function of Mach number are shown in Figure 19, which also shows the results of three ballistic drop tests. The region of neutral static stability at M = 0.99 apparent on the wind tunnel results did not show up in the full-scale test results, possibly because the flight Mach number was changing. The over-all correlation appeared satisfactory and no effort was made to correlate dynamic stability parameters other than to note that both wind tunnel and free flight tests indicated a damped system.

Figure 20 shows a line drawing of another bluff store designated Configuration 3. Figures 21 and 22 are comparative data from wind tunnel and free flight partial scale drop tests.[7] The single-degree-of-freedom wind tunnel dynamic stability tests were conducted at the Cooperative Wind Tunnel. The large variations in static stability near M = 0.90 apparent in the wind tunnel data do not appear in the free flight case. This phenomenon has also been attributed to the rapidly changing Mach number, although it could be a Reynolds number effect.

Conclusions

Some conclusions about dynamic stability testing may be drawn from the data presented. All these conclusions apply to low-fineness-ratio, finned bluff bodies flying at transonic speeds.

First, single degree-of-freedom, free-oscillation, dynamic stability wind tunnel tests present a good quantitative picture of static stability, and at least a qualitive picture of dynamic stability.

Second, it has been Sandia's experience that Mach number is the most important single variable in this region. Reduced frequency and Reynolds number, at least within the limits examined, show small secondary effects.

Finally, a single-degree-of-freedom, free-oscillation system may be satisfactorily simulated using an unbalanced model oscillating in the yaw plane. However, the model should be balanced about the center of rotation whenever possible, simply as good testing technique.

REFERENCES

1. Alexander, F. C., Jr., History of Sandia Corporation Through Fiscal Year 1963, December 1, 1963.

2. Maydew, R. C., "Analysis of Dynamic Wind Tunnel Tests," Sandia Corporation, Organization 5142-2, December, 1952, unpublished report.

3. Rowe, P. W., An Introduction to Aerodynamic Stability, Sandia Corporation, SCTM 220-56(51).

4. Clark, E. T., Sandia Corporation, SCTM 43-53-51, March, 1953, unpublished report.

5. Meyer, E. J., An Analysis of Wind Tunnel Dynamic Testing of Unbalanced Models in the Yaw Plane, Sandia Corporation, SCTM 30-58(51), February, 1958.

6. Loncharich, R. J., "Correlation of Wind Tunnel Data and Full-Scale Drop Test Data," Sandia Corporation, SC-4143(TR), February, 1958, unpublished report.

7. Curry, W. H., Results of the Partial Scale Flight Test Program, Sandia Corporation, SCTM 92-54(51), May, 1954.

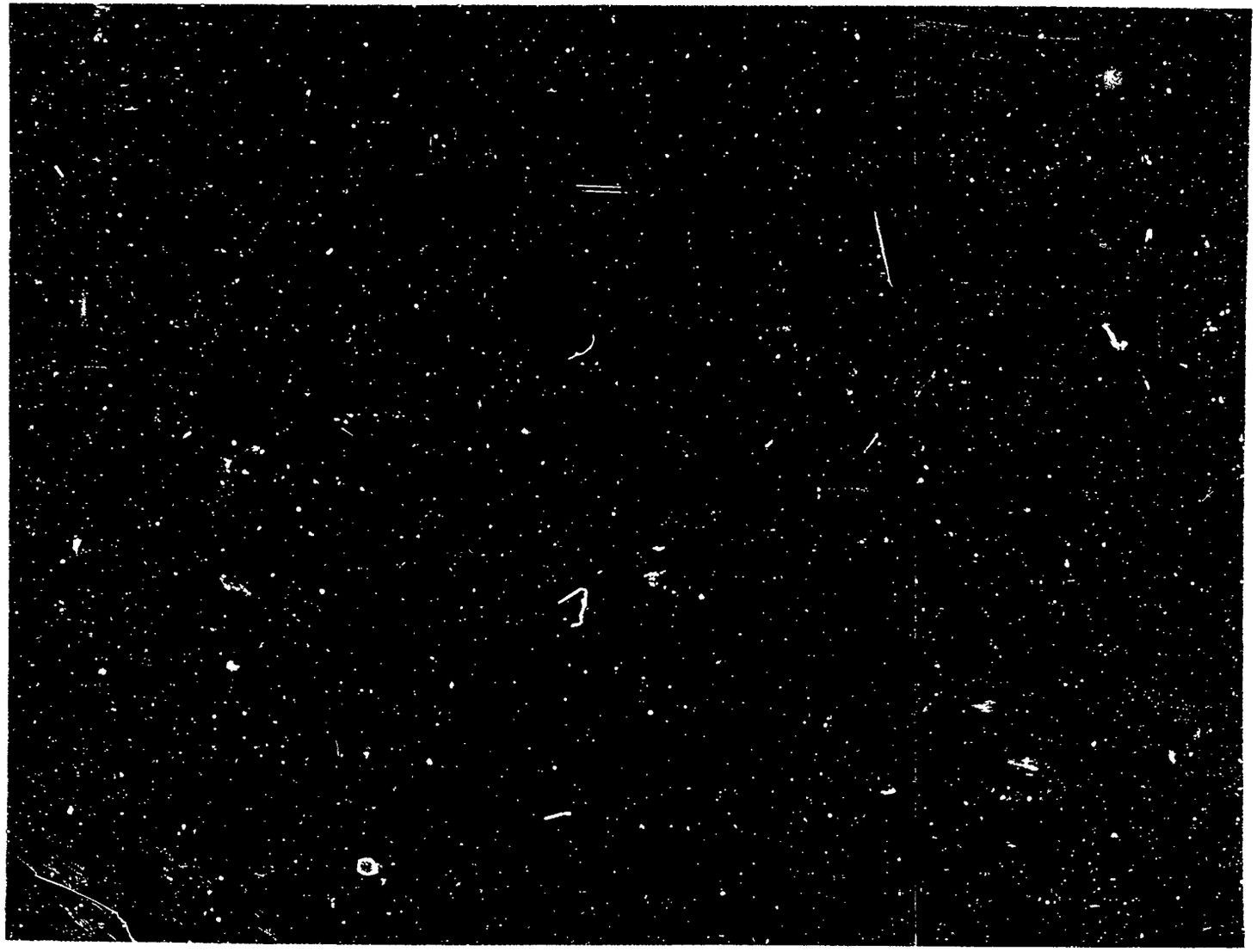

Figure 1 -- Little Boy

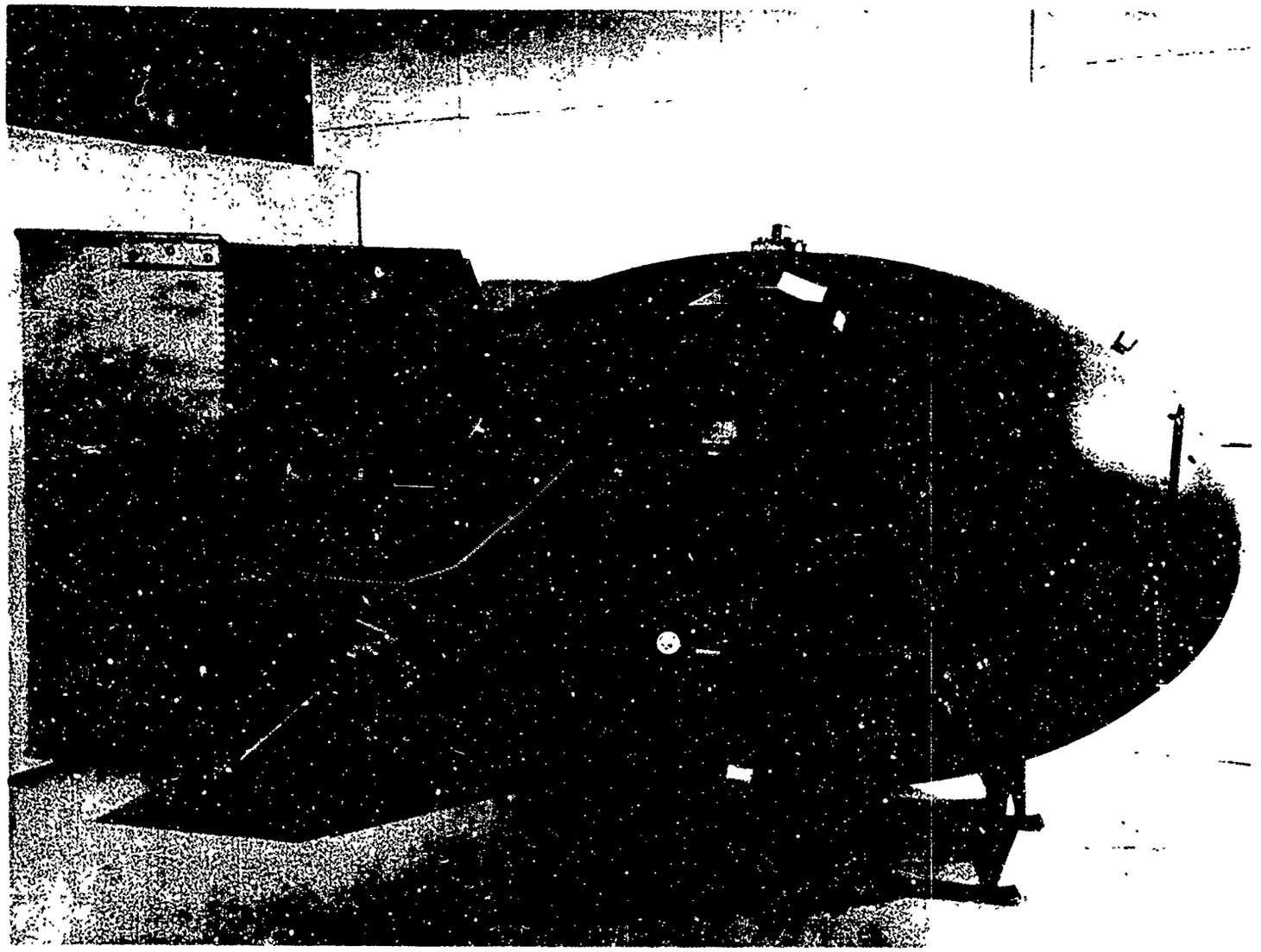

Figure 2 -- Fat Man

Figure 3

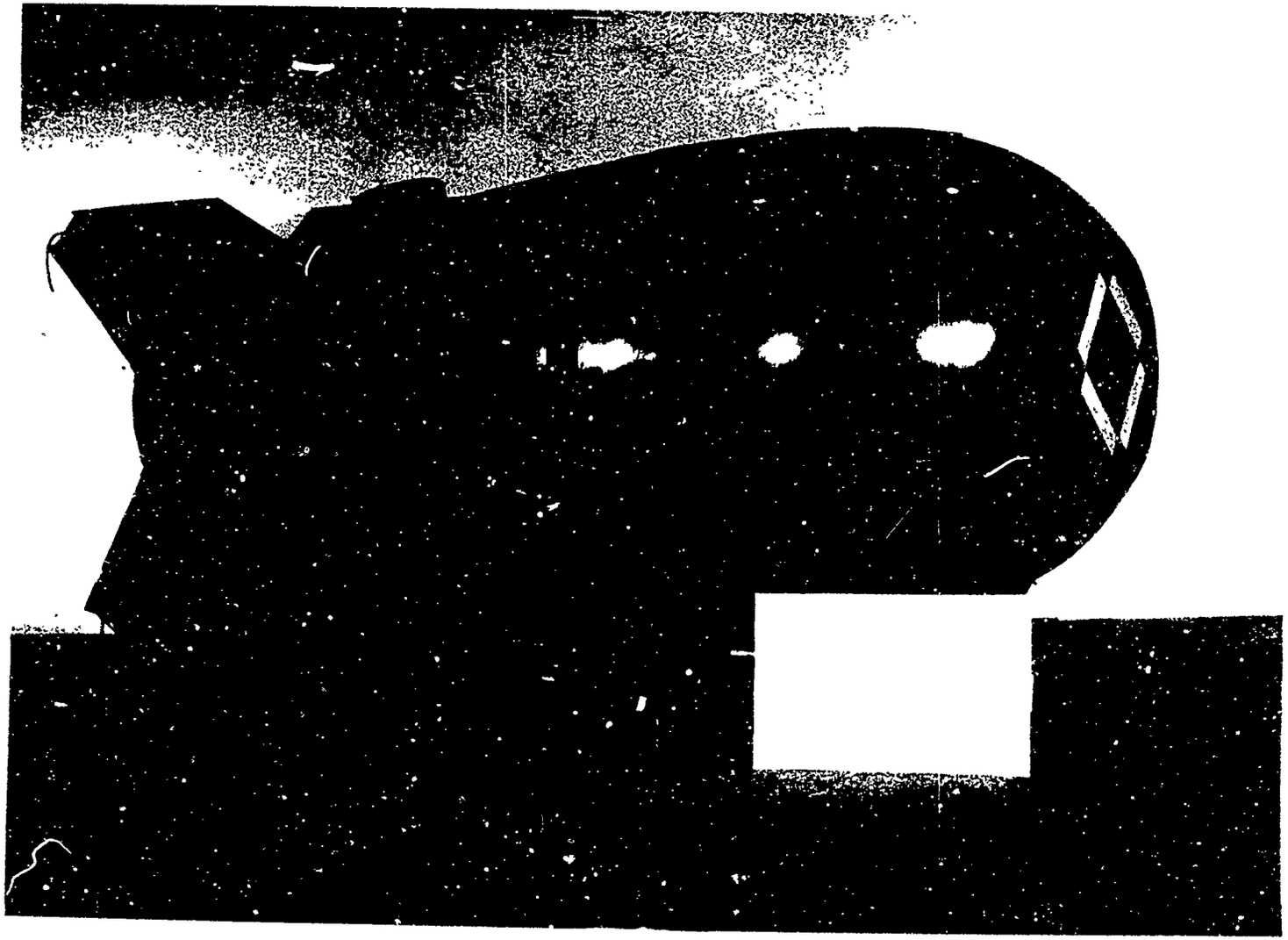

Figure 3

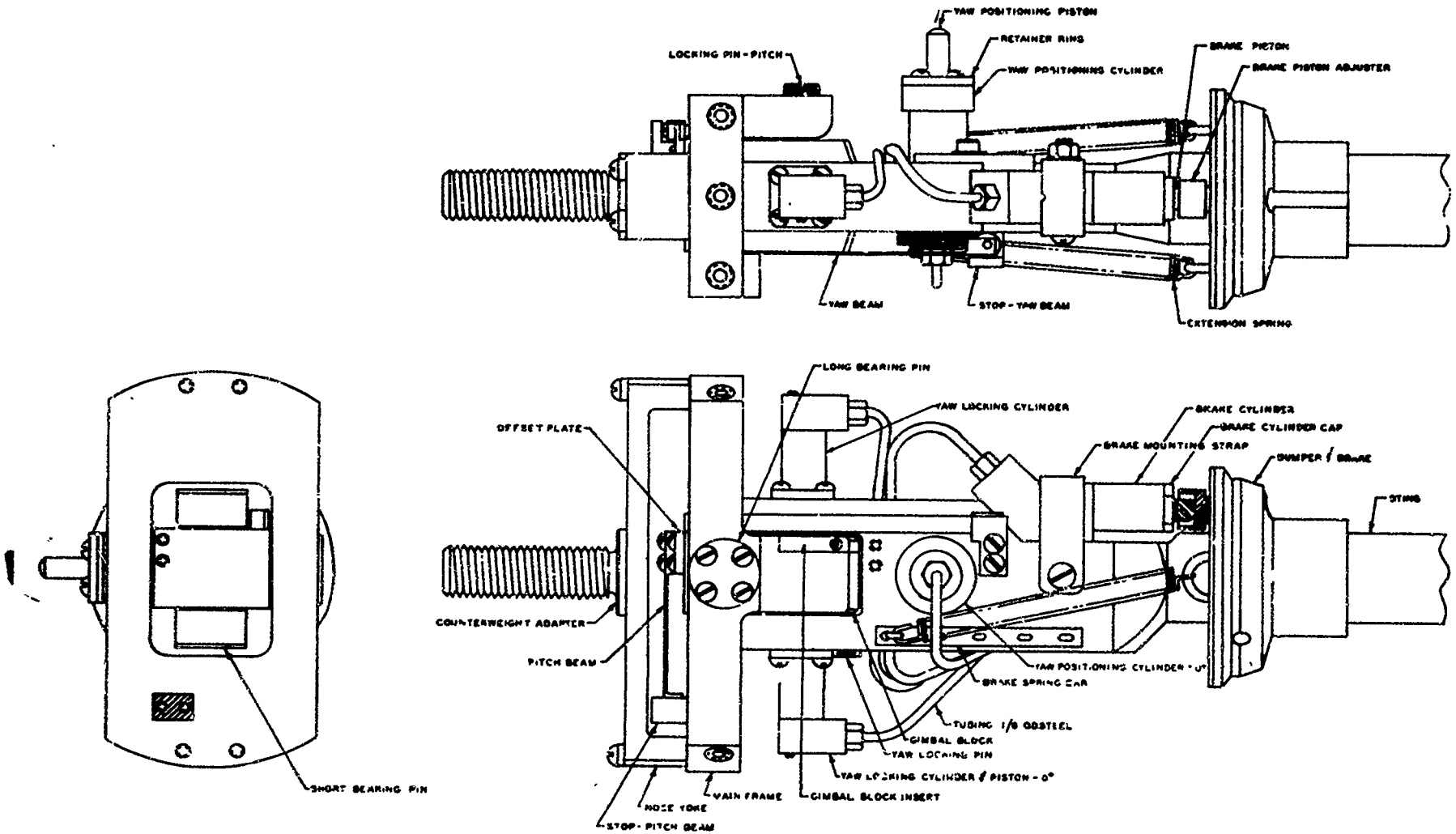

Figure 5 -- Dynamic Rig No. 4

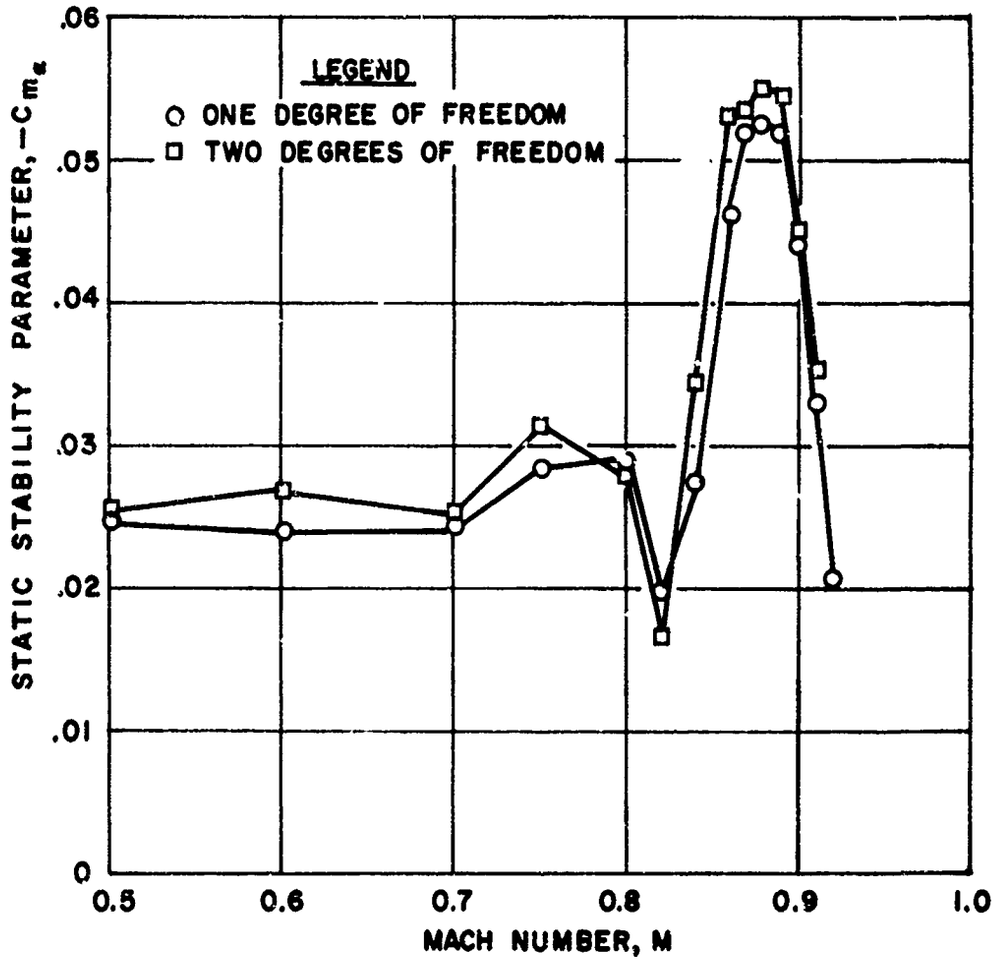

Figure 6 -- Effect of One and Two Degrees of Freedom on Static Stability

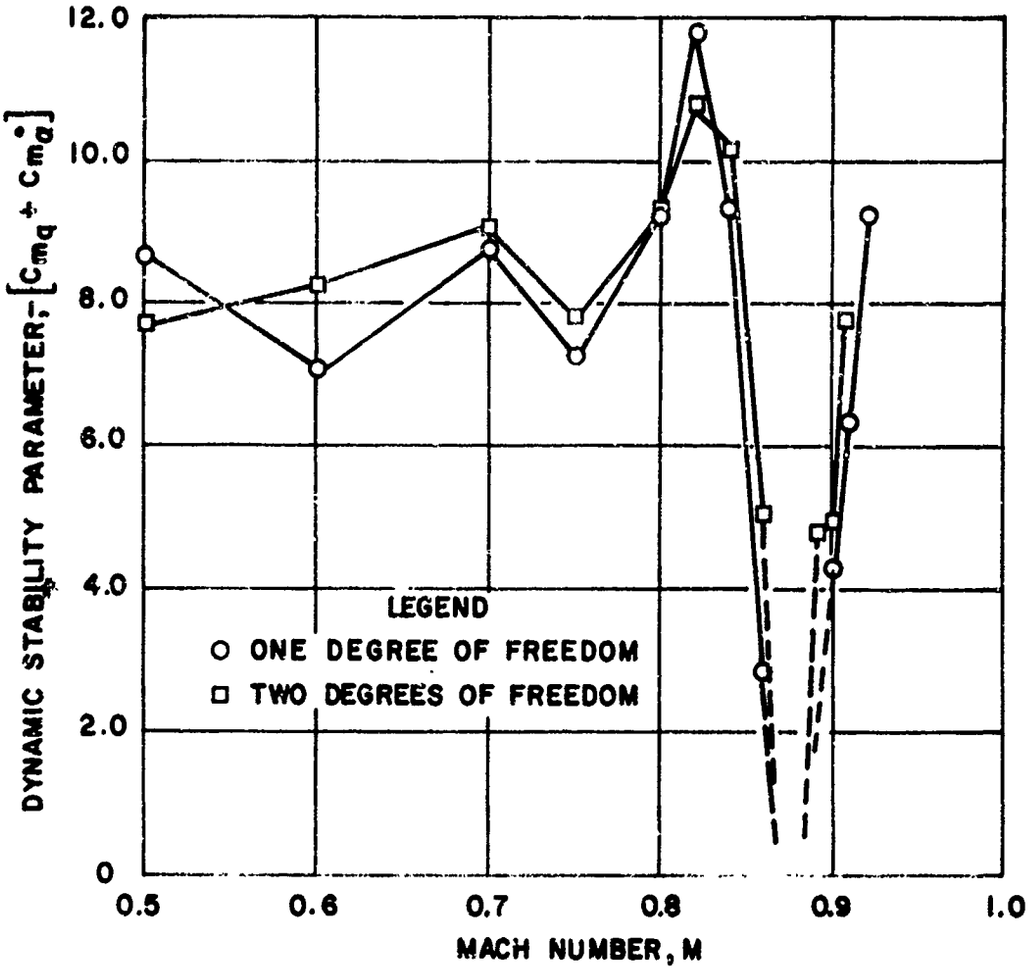

Figure 7 -- Effect of One and Two Degrees of Freedom on Dynamic Stability

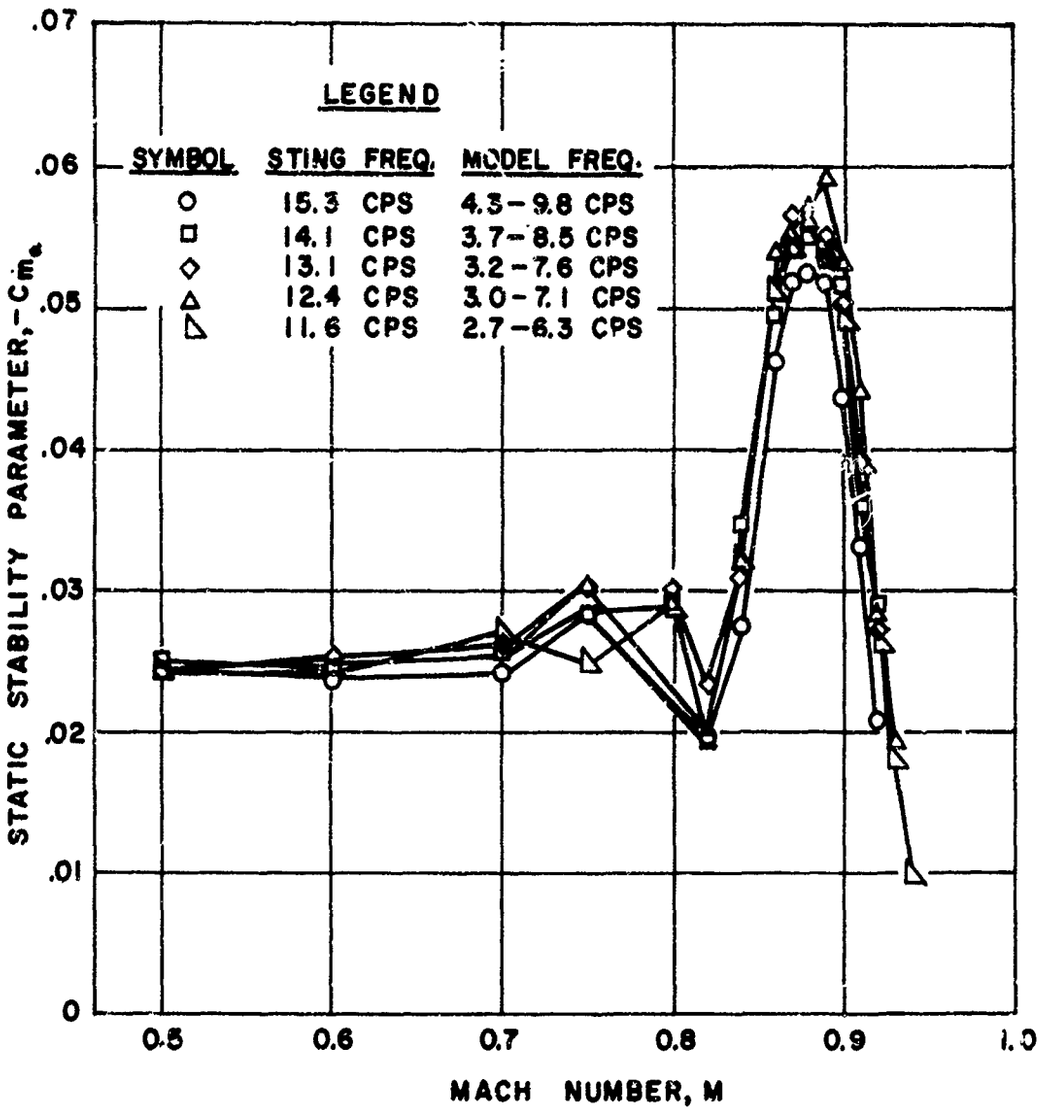

Figure 8 -- Effect of Model and Sting Natural Frequencies on Static Stability Parameter

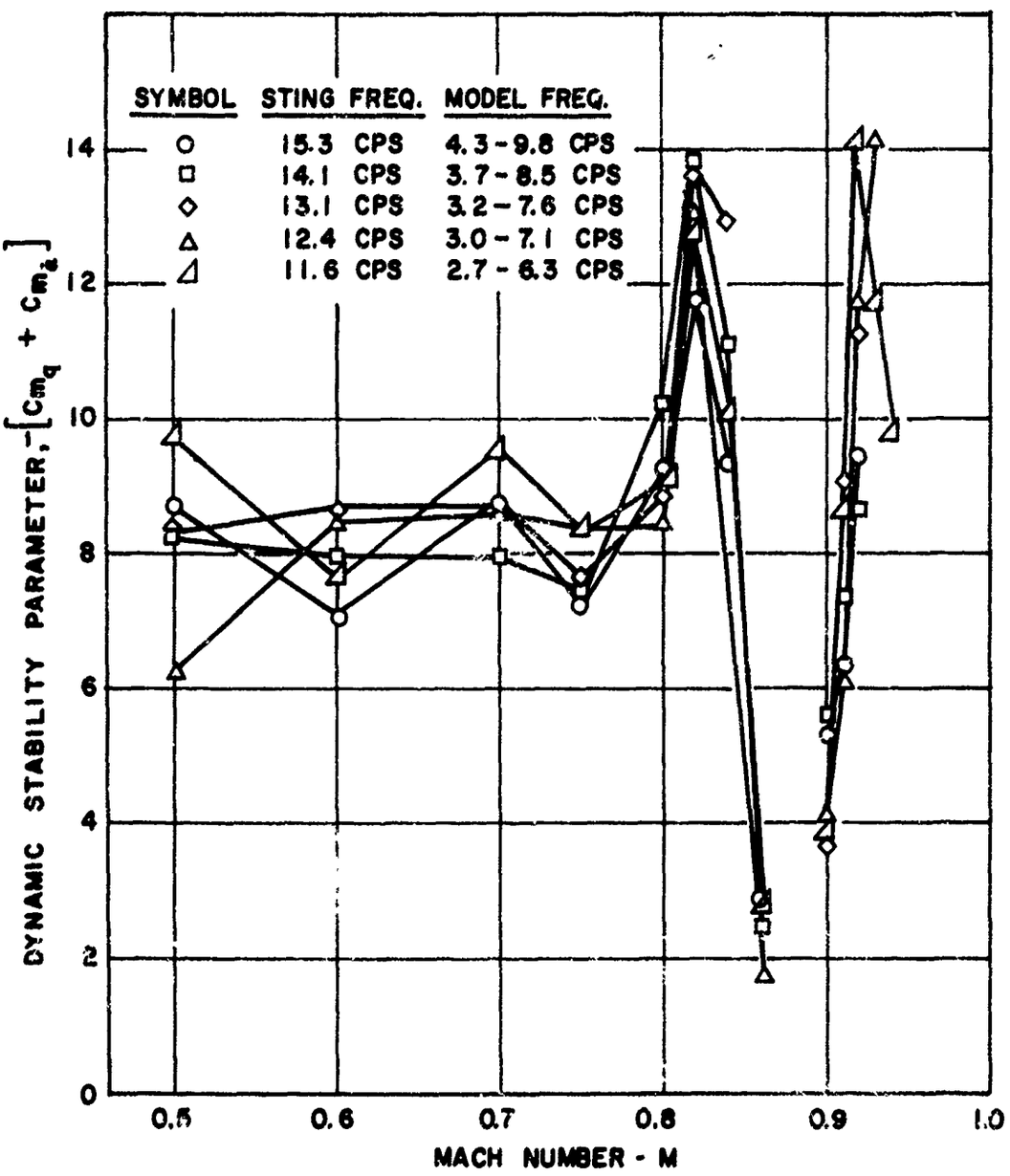

Figure 9 -- Effect of Model and Sting Natural Frequencies on Dynamic Stability Parameter

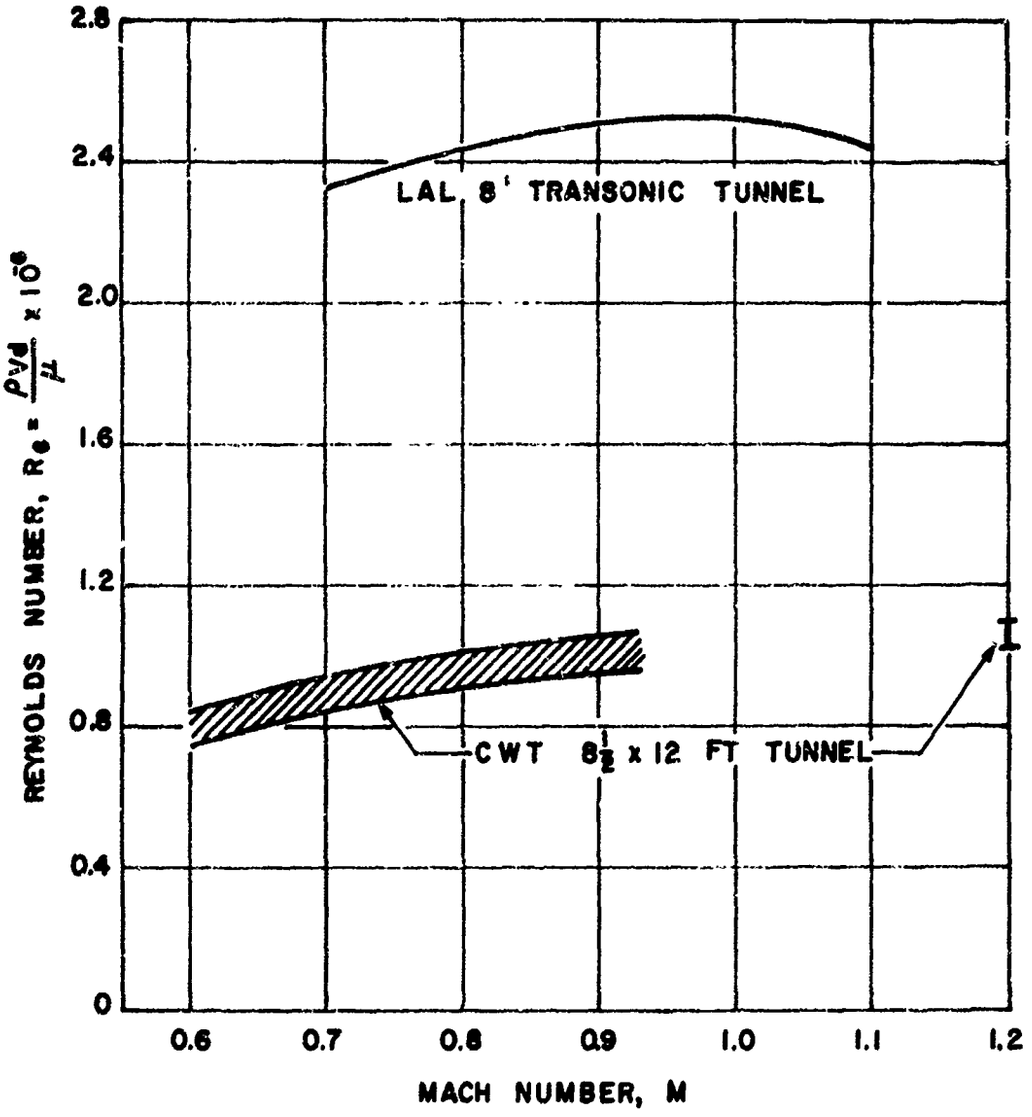

Figure 10 -- Variation of Model Reynolds Number with Mach Number for Cooperative Wind Tunnel and LAL 8 foot Tunnel

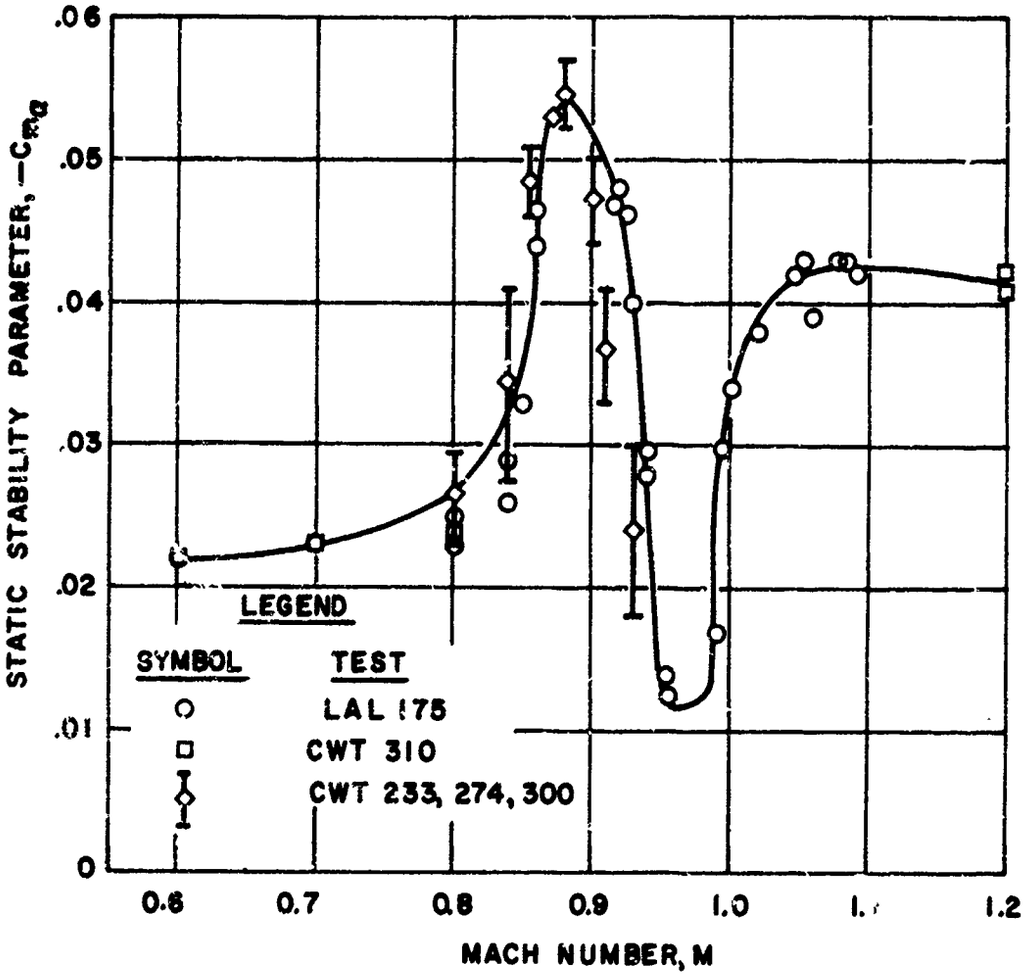

Figure 11 -- Static Stability Parameter Versus Mach Number from Several Wind Tunnel Tests

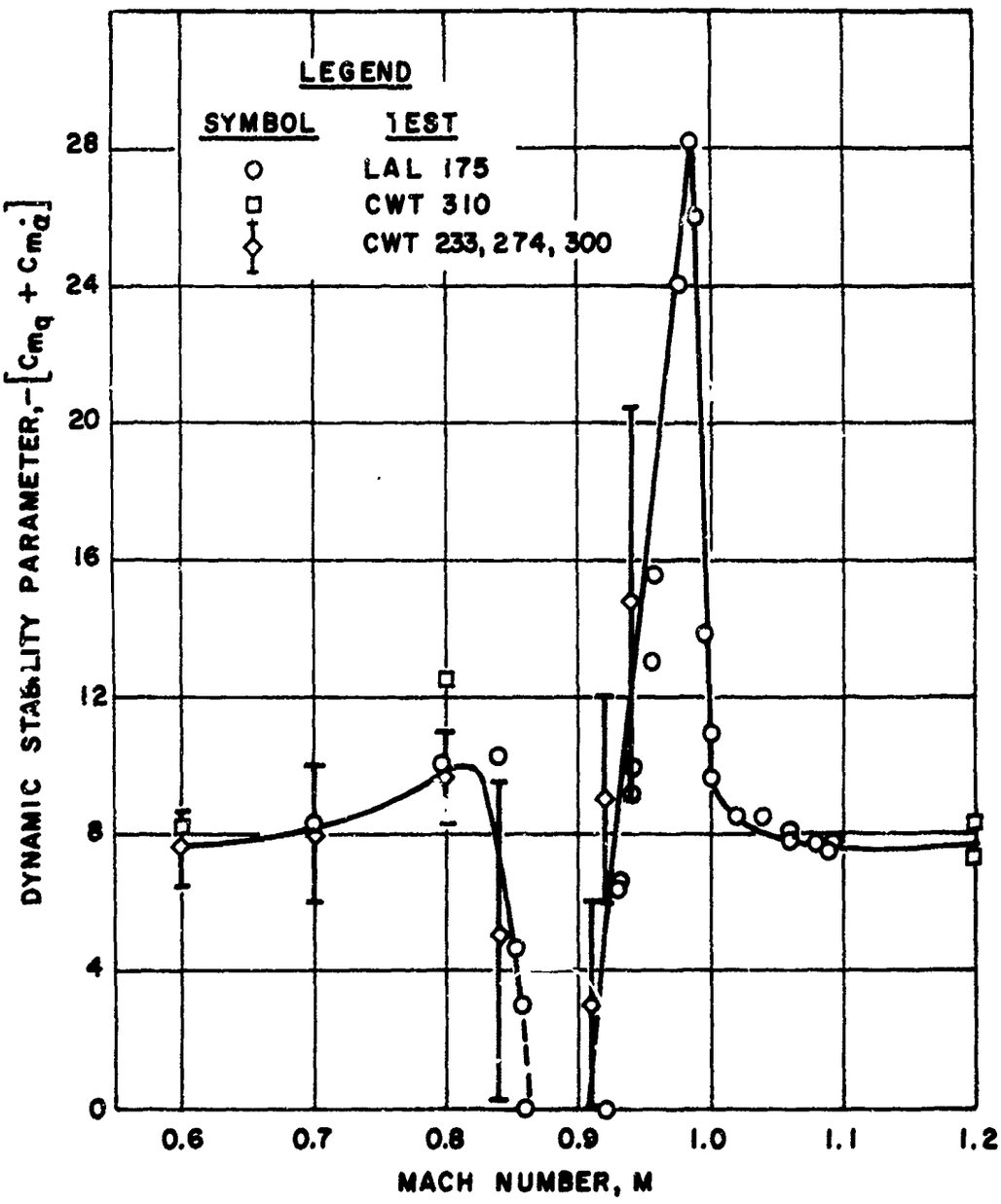

Figure 12 -- Dynamic Stability Parameter Versus Mach Number from Several Wind Tunnel Tests

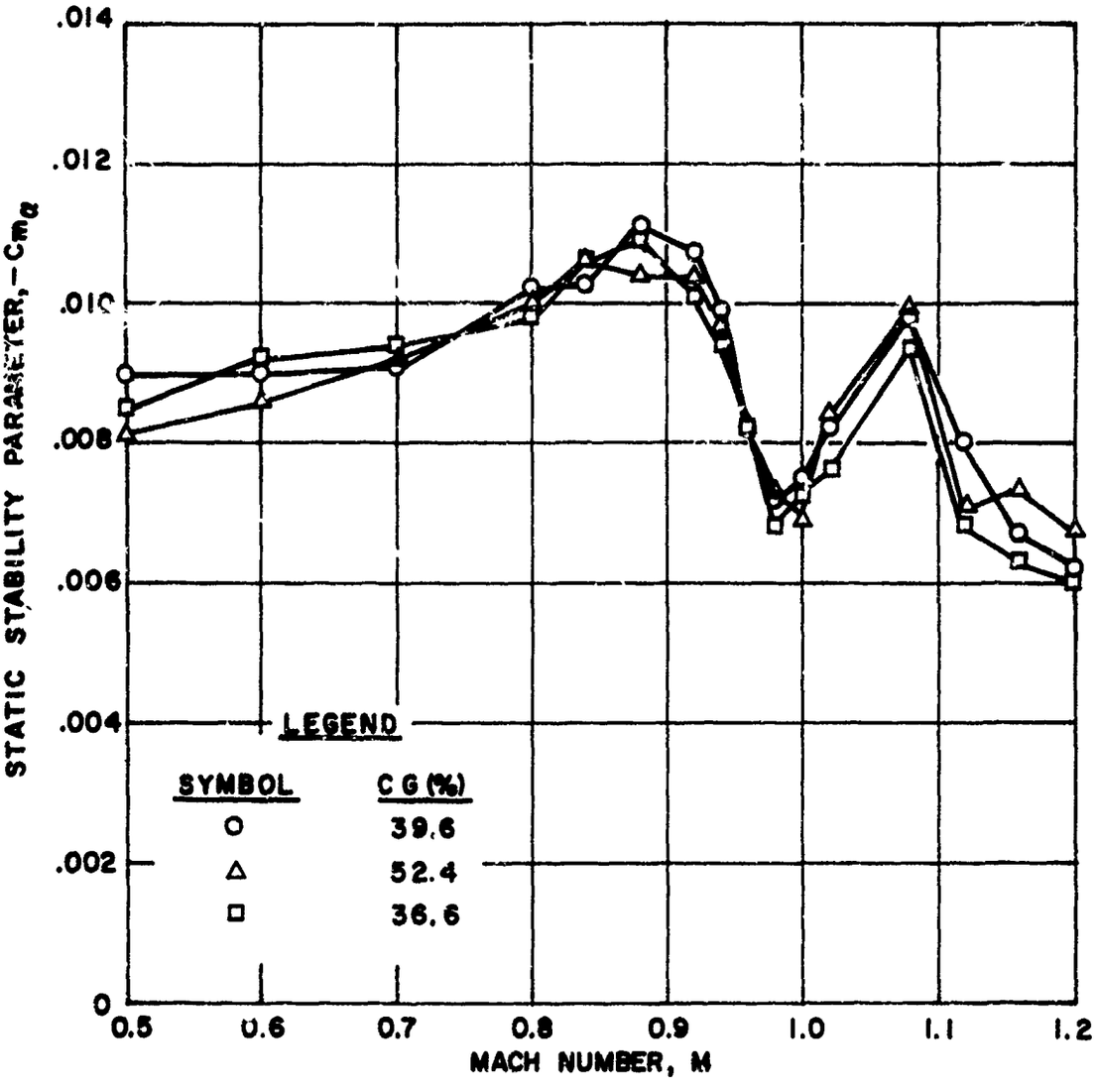

Figure 13 -- Effect of Model Unbalance on Static Stability Parameter—Stable Configuration. Center of Rotation at 39.6% of Length

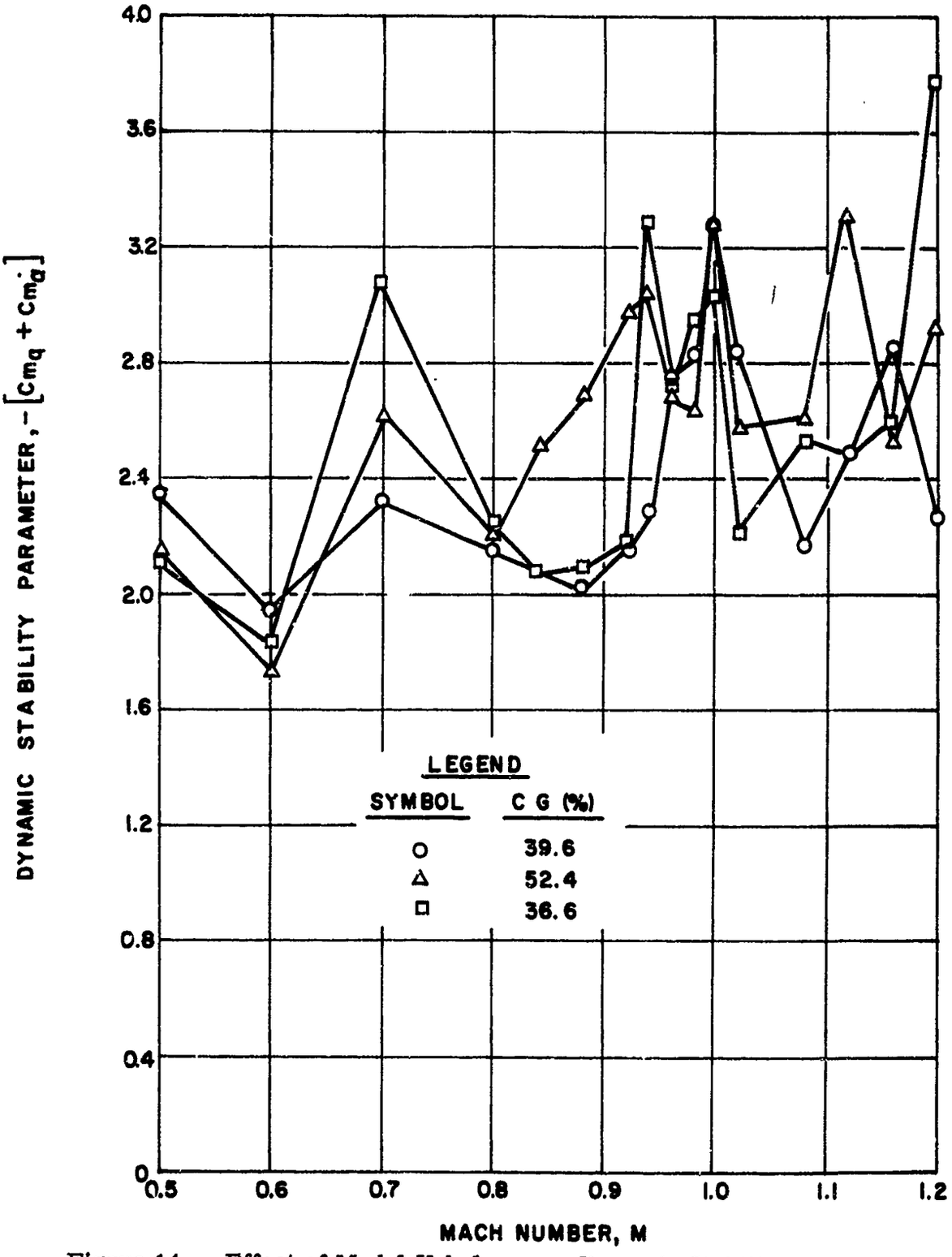

Figure 14 -- Effect of Model Unbalance on Dynamic Stability Parameter—Stable Configuration. Center of Rotation at 39.6% of Length

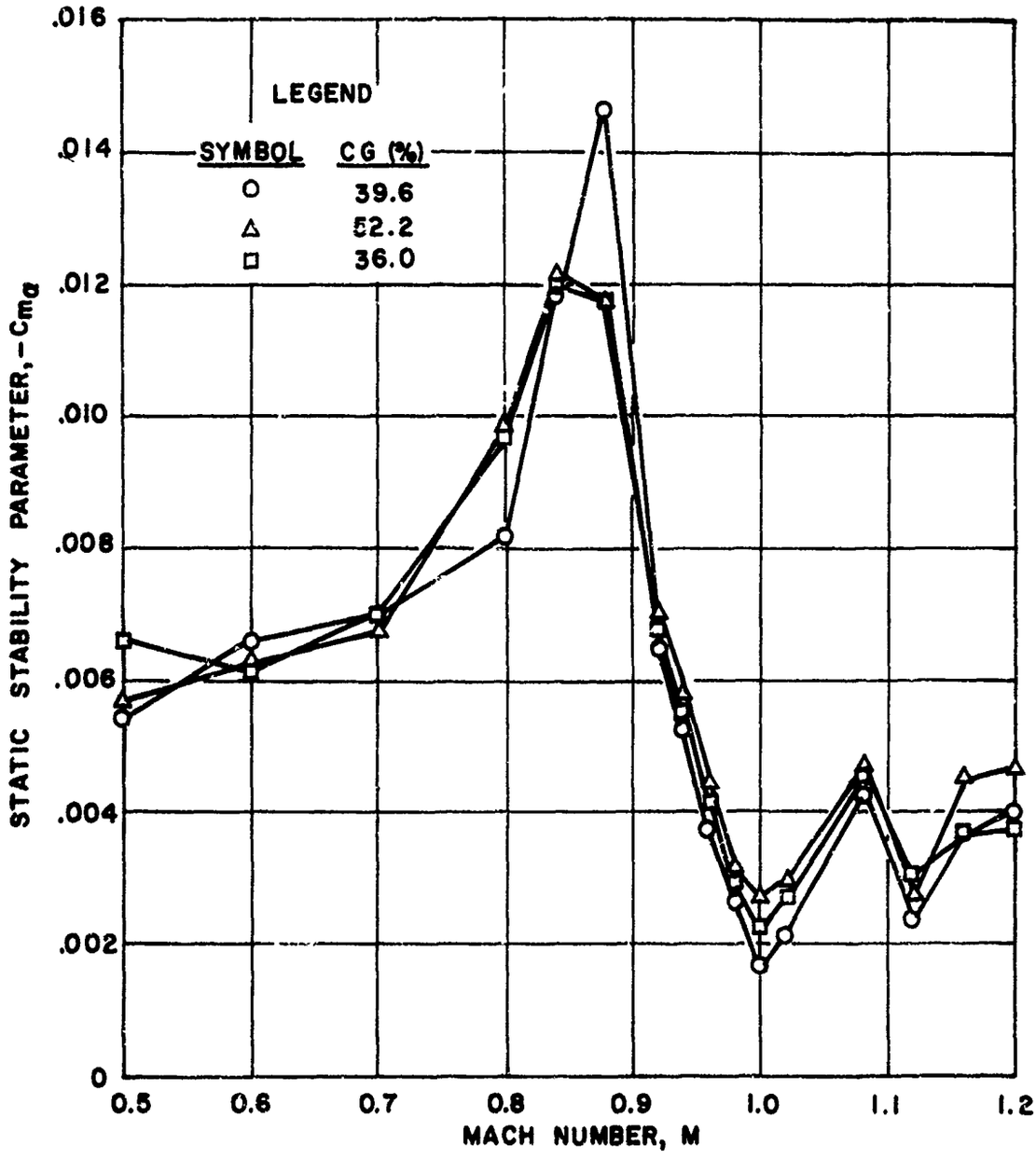

Figure 15 -- Effect of Model Unbalance on Static Stability Parameter—Configuration Possessing Region of Neutral Dynamic Stability. Center of Rotation at 39.6% of Length

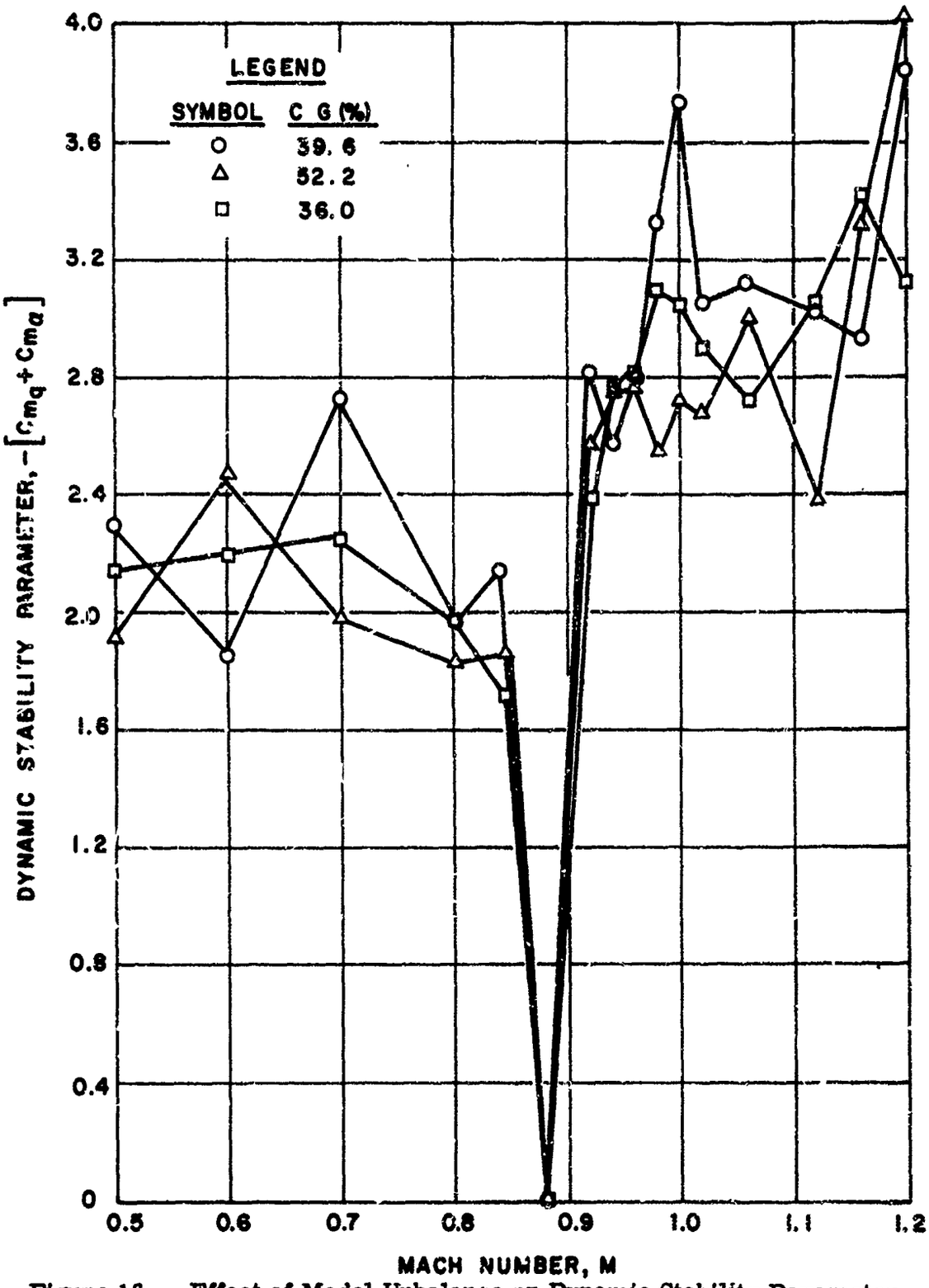

Figure 16 -- Effect of Model Unbalance on Dynamic Stability Parameter—Configuration Possessing Region of Neutral Dynamic Stability. Center of Rotation at 39.6% of Length

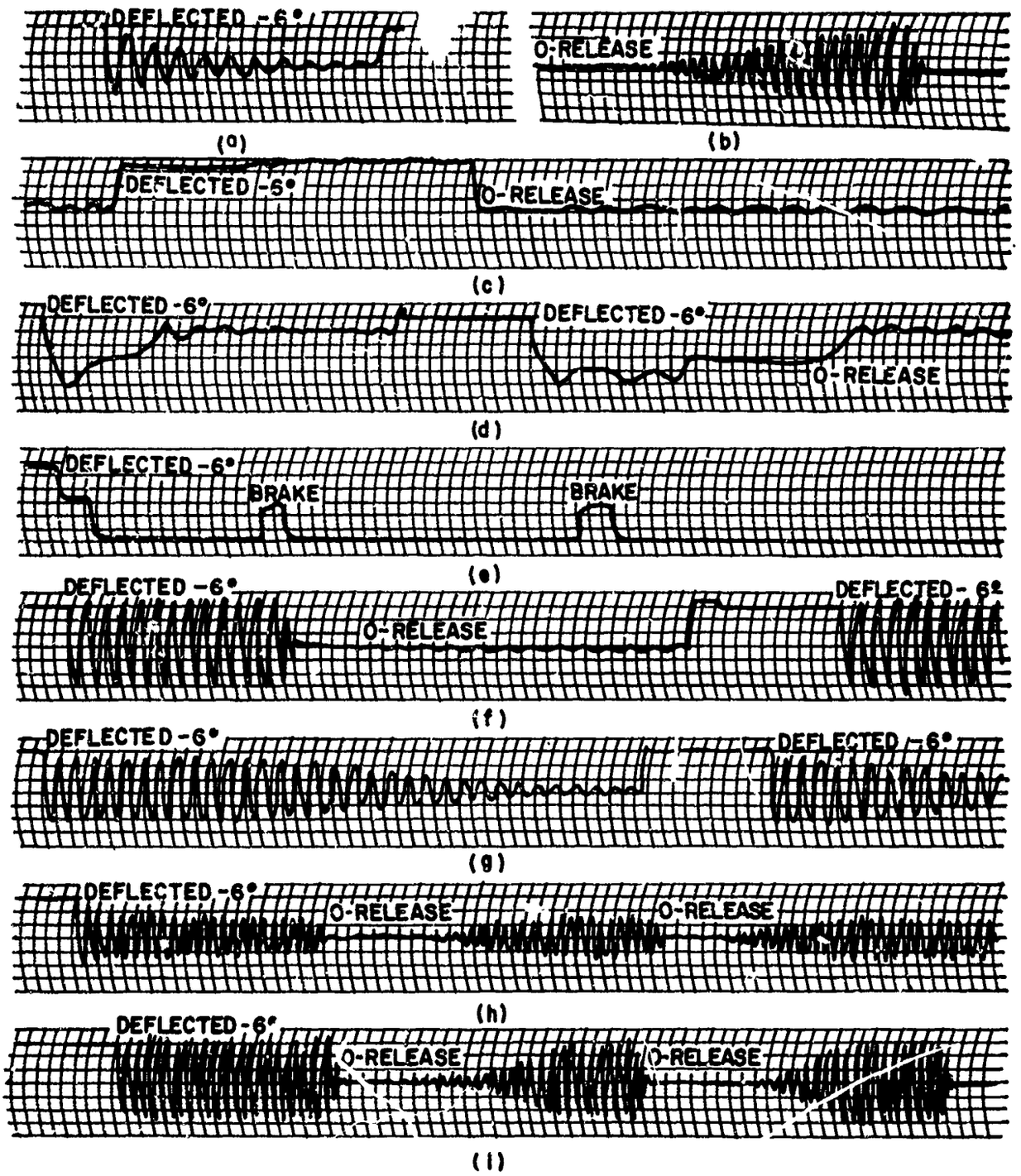

Figure 17 -- Typical Single-Degree-of-Freedom Stability Patterns

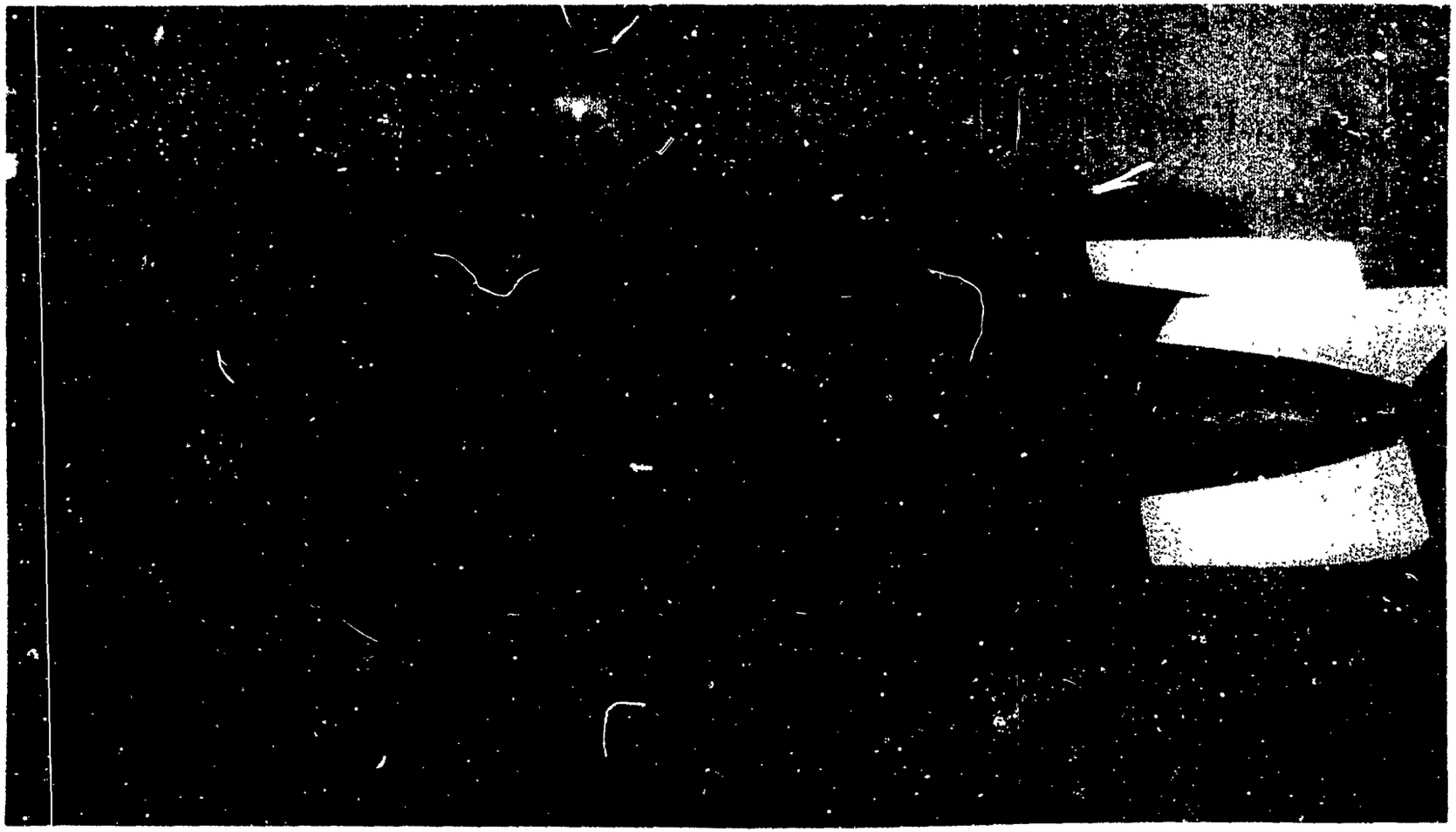

Figure 18 -- Fineness Ratio 4.8 Bluff Store

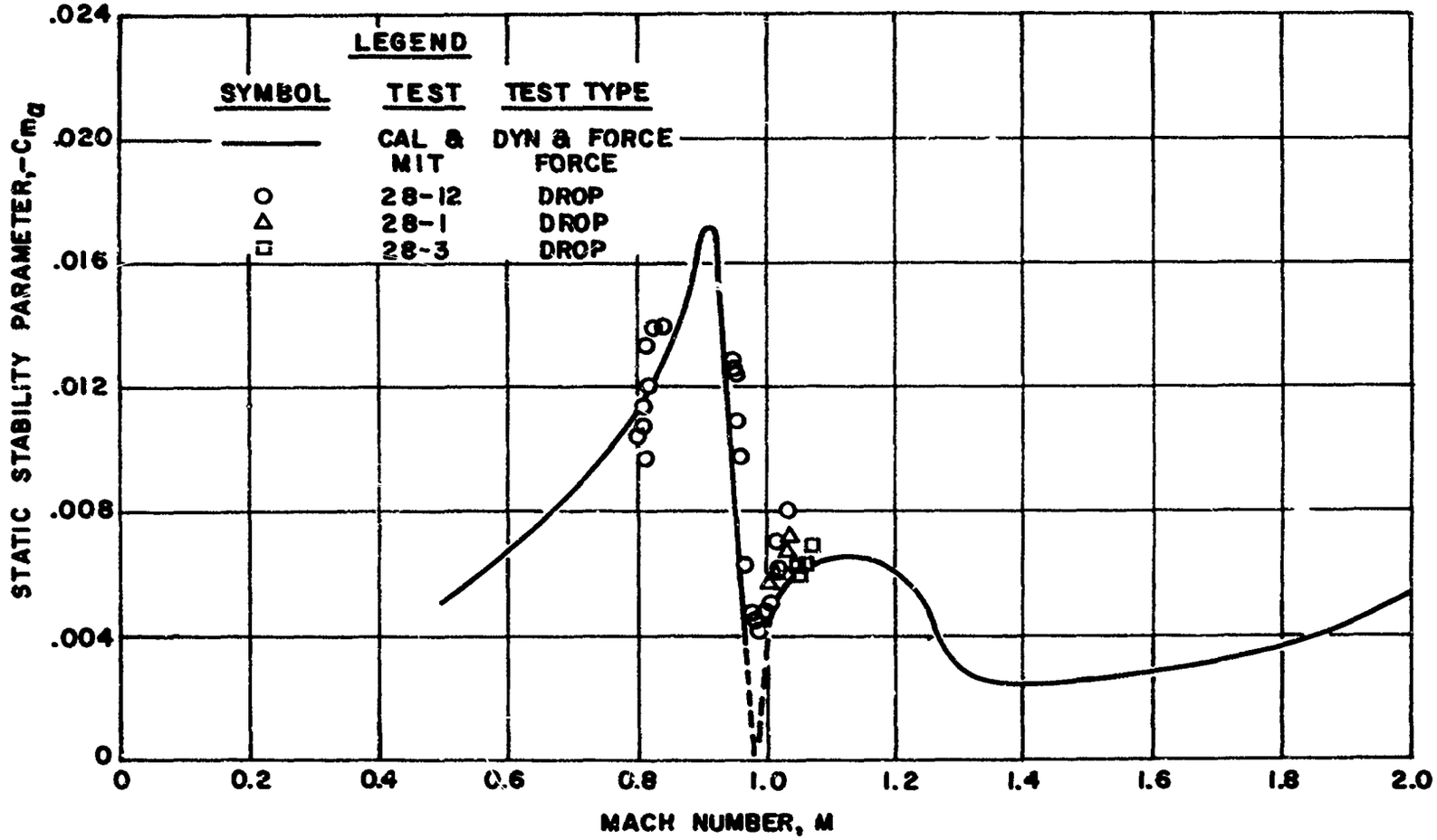

Figure 19 -- Wind Tunnel to Full-Scale Correlation of Static Stability on a Fineness Ratio 4.8 Store

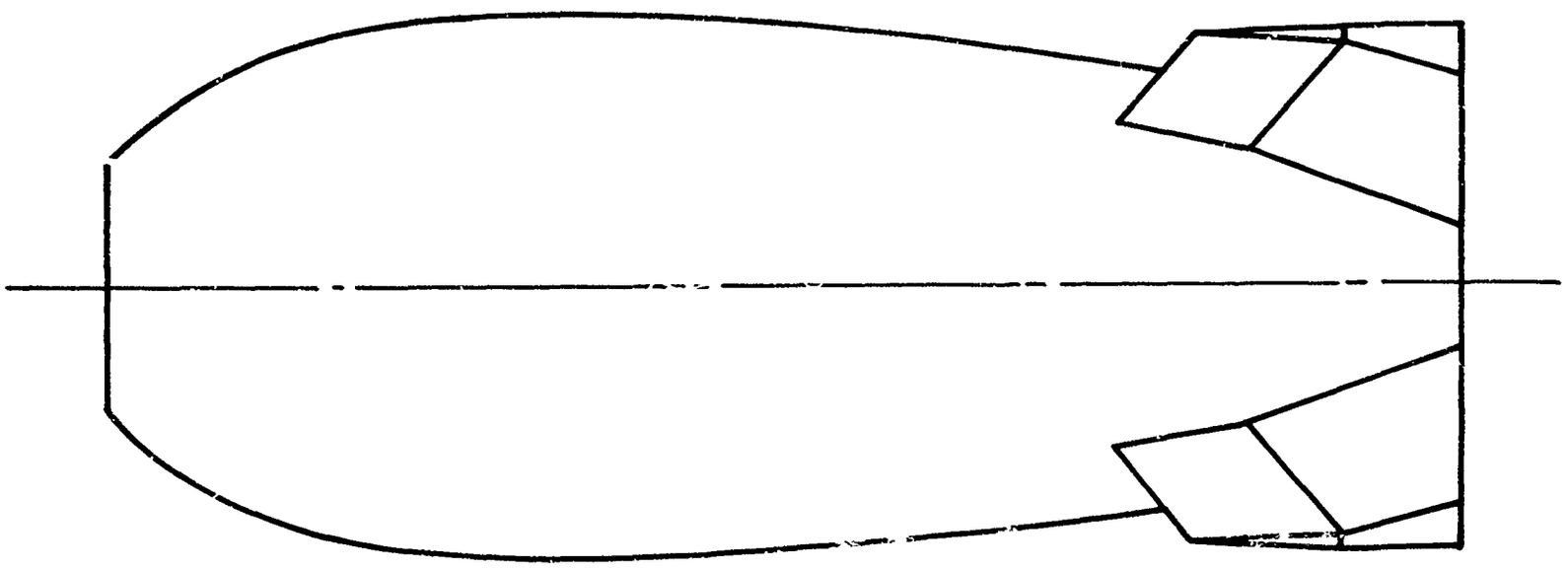

Figure 20 -- Configuration 3

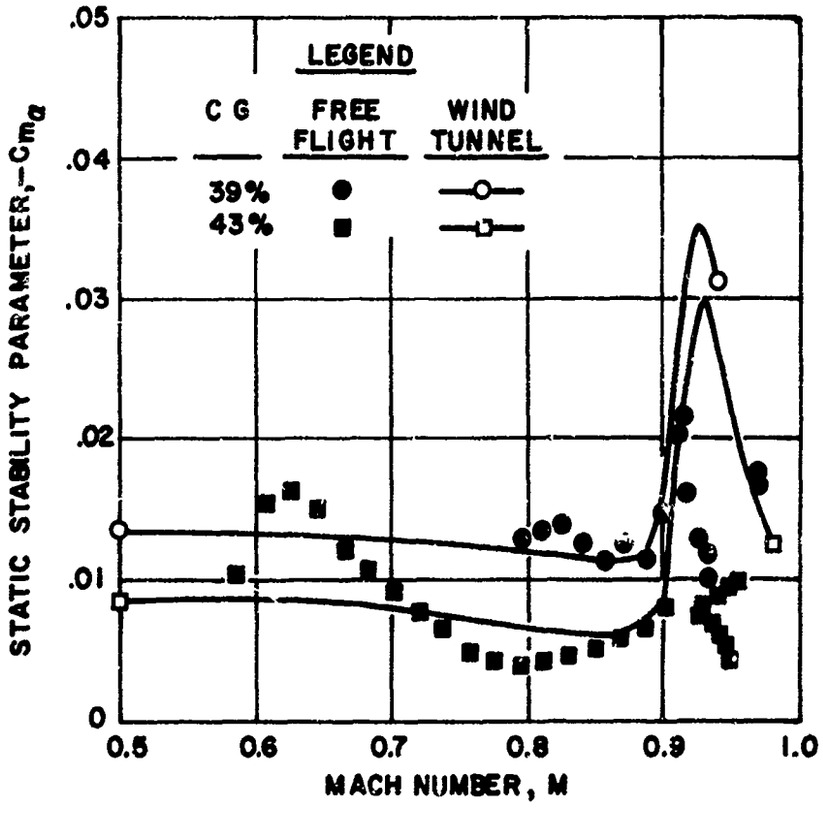

Figure 21 -- Comparison of Configuration 3 Static Stability Derived from Wind Tunnel and Quarter-Scale Flight Tests

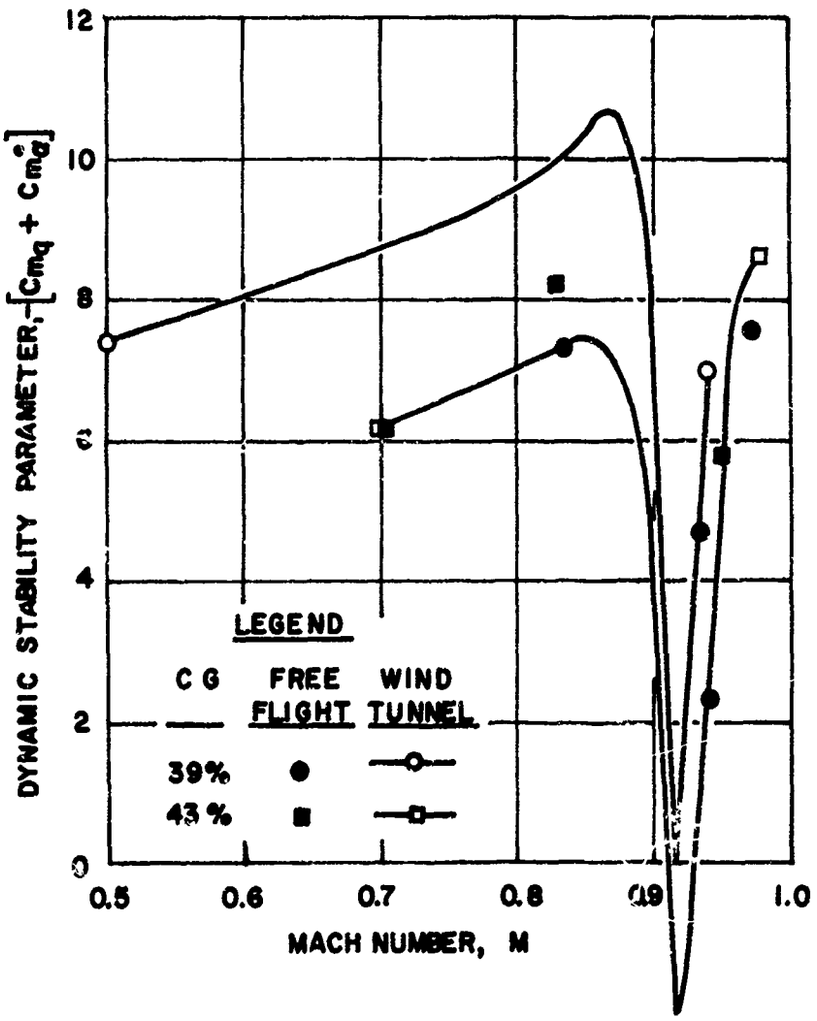

Figure 22 -- Comparison of Configuration 3 Dynamic Stability Derived from Wind Tunnel and Quarter-Scale Flight Tests

DISCUSSION

Lars Ericsson:

Did you have ridges to steady the shock, restrict the shock movement and did you measure dynamically the effect with and without this roughness on the surface?

J. Reed:

Do you mean with and without spoiler bands?

Lars Ericsson:

Yes.

J. Reed:

The effect of spoiler bands was to reduce the band at which the store was dynamically unstable.

Lars Ericsson:

The Mach number range?

J. Reed:

The spoilers decreased both the Mach number band dynamic instability and the amplitude of oscillation.

Lars Ericsson:

Secondly, in regard to this effect of nose bluntness one can produce a certain nose drag either by having an elliptic nose shape for instance, or by taking a flat face and then turn an elliptic fairing to get a smooth shoulder. In the latter case the sharp curvature is right in the front. The effect is to decrease the Mach number region in which nose induced separation occurs because the boundary layer has a chance to reattach. It separates but reattaches before the shoulder and you don't get that massive separation downstream.

J. Reed:

Yes. The problem that we had was that we really could not do that because we did not have room. The whole store was compressed into a fineness ratio of 2.13 and we didn't have any room to increase the nose length to make a longer ogive there. We did study that effect later and the data indicates that you are correct.

G. Chrusciel:

Did you ever try testing the configuration with both increasing and decreasing Mach number over the Mach number range?

J. Reed:

Yes. Our standard testing technique was to bring the tunnel up in velocity with the model free to oscillate and watch the recorder. As best we could determine there was no effect. We were in a wind tunnel where you could not increase or decrease the Mach number rapidly, and we could detect no effect of either increasing or decreasing the Mach number at the rate at which we were able to do it.

G. Chrusciel:

What I had reference to in Polaris testing in which you could get a supersonic or a subsonic flow pattern established right around Mach 1 depending upon if you approached it from lower speeds or from higher speeds which was quite pronounced in the data.

R. Meyer:

I wondered if you could observe fin effectiveness on these blunt shapes. Well, I presume the fin effectiveness was considerably down and assuming that, could you say whether it was just a lowered or decreased dynamic pressure into the tail surfaces or was it a downwash phenomena on these fins?

J. Reed:

I think that it was separation since the body came down with such a steep curve after the maximum diameter that the flow tended to separate right off of the maximum diameter. By the way, there is a little story on the double wedge fins. Some of the people from BRL might remember when we fired numerous ballistic rounds trying to come up with a stable configuration for the Mark IV and somebody suggested to the physicists that they use a double wedge air foil-meaning a diamond airfoil. The physicists did not know what they meant, so they had a double wedge-5 degree, then 25 degree-air foil and it worked. Later they tried a diamond air foil and it did not work.

THE DESIGN AND PERFORMANCE OF A DYNAMIC MODEL DRIVE SYSTEM

by

D. L. Tinnes

Marshall Manned Space Flight Center

NASA

Huntsville, Alabama

This system uses a low mass, short-coupled electromagnetic drive system suitable for payload type bodies. Unique approaches to electrical feedback for stabilization and measurement of sustaining power are used.

I. SUMMARY

This paper describes the initial design and development of a forced oscillation balance system for measurement of dynamic stability parameters of Saturn vehicle payload bodies in the MSFC 14 x 14 Inch TWT. The mechanical and electrical characteristics of the system are discussed in detail and preliminary performance results are described. This system incorporates several unique features in its design and operation which contribute to its utility as an experimental instrument; most of these could be applied to the design of other balance systems tailored to meet other sets of program requirements.

II. INTRODUCTION

The desire for dynamic stability test capability for Saturn vehicle payload shapes in the MSFC 14 x 14 Inch Trisonic Wind Tunnel lead to the development of the forced oscillation balance system described in this paper.

Analysis of the probable test workload gave the following guidelines for design of the system:

A. Model Shape - Two principal configurations were considered, an LES-Apollo with optional 1 - diameter skirt, and an LES-Apollo - Service Module - LEM Adapter with optional 1 - diameter skirt (See Figure 2).

B. Centers of Rotation - The widest possible range of locations of the center of rotation was desired for each configuration.

C. Angle of Attack Capability - Trim angles of attack up to 8° were desired, with oscillation amplitudes up to $\pm 2^{\circ}$.

D. Frequency - The ability to vary test frequency and a high frequency capability were desired.

III. SYSTEM DESIGN

Mechanical

Mechanically the most distinctive feature is the use of torsion flexures to provide (and vary) the spring constant of the system. (See Fig. 1). A Bendix "Free-Flex" crossed flexure pivot is used to establish the center of rotation and to transmit aerodynamic loads to the sting. A pair of torsion bars are mounted symmetrically on the axis of rotation to provide restoring torque for the system. They are attached independently of the motor and the model so that they may be readily removed and replaced without further disassembly of the balance. In this way the torsional spring constant of the system (and consequently the natural frequency) may be changed during a test in the wind tunnel. These torsion bars also carry the strain gage bridges which provide the displacement signal to the data acquisition system.

SYSTEM DESIGN (Cont'd)

Mechanical

The structure is integrated to reduce weight, with a central beam which serves as the principal structural member for the balance and the model, as well as providing a frame for the motor coil. This beam is made in two pieces; the rear piece (Item "B", Fig. 1) serves as the motor coil frame while the front section (Item "C", Fig. 1) contains the mount for the Bendix pivot. Interchangeable front sections thus permit varying the center of oscillation without any other structural changes in the balance or model.

All parts of the balance - motor structure are designed and assembled to permit easy repair or replacement. This is important since the life expectancies of some components are measured in hours at a frequency of 100 cps. In particular, the Bendix pivot has an expected life of less than 40 minutes at 100 cps, carrying a resultant aerodynamic load of 60 lbs. These conditions represent the worst case for the configuration shown in Fig. 2b, so that the actual service life of the pivot should be somewhat greater, but this example demonstrates the need for ease of maintenance.

An additional benefit obtained from this type of mechanical construction is the capability to tailor the balance to the requirements of the test program. The balance described in this paper was designed to satisfy the needs of a particular test program in the areas of model shape, centers of rotation, angle of attack requirements, and oscillation frequency, as described in the Introduction. This was accomplished by providing maximum flexibility in these areas, however, rather than designing rigidly to meet the immediate requirements. For example, the "Free-Flex" pivot chosen was the smallest which could carry the aerodynamic loads involved in the tests, in order to permit the most forward possible location of the oscillation center in the body of Fig. 2a. For a program involving a shape with a higher C_L (such as a lifting body or winged booster), pivots of this type are available which permit doubling or quadrupling load capacity with relatively modest increases in pivot diameter and length; in fact, capacity is almost exactly proportional to the square of the diameter of the pivot, and a unit capable of indefinite life at loads greater than the capacity of the model support mechanism in our 14 x 14 Inch TWT is only 5/8 inch in diameter.

The model and balance are balanced statically as a unit to locate the C.G. at the center of rotation for each test configuration. Where possible this is accomplished through the use of interchangeable escape rockets of different weights. In this way the dynamic input to the sting in the vertical direction is reduced to a negligible value, and no struts or stay wires are required on the sting.

SYSTEM DESIGN (Cont'd)

Electrical

The approach used in the design of the system incorporates a direct electro-magnetic drive, or oscillating motor, within the body of the model to be tested. (See Fig. 1). Ideally, a forced-oscillation dynamic balance system should have a good signal-to-noise ratio, low mass to permit high natural resonant frequency, a high ratio of aerodynamic to total damping, adequate torque and power to replace system losses and permit reasonable acceleration times, and an aerodynamically clean configuration. Tests on the bench and in the MSFC 14 x 14 Inch TWT indicate that all goals have been met or exceeded. (See IV Test Results). The design is discussed here in terms of these goals.

The signal-to-noise criterion has been well satisfied, as can be seen in Fig. 4. The figure does show a low amplitude, high frequency signal superimposed on the driving torque. This noise was noted before the test began and is attributed to electrical pick up on the unshielded signal leads to the amplifier powering the motor. Proper shielding will be incorporated to eliminate this noise. It is worth mentioning that all data is unfiltered, eliminating the possibility of phase shifts due to filter phase characteristics.

Utilizing direct magnetic torque coupling to the model has eliminated the mechanical noise that would otherwise be measured along with torque in mechanically coupled systems. Also, the extremely narrow band-pass characteristic of the balance filters out almost all environmental noise.

The system possesses excellent frequency capability. Elimination of the mechanical torque member has reduced the inertia of the balance and simplified it to a single degree-of-freedom mechanical system. The resonant frequency of the model on the bench is 64 cps with the torsion bars that are presently installed. As described previously, it is only necessary to exchange torsion bars within the model to increase the frequency to a value of over 100 cps, and even higher frequencies should be possible.

Pre-test evaluation of the damping in the system indicated very low damping. Calibration in the evacuated test section of the wind tunnel during the test substantiated this and indicated that the non-aerodynamic damping present is almost entirely structural. Since damping of this type is a linear function of displacement amplitude and is independent of the frequency, under some conditions it may be more favorable to test at very low amplitude. Some evidence of this may be seen in comparing runs 5 and 6 in the data table given in Section IV. The test data given in the table also indicates a consistent favorable ratio of aerodynamic to total damping. The value of the equivalent viscous damping coefficient obtained from calibration in vacuum was 0.18 in.-lb.-sec/degree.

SYSTEM DESIGN (Cont'd)

Electrical

The torque capability of the motor now in use is 1.11 in.-lbs. per amp of current. During tunnel testing, the maximum torque that was applied to the motor was ±5.55 in.-lbs. at approximately five cycles off resonance. At resonance, the greatest torque required of the motor was ±1.67 in.-lb. Due to the low inertia of the system and the torque reserve of the motor, the model can be rapidly accelerated.

By optimizing the motor's field and the armature coil, it is feasible to create a torque capability at least 5 times greater than is presently available in the prototype motor. Torque calculations for motor design and calibration are given in Section VI.

Figure 3 is a block diagram of the control and data acquisition circuit in use at this time, illustrating the relative simplicity of the electronic requirements. To date only normal control of frequency and amplitude have been used but a complete closed-loop system will be operational in the near future.

IV. TEST RESULTS

A preliminary aerodynamic test was conducted on April 19, 1965, to permit evaluation of the system under operating conditions. For this test the frequency and amplitude were controlled manually. A tabulation of the data obtained is given below.

Run Number	Mach Number	Trim Angle of Attack	Frequency (cps)	Oscillation Amplitude	F_t, Total Damping (in-lb-sec)	F_a, Aerodynamic Damping (in-lb-sec)	$\frac{F_a}{F_t} \times 100\%$
1	0.95	0°	61	$\pm 1.48^\circ$	0.084	0.060	72%
2	0.95	2°	61	$\pm 1.48^\circ$	0.116	0.093	80%
3	1.10	0°	61	$\pm 1.54^\circ$	0.153	0.129	84%
4	1.10	2°	61	$\pm 1.48^\circ$	0.166	0.142	86%
5	1.46	0°	61	$\pm 1.48^\circ$	0.107	0.083	78%
6	1.46	0°	61	$\pm 0.59^\circ$	0.081	0.065	80%

This table illustrates the consistently large values obtained for aerodynamic damping expressed as a percentage of the total measured. The data given here covers the transonic range, which is of most immediate interest. Two runs were also made at Mach 2.99 and trim angles of 0° and 2°; F_a was over 50% of F_t for both of these runs, at oscillation amplitudes of $\pm 1.5^\circ$.

V. PERFORMANCE CHARACTERISTICS

In summation, the system has the following operating characteristics which contribute to its usefulness as an experimental instrument.

A. The driving torque to the model is provided by direct electromagnetic coupling, with no intermediate mechanical elements. This results in extremely low noise in the torque signal and a very high signal-to-noise ratio. No filtering of the output signals is required, eliminating a possible source of phase error.

PERFORMANCE CHARACTERISTICS (Cont'd)

B. Since the torsion bars are not loaded by the static aerodynamic loads, K_t, the mechanical torque coefficient is essentially constant for all test conditions, and no calibration is required. The maximum change in K_t for this prototype balance is less than 1%, using torsion bars giving f_N = 64 cps.

C. The balance has high frequency capability. For the test program using the model and balance in their present form oscillation frequency will be limited to approximately 100 cps because of the high loads imposed on the escape tower structure; for a more compact shape, a useful frequency of at least 200 cps is anticipated.

D. Direct electrical data output is provided, with relatively simple electronic requirements. This suggests the possibility of building all of the control and acquisition electronics into a single compact unit. This "suitcase" would make the system portable and allow selection of the test facility to suit program requirements, or permit tests of the same hardware in a number of facilities.

E. The high torque and power available permit almost instantaneous acceleration, an important feature for operation in short-duration blowdown facilities. During the preliminary test, ten or more frequency changes could be made and steady-state outputs obtained in a run time of about 60 seconds, with only manual control of frequency and amplitude.

F. The flexible mechanical design permits inexpensive modifications to "tailor" the system to meet test requirements.

G. The high power available, and good heat transfer and cooling permit large inputs for off-resonance operation. The useful bandwidths for the near 60 cps resonance of the preliminary test were 10 cycles at $\Delta\alpha = \pm 1.5^{\circ}$ and 20 cycles at $\Delta\alpha = \pm 0.5^{\circ}$.

H. The design of the balance permits an aerodynamically clean configuration, with no external rods or wires.

VI. CALCULATIONS

F = damping (in-lb-sec)
ℓ = coil length (in)
e = back emf (volts)
i = current in coil (amps)
θ = amplitude (radians)
B = field strength (lines/in^2)
d = moment arm (in)
T = torque (in-lb)
ω = frequency (radians/sec)
r = velocity (radians/sec)

For the system vibrating at resonance,

$$F = \frac{T}{\dot{\theta}} = \frac{T}{\omega\theta}$$

$$T = d(\text{Force}) = 0.885\, B\ell i d \times 10^{-7}$$

$$\frac{T}{i} = 0.885\, B\ell d \times 10^{-7} \text{ (in-lb/amp)}$$

$$e = B\ell r \times 10^{-8} = B\ell\omega\theta \times 10^{-8}$$

$$\frac{\omega\theta}{\ell} = \frac{10^8}{B\ell} \text{ (radian/volt-sec)}$$

$$F = \frac{T}{i} i \Big/ \frac{\omega\theta}{\ell}\ell = \frac{(0.885\, B\ell d \times 10^{-7})(B\ell \times 10^{-8})\dot{i}}{\ell}$$

$$F = \frac{\dot{i}}{\ell}\, 0.885\,(B\ell)^2 d \times 10^{-15}$$

For the prototype system, calibration gave $B\ell = 4.77 \times 10^6$

$$\therefore\ F = \frac{\dot{i}}{\ell}\, 0.885\,(4.77)^2 \times 10^{-3} d$$

$$F = \frac{\dot{i}}{\ell}\, 0.05; \text{ with } d = 2.5$$

Off resonance this becomes,

$$F = \frac{\dot{i}}{\ell}\, 0.05 \cos\phi, \text{ where } \phi \text{ is the phase angle}$$

The value obtained for $B\ell$ indicates a field strength of about 10^4 (lines/in^2). Values of B approaching 5×10^4 should be possible; also ℓ could be approximately doubled in obtaining an impedance match for the 16 Ω taps on the power amplifier. These changes should produce the torque increase mentioned in Section III.

VII FIGURES

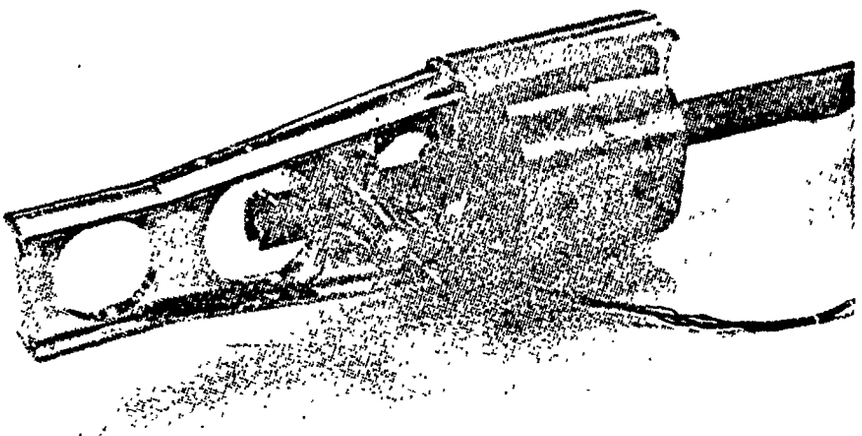

Balance Assembly

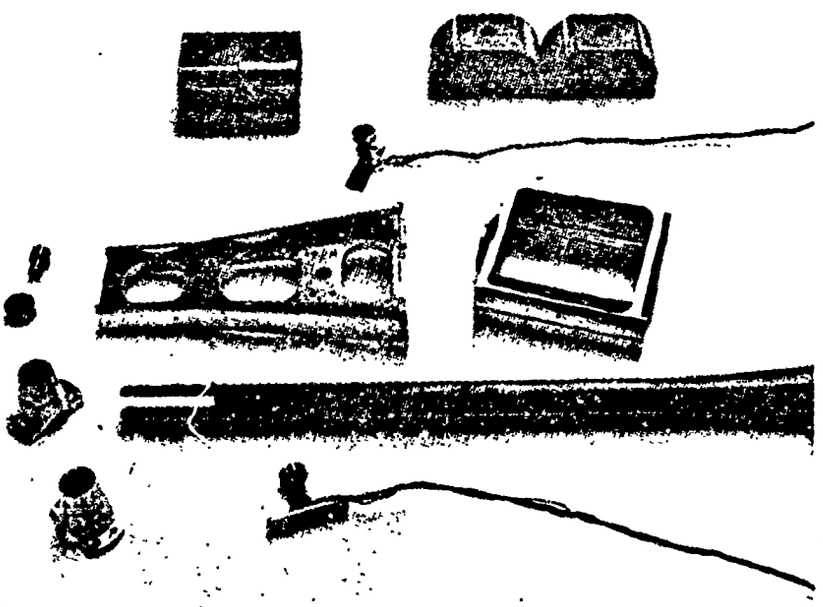

Components

Figure 1

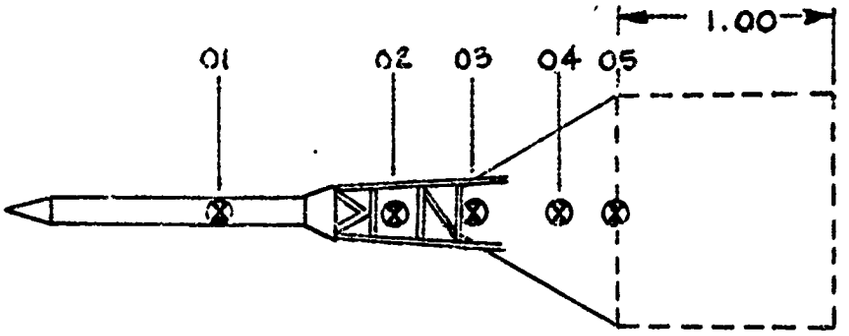

Figure 2A

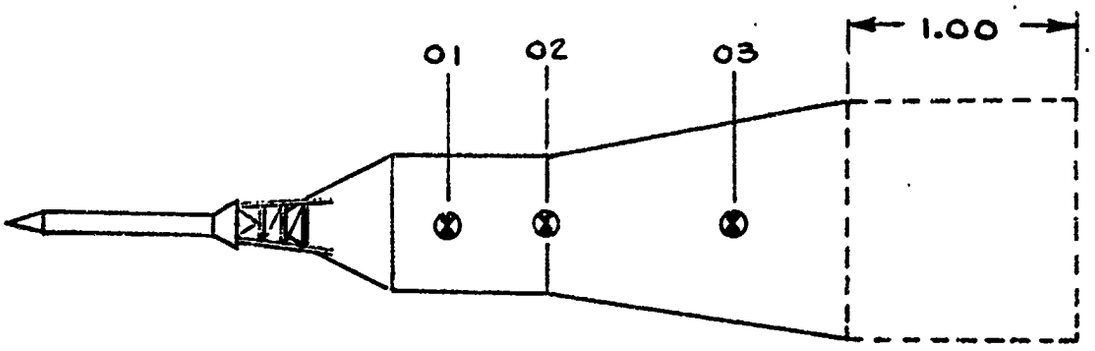

Figure 2B

Test Configurations

Figure 2

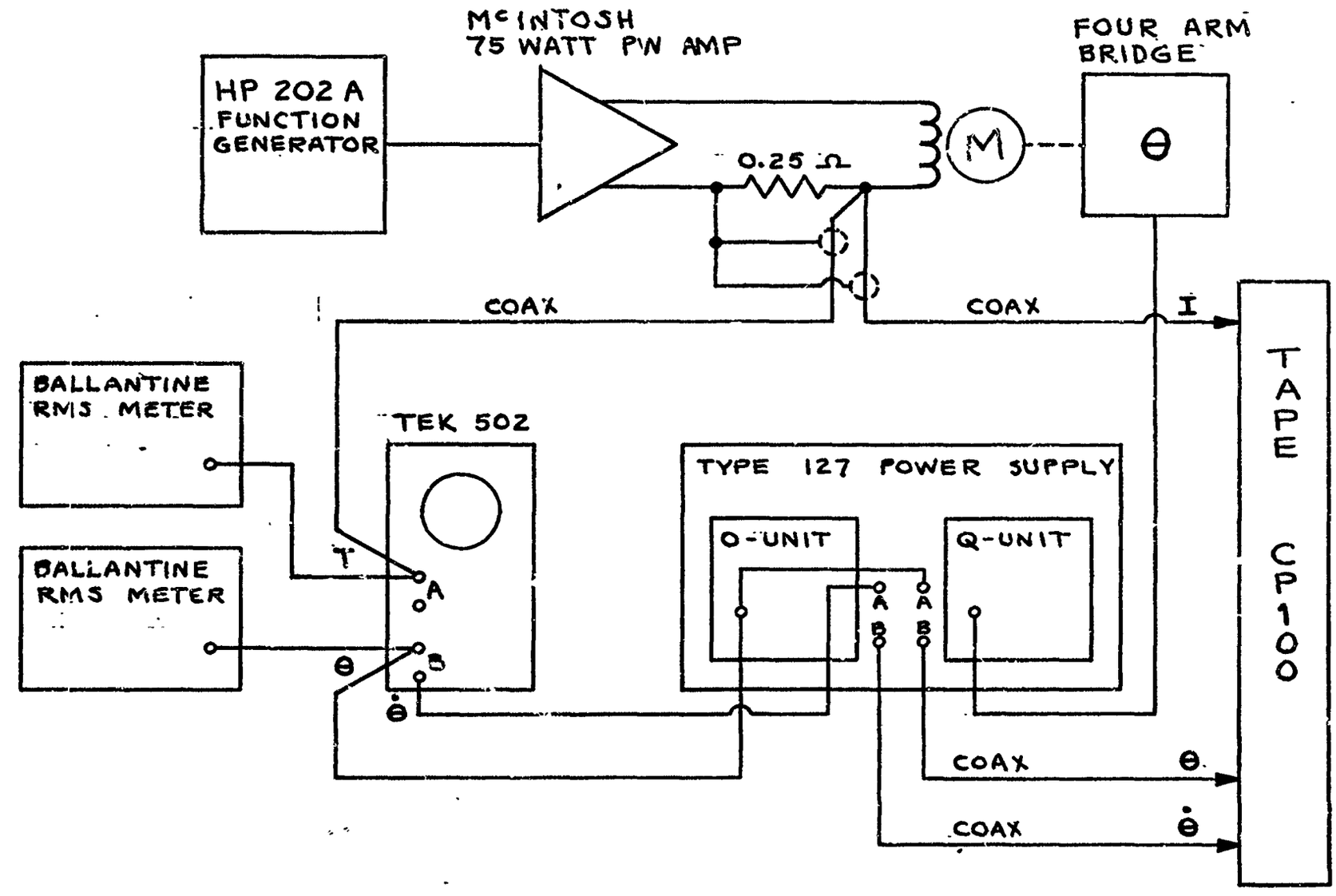

Circuit Diagram
Figure 3

Oscilloscope Records - Run #6

f = 61 cps M = 61 cps

$\alpha = 0^{\circ}$ $\Delta\alpha = \pm 0.5^{\circ}$

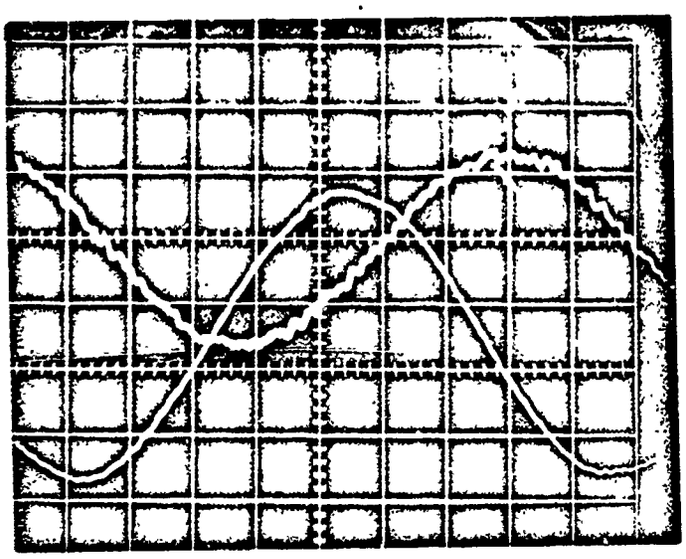

Top = torque
Bottom = displacement

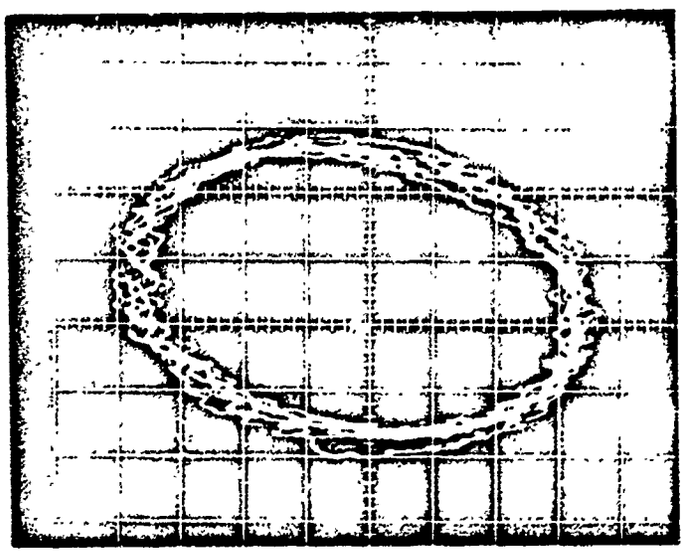

Horizontal = torque
Vertical = displacement

Typical Test Data
Figure 4

DISCUSSION

D. Coen:

Dave, is this basically a so-called resonate-type system?

D. L. Tinnes:

It is a tuning fork, literally. It is extremely sharp. The off resonance capability is due to the large electrical power input available, and not to any inherent design in the balance mechanics.

D. Coen:

What is the actual driving mechanism?

D. L. Tinnes:

It is an oscillating motor. The field is provided by permanent magnets and the signal is on a coil which is attached to the model.

L. K. Ward:

You do incorporate resolvers in the system to resolve the torque signal when you are off of resonance.

D. L. Tinnes:

We can resolve off resonance by recording the displacement off the torsion bars; they are gaged. We get the displacement and torque display, to determine resonance from a figure such as this lissajous plot.

L. K. Ward:

Correct. When they are 90 degrees out-of-phase, you are on resonance, but the point is as you move off from resonance then you have to resolve the torque signal into its in and out-of-phase components as compared to the displacement signal.

D. L. Tinnes:

This is easy. We can make at least a crude calibration right off the scope from the figure for this phase angle. This is what you are talking about?

L. K. Ward:

Right.

D. L. Tinnes:

We can get the phase angle from this figure. It is much more accurate to determine it through an electrical circuit, but we have done this in the data we have presented here.

Bill Neighbors:

I am a little bit more familiar with what you were asking there as I have been responsible for the electrical end.

D. L. Tinnes:

This is my co-author here.

Bill Neighbors:

I provided two bridges per torsion bar--one bridge for displacement and one bridge for spare and two for resolving. I had another scheme in mind for acquisition and then I provided these extra bridges for resolving in case the other scheme I had failed, but the method of acquisition looks real good. I believe there will be no problem in determining phase shifts. I believe this is why you are thinking about this--resolving the torques into the real and sort of reactive components.

L. K. Ward:

The in- and out-of-phase components.

Bill Neighbors:

Right. So we have the capability already built in to resolve the torque but I really don't see the need to go through with it. We have new torsion bars in design and I am not planning to gage them for that purpose.

L. K. Ward:

I have an additional question. What is the purpose of obtaining data at these higher frequencies?

D. L. Tinnes:

I understand that it reduces one area of uncertainity--that we can scale the full scale frequency to our model scale.

L. K. Ward:

Right. $\omega d/2V$ but these are pretty high frequency for this scaling parameter. This is on the Apollo Launch Escape Vehicle?

D. L. Tinnes:

That is right.

L. K. Ward:

Bass, we ran these at fairly low frequencies, were we way out of line?

Bass Redd:

No, I think not. We were basically looking for dynamic stability problems on the spacecraft, and I assume that you are looking for dynamic derivatives to get a structural response--is this not correct?

D. L. Tinnes:

This is essentially true.

Bass Redd:

We were worried about rigid body motions; he is basically worried about individual short coupling body responses for structural response.

D. L. Tinnes:

I might say that the program which I have referred to here a couple of times which this system was designed to provide experimental verification for a quasi-steady theory of Mr. Lars Ericsson.

CLOSING REMARKS

C. J. Schueler:

I know it would certainly be impossible to even attempt to summarize in the short time available some of the high points of this meeting; however, if you will permit me a few observations. Many of us that are involved in operating test facilities often do not have the full appreciation of some of the problems that have been encountered in flight. Some of the papers that we heard in the earlier part of our meeting dealing with the analysis of flight data certainly will allow us now to have a little more appreciation of the problem and possibly reflect more on this so that we can see where we can extend the role of ground test facilities in trying to find a solution to these problems. I think one rather obvious observation is the significant progress that has been made in the last couple of years in developing the theoretical, inviscid methods for the hypersonic and hypervelocity flow regime and also those theories that have been developed to study the influence of ablation. However, I would like to mention that it remains to extend theories of this type to account for the viscous interaction effects at hypervelocity speeds and low Reynolds numbers. I think this is a problem that wasn't treated sufficiently at this meeting. Methods of reducing wind tunnel and free flight data appear to be undergoing a very thorough examination to more clearly understand the meaning of the results from the ground test facilities especially where these large nonlinearities exist. A question of how does one simulate the effects of ablation in a wind tunnel is being approached in several different ways and we have seen some rather clever techniques these past few days that are being employed to try to handle this particular problem. This appears to be an area that will continue to receive attention for sometime to come and probably at our next workshop will be one of the key topics for discussion. Free flight testing in the wind tunnel continues to be a very useful technique, and there appears to be many new applications and efforts toward improvement of the equipment and also the quality of the results. I would like to thank all of our speakers for their very excellent papers. I would like to thank all of our Session Chairmen for the fine job that they have done and especially you who have actively participated in this workshop to make it most interesting for all of us.